Italian National Agency for New Technologies,
Energy and Sustainable Economic Development

High Performance Computing on CRESCO infrastructure: research activities and results 2014

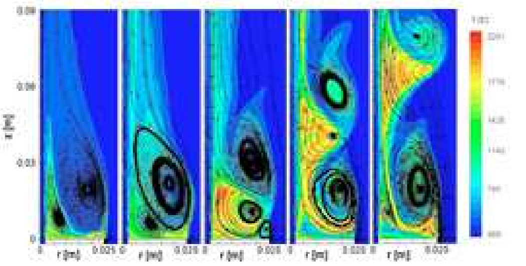

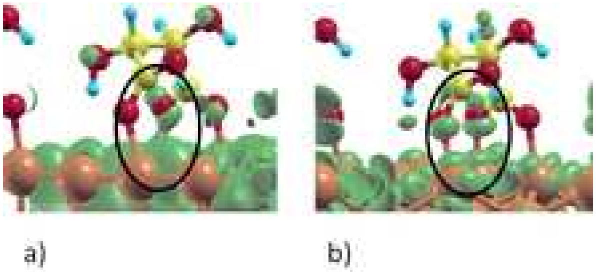

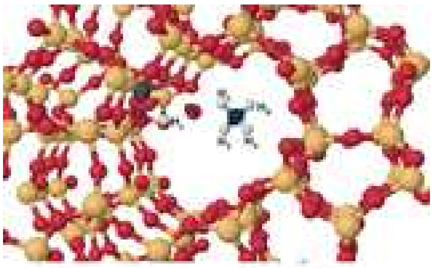

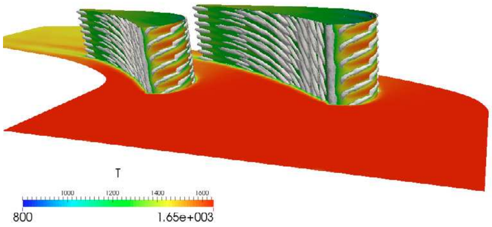

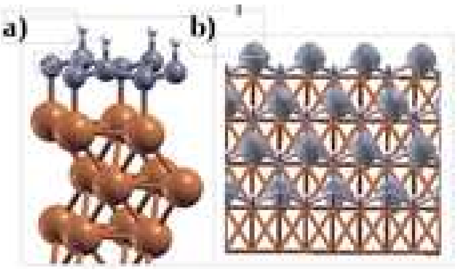

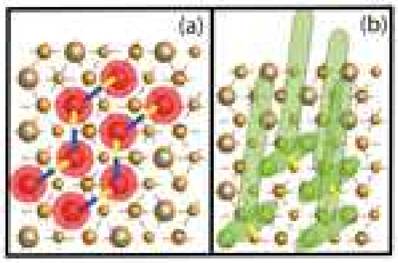

December 2015

Contributions provided by a selection of users of the CRESCO infrastructure.

Scientific Editor: *Fiorenzo Ambrosino*, ENEA, DTE-ICT-HPC, CR Portici

Acknowledgements: We wish to thank *Filippo Palombi* that contributed to the editing of this Volume.

Cover: *Amedeo Trolese*, ENEA, DTE-ICT-PRA, CR Frascati

ISBN: 978-88-8286-325-8

Contents

Foreword

During the year 2014 CRESCO high performance computing clusters have provided more than 47 million hours of core computing time, at a high availability rate, to more than one hundred users, supporting ENEA research and development activities in many relevant scientific and technological domains. In the framework of joint programs with ENEA researchers and technologists, computational services have been provided also to academic and industrial communities.

This report, the sixth of a series started in 2008, is a collection of 28 papers illustrating the main results obtained during 2014 using CRESCO HPC facilities in various fields such as material science, efficient combustion, climate research, nuclear technology, plasma physics, biotechnology, aerospace, complex system physics. The report shows the variety of the applications of high performance computing, which has become an enabling technology for science and engineering.

ENEA Portici Research Centre near Naples is the location hosting the main ENEA computational resources since 2008. This is a result of the CRESCO Project (Computational Centre for Research on Complex Systems), co-funded, in the framework of the 2001-2006 European Regional Development Funds Program by the Italian Ministry of Education, University and Research (MIUR).

In 2014 the ENEAGRID computational resources attained the level of about 9000 computing cores (in production) and a raw data storage of 900 TB. Those values have been reached thanks to the availability of the new cluster CRESCO4 (4864 core Intel, 100 Tflops, QDR Infiniband network) installed within the TEDAT project funded by MIUR in the framework of the 2007-2013 European Regional Development Funds Program. At the end of 2014 are also been shut-down the first two CRESCO clusters installed in 2008 namely CRESCO1 (Tigertown CPU) and 256 nodes of CRESCO2 (Clovertown CPU); those systems in the years became obsolete for being used in HPC, therefore part of them have been reused in various not CPU-intensive tasks such as general ENEA ICT applications.

The Project CRESCO provided the resources to set up the first HPC x86_64 Linux cluster in ENEA, achieving a computing power relevant on Italian national scale (it ranked 126 in the HPC Top 500 June 2008 world list, with 17.1 TFlops and 2504 cpu cores). It was later decided to keep CRESCO as the signature name for all the Linux clusters in the ENEAGRID infrastructure which integrates all ENEA scientific computing systems, and is currently distributed in six Italian sites.

The success and the quality of the results produced by CRESCO stress the role that HPC facilities can play in supporting science and technology for all ENEA activities, national and international collaborations, and the ongoing renewal of the infrastructure provides the basis for a similar role in the forthcoming years.

Dipartimento Tecnologie Enegretiche, Divisione per lo Sviluppo Sistemi per l'Informatica e l'ICT, CRESCO Team

CRESCO Team and people involved in the management of ENEA-GRID infrastructure in 2014 were:
Dante Abate, Fiorenzo Ambrosino, Giuseppe Aprea, Tiziano Bastianelli, Francesco Beone, Riccardo Bertini, Giovanni Bracco, Marco Caporicci, Beatrice Calosso, Marta Chinnici, Roberto Ciavarella, Antonio Colavincenzo, Aniello Cucurullo, Pietro D'Angelo, Matteo De Rosa, Pasquale De Michele, Agostino Funel, Graziano Furini, Dante Giammattei, Simone Giusepponi, Roberto Guadagni, Guido Guarnieri, Alessandro Italiano, Simone Magagnino, Angelo Mariano, Giorgio Mencuccini, Carlo Mercuri, Silvio Migliori, Patrizia Ornelli, Filippo Palombi, Salvatore Pecoraro, Antonio Perozziello, Samuele Pierattini, Salvatore Podda, Fabrizio Poggi, Giovanni Ponti, Andrea Quintiliani, Alessio Rocchi, Carlo Scio, Fabio Simoni

LES study of a bluff-body burner fluid dynamics

I. Cornacchia[*]*, E. Giacomazzi*[1]*, F.R. Picchia*[1]*, D. Cecere*[1] *and N. Arcidiacono*[1]

[1] *IPSE, Casaccia Research Center, ENEA - Rome, ITALY*

Abstract. The bluff-body burner provides a flame suitable for the study of turbulence-chemistry interactions. Bluff-body burners also bear a great similarity to practical combustors used in many industrial applications. This geometry is, therefore, a suitable compromise as a model problem because it has some of the complications associated with practical combustors while preserving relatively simple and well-defined boundary conditions. A bluff-body burner is simulated at two different conditions: a non-reactive and a reactive one. LES numerical simulations were performed by means of the in-house code *HeaRT (Heat Release and Turbulence)* using parallel computers available at CRESCO4. In the non-reactive case, two simulations of two different turbulent subgrid scale models were performed: the Dynamic Smagorinsky model and the Transported SGS Kinetic energy (K^{sgs}) non-dynamic model. The reactive case simulation, instead, is characterized by a non-premixed flame of CH_4/H_2 and air and it is simulated using the k^{sgs} non-dynamic turbulent subgrid model. The effects of two different chemical kinetic mechanism were analysed: the fast chemistry and the detailed chemical mechanism of Law. The results of these simulations are compared to data available in literature.

1 Test - cases description

The burner is centred in a coflowing stream of air and consists of a circular bluff-body of 50 mm diameter with an orifice at its centre for the main fuel with a diameter of 3.6 mm. A complex flow pattern forms downstream of the face of the bluff-body where a recirculation zone is formed to produce enough hot gases to stabilise the flame to the burner. At sufficiently high fuel velocity, the jet flow penetrates through the recirculation zone and forms a jet-like flame further downstream. The jet flame can be extinguished in a region downstream of the recirculation zone where turbulence is well developed and the finite rate chemistry effects are significant. The flame may also reignite further downstream where turbulent mixing rates are relaxed.

1.1 Computational domain and grid set-up

The bluff-body burner is simulated at two different conditions: a non-reactive and a reactive one. The grid and computational domain are the same in both cases. The computational domain is 0.30 m in the axial direction downstream and 0.020 m upstream

---

[*] Corresponding author. E-mail: `isabella.cornacchia@hotmail.com`.

of the bluff-body. It has a radius of 0.075 m. As the image on the left of Figure 3 shown, the domain is axially symmetric and it is divided into three zones:

- ZONE 0 is the main zone downstream of the bluff-body;
- ZONE 1 is the internal zone of the jet duct;
- ZONE 2 is the zone of coflowing air upstream of the bluff-body.

A two-dimensional, structured, stretched grid has been created: it is characterized by 600 nodes in axial and 200 nodes in radial direction. Then, it has been extruded, from 2D domain, by a rotation of an angle of 120° around the z axis (the image on the left of Figure 3). The computational accuracy, in general, is strongly sensitive to boundary conditions. An inlet condition has been used for the inlet fluxes in ZONE 1 and 2. On the duct walls and on the ceramic bluff-body a viscous, adiabatic, non porous wall condition is implemented. At the exits, a partially non-reflecting NSCBC outlet condition (with a reflecting coefficient of 0.5) is implemented.

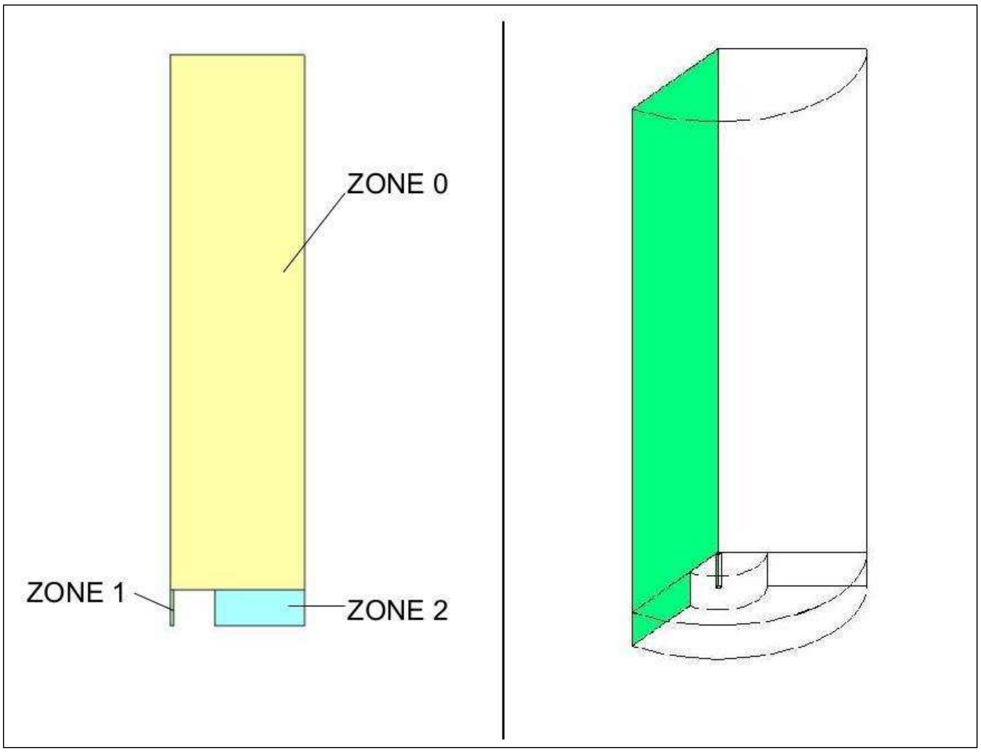

Figure 1: 2D and 3D domain

2 LES approach

Turbulent combustion is governed by a set of transport equations expressing the transport of mass, momentum, energy, species mass fraction and by a thermodynamic equation of state describing the gas behaviour: the Navier-Stokes equations. In principle, there is no difficulty in solving these equations, but to reduce computational costs modelling is necessary: LES approach is used. In LES, Navier-Stokes equations are filtered in space, hence, scales larger than the filter size Δ are resolved, while the smaller ones are modelled. For turbulence, the dissipative effects of subgrid scales can be explicitly modelled by means of a SubGrid Scale (SGS) model, i.e. by introducing a subgrid eddy viscosity, Eddy Viscosity Model, that links subgrid stresses ${\tau_{ij}}^{sgs}$ to strain rate ϵ_{ij}. In this work, two SGS models have been taken into account: the Dynamic Smagorinsky model [1] and the Trasported SGS kinetic energy (k^{sgs}) model [2]. For combustion, the EDC (Eddy Dissipation Concept) model proposed by Magnussen [3] is implemented. According to this model, the total space is subdivided into a reaction space, called "fine structures", and "surrounding fluid". All reactions of the gas phase components are assumed to take place within this space which represents the smallest turbulence scales where all turbulent energy is dissipated into heat. All reactions in the surrounding fluid are neglected. Two different approaches to estimate the volume fraction γ^* occupied by the small reactive fine structures in each computational cell are implemented: the Localized Turbulent Scales Model (LTSM) [4] and the Fractal model [2]. These two models have been used respectively in the detailed chemical kinetic model of Law [5] and in the fast chemistry kinetic model [6].

3 Results

In the non-reactive case, two 3D simulations with two different turbulent subgrid scale models were performed: the Dynamic Smagorinsky model and the Transported SGS Kinetic energy (k^{sgs}) non-dynamic model. Two vortices are found in the recirculation zone, characteristic of a "jet-dominant" flow. The outer vortex is stable and extends up to 1 bluff-body diameter axially and 80 % bluff-body diameter radially. The inner vortex is adjacent to the jet and it is narrower than the outer one. Three mixing layers are identified inside the recirculation zone: between the outer vortex and the coflow air, the outer vortex and the inner vortex and the inner vortex and the jet.

Numerical results are compared with experimental data collected, for the same flow and boundary conditions, by the Sandia National Laboratories and the University of Sydney [7]. Since in some cases there were disagreements between measured and computed quantities, results of the same test-case LES simulation carried out by Tomasz G. Drozda of the Pittsburgh University [8] are also taken into account.

Radial profiles of the axial and radial mean velocity and their RMS were analysed. Mean axial velocity radial plots show that in axial locations in the vicinity of the jet exit, the k^{sgs} non-dynamic model simulation has a good agreement with the experimental data especially in the zone of the bluff-body. Downstream, the centreline velocity is overpredicted by both the Dynamic Smagorinsky model and the k^{sgs} model. It can be due to the fact that the computational domain is a slice of a cylinder and the velocity on the axis is imposed equal to zero; as a consequence along the axis there are not enough fluctuations and the momentum does not decay as fast as in the experiment. The mean radial velocity plots show that all numerical results underpredict the measured data. It can be due to the fact

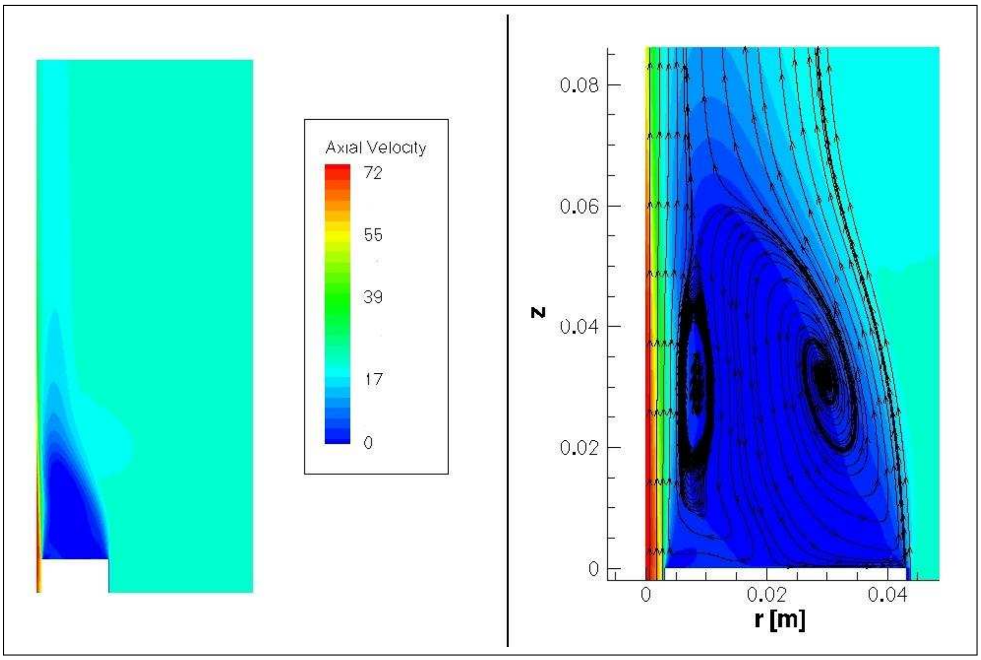

Figure 2: Mean axial velocity field and recirculation zone

that no conditioning was used for the radial velocity measurements and it may lead to a higher error for this component. However, all the numerical simulations show similar trends. Finally, the computed and measured RMS fluctuations of mean axial and radial velocity plots show a low peak in the outer shear layer between the coflow and the outer vortex and an high peak in the shear layer between the jet and the inner vortex. In the axial location in the vicinity of the jet exit, the Smagorinky dynamic predictions of both RMS fluctuations of axial and radial velocity show a good agreement with the experimental data. However, because of the previously mentioned boundary condition, in correspondence of the axis, in that zone RMS fluctuations predictions are underpredicted by the k^{sgs} and the Smagorinsky dynamic simulations. Downstream, all simulations predictions have similar trends, but there is not an agreement with the measured data as good as in the previous axial locations. In the k^{sgs} subgrid model simulation, three sampling points were introduced to carry out the fluctuating kinetic energy spectrum (Figure 3): m1 on the axis at the jet exit, m2 downstream m1 and m3 on the axis downstream m2. The m2 and m3 spectrum plots show two of the characteristic slopes of the energy spectrum: the $k^{-5/3}$ law, typical trend of the inertial subrange and the k^2 slope, typical of the forced turbulence. The m1 kinetic energy spectrum plot shows a trend that does not decrease as the other two. It is due to the location of this sample: it is on the axis immediately after the jet outlet in a zone of fluid expansion where there is the effect of the edge that does not lead to an energy transfer to small scales.

In the reactive case, a Transported SGS Kinetic energy (k^{sgs}) non-dynamic turbulent model and a fast chemistry chemical model simulation was implemented. As in the non-

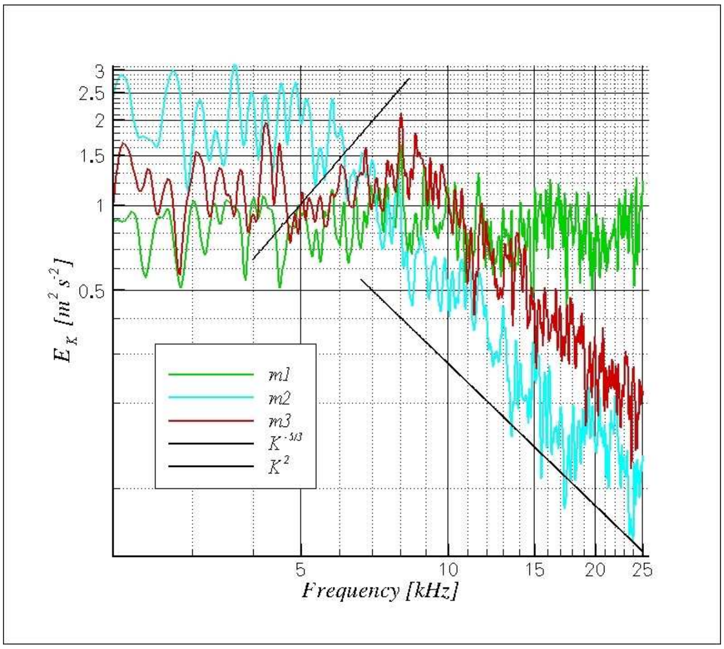

Figure 3: Kinetic energy, E_k, spectra of the three samples m1, m2, m3

reactive case, the main features of a ”jet-dominant” flow are found in the recirculation zone. However, the big disagreement between the measured and computed radial plots led to a more detailed analysis. Two 2D LES simulations with two different chemical kinetics were implemented to study the flow field development and the validity of the chemical kinetic model implemented. Indeed, in addition to the fast chemistry model simulation, a 2D simulation with the detailed chemical kinetic mechanism of Law is carried out. The analysis of the recirculation zone dynamics shows that the two 2D simulations provide the same behaviour: there is a shedding of irregular eddies from the inner edge of the bluff-body and an intense mixing inside the recirculation zone. Otherwise, the inner vortex is narrower than in the previous 3D analysis.

This leads to the conclusion that the disagreements in the computed radial plots were due to the flow field that was not fully developed. From the chemistry point of view, the detailed chemical kinetic model produces temperature distribution in better agreement with the experimental data than the fast chemistry. Hence, a 3D simulation with the detailed chemistry kinetic model is carried out. Numerical results of the 2D fast chemistry and both the 2D and 3D detailed chemical kinetic models are compared with the HM1, HM1E-s2 and B4F3-A experimental data set. The total sampling time is a little more than one recirculation zone dynamics cycle. Mean axial velocity plots show that the 3D simulation predictions are very close to the experimental data in the vicinity of the jet exit, but downstream, the centerline velocity is overpredicted. Also in this case, it is likely due to the computational domain that is a slice of a cylinder and then the momentum does not decay along the axis. Another consequence of this boundary condition is that the length

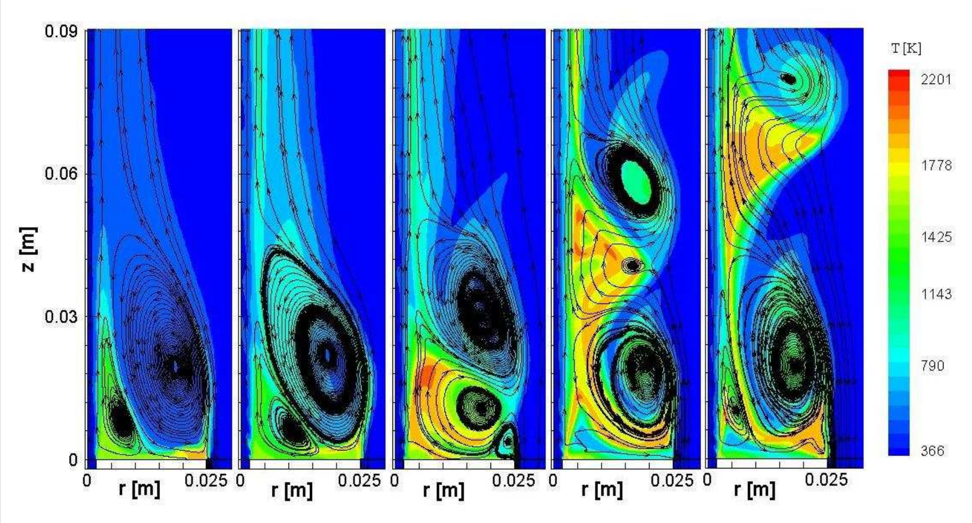

Figure 4: Recirculation zone dynamics in the fast chemistry mechanism simulation

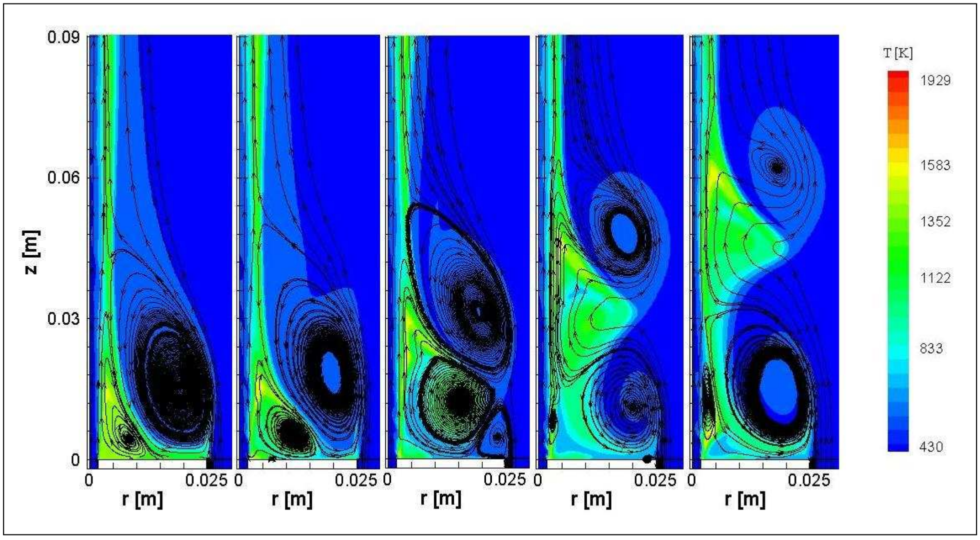

Figure 5: Recirculation zone dynamics in the detailed chemical kinetic mechanism simulation

of the recirculation zone is underpredicted. In fact, because the mean velocity decay rate does not decrease along the centreline, the transfer of momentum from the axial to radial direction is underpredicted. The mean radial velocity plots shows that in axial locations in the vicinity of the jet exit, computed and measured data have the same trends, but their values are in disagreement. It can be a consequence that no conditioning was used for the radial velocity measurements and it leads to a higher error for this component. The RMS fluctuations of axial and radial velocity components show the effects of a 3D LES simulations. Indeed, the fluctuations level of the 3D simulation is higher than the 2D one. In all plots, but especially for the radial fluctuations, the peak of the 3D simulation is quite similar to the peak of the measured data. However, in the zone of the axis, because a boundary condition imposes a radial velocity equal to zero, the RMS fluctuations are underpredicted by all the simulations. Finally, the temperature plots of the 3D simulation show a good agreement with the experimental data. The disagreement in the other axial locations can be due to lower turbulence predicted in a slice domain.

4 Conclusions

Both non-reactive and reactive simulations results show disagreement in the centreline velocity. Since it occurs independently from the subgrid model implemented, it is probably due to the computational domain itself. In particular, the fact that the domain is characterized by a slice of 120° of a cylinder has, as a consequence, that along the axis, the momentum does not decay as quickly as in the experiments. In this way also the transport of the axial momentum to the radial one is reduced. In particular, in the reactive case, it leads to strong effects on turbulence-chemistry interactions in the zone of the flame neck that affect the flow also downstream.

In the future, for both the non-reactive and reactive case, a 3D simulation with the complete cylinder will be implemented in order to avoid the boundary conditions along the axis. In particular, for the reactive case, the detailed chemical kinetic model will be implemented. Considering the high computational costs of these simulations, in the new ones, Navier-Stokes equations preconditioning or a pseudo compressible formulation will be implemented in order to have a time-step of almost two order of magnitude larger.

5 Cresco4 Performance

5.1 Non-reactive case

Cresco4 performance was almost the same for both the 3D non-reactive simulations studied. An example of processors scalability is shown in the table below:

Number of Processors	Δt
144	0.22s
192	0.12s
240	0.13s

5.2 Reactive case

Cresco4 processors scalability of the final 3D detailed chemical kinetic model simulation is shown in the table below:

Number of Processors	Δt
64	0.23s
128	0.12s
192	0.3s

References

[1] Germano M., Piornelli U., Moin P., Cabot W.H.:"A dynamic subgrid-scale eddy viscosity model", Physics of Fluids A, Vol 3, 1760-1765, 1991.

[2] Giacomazzi E., Bruno C., Favini B.,: "Fractal modelling of turbulent mixing", Combustion Theory Modelling 3, 637-655, 1999.

[3] Magnussen, B.F.: "The Eddy Dissipation Concept for Turbulent Combustion Modeling. Its Physical and Practical Implications", Norwegian Institute of Technology, Report N-7034, Trondheim, Norway, October 17, 1989.

[4] Giacomazzi E., Cecere D., Picchia F.R., Arcidiacono N.: "Sviluppo di un Modello LES per Fiamme Turbolente Premiscelate", Ricerca di Sistema elettrico, Settembre 2014.

[5] Sankaran R., Hawkes E.R., Chen J.H., Lu T., Law C.k.: " Structure of a spatially developing turbulent lean methane-air Bunsen flame", Proceedings of the Combustion Institute, Vol 31, 1291-1298, 2007.

[6] Giacomazzi E., Battaglia V., Bruno C.: "The coupling of the turbulence and chemistry in a premixed bluff-body flame as studied by LES", Combustion and flame 138, 320-335, 2004.

[7] University of Sydney, Thermal Research Group website, Bluff-body Flames, http://www.mech.eng.usyd.edu.au/thermofluids/bluff.htm, 2005.

[8] Drozda T. G.: "Implementation of LES/SFMDF for prediction of non - premixed turbulent fames", University of Pittsburgh, 2005.

A first principles study on the Fe(1 0 0)/Pb corrosion phenomena

Simone Giusepponi[*], *Massimo Celino*

ENEA, C. R. Casaccia, via Anguillarese 301, 00123 Rome, Italy

Abstract. The corrosions of structure materials such as stainless steel in liquid Pb metal are a big obstacles for the application of the liquid Pb into the fast breeder reactors as the coolants. The present work is trying to seek the atomic mechanism of the corrosion phenomena from the point-of-view of the ab-initio framework.

1 Introduction

The ferritic/martensitic steels will be widely used in the next generation of nuclear reactors due to their high thermal conductivities, high resistance to swelling, low expansion coefficients, and so on. In accelerator driven systems (ADS), they are chosen as the structural materials and the containers for liquid heavy metals and alloys, which are selected as the spallation target and the coolant. However, steels can be severely corroded if they are exposed to liquid metals and alloys directly at high temperatures. The so called liquid metal corrosion problem has been recognized as one of the most critical issues in the development of ADS. So far, very few theoretical researches have been carried out on this problem, then, the corrosion phenomena lacks in the theoretical explanation and in the detailed knowledge of the atomic processes. To satisfy these deficiencies, it is necessary to explore the interaction details of atoms at the interface of the corrosive environment and the vessel. Specifically, how the liquid atoms deposit onto the surface, and how the deposited liquid atoms affect the escape of Fe atoms from the steel surface. For these reasons, in this work, we focus our attention on the interaction between liquid Pb atom and the Fe surface, in the framework of the ab-initio computations.

2 Computational details

The first-principles PWscf (Plane-Wave Self-Consistent Field) code of the Quantum ESPRESSO has been used [1, 2] to accurately characterize Iron and Iron surface properties. PWscf performs many different kinds of self-consistent calculations of electronic-structure properties within Density-Functional Theory (DFT), using a Plane-Wave (PW) basis set and Pseudo-Potentials (PP) [3, 4].

---

[*] Corresponding author. E-mail: `simone.giusepponi@enea.it`.

The Fe.pbe-sp-van_ak.UPF Vanderbilt ultrasoft pseudopotential [5, 6, 7] with generalized gradient spin approximation (GGSA) and Perdew-Burke-Ernzerhof (PBE) [8] approximant GGA exchange–correlation potential, available in the Quantum ESPRESSO library was employed. All the calculations are performed in the supercell approximation with periodic boundary conditions (PBC) meant to mimic an infinitely extended system. We considered a cubic supercell composed by a $2 \times 2 \times 2$ array of bcc conventional cells and 16 Fe atoms. The electronic wave functions were expanded in a plane-wave basis set with a kinetic energy cut-off equal to 540 eV and $8{\times}8{\times}8$ Monkhorst-Pack k–point mesh is employed [9]. The energy minimization is performed by using conjugate gradient (CG) minimization energy method, with the convergence threshold for self consistency equal to 10^{-7} Ry. Broyden-Fletcher-Goldfarb-Shanno (BFGS) quasi-newton algorithm is used to perform geometry optimization. Ionic relaxation is stopped when both the following conditions are satisfied: energy changes less than 10^{-4} Ry between two consecutive self consistent field (SCF) steps and all components of all forces are smaller than $5 \cdot 10^{-4}$ Ry/Bohr.

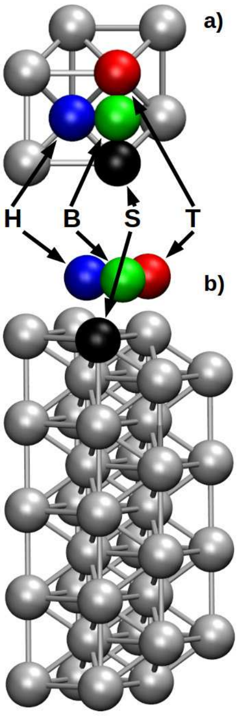

Figure 1: a) Top and b) side view of the simulated system. Top (T), bridge (B), hollow (H) and substituted (S) sites are in red, green, blue and black, respectively.

By total energy calculations we derived lattice parameters a, bulk modulus B and elastic constants C_{ij}. Moreover, to characterize the iron surface, the surface energy per unit area γ and the percent change of the surface relaxation $\Delta_{ij} = (d_{ij} - d_0)/d_0$ were calculated, where d_{ij} is the spacing between layers i and j and d_0 is the equilibrium layer spacing [10, 11]. To quantifies the interation of an added atom (adatom) on the surface, the binding energy (E_b) was calculated as:

$$E_b = E(slab + ada) - E(slab) - E'(ada) \tag{1}$$

where $E(slab{+}ada)$ is the total energy of the relaxed surface+adatom system, $E(slab)$ is the total energy of the relaxed clean surface and $E'(ada)$ is the total energy of an isolated adatom. A more negative binding energy indicates a more favourable structure.

3 Bulk iron and iron surface

Considering the curve trends of the total energy with respect to the side dimension and to the volume of the supercell we derived for equilibrium lattice parameters a_0 and bulk modulus B the following values: $a_0 = 2.866$ Å and $B = 166$ GPa. Moreover the elastic constants were calculated and attainig the subsequent values: $C_{11} = 224$ GPa, $C_{12} = 137$ GPa, and $C_{44} = 89$ GPa. These values are in agreement with experimental and theoretical results.

Having checked the reliablility of our numerical model for the iron bulk sistem, we considered an iron surface. Surface was cleaved from a crystal structure of bcc iron corresponding to the (100) Miller plane: Fe(100). Experiments have shown that this is the most likely cleavage plane of iron [12]. A vacuum space of $\simeq$15 Å was inserted in the z-direction to mimic a two dimensional surface. This has been shown to be sufficient to eliminate interations between mirror images in z-direction due to the PBC (see Fig. 1). Surfaces with increased number of slabs were examined to evaluate the optimal number of slab to take in consideration. Each slab is composed with 2×2 crystal unit cell with lattice parameters calculated from the bulk system ($L_x = L_y = 2 \times a_0$) and a 8×8×1 k–point mesh is employed. The linear growth of the total energy E^N_{slab} with respect of the number of the slabs N, permits to calculate the surface energy σ of Fe(100) using the following equation [10, 11]:

$$E^N_{slab} \approx 2\sigma + NE_{bulk} \tag{2}$$

where E_{bulk} is the bulk total energy. Calculations for the surface energy per unit area $\gamma = \sigma/A$ where $A = L_x \times L_y$, gave γ = 2.3 J/m^2. The obtained result is comparable to other numerical calculations [13, 14, 15], and to the available experimental values of 2.41 and 2.55 J/m^2, although the latter values were measured for the polycrystalline surface [16, 17].

The surface relaxation of the Fe(100) were also analysed. Surface relaxation is characterized as the percent change $\Delta_{ij} = (d_{ij} - d_0)/d_0$ of the spacing d_{ij} between layers i and j versus the equilibrium layer spacing d_0. For the Fe(100) surface d_0 is $a_0/2$. A positive value indicates expansion, whereas a negative one indicates a contraction of the spacing. Analyzing the surface relaxation of the system we measured that Δ_{12} = -3.5%, Δ_{23} = +2.1%, Δ_{34} = +0.44% and Δ_{45} = -0.28% (see the second column of Tab. 1). Relaxations of inner layers are neglible. In panel a1) of Fig. 2 are shown the relaxed top four layers of Fe(100) surface.

4 Defective iron surface

To have a primary insight into the corrosion process of liquid lead on solid iron, we started considering the system in which a Pb adatom is absorbed on the Fe(100) surface. Three different positions were considered (see Fig. 1): top site (T), bridge site (B) and hollow site (H). For each absorption site the binding energy (E_b) was calculated; a more negative binding energy indicates a more favourable structure. Results for Pb adatoms are reported in the Tab. 1. The E_b energies are all negative, then this result indicates that the absorption of a Pb atom is a energetically favourable process. Moreover, we observe that the hollow site is the most stable site (-3.73 eV), followed by the bridge site (-3.14 eV) and then by the top site (-2.83 eV), which is the last stable. Others numerical works have highlighted same conclusions [18, 19]. To have a better understanding of the event we considerated also the interaction of the Fe(100) surface with an isolated Fe adatom. The binding energy were calculated and results are reported on the Tab. 1. As before, also for Fe adatom the hollow site is the most stable site (-3.61 eV), followed by the bridge site (-2.51 eV) and then by the top site (-1.68 eV). Moreover, it is worth to note that configurations with Pb adatom are more stable than the corresponding ones with Fe adatom. This indicates that is more energetically favourable to have a Pb atom on the iron slab rather than continue the iron surface with a Fe atom. In panels b1) and c1) of Fig. 2 are shown the completely relaxed surfaces relative to the hollow sites, respectively. With regard of the structural analysis of these six configurations, for Pb adatom, there still is a contraction of the spacing between the first and the second layer (Δ_{12} are all negative) and an expansion of the the spacing between the second and the third layer (Δ_{23} are all positive). On the contrary, we observe that for Fe adatom, we have an expansion of the spacing between the first and the second layer for Top (Δ_{12}=0.12%) and Hollow (Δ_{12}=0.59%) sites. Instead, there is a contraction only for Bridge site (Δ_{12}=-2.5%). Values of Δ_{23} are similar to those of the Pb adatom cases. Results for surface relaxations Δ_{ij} are summarized in the first block of Tab. 1.

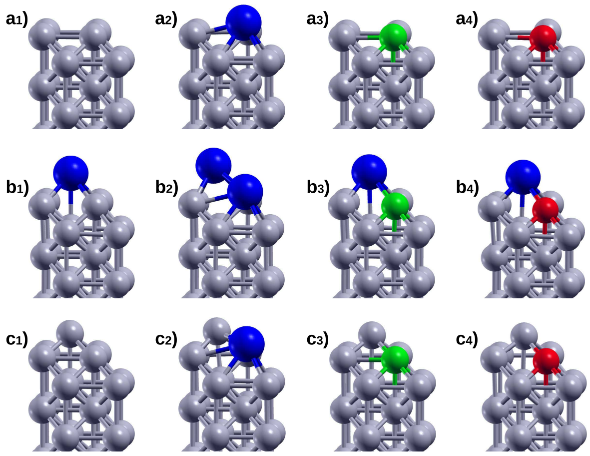

Figure 2: Relaxed Fe(1 0 0) surfaces with/without substituted atom and with/without adatom in hollow site (see text).

To further evaluate the interation between iron and lead, we considered the previous systems in which a iron atom on the surface (position S in Fig. 1) is replaced by a lead atom. In panel a2) of Fig. 2 is shown the completely relaxed Fe(100)$_{\mathrm{Pb}}$ surface. We observe that the larger dimension of the Pb atom compared to the Fe atom entails a change in the shape of the outer layer, this induces a sharp variation in the percent change of the surface relaxation, now we have a expansion of the outer layer Δ_{12} = 7.9%. Then, energetical and structural considerations are taken into account with regard to the addition of a Pb(Fe) adatom in the Hollow site. The E_b of a Pb atom and of a Fe atom in H site are -3.19 eV and -2.99 eV, respectively. In panel b2) and c2) of Fig. 2 are depicted the corresponding two relaxed configurations. The bonding energies are weakened compared to the clean Fe(100) with Pb or Fe adatoms, though, it is more important to highlight that the configuration with a Pb adatom on the Fe(100)$_{\mathrm{Pb}}$ surface it is more stable than that in which there is the Fe adatom. Moreover, we have Δ_{12} = 9.2% and Δ_{23} = 2.3% for the former case and Δ_{12} = 11.8% and Δ_{23} = 1.5% for the latter case. The large dimension of Pb atom causes a great expansion of the outer layer. Results for E_b and Δ_{ij} for Fe(100)$_{\mathrm{Pb}}$ surface with/without Pb/Fe adatom in H site, are summarized in the second block of Tab. 1.

Finally, we examined the role of two of the major alloying elements in steel. We considered the two systems in wich a surface iron atom (position S in Fig. 1) is replaced with a chromium/nickel atom. In panels a3) and a4) of Fig. 2 are shown the completely relaxed Fe(100)$_{\mathrm{Cr}}$ and Fe(100)$_{\mathrm{Ni}}$ surfaces, respectively. Concerning the surface relaxations, great difference is not perceived, in fact Δ_{12} = -4.5% and Δ_{23} = 1.9% for Cr alloying and Δ_{12} = -4.6% and Δ_{23} = 2.1% for Ni alloying. The presence of the alloying element causes an increase in the contraction of the outer layer compared to the clean Fe(100) surface which is -3.5%. As done before we investigate the different behaviour of these two doped iron surfaces with an extra Pb/Fe atom in H site. The binding energies of an adatom on

Table 1: Binding energy E_b (eV) for the Pb/Fe adatom in the top (T), bridge (B) and hollow (H) sites. Percent change (%) of the surface relaxation/contraction Δ_{ij}.

	Fe(100)						
adatom		Pb			Fe		
site		T	B	H	T	B	H
E_b (eV)		-2.83	-3.14	-3.73	-1.68	-2.51	-3.61
sur. rel.							
Δ_{12} (%)	-3.5	-1.8	-2.8	-1.3	0.12	-2.5	0.59
Δ_{23} (%)	2.0	1.5	2.1	1.6	1.2	2.0	1.5
Δ_{34} (%)	0.44	0.70	0.96	1.1	1.1	0.78	0.96
Δ_{45} (%)	-0.25	0.36	0.38	0.55	0.54	0.44	0.95

	Fe(100)$_{Pb}$			Fe(100)$_{Cr}$			Fe(100)$_{Ni}$		
adatom		Pb	Fe		Pb	Fe		Pb	Fe
site		H	H		H	H		H	H
E_b (eV)		-3.19	-2.99		-3.69	-3.63		-3.46	-3.68
sur. rel.									
Δ_{12} (%)	7.9	9.2	11.8	-4.5	-2.7	-1.3	-4.6	-3.0	-0.89
Δ_{23} (%)	1.9	2.3	1.5	1.9	1.5	0.42	2.1	0.39	1.4
Δ_{34} (%)	0.52	0.68	0.38	0.26	0.78	0.07	0.31	-0.68	0.50
Δ_{45} (%)	0.46	0.82	0.44	-0.05	0.44	-0.07	0.03	-0.93	0.61

the Fe(100)$_{\mathrm{Cr}}$ are similar: E_b = -3.69 eV for Pd and E_b = -3.63 eV for Fe, respectively. However, the surface relaxations are different for the two cases. A Pb adatom in Hollow site (panel b3) of Fig. 2) gives rise to a contraction of the distance between the first and the second layer Δ_{12} = -2.7% and a expansion of the distance between the second and third layer Δ_{23} = 1.5%. A Fe adatom in hollow site (panel c3) of Fig. 2) causes less pronounced changes: Δ_{12} = -1.3% and Δ_{23} = 0.42% (see the third block of Tab. 1). Regarding the Fe(100)$_{\mathrm{Ni}}$ surface we calculated the binding energies of an adatom on the Hollow site: we have E_b = -3.46 eV for Pd and E_b = -3.68 eV for Fe, respectively. In the fourth block of Tab. 1 are also reported the percent change of the surface relaxations. We computed Δ_{12} = -3.0% and Δ_{23} = 0.39% for Pb adatom, and Δ_{12} = -0.89% and Δ_{23} = 1.4% for Fe adatom, respectively. In panel b4) of Fig. 2 is shown the relaxed configuration of the Fe(100)$_{\mathrm{Ni}}$ surface with Pb adatom, whereas, in panel c4) of Fig. 2 is shown the same surface with Fe adatom.

5 acknowledgments

The computing resources and the related technical support used for this work have been provided by CRESCO/ENEAGRID High Performance Computing infrastructure and its staff [20]. CRESCO/ENEAGRID High Performance Computing infrastructure is funded by ENEA, the Italian National Agency for New Technologies, Energy and Sustainable Economic Development and by Italian and European research programmes, see http://www.cresco.enea.it/english for information.

References

[1] P. Giannozzi et al. *J. Phys.: Condens. Matter.*, 21:395502, 2009.

[2] www.quantum-espresso.org.

[3] P. Hohenberg and W. Kohn. *Phys. Rev.*, 136:B864, 1964.

[4] W. Kohn and L. J. Sham. *Phys. Rev.*, 140:A1133, 1965.

[5] D. Vanderbilt. *Phys. Rev. B*, 41:7892, 1990.

[6] K. Laasonen, R. Car, C. Lee, and D. Vanderbilt. *Phys. Rev. B*, 43:6796, 1991.

[7] K. Laasonen, A. Pasquarello, C. Lee, R. Car, and D. Vanderbilt. *Phys. Rev. B*, 47:10142, 1993.

[8] J. P. Perdew, K. Burke, and M. Ernzerhof. *Phys. Rev. Lett.*, 77:3865, 1996.

[9] H. J. Monkhorst and J. D. Pack. *Phys. Rev. B*, 13:5188, 1976.

[10] V. Fiorentini and M. Methfessel. *J. Phys. Condens. Matter*, 8:6525, 1996.

[11] N. E. Singh-Miller and N. Marzari. *Phys. Rev. B*, 80:235407, 2009.

[12] W. R. Tyson, R. A. Ayres, and D. F. Stein. *Acta Metallurgica*, 21:621, 1973.

[13] L. Vitos, A. V. Ruban, H. L. Skriver, and J. Kollár. *Surf. Sci.*, 411:186, 1998.

[14] M. J. S. Spencer, A. Hung, I. K. Snook, and I. Yarovsky. *Surf. Sci.*, 513:389, 2002.

[15] P. Błoński and A. Kiejna. *Surf. Sci.*, 601:123, 2007.

[16] W. R. Tyson and W. A. Miller. *Surf. Sci.*, 62:267, 1977.

[17] A. R. Miedema. *Z. Metallkunde*, 69:287, 1978.

[18] Song Chi, Li Dong-Dong, Xu Yi-Chung, Pan Bi-Cai, Liu Chang-Song, and Wang Zhi-Guang. *Chin. Phys. B*, 23:056801, 2014.

[19] Y. Xu, C. Song, Y. Zhang, C. S. Liu, B. C. Pan, and Z. Wang. *Phys. Chem. Chem. Phys.*, 16:16837, 2014.

[20] G. Ponti et al. *Proceedings of the 2014 International Conference on High Performance Computing and Simulation, HPCS 2014*, art. no. 6903807:1030, 2014.

Multi-Resolution Techniques for a Compressible Staggered LES Numerical Code

Giacomo Rossi[1]*, *Bernardo Favini*[1], *Eugenio Giacomazzi*[2], *Franca Rita Picchia* [2], *Donato Cecere* [2] *and Nunzio M. S. Arcidiacono*[2]

[1]*Sapienza University, Mechanical and Aerospace Engineering Department,*
Via Eudossiana 18, 00184, Rome, Italy

[2]*ENEA, Laboratory of Engineering of Processes and Systems for Energy,*
Via Anguillarese 301, 00123, S. M. di Galeria (Rome), Italy

ABSTRACT. A numerical technique for mesh refinement in the HeaRT (Heat Release and Transfer) numerical code is presented. In the CFD framework, Large Eddy Simulation (LES) approach is gaining in importance as a tool for simulating turbulent combustion processes, also if this approach has a high computational cost due to the complexity of the turbulent modeling and the high number of grid points necessary to obtain a good numerical solution. In particular, when a numerical simulation of a big domain is performed with a structured grid, the number of grid points can increase so much that the simulation becomes impossible: this problem can be overcomed with a mesh refinement technique. Mesh refinement technique developed for HeaRT numerical code (a staggered finite difference code) is based on a high order reconstruction of the variables at the grid interfaces by means of a least square quasi-eno interpolation: numerical code is written in modern Fortran (2003 standard o r newer) and is parallelized using domain decomposition and message passing interface (MPI) standard. The mesh-refinement algorithm is fully validated by means of a CH_4-H_2-Air slot flame numerical simulation.

1 Introduction

In the Large Eddy Simulation framework, a numerical grid with high spatial resolution is mandatory to obtain a satisfactory numerical solution of the flow field with turbulent combustion: with multi-block structured grids, both in Cartesian and cylindrical coordinates, this goal isn't always possible to achieve, especially when the numerical simulation is performed on a domain with big dimension and very small elements (like bluff bodies and fuel injectors).

The numerical simulation of the "Sandia Flame A" jet performed by the mean of HeaRT numerical code [3] can be chosen as example: this test case is a $CO/H_2/N_2$ (percentage 40/30/30 in volume) non-premixed, unconfined, turbulent jet flame. The fuel is injected

---

[*] Corresponding author. E-mail: `giacomo.rossi@uniroma1.it`.

at 292K from a straight circular tube with squared-off ends (inner diameter 4.58mm, outer diameter 6.34mm), with a bulk velocity of 76ms^{-1}; the air at 290K and wet (molar fraction of water 0.012) coflows at 0.75ms^{-1}.

The geometrical features don't allow to produce a structured cylindrical mesh with a high spatial resolution on the wall duct and concurrently with a manageable number of grid nodes: in the first numerical simulation of the test case entire domain, performed on a computational grid with 63452 nodes, the flame blows off because at the inlet way out the flow field isn't well predicted.

A second numerical simulation, performed only on the anchoring zone (a domain with r_{max} =1.5cm and z_{max} =2cm), with a computational grid of 206349 nodes (that permit to obtain a 1.0×10^{-5}m spatial resolution close to the nozzle), allows to underline the vortex shedding phenomena that occur on the duct wall and that permit a stable flame anchoring.

So it is clear that in this test case, where there's a big difference between the total length of the domain and the wall thickness, with a structured grid it is impossible to obtain a satisfactory compromise between total number of nodes and adequate spatial resolution: a mesh refinement technique can overcome this limitation, because it makes possible to use a grid with a high spatial resolution in a well enclosed zone and to restrict the number of grid nodes in the remaining part of the domain. A mesh refinement technique, is also very useful in combination with Immersed Volume Method (IVM) technique, already implemented in the HeaRT numerical code and successfully validated [1].

2 Multi-Resolution Algorithm

The multi-resolution algorithm developed for the HeaRT code is based on the joined-grids approach. With the joined-grids approach, on the computational domain, multiblock grids with different spatial resolution can be placed side by side. The resolution of the block is identified from a parameter, named *level*: a grid block of level 1 is the coarsest, a grid block of level n is the finest (where n is the maximum number of levels that are present in the computational grid). There's no limit to grid block junction: a grid block of level n can be adjacent to a grid block of level $n + 2$.

If only one grid level is present (no mesh refinement adopted), variable values on ghost cells are obtained from a simple copy of the corresponding "real" cells of the neighboring grid block.

With the joined-grids approach, copy isn't the appropriate operation for the communication between grid blocks with different spatial resolution, so two new reliable procedures have been developed: the first, that transfers variable values from fine to coarse grid is called *restriction* and the second, that makes the opposite operation, is called *prolongation.*

2.1 Communication Procedures

2.1.1 Restriction

Restriction procedure is used for communication of numerical solution from level l to level $l-1$. For scalar variables (collocated at the center of the cell), coarse value $\Phi(I, J, K)$ is obtained from fine values $\phi(i, j, k)$ by means of a weighted sum of fine values, where the weights are the volume fractions of each fine cell contained in the coarse one.

For momentum ρU, collocated at the positive faces of a cell, coarse grid value $\Phi(I, J, K)$ is obtained from fine values $\phi(i_n, j, k)$ by means of a weighted sum of fine values, where the weights are the area fractions of each fine cell contained in the coarse one.

2.1.2 Prolongation

For prolongation, an accurate interpolation algorithm was chosen, and therefore the communication “operator” has a big complexity.

The selected algorithm is the same for both scalar and momentum prolongation: fine value is obtained by the solution, via least-square method, of an overdeterminated system of equations; these equations originate from the Taylor series expansion of the variable values for any coarse point that belongs to the interpolation stencil.

3 Validation

In this section the numerical simulations of a significant test case, obtained with the joined-grids technique, are presented: two Large Eddy Simulations of a lean premixed CH_4/H_2–Air slot flame.

3.1 Problem Configuration and Simulation Setup

The simulations were performed in a slot-burner Bunsen flame: the domain configuration and the boundary conditions are described in [2].

The two-level grid (JG2) has been created starting from the grid already used in a previous LES performed (SL) on the same test case by means of HeaRT code [2]: in the central reaction zone, the new grid is the same of the grid used in the previous simulation; the side and the upper zones (where flow field is calm), are obtained from the “old” grid keeping one node and deleting its next one, in each direction.

The computational grid of the second numerical simulation with joined grid approach (JG3) is obtained from the JG2 grid: the finest zone (level 3) has the same resolution of the level 2 of JG2 simulation, but its smaller in y and in z direction; outside this zone, the grid is obtained from the JG2 grid keeping one node and deleting its next one, in each direction.

Table 1: Grid comparison between the previous simulation (Single Level) and the actual simulations (Joined Grids)

	Single Level (SL)	Two Levels (JG2)	Three Levels (JG3)
Computational blocks (for level)	4	5 (1), 4 (2)	3 (1) 3 (2), 4 (3)
Computational nodes	3969480	2416950	1548390
Grid levels	1	2	3
Grid points (for level)	3969480	234630 (1), 2116320 (2)	33030 (1), 130080 (2), 1385280 (3)

The computational grid of JG2 simulation has about 1500000 nodes less than the SL grid, while the JG3 grid has about 870000 nodes less than the JG2 grid: the JG3 computational grid has just over one third of the total nodes of SL grid.

Both JG2 and JG3 simulations are performed on 256 cores of Cresco 4 ENEA cluster; to compute all the statistics, a large amount of data has been collected: as example, for the JG3 numerical simulation, more than 250 gasdynamic fields (composed by ten zone files) have been stored and post-processed on the Cresco 4 HPC facility: the total amount of disk space used is about 250GB.

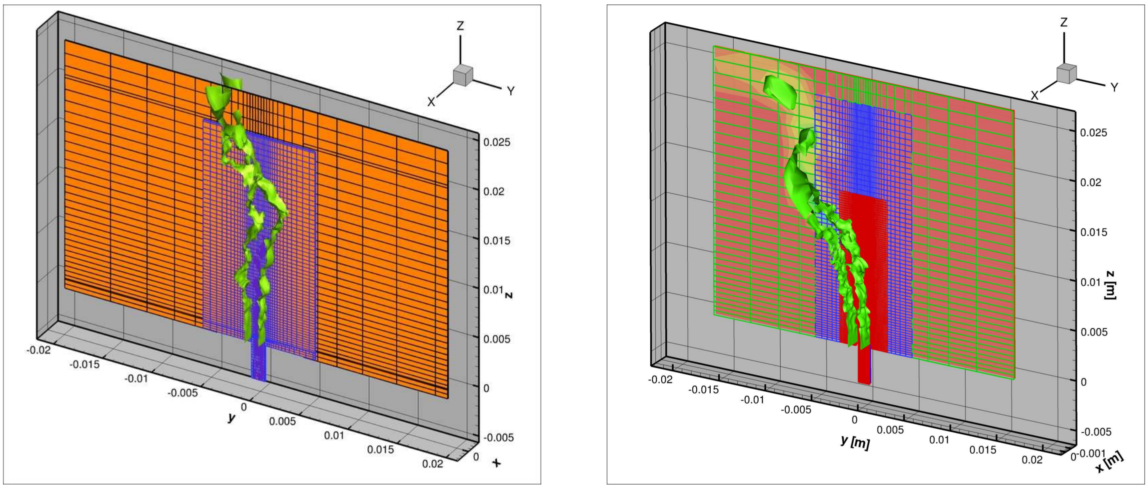

Figure 1: Domain configurations for JG2 (left) and JG3 (rigth) numerical simulations; isosurface of temperature T = 1600K. JG2: level 1 (black) and level 2 (blue) grids (only one line each four is represented); JG3: level 1 (green), level 2 (blue) and level 3 (red) grids (only one line each two is represented).)

In figure **??** (left) average and rms profiles of streamwise velocity at two heights (where the injection is at $z = 0.00$ mm), are plotted: it is evident a very good agreement between JG2 (solid lines), JG3 (solid lines with cross) and SL (dashed lines) LES simulation data; the communication procedures described in section 2.1 don't modify both trend and maximum and minimum positions.

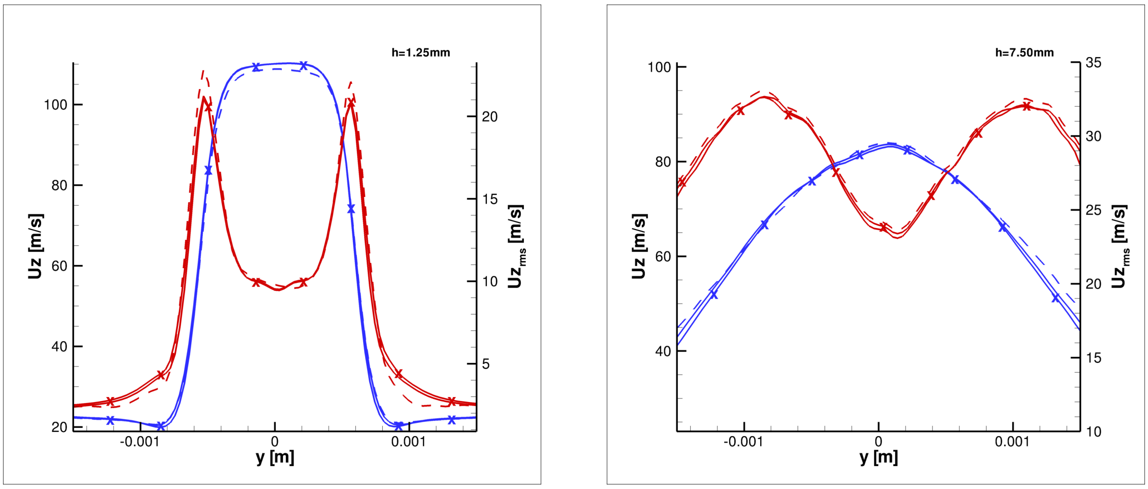

Figure 2: Streamwise Velocity Mean (blue) and rms (red) profiles at two heights above injection (left: $z = 1.25$ mm; right: $z = 7.00$ mm): comparisons between SL (dashed lines), JG2 (solid lines) and JG3 (solid lines with crosses)

4 Concluding Remarks

By mean of this technique, based on the joined-grids approach, is possible to obtain some important targets.

First, it is possible to reduce, in a considerable way, the total number of grid points without any significant loss of accuracy: the 3 levels computational grid used in the numerical simulation of the slot flame has about one third, in terms of computing nodes, with respect to the single level grid; this permits to obtain smaller output files (the size is reduced from $\sim$ 800MB to $\sim$ 270MB) and therefore an important saving of disk space, post-processing times and computational resources.

The computational nodes number reduction has furthermore a positive effect on single iteration (or time step) computing times: for a few number of cores (up to 16), the joined-grids numerical simulations has a computing time shorter than the single level simulation; for a higher number of cores, the advantage of joined-grids algorithm is not so clear. One the reasons is the domain decomposition algorithm adopted in the HeaRT code, that makes impossible a concentration of CPUs on the finest zone, because it is limited on a "structured" decomposition of the numerical grid; another reason is more likely the poor efficiency of the joined-grids procedures, that have to be analyzed to discover all the possible bottlenecks, cache misses and every other problems in memory management.

References

[1] D. Cecere and E. Giacomazzi. An immersed volume method for large eddy simulation of compressible flows using a staggered-grid approach. *Computer Methods in Applied Mechanics and Engineering*, 280:1–27, 2014.

[2] E. Giacomazzi, D. Cecere, F. R. Picchia, and N. M. S. Arcidiacono. Sviluppo di un modello les per fiamme turbolente premiscelate. Technical Report 255, ENEA, 2014.

[3] E. Giacomazzi, F. R. Picchia, N. M. S. Arcidiacono, D. Cecere, F. Donato, and B. Favini. Unsteady simulation of a co/h2/n2/air turbulent non-premixed flame. *Combustion Theory and Modelling*, 12:1125–1152, 2008.

DFT study of OTS-SAM coatings on (111) Si surface as gate dielectrics for organic thin film transistors.

Fabrizio Gala[1][*], *Giuseppe Zollo*[1]

[1]*Dipartimento di Scienze di Base e Applicate per l'Ingegneria (Sezione di Fisica), Universitá di Roma "La Sapienza", Via A. Scarpa 14-16, 00161 Rome Italy*

Abstract. Many nano-material systems are currently under consideration as possible candidates for gate dielectric insulators in both metal-oxide-semiconductor (MOSFET) and organic (OFET) field-effect transistors. In this contribution, the possibility of employing self-assembled monolayers (SAMs) of hydroxylated octadecyltrichlorosilane (OTS) chains on a (111) Si substrate as gate dielectrics is discussed; in particular *ab initio* theoretical simulations have been employed to study the structural properties, work function modifications, and the insulating properties of OTS thin film coatings on Si substrates.

The process of miniaturization of micro-electronic components (i.e. reducing the size of a device smaller and make it work faster) is one of the main goals of modern technology; as the total transistor size comes down to few nm, only few atoms would work as a transistor; organic molecules, thanks to the size, are expected to play a key role in molecular electronics[24]. Self-assembled monolayers (SAMs) have been recently studied and reviewed in detail[12, 11, 13, 22], because of their possible use in low cost devices for applications in many fields. Among the possible choices for the chemical species involved in the formation of SAM films, alkyl-silanes exhibit appealing properties, such as low mechanical friction[13] or high level of hydrophobicity[2, 3], when employed in the functionalization of silicon surfaces. Alkyl chains deposited on Si or SiO_2 exhibit high insulating properties, thus being excellent candidates for gate dielectrics in low-voltage OTFTs, suppressing carrier tunneling thanks to their highly ordered aliphatic chains, even though they are only a few nanometer in thickness, provided that a good control of film quality is achieved[1, 21, 4], making this system highly appealing for the fabrication of efficient organic thin film transistors (OTFTs) at the nanoscale, where silicon dioxide (SiO_2) behaves as a poor insulator with high leakage currents. In addition it is possible to modify the surface terminating group of the SAM by exploiting compatible organic/inorganic interactions resulting in improved device performances[18].

Generally speaking, an organic monolayer formed through self-assembling should be a close-packed and highly ordered structure as schematically sketched in Fig.1; however, defects or incomplete domain boundaries may occur during the SAM formation[23, 20];

---

[*] Corresponding author. E-mail: `fabrizio.gala@uniroma1.it`.

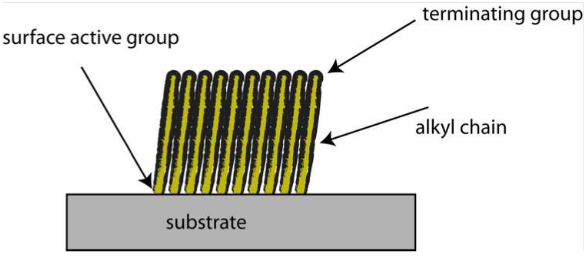

Figure 1: (Color online) Close-packed and highly ordered organic monolayer of alkyl chains on a substrate formed through self-assembling.

hence, SAM coatings are quite often non uniform being characterized by neighbouring, small sized, ordered domains [23] with different orientations and disordered domain boundaries; in a field emitting transistor (FET) this would be catastrophic, as semiconductor molecules may penetrate the SAM film, reducing the effective dielectric thickness and creating low-resistence current paths trough the SAM film; thus a key challenge for realizing an efficient OTFT lies in developing gate dielectrics with low leakage current, low interface trap density, and high capacitance for low-voltage OTFTs. Our previous calculations[7] have shown that SAM coatings made of octadecylthrichlorosilane ($(CH_3(CH_2)_{17}Si(OH)_3$, OTS in the following) shows many appealing properties for a gate dielectric material; hydroxylated OTS molecules adsorbed on the hydrogenated (111) Si surface, in fact, show a negative adsorption energy; that is lower, however, than the adsorption energy of a pure alkyl chain. Despite this fact, the ground-state configuration of both the isolated and two adjacent OTS chain exhibit some favorable properties that make OTS particularly suitable for Si functionalization with homogeneous, uniform, and stable hydrophobic self-assembled monolayers. Indeed, the ground-state adsorption geometry shown in Fig.2(a), is almost orthogonal to the (111) surface, with a low value of the tilt angle that, contrarily to the pure alkyl chain case , prevents the steric hindrance of the neighbouring surface adsorption sites by the deposited molecule (see the inset of Fig. (2)(a)).

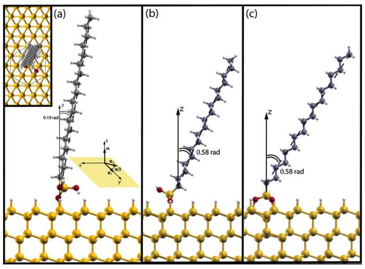

Figure 2: (Color online) Fully relaxed configurations of the (1:1) (a), (1:2) (b), and (1:3) (c) OTS adhesion on the hydrogenated (111) Si surface.

The interaction between two hydroxylated OTS polymers adsorbed at adjacent sites on the (111) Si surface depends on the local dipole field in the vicinity of the polymer chain that, unlike the pure alkyl chain case, is strongly affected by the presence of the hydroxyl polar groups. The OH groups, in fact, favour the interaction, via an H bond, of the OTS with the positive charges of the unscreened in Fig.(3), drawn in the plane containing the

O-H-O atoms, evidences the existence of a significant potential energy region connecting the two adjacent polymers that is the result of the H bond between the O lone pair (that is located below the plane where the density map is considered) and the positive H (see Fig.3).

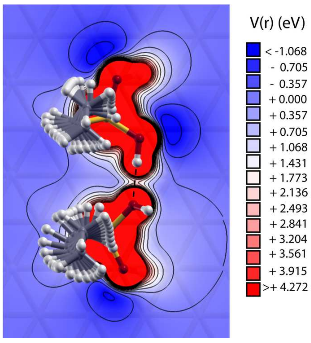

Figure 3: (Color online) Density map of the electrostatic potential for the ground-state configurations of two OTS polymers adsorbed at adjacent sites on the hydrogenated (111) Si surface. The density maps has been drawn on the plane parallel to the (111) Si surface, namely the one that in the OTS case contains the (almost) linear H bond between the OH radicals of the two molecules.

The adsorption of OTS at adjacent sites is, therefore, not only allowed but energetically favoured because the interaction energy between two adjacent molecules is driven by the H bond formed between two hydroxyl groups belonging to the different molecules.

From the electrostatic point view a modification of the substrate work function induced by SAM deposition has to be expected to occur in the case of OTS on Si surfaces[8], affecting, as a consequence, the properties of devices based on this technology. As pointed out previously, a self-assembled thin film monolayer should be a close-packed and highly ordered structure; however, defects or incomplete domain boundaries may occur during the SAM formation[20]. Hence, SAM coatings are quite often nonuniform, being characterized by neighbouring, small sized, ordered domains[23] with different orientations and disordered domain boundaries. Moreover, the coating properties can be deeply affected by the deposition parameters and methods used, favouring, for instance, multiple covalent attachments with the surface, which has been referred to as "poor self-assembly"[5] because of the significant lowering of the bonding density. Indeed, according to NMR and IR measurements performed on methyl-n-alkylsilanes, there is evidence that such polymeric structures, which are quite similar to OTSs, can bind the Si surface through either a single covalent bond (referred to as (1:1) structures) or two covalent bonds ((1:2) structures)[17]. Each of the previously mentioned defects, discontinuities, or poor "self-assembly" features in the OTS SAM, dramatically affect the coating properties of the functionalized Si surface, resulting in poor device performance when employed in FET technology; especially those exploiting the work function modification of the Si substrate induced by the deposited layer. Work function changes have been recently computed[8] through the "Z-potential" obtained by solving the Poisson equation (given the total charge density) and then by averaging the electrostatic potential $V_{el}(\mathbf{r})$ in the xy plane:

$$\bar{V}(z) = \frac{1}{A}\int_A dxdyV_{el}(\mathbf{r}) = -\frac{e}{2\epsilon_0 A}\int_0^c |z' - z|\bar{\rho}(z')dz' = \frac{1}{2\epsilon_0 A}\Big(d(0) - 2d(z)\Big) \tag{1}$$

where

$$d(z) = \int_z^c (z' - z)\bar{\rho}(z')dz' \tag{2}$$

and resulting in $\Delta\Phi = \Phi^{\mathrm{OTS/H:Si}} - \Phi^{\mathrm{H:Si}} = -e\Delta\bar{V}(\infty)$, with c being the supercell size along z, A the surface area, z the coordinate of an arbitrary plane parallel to the surface, $\bar{\rho}(z)$ the xy average of the total charge, evaluated from first-principles calculations.

Table 1: Adsoprtion energies, tilt Angles, work function changes, and surface dipole moment changes with respect to the bulk Si:H case for single molecule adhesion configurations involving n bonds with $1 \leq n \leq 3$

Configuration	E_{ads} (eV)	θ_{tilt} (rad)	$\Delta\Phi$ (eV)	Δd_s (D)
(1:1)	-0.64	0.19	-170	1.95
(1:2)	-0.90	0.58	-87	1.17
(1:3)	-1.30	0.58	–50	0.57

The $d(z)$ partial dipole moment (referred to the vacuum region) along the z direction should be ideally calculated as the partial dipole at a reference z plane deep in the Si bulk, dividing it into two neutral subunits[14]. Eq. (1), together with the assumption that $\bar{V}^{\mathrm{H:Si}}(\infty) = 0$, implies $d^{\mathrm{H:Si}}(0) = 0$. Therefore, the work function difference with respect to the hydrogenated Si surface is:

$$\Delta\Phi = -\frac{e}{2\epsilon_0 A} d^{\mathrm{OTS/H:Si}}(0) \tag{3}$$

The fully relaxed structures of the (1:1), (1:2), and (1:3) OTS ground-state adsorption configurations on the (111) Si surface are drawn in Fig. 2; the adsorption energy values calculated on the basis of the eq. (3) are listed, together with the relevant tilt angles, in Table 1 and reveal that all the adsorption reactions are exothermic with larger adsorption energy for multiple covalent bonds per molecule, ranging from 0.64 eV per bond for the (1:1) case to 0.43 eV per bond for (1:3). The work function differences $\Delta\Phi$ with respect to the bare H:Si surface have been calculated with eq. (3) where $d(0)$ has been considered at the central Si layer of the three-layer slab and the work function of the H:Si slab has been estimated to be 6.46 eV. $\Delta\Phi$ values are listed in the third column of Table 1 and demonstrate that the molecular dipole for all the ground-state configurations studied lowers the work function with respect to the hydrogenated (111) Si surface, thus reducing the energy needed to extract an electron from the bulk Si and increasing the hole isolation properties. This is consistent with the observed reduction of the negative partial dipole moment at the topmost Si layer for the functionalized surface with respect to the hydrogenated one.

Under some a few general assumptions the work function change referring to the hydrogenated Si surface can be cast into:

$$\Delta\Phi[n] = -\frac{e}{2\epsilon_0 A}\Delta d_s[n] \tag{4}$$

where n is the number of SAM molecules adsorbed on the surface and $\Delta d_s[n]$ is the corresponding surface dipole change (projected on the surface normal) with respect to the H:Si case. The relationship between the work function and the surface dipole is drawn in Figure 4, demonstrating a clear linear dependence of the work function on the surface dipole for the various configurations studied. At full coverage, it is expected that, for each OTS molecule adsorbed with the (1:1) stoichiometry, one of the two free hydroxyl groups binds the adjacent adsorbed molecule through a planar H-bond carrying no dipole moment in the z direction, while the other is, in principle, free to point up or down with respect to the normal direction of the surface; a schematic picture of such self-assemblyng is depicted in Fig.(4(a). By using the above-discussed linear dependence between $\Delta\Phi$ and Δd_s, the calculated value of $\Delta d_s^{\mathrm{full}}$ can be used to extrapolate the work function difference with respect to the hydrogenated (111) Si surface, which results in $\Delta\Phi^{\mathrm{full}} = -2.04 \pm 0.04$ eV.

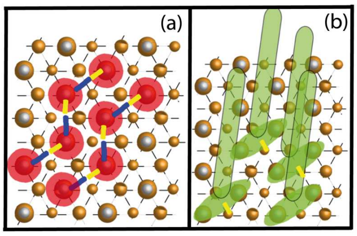

Figure 4: (Color online) Schematic representation of OTS full coverage in both the (1:1) and (1:2) case ((a) and (b) respectively). The blue and yellow lines in (a) represents the hydroxyl groups of OTS adjacent molecules (red circles) forming a H-bond; while in (b) the (1:2) OTS adhesion configuration is sketched in green together with the only free hydroxyl group in yellow.

In the present work, the dielectric properties of OTS-SAMs on the (111) Si surface have been studied by first-principles calculations based on density functional theory (DFT)[1]. When an external electric field **E** is applied, the partial dipole depends on it in the following way:

$$d_{\mathrm{E}}(z) = \int_z^c (z' - z)\rho_{\mathrm{E}}(z')dz' \tag{5}$$

($\rho_{\mathrm{E}}(z)$ now is the xy average of the total charge in presence of a static external electric field **E**) and permits to evaluate the macroscopic electrostatic potential as a function of z, thus allowing to calculate the averaged internal electric field inside the slab. Using eq. (1)

---

[1] A generalized gradient approximation (GGA), using the Perdew-Burke-Ernzerhof formula[15](PBE) for the electron exchange and correlation energy have been employed, and norm-conserving pseudopotentials have been constructed with the Troullier-Martins scheme[19] in the framework of a plane-wave basis set expansion. All the first-principles calculations have been performed using the parallel version of QUANTUM-ESPRESSO package[9], with a plane-wave energy cutoff of 150 Ry for the wave functions. A six-layer slab of 48 atoms having 8 Si atoms per layer and a vacuum region of ~ 43 Å have been employed, together with (4x4x1) Mokhorst-Pack k-point grid for the Brillouin zone sampling, while relaxation patterns have been obtained with a Broyden-Fletcher-Goldfarb-Shanno (BFGS) method[6] plus semi-empirical long range corrections[10] and an external electric field of 0.002 a.u. of amplitude. The ionic minimization was done until the convergence threshold of 0.001 a.u. of the total force was achieved.

it is possible to write the electrostatic potential in presence of an external static electric field of absolute value E as:

$$\bar{V}_{\mathrm{E}}(z) = \frac{e}{\epsilon_0 A}\left(\frac{d_{\mathrm{E}}(0)}{2} - d_{\mathrm{E}}(z)\right) - zE \tag{6}$$

being A the xy surface area. Differentiation of Eq. (6) leads to the total electric field:

$$\mathbf{E}^{(\mathrm{E})}_{\mathrm{tot}} = -\vec{\nabla}\bar{V}_{\mathrm{E}}(z) = \left(\frac{e}{\epsilon_0 A} d'_{\mathrm{E}}(z) + E\right)\hat{\mathbf{k}} = \mathbf{E}^{(\mathrm{E})}_{\mathrm{int}} + \mathbf{E} \tag{7}$$

where $\hat{\mathbf{k}}$ is the unit vector along the z direction. As we are interested in the macroscopic dielectric function, the internal field has to be averaged between two reference points (say z_1 and z_2 with $z_2 \geq z_1$) to eliminate local field effects, giving:

$$\langle \mathbf{E}^{(\mathrm{E})}_{\mathrm{int}} \rangle = \frac{1}{z_2 - z_1}\int_{z_1}^{z_2} \mathbf{E}_{\mathrm{int}}(z)dz = \frac{e}{\epsilon_0 A(z_2 - z_1)}\int_{z_1}^{z_2} d'_{\mathrm{E}}(z)dz\hat{\mathbf{k}} = \frac{e}{\epsilon_0 A}\frac{d_{\mathrm{E}}(z_2) - d_{\mathrm{E}}(z_1)}{z_2 - z_1}\hat{\mathbf{k}} \tag{8}$$

On the other hand, for a polarized dielectric linear slab in presence of an external electric field, the macroscopic polarization $\mathbf{P}_{\mathrm{E}}$ between two reference points z_1 and z_2 can be obtained as:

$$\mathbf{P}_{\mathrm{E}} + \epsilon_0 \langle \mathbf{E}^{(\mathrm{E})}_{\mathrm{int}} \rangle = 0 \tag{9}$$

provided that both z_1 and z_2 in $\langle \mathbf{E}^{(\mathrm{E})}_{\mathrm{int}} \rangle$ satisfy the neutrality condition $d'(z_i) = 0 \ \forall i = \{1, 2\}$. Eq. (9) permits to evaluate the static linear susceptibility χ as the polarization response of the system to the total electric field:

$$\delta\mathbf{P} = \epsilon_0 \chi \delta \mathbf{E}^{(\mathrm{E})}_{\mathrm{tot}} \tag{10}$$

where $\delta\mathbf{P}$ is the difference between the macroscopic polarization with and without external electric field. Then the static dielectric constant can be easily obtained in connection with eq.(8) as:

$$\epsilon_r = \left(1 + \frac{\delta E^{(\mathrm{E})}_{\mathrm{int}}}{E}\right)^{-1} \tag{11}$$

where $\delta E^{(\mathrm{E})}_{\mathrm{int}}$ is the difference between the average internal electric field with and without a static external field $\mathbf{E}$. The above sketched method has been tested on a perfect hydrogenated (111) Si surface by varying the external field and letting the supercell to relax, and the results obtained for partial dipoles evaluated through Eq. (5) are shown in Fig. 5, with z_1 and z_2 values chosen at the local maxima in the bulk (see Fig. 5); our calculated values for the dielectric constant ϵ_0^{Si} through eq. (11) gives the value of 11.8 in very good agreement with the experimental value of 11.9.

Next we have addressed the problem of evaluating the polarization of the various blocks forming the OTS molecule adsorbed on the surface, in the spirit of applying the same decomposition of partial dipoles previously used[8] to evaluate work function changes. The idea is to obtain a reliable value of the surface dipole to be employed in estimating the internal macroscopic electric field with and without an external field, and the corresponding

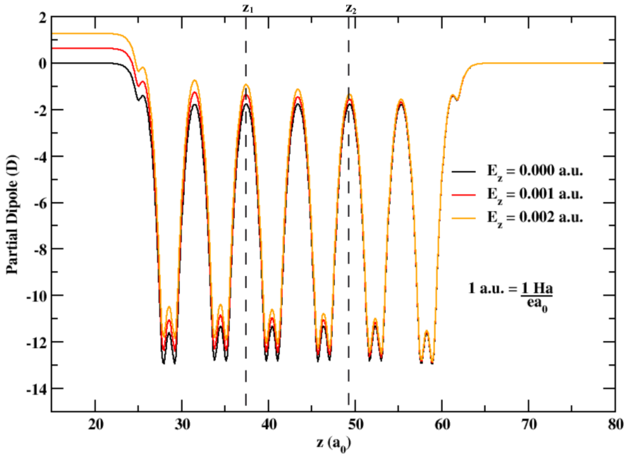

Figure 5: (Color online) Partial dipoles inside the hydrogenated (111) Si surface for different applied external electric field.

dielectric constant $\epsilon_0^{\text{OTS/H:Si}}$. Due to numerical stability, we have found convenient to split the integral in Eq. (5) as it is shown in Fig. 6 where the various partial dipole contributions are evidenced, namely the one belonging to the bonding group of the OTS molecule ($d_{\text{Si-O-Si}} + d_{\text{OH}}$), the partial dipole of the alkyl chain ($d_{(\text{CH})_2}$), and finally the methyl group ($d_{(\text{CH})_3}$).

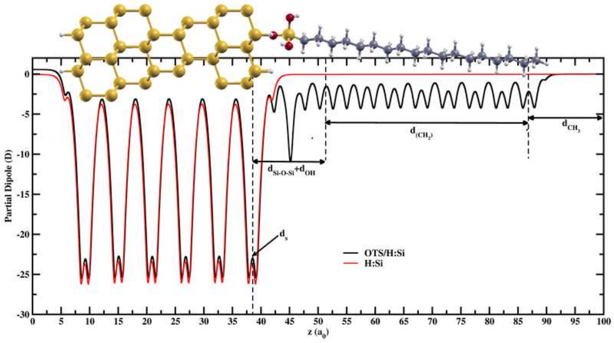

Figure 6: (Color online) Partial dipole as a function of z, for the OTS adsorbed on the Si surface (black line) and for the H:Si slab (red line). Partial dipoles of the sub-units specified in Table 2 are evidenced, together with the special points dividing the structure into two neutral sub-units, where partial dipoles evaluated through Eq. (2) agree with the usual definition.

Except for the orientation of the hydroxyl groups, the ionic relaxation of the OTS molecule in presence of an external electric field, affects only slightly the relaxed atomic positions of the configuration with no external field. On the contrary, the two free OH groups have rotated their angles with respect the z direction of $\Delta\theta^{(\uparrow)} \sim 6.5°$ and $\Delta\theta^{(\downarrow)} \sim 2.3°$, where $\theta^{(\uparrow)}(\theta^{(\downarrow)})$ is referred the the hydroxyl groups pointing up (down). The new polarization values of the different contributions are reported in Table 2. The values reported in Table 2 for the partial dipole of the CH$_3$ radical are those obtained for an isolated OTS molecule, while in presence of an adjacent molecule repulsive effects between the alkyl chains have to be considered. Thus the $d_{\mathrm{CH_3}}$ term has been revised in a system mimicking the full coverage of the Si surface; in particular, we have taken the dipole moment of the methyl groups of a full coverage system consisting of a densely packed array of $\mathrm{CH_3(CH_2)_{17}CH_3}$ molecules that resembles what we would have in a typical full coverage of the H:Si slab, provided the PBCs are applied.

The new $d_{\mathrm{CH_3}}$ values obtained in this way are -1.34 D and -1.25 D for E = 0.000 a.u. and E = 0.002 a.u. respectively. At full coverage, we expect that of the two hydroxyl groups of each OTS molecule, one forms an H-bond with and adjacent molecule, while the other points downard as schematically shown in Fig.4; in this case the data reported predict a variation in the surface partial dipole moment, due to the applied external electric field, of $\Delta d_s \sim 4.6$ D, corresponding to a static relative dielectric constant of $\epsilon_r^{\mathrm{OTS/H:Si}} \sim 5.1$. In terms of equivalent $\mathrm{SiO_2}$ thickness our prediction brings to:

$$l_{\mathrm{eq}} = l_{\mathrm{OTS}} \frac{\epsilon_r^{\mathrm{OTS/H:Si}}}{\epsilon_r^{\mathrm{SiO2}}} \sim 36.6\ \text{Å} \tag{12}$$

(with $\epsilon_r^{\mathrm{SiO2}} \sim 3.9$) that is a very good result in terms of insulating properties when alkyl chains are employed ad gate dielectrics in Si-based FET devices. The above result, however, is based on some approximations and hypotheses assumed concerning the alkyl chain and the orientation of the hydroxyl groups that are still under consideration for robustness.

Table 2: Partial dipole with and without an applied external electric field for various elements of the OTS molecule needed to evaluate surface partial dipoles at full coverage.

	E = 0.000 a.u.	E = 0.002 a.u
$d_s^{\mathrm{H:Si}}$	-23.71 D	-23.45 D
$d_{\mathrm{Si\text{-}O\text{-}Si}}$	2.22 D	2.40 D
$d_{\mathrm{OH}}^{(\downarrow)}$	-1.015 D	-0.92 D
$d_{\mathrm{OH}}^{(\uparrow)}$	1.015 D	1.11 D
$d_{(\mathrm{CH_2})}$	0.65 D	1.51 D
$d_{\mathrm{CH_3}}$	-2.18 D	-2.03 D

In conclusion, using first-principles calculations based on the density functional theory, we have studied the ground state configurations and the energetics of hydroxylated OTS polymers adsorbed on the (111) H:Si surface and the interaction between two polymeric chains adsorbed at adjacent sites. Our study has been focused on those aspects, such as configurational properties and dipolar interactions, playing a crucial role for the onset of self-assembling phenomena that are beneficial for uniform and stable hydrophobic functionalization of Si. It has also been demonstrated that, in the case of perfect OTS-SAM adhering to the Si surface with one covalent bond per molecule, the self-assembly mechanism involves H-bonds between hydroxyl groups of neighbouring of OTS molecules while multiple covalent bonding between a (111) Si surface and a OTS molecule has been explored as a possible source of irregularities and disorder.

The Z-potential and the partial dipoles have been calculated and decomposed in parts that have been employed as the building blocks of a simple superposition toy model that has been validated for the various configurations considered, showing that it is appropriate to predict the surface dipole and the work function. The usage of such a model has allowed to extrapolate the surface dipole and the work function to full coverage, giving $\Delta\Phi$ of uniform coatings in the (1:1) and (1:2) adsorption motifs. In particular we have found that the (111) Si surface coated with a uniform and regular OTS SAM exhibits a lower electron work function by nearly 2 eV with respect to the hydrogenated surface thus enhancing the hole confinement of such coated surface. Next, we have calculated the static dielectric constant of a regular and uniform OTS SAM coating by assuming some approximations. The obtained value of $\epsilon_r^{\mathrm{OTS/H:Si}} \sim 5.1$, that, however, should be considered as a first approximation of the actual value due to the assumptions employed, is enough robust to show that, compared to silica insulators, the OTS-SAM coatings are attractive candidates as gate dielectrics in FET technology because of better isolation properties.

The computing resources for this work have been provided by the CRESCO3 and CRESCO4 section of ENEAGRID High Performance Computing infrastructure and its staff[16]. CRESCO/ENEAGRID High Performance Computing infrastructure is funded by ENEA, the Italian National Agency for New Technologies, Energy and Sustainable Economic Development and by Italian and European research programmes, see http://www.cresco.enea.it/english for information.

References

[1] C. Boulas, J. V. Davidovits, F. Rondelez, and D. Vuillaume. *Physical Review Letters*, 76:4797–4800, 1996.

[2] M. Chinappi and C. M. Casciola. *Phys. Fluids*, 22:042003, 2010.

[3] M. Chinappi, F. Gala, G. Zollo, and C. M. Casciola. *Phil. Trans. R. Soc. A*, 369:2537, 2011.

[4] J. Collet and D. Vuillaume. *Applied Physics Letters*, 73:2681, 1998.

[5] A.Y. Fadeev and T.J. McCarthy. *Langmuir*, 16:7268, 2000.

[6] R. Fletcher. *The Computer Journal*, 13:317, 1970.

[7] F. Gala and G. Zollo. *Phys. Rev. B*, 84:195323, 2011.

[8] F. Gala and G. Zollo. *Journal of Physical Chemistry C*, 116:24935?24942, 2012.

[9] P. Giannozzi, S. Baroni, N. Bonini, M. Calandra, R. Car, C. Cavazzoni, D. Ceresoli, G. L. Chiarotti, M. Cococcioni, I. Dabo, A. Dal Corso, S. de Gironcoli, S. Fabris, G. Fratesi, R. Gebauer, U. Gerstmann, C. Gougoussis, A. Kokalj, M. Lazzeri, L. Martin-Samos, N. Marzari, F. Mauri, R. Mazzarello, S. Paolini, A. Pasquarello, L. Paulatto, C. Sbraccia, S. Scandolo, G. Sclauzero, A. P. Seitsonen, A. Smogunov, P. Umari, and R. M. Wentzcovitch. *J. Phys.: Condens. Matter*, 27:1787–1799, 2006.

[10] S. Grimme. *Journal of Computational Chemistry*, 79:272, 2001.

[11] J. P. Hong, A. Y. Park, S. Lee, J. Kang, and N. Shin amd D. Y. Yoon. *Applied Physics Letters*, 92:143311, 2008.

[12] D. Kälblein, T. Weitz, H. J. Böttcher, F. Ante, U. Zschieschang, K. Kern, and H. Klauk. *Nanoletters*, 11: 53095315, 2011.

[13] J. M. D. Lane, M. Chandross, C. D. Lorenz, M. J. Stevens, and G. S. Grest. *Langmuir*, 24:5734, 2008.

[14] A. Natan, L. Kronik, and Y. Shapira. *Appl. Surf. Sci.*, 252:7608, 2006.

[15] J.P. Perdew, K. Burke, and M.Ernzerhof. *Phys. Rev. Lett.*, 77:3865, 1996.

[16] G. Ponti, F. Palombi, D. Abate, F. Ambrosino, G. Aprea, T. Bastianelli, F. Beone, R. Bertini, G. Bracco, M. Caporicci, B. Calosso, M. Chinnici, A. Colavincenzo, A. Cucurullo, P. dAngelo, M. De Rosa, P. De Michele, A. Funel, G. Furini, D. Giammattei, S. Giusepponi, R. Guadagni, G. Guarnieri, A. Italiano, S. Magagnino, A. Mariano, G. Mencuccini, C. Mercuri, S. Migliori, P. Ornelli, S. Pecoraro, A. Perozziello, S. Pierattini, S. Podda, F. Poggi, A. Quintiliani, A. Rocchi, C. Scio, F. Simoni, and A. Vita. The role of medium size facilities in the hpc ecosystem: the case of the new cresco4 cluster integrated in the eneagrid infrastructure. *IEEE HPCS*, 6903807:1030–1033, 2014.

[17] P. Roumeliotis and K. K. Unger. *Journal of Chromatography*, 149:211, 1978.

[18] M. Salinas, C.M. Jäger, A.Y. Amin, P.O. Dral, T. Meyer-Friedrichsen, A. Hirsch, T. Clark, and M. Halik. The relationship between threshold voltage and dipolar character of self-assembled monolayers in organic thin-film transistors. *Journal of The American Chemical Society*, 134:12648–12652, 2012.

[19] N. Troullier and J.L. Martins. *Phys. Rev. B*, 43:1993, 1991.

[20] A. Ulman. *Chem. Rev.*, 96:1533, 1996.

[21] D. Vuillaume, C. Boulas, J. Collet, J. V. Davidovits, and F. Rondelez. *Applied Physics Letters*, 69:1646, 1996.

[22] M. Wang, K. M. Liechti, V. Srinivasan, J. M. White, P. J. Rossky, and M. T. Stone. *Journal of Applied Mechanics*, 73:769, 2006.

[23] A. A. Yasseri, S. Sharma, T.I. Kaminis, Q. Xia, S. Y. Chou, and R. F. W. Pease. *Applied Physics Letters*, 89:153121, 2006.

[24] H. Zhang, X. Guo, J. Hui, S. Hu, W. Xu, and D. Zhu. *Nanoletters*, 11:4939–4946, 2011.

A High Resolution Numerical Model to Study the Coastal Processes in the Adriatic Sea

G. Sannino[1]*, *W. J. McKiver*[2] *and D. Bellafiore*[2]

[1] *ENEA Centro Ricerche Casaccia, Via Anguillarese 301, 00123 Roma, Italy*

[2] *ISMAR-CNR, Arsenale – Tesa 104, Castello 2737/F, 30122 Venice, Italy*

Abstract. A high resolution implementation of MITgcm for the Adriatic Sea is presented. The model has been developed in the framework of the Italian national flagship project RITMARE, and in particular it has been devoted to investigate the ocean model capability in capturing vertical hydrodynamic coastal processes in the North Adriatic Sea. The model run on CRESCO4.

1 Introduction

In the framework of the Italian national flagship project RITMARE has been conducted a specific study [1] to investigate the actual ocean model capability in capturing vertical hydrodynamic coastal processes in the North Adriatic Sea. The Adriatic Sea has been chosen because it is a typical example of a water body that is strongly linked to its coastal system, being a semi-enclosed basin with a particular topography, having a very shallow northern area becoming deeper towards the south, and a large number of fresh-water sources. This makes it prone to Deep Water (DW) events, when cold north-easterly winter winds induce water sinking in the shallow Northern Adriatic. These extreme DW events have many complex influences and thus are particularly challenging to understand and model, though their impact on the general circulation has made them an important topic of research. In [1] the authors focused their attention on one particularly strong DW formation event that occurred in the beginning of 2012. In particular they implemented two very different numerical models, SHYFEM (Shallow water HYdrodynamic Finite Element Model) and MITgcm (Massachusetts Institute of Technology general circulation model), in order to compare their strengths and weaknesses in representing these DW formation processes. In order to speedup the research, the two models have been run in parallel on different clusters. In particular MITgcm has been run on the ENEA cluster CRESCO4. In the following the MITgcm model implementation and setup as well as a validation analysis will be shown.

---

[*] Corresponding author. E-mail: `gianmaria.sannino@enea.it`.

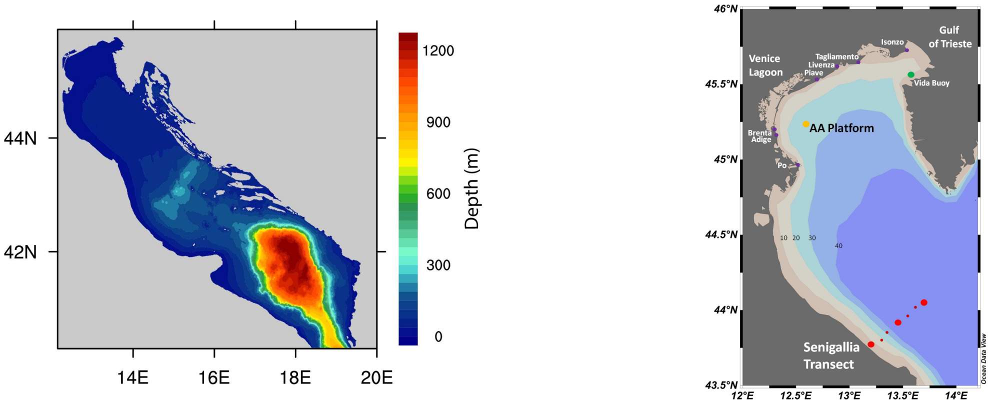

Figure 1: (left) Model bathymetry and computation domain. (right) Map showing location of data sources used for validating the model : CTD data (red dots), Acqua Alta CNR Platform (yellow dot), Vida buoy (green dot). Purple dots show the location of river inputs.

2 Model implementation and simulation setup

The model implemented in this study is the MITgcm. The MITgcm solves both the hydrostatic and nonhydrostatic Navier-Stokes equations under the Boussinesq approximation for an incompressible fluid with a spatial finite-volume discretization on a curvilinear computational grid. The model formulation, which includes implicit free surface and partial step topography, is described in detail by [2] and [3]. The model domain, that covers the entire Adriatic Sea, is discretized by a non-uniform curvilinear orthogonal grid of 4321296 points. The 2D domain has been decomposed in order to use 1728 cores of CRESCO4. However the model showed a very good scalability up to 3888 cores. Model horizontal resolution Dx (Dy) smoothly increase from about 400m (700m) at the southern boundary up to 200m (400m) at the northern coasts. The model has 100 vertical z levels with a thickness of 1m in the upper 23m gradually increasing to a maximum of 17m for the remaining 64 levels. As in [4] and [5], an implicit linear formulation of the free surface is used. The model uses constant horizontal eddy coefficients for momentum (viscosity: $10\text{m}^2\text{s}^{-1}$), temperature, and salinity (diffusivity: $2\text{m}^2\text{s}^{-1}$). Vertical eddy viscosity and diffusivity coefficients are computed in the MITgcm using the turbulence closure model developed by [6] for the atmosphere and adapted for the oceanic case by [7]. The river runoff is considered explicitly and modeled as a lateral open-boundary condition. As in [8] the rivers are included by introducing small channels in the bathymetry that simulate the river bed close to the coast. Velocity is imposed at the upstream end of each channel, and when the velocity is multiplied by the cross-sectional area of the channel, the prescribed discharge rate is quantified. No flux conditions for either momentum or tracers and no slip conditions for momentum are imposed at the solid boundaries. Bottom drag is expressed as a quadratic function of the mean flow in the bottom layer: the (dimensionless) quadratic drag coefficient is set equal to 0.002. The net transport through the southern open boundary is corrected during run–time at each time step to balance the effects of river discharge and of the evaporation minus precipitation budget on the surface level. This solution prevents any unrealistic drift in the sea surface elevation. Tides are imposed as a barotropic velocity at the southern boundary. At the surface, the wind drag coefficient is computed following the default MITgcm formulation:

$$Cd = \frac{0.0027}{U_{10}} + 0.000142 + 0.0000764\,U_{10}\,, \tag{1}$$

where U_{10} is the wind speed at 10m. To reproduce the surface heat fluxes, shortwave radiation from the atmospheric model is imposed, whereas the longwave radiation is computed according to the [9] formula. Bulk formulas are computed considering the sea surface temperature, the winds at 10m height, the dry air temperature and the air pressure at 2m, and the relative humidity as inputs. The latent heat flux and the sensible heat flux are computed according to the [10] and [11] formulation. The model simulation begins in December 2011 and is run until the end of April 2012. This period covers the DW event in the beginning of 2012. The time steps used was 10s. Output fields and diagnostics are produced every three simulated hours. Temperature and salinity are initialized, interpolating 3–D values on the two grids, and forced at the open boundary at the Otranto Strait, from AFS (Adriatic Forecasting System) data. AFS data are provided with 2km horizontal resolution, 3–dimensional fields on a sigma level system, daily means. Tidal water level and surge data are provided from the OTIS tidal model and AFS sea–surface height data. River inputs have been explicitly included for the Po, Adige, Brenta, Livenza, Piave, Tagliamento and Isonzo rivers. The Po river discharge is provided by ARPA Emilia Romagna (ARPA-SIMC), daily values. The Tagliamento and Isonzo river discharge are provided by Regione Friuli Venezia Giulia (Servizio Idrografico) with a frequency of 30min and are measured by two tide gauges in front of the river mouths. The period chosen for the present run is not covered by measured discharge data for the other rivers, therefore climatological values computed on a large daily dataset covering the period 2005–2010 are used. All the river boundaries are forced with measured water temperature timeseries from the year 2007, collected on the Tagliamento, except the Isonzo river that uses its own measured timeseries, available for the same year. Where data are missing in the Tagliamento and Isonzo measured timeseries, gaps are filled with climatological data. In Fig. 1 we show the map of the model bathymetry used in MITgcm, and the location of data sources used for validating the model and the river inputs.

3 Model validation

In order to validate the hydrostatic model simulation, a number of observational data sets are used:

- CTD transects of temperature and salinity are provided from a cruise with the R/V DallaPorta, along the Senigallia Transect (Fig. 1 right panel), where temperature and salinity profiles were acquired for the 27 March 2012.
- Sea surface temperature (SST) from satellite data obtained using Moderate Resolution Imaging Spectroradiometer (MODIS). We selected the MODIS-Aqua SST for

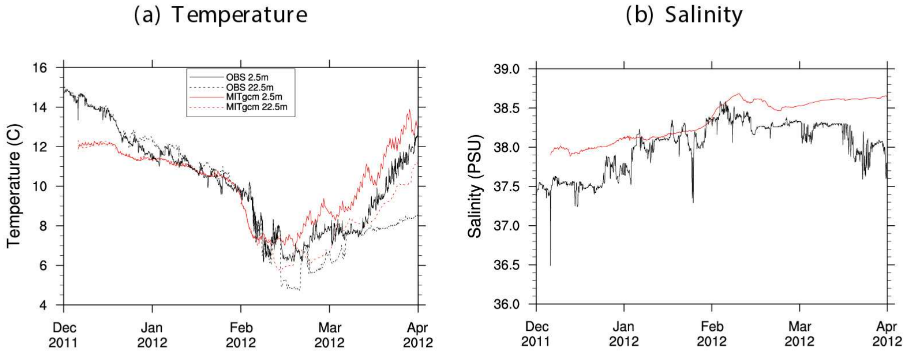
(a) Temperature

(b) Salinity

Figure 2: Timeseries of surface (solid) and bottom (dashed) temperature (left) and surface salinity (right) for MITgcm (red) and the Vida buoy observations (black).

Location	Variable	Bias	RMSE	Correlation
Vida Buoy	Temperature (2m) [°C]	0.19	1.11	0.88
	Temperature (22m) [°C]	-0.04	1.12	0.94
	Salinity (2m) [psu]	0.31	0.37	0.73

Table 1: Statistical analysis of simulated water temperature and salinity timeseries computed at the Vida Buoy. Analyses provided are the difference between mean of observations and simulations (BIAS), the root mean square error (RMSE) and the correlation.

the Adriatic Sea, acquired during daytime on the 26 January, 5 and 16 February 2012.

- In the Gulf of Trieste, timeseries of surface (2.5m) temperature and salinity and bottom (22.5m) temperature from the Vida Buoy (Fig. 1 right panel) are used to validate the models output. Also surface (2m) and bottom (12m) temperature, salinity and density anomaly from sensors installed at the CNR Platform Acqua Alta (AA Platform in Fig. 1 right panel) are available for model validation, for the time window 1 December 2011 to the 31 March 2012.

Due to the limited number of pages the validation shown in the report is limited to the VIDA buoy comparison. A more complete analysis can be found in [1]. In Fig. 2 the timeseries of surface and bottom temperature as well as surface salinity from the VIDA buoy is shown. In the lead up to the event, up to the end of January, the models reproduce well the surface and bottom temperatures. Also it captures the onset of the event, registering the starting moment of the cold water sinking at the beginning of February. However the model overestimates the minimum temperature values reached during the event. MITgcm reproduces the surface temperature before the event, with just a small underestimation in the first simulated month. However bottom temperature is closer to the observations during the event, and the greater difference in the temperature values between surface and bottom, indicates that MITgcm has an unstable stratification and less mixing during the DW event. From the statistical analysis of the whole temperature timeseries, which is shown in Table 1, it is evident that the model well reproduces measurements, with biases always lower than 0.3C. Correlation is high both for surface and bottom temperature data, while slightly lower for salinity. The model shows higher errors in reproducing the timeseries variability, as expressed by RMSE values of around 1°C. Considering that the model does not imply any kind of data assimilation, the results of the validation (included those not included in this report, but extensively discussed in [1]) can be considered adequate to perform the comparing study proposed in RITMARE [1].

References

[1] W. J. Mc Kiver, G. Sannino, F. Braga, and D. Bellafiore. Investigation of model capability in capturing vertical hydrodynamic coastal processes: a case study in the North Adriatic Sea. *Ocean Science*, (Submitted).

[2] J. Marshall, C. Hill, L. Perelman, and A. Adcroft. Hydrostatic, quasi-hydrostatic, and nonhydrostatic ocean modeling. *J. Geophys. Res.*, 102:5733–5752, 1997a.

[3] J. Marshall, A. Adcroft, C. Hill, L. Perelman, and C. Heisey. A finite-volume, incompressible Navier Stokes model for studies of the ocean on parallel computers. *J. Geophys. Res.*, 102:5753–5766, 1997b.

[4] J. Sanchez-Garrido, G. Sannino, L. Liberti, and G. Lafuente. Numerical modelling of three-dimensional stratified tidal flow over Camarinal sill, Strait of Gibraltar. *J. Geophys. Res.*, 116:1978–2012, 2011.

[5] G. Sannino, J. C. Sanchez Garrido, L. Liberti, and L. Pratt. Exchange flow through the Strait of Gibraltar as simulated by a-coordinate hydrostatic model and a z-coordinate nonhydrostatic model. *In: The Mediterranean Sea: Temporal Variability and Spatial Patterns*, John Wiley & Sons Inc.:25–50, 2014.

[6] P. Bougeault and P. Lacarrere. Parametrization of orography-induced turbulence in a mesoscale model. *Monthly Weather Review*, 117:1872–1890, 1989.

[7] P. Gaspar, Y. Gregoris, and J.-M. Lefevre. A simple eddy kinetic energy model for simulations of the oceanic vertical mixing: tests at station papa and long-term upper ocean study site. *J. Geophy. Res.*, 95:16179–16193, 1990.

[8] S. Querin, A. Crise, D. Deponte, and C. Solidoro. Numerical study of the role of wind forcing and freshwater buoyancy input on the circulation in a shallow embayment (Gulf of Trieste, Northern Adriatic Sea). *J. Geophys. Res.*, 111:C03S1, 2006.

[9] N. E. Clark, L. Eber, R. M. Laurs, J. A. Renner, and J. F. T. Saur. Heat exchange between ocean and atmosphere in the eastern North Pacific for 1961. *71 NOAA Tech. Rep. NMSF SSRF-682*, US Department of Commerce, Washington D.C., 1974.

[10] W. Large and S. Pond. Open ocean momentum flux measurements in moderate to strong winds. *J. Phys. Oceanogr.*, 11:324–336, 1981.

[11] W. Large and S. Pond. Sensible and latent heat flux measurements over the ocean. *J. Phys. Oceanogr.*, 12:464–482, 1982.

Ab-Initio Molecular Dynamics Simulation of High Temperature GeO_2

G. Mancini[1]*, M. Celino[2] and A. Di Cicco[1]

[1] Università di Camerino, Via Madonna delle Carceri 62032, Camerino (MC), Italy

[2] ENEA, C. R. Casaccia, Via Anguillarese 301, 00123 Roma, Italy

Abstract. We made a series of molecular dynamic simulations to get a representative, high temperature GeO_2 system to eventually be quenched down to room temperature so as to obtain an amorphous system to be studied under pressure for comparison to experimental results. We carefully generated an initial configuration such that all simulations have entirely been carried out by ab-initio methods in the range 10K-3000K.

1 Introduction

The study of liquid and amorphous GeO_2 holds a particular interest among material sciences and physics researchers, due to the fact that GeO_2 presents many structural similarities with SiO_2 - short range order is the same - whilst undergoing phase transitions at much lower pressures. Moreover the differences between GeO_2 and SiO_2 glasses at the medium-range scale, allow glass transition temperature of GeO_2 to be considerably lower than for SiO_2. In addition, thanks to its higher electron and hole mobilities and its lower operating voltages, germanium is gaining increasing consideration for replacing silicon in solid state devices.

Due to currently available computational powers, molecular dynamics simulations are more and more often carried out to flank experimental results on Ge compounds.

On the base of the simulations we performed on a *numerical sample* made of Ge atoms [1, 2], we started a molecular dynamics study of GeO_2. As a preliminary step, our first goal was to get a representative GeO_2 system well over its melting temperature as a starting point to eventually obtain liquid and amorphous GeO_2 to be studied under external hydrostatic pressures.

In this paper we present the preliminary results obtained in simulating a system of 240 atoms, 160 oxygen and 80 germanium, at 3000K by first–principles molecular dynamics. First principles simulations require a suitable initial configuration, virtually at 0K, to be heated up to a target temperature through a series of equilibrated states at intermediate

---

[*] Corresponding author. E-mail: `giorgio.mancini@unicam.it`.

temperatures. It is known that the generation of initial configurations of GeO_2 to be gradually heated up is a delicate process; it is not unlikely to obtain a system for which the simulations diverge during the very first steps. This and the fact that first-principles simulations take long computation times to reach the temperatures of interest, are the reasons for which first-principles simulations are often started at high temperatures on initial configurations obtained by classical molecular dynamics methods [3].

Our approach has instead been to perform the entire simulation using ab-initio methods to get a liquid GeO_2 system at high temperature to be used as a starting system to obtain numerical samples of GeO_2, liquid and amorphous, to be characterized at the GeO_2 melting point (1389K) and at 300K, respectively.

2 Computational details

We considered for our system a density $\rho = 3.66$ gr/cm^3, corresponding to the experimental density for GeO_2 in the temperature range of our interest [3], giving a cubic simulation cell edge of 1.56nm. To ensure that our final results were independent on the initial atomic positions, the starting configuration has been generated placing the atoms at random in the simulation cell imposing that mutual distances Ge-Ge, O-O, Ge-O were larger than certain suitable thresholds [4] (this procedure designs a highly defective starting configuration, well apart from the crystalline counterpart).

We further disordered the configuration by constant temperature and constant pressure MD equilibration at high temperature (T = 3000K), at which atoms covered a distance as long as about 2nm ensuring the final configuration retains no memory of the initial positions.

The software we used is CPMD (Car-Parrinello Molecular Dynamics) [5, 6].

The self consistent evolution of the electronic structure during the motion is described within density functional theory. A generalized gradient approximation (BLYP-GGA) has been adopted for the exchange and correlation part of the total energy [7, 8] and norm conserving pseudo-potentials have been used for the core-valence interactions.

A particular attention was paid to choose the cutoff value for plane waves; the electronic wave functions were expanded in plane waves up to a kinetic energy of 60Ry to get a low relative error on computed forces - the order of a few percent [9] – and shorter computation times while retaining a good computational accuracy.

After the initial wave function and geometry optimizations, the system was taken and equilibrated up to 10K, 50K, 100K,150K, 200K, respectively, and subsequently taken up to 3000K by steps of 100K. An integration time step of 3a.u. (0.072fs) was used for the initial optimizations, whereas a time step of 5a.u. (0.12fs) was used at all temperatures for a total simulation in temperature 50ps long (24ps of which at 3000K).

During the equilibration of the system at each intermediate stage a Nosè thermostat was used for each degree of freedom to control the ions temperature [10, 11, 12]. The characteristic frequency for the thermostat was 1000cm^{-1}. A second Nosè thermostat was used to control the fictitious electronic kinetic energy. This thermostat prevents the electronic wave functions from drifting away from the instantaneous ground state (the Born-Oppenheimer surface), by removing excess fictitious kinetic energy. This drift is particularly large for metals. The characteristic frequency for the electrons thermostat was 10000cm^1 and the target kinetic energy was chosen according to [13]. The Nosè thermostat on the electrons was used throughout the simulation and proved to be an effective way of keeping the electrons on the Born-Oppenheimer surface.

3 Computational resources

Fig. 1 shows the pair distribution function for the final GeO_2 system at 3000K after a 24ps long equilibration. As expected, the atoms has undergone relatively large displacements and the new configuration is well apart from the initial one: the final geometry correctly shows the typical mutual distances O-O, Ge-Ge, Ge-O reported for GeO_2 systems at the same temperature [4].

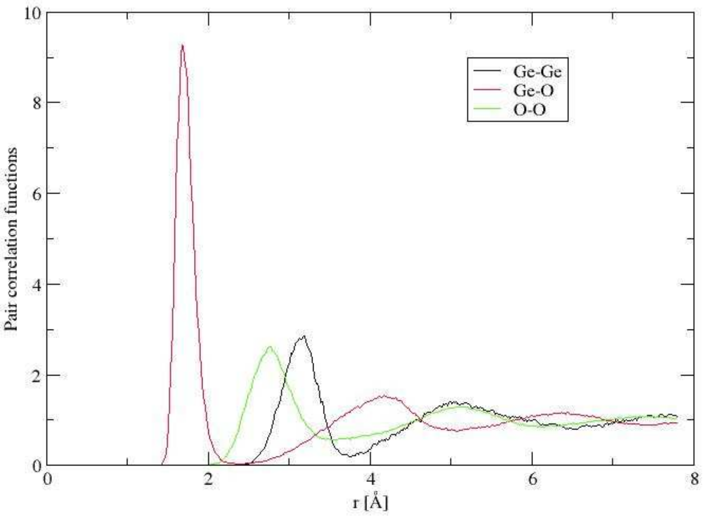

Figure 1: Radial distribution function from the simulated GeO_2 system at 3000K.

We can then conclude that we actually have obtained a reliable GeO_2 system at high temperature by first-principles molecular dynamics. Starting from this very result, the evolution of our system when taken down to 1389K is currently being computed; the additional results will hopefully be object of future communications.

References

[1] G Mancini, M. Celino, and A. Di Cicco. Ab-initio Study of amorphous Germanium. *in High Performance Computing on CRESCO infrastructure: research activities and results 2012*, ISBN: 978-88-8286-302-9:87–91, 2014.

[2] G. Mancini, M. Celino, and A. Di Cicco. First-principles study of amorphous germanium under pressure. *in High Performance Computing on CRESCO infrastructure: research activities and results 2013*, ISBN: 978-88-8286-312-8:97–105, 2015.

[3] M. Hawlitzky, J. Horbach, S. Ispas, M. Krack, and K. Binder. Comparative classical and *ab initio* molecular dynamics study of molten and glassy germanium dioxide. *J. Phys.: Condens. Matter*, 20:15, 2008.

[4] M. Micoulaut, L. Cormier, and G. S. Henderson. The structure of amorphous, crystalline and liquid GeO_2. *J. Phys.: Condens. Matter*, 18:R753–R784, 2006.

[5] CPMD v3.13.2. copyright ibm corp 1990-2008. *copyright mpi fr festkrperforschung stuttgart*, 1997-2001.

[6] W. Andreoni and A. Curioni. New advances in chemistry and material science with CPMD and parallel computing. *Parallel Computing*, 26:819–842, 2000.

[7] A. D. Becke. Density-functional exchange-energy approximation with correct asymptotic behavior. *Phys. Rev. A*, 38:3098, 1988.

[8] C. Lee, W. Yang, and R. G. Parr. Development of the Colle-Salvetti correlation-energy formula into a functional of the electron density. *Phys. Rev. B*, 37:785, 1988.

[9] The CPMD Consortium. Car-Parrinello Molecular Dynamics: An ab initio Electronic Structure and Molecular Dynamics Program. *Manual for CPMD*, version 3.15.1.

[10] M. Parrinello and A. Rahaman. Polymorphic transitions in single crystals: a new molecular dynamics method. *J. Appl. Phys.*, 52:7182–7190, 1981.

[11] S. Nosé. A molecular-dynamics method for simulations in the canonical ensemble. *Mol. Phys.*, 52:255–268, 1984.

[12] S. Nosé. A unified formulation of the constant temperature molecular dynamics methods. *J. Chem. Phys.*, 81:511–519, 1984.

[13] P. Blöchl and M. Parrinello. Adiabaticity in first-principles molecular dynamics. *Phys. Rev. B*, 45:9413–9416, 1992.

HPC resources allow to simulate Fluoride Riboswitch Recognition Site using Ab Initio Molecular Dynamics

R. Credentino[1]* *and L. Cavallo*[1]

[1]*KAUST Catalysis Research Center, Physical Sciences and Engineering Division*
King Abdullah University of Science and Technology,
Thuwal 23955-6900, Kingdom of Saudi Arabia

Abstract. Ab Initio Molecular Dynamics of the fluoride riboswitch center, taking in account esplicit solvent, requires huge amount of computational resources. Using the Cresco4 HPC resource, we are able to demonstrate that riboswitch center is stable by its own and, once assembled, does not rely on any additional factor from the overall RNA fold[1]. Further, we are able to predict the pK_a of the water molecule bridging two Mg cations. We also demonstrate that the halide selectivity of the fluoride riboswitch is determined by the stronger MgF bond, which is capable of keeping together the cluster. Replacing F^- with Cl^- results in a cluster that is unstable under dynamic conditions.

1 Introduction

Riboswitches are short mRNA segments in the 5'-untranslated region, deputed to control gene expression by their expression platform, in response to the selective binding of a metabolite to their aptamer region. Fluoride sensing riboswitches, common to bacterial and archaeal species, have been shown to regulate the expression of genes that encode fluoride exporters [2]. Beside their capability to target the small fluoride anion with good efficiency, they remarkably reject other small anions, including chloride. A crystallographic structure has been recently solved for the fluoride-bound form of riboswitch from Thermotoga petrophila [3]. This structure evidenced that, in the middle of a pseudoknot scaffold, the fluoride is the central unit keeping together a small cluster of three Mg^{2+} cations, see Fig. 1, whose coordination sphere is completed by oxygen atoms of five inwardly pointing backbone phosphate groups (some of them bridging two Mg^{2+} ions) from two distinct segments of the riboswitch sequence, and by water molecules, one of them bridging two of the Mg^{2+} ions.

The high fluoride selectivity and the structure of the recognition site in the fluoride riboswitch raises a series of questions. Among them are the following: *i*) Is the small Mg^{2+}/F/phosphate/water cluster at the center of the riboswitch a stable entity on its

---

[*] Corresponding author. E-mail: `rcredendino@unisa.it`.

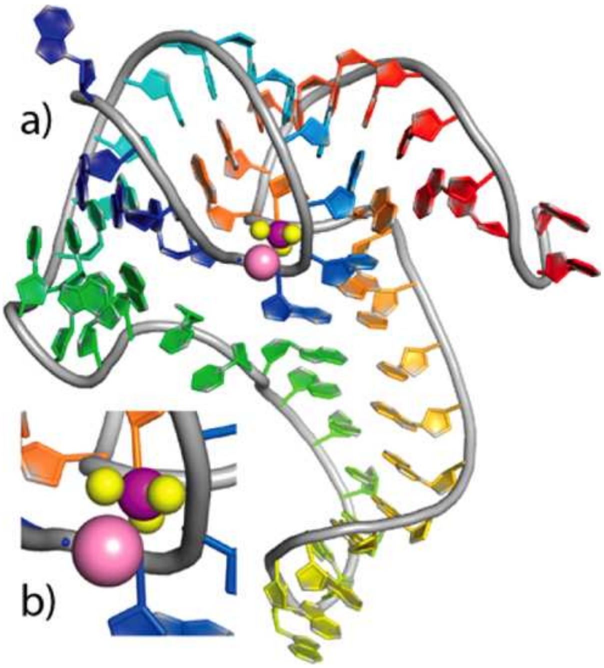

Figure 1: Schematic representation of the fluoride riboswitch in a rainbow spectrum, from 5' end (blue) to 3' end (red). Yellow and purple spheres, Mg^{2+} and F^- ions of the central cluster. Pink sphere, the K^+ ion.

own? *ii*) Considering that water molecules bridging metal cations are known to be quite acidic, what is the acidity of the water molecule bridging two Mg^{2+} cations in the F-cluster at the center of the fluoride riboswitch? *iii*) What is the origin of the halide selectivity?

Naturally, to provide a clear answer to three fundamental questions based on static and dynamic density functional theory (DFT) calculations, is necessary to choose well performing software and hardware resources. A good combination of these two items results CP2K software [4] on Cresco4 hardware.

Indeed, CP2K, a freely available (GPL) program, written in Fortran 95, allows to perform atomistic and molecular simulations of solid state, liquid, molecular and biological systems and recently it was implemented linear scaling Kohn-Sham Density Functional Theory (KS-DFT) calculations. This method achieves linear scaling (in the number of atoms) by the use of a massively parallel sparse matrix library DBCSR, which has been designed by the CP2K developers specifically for atomistic simulation. Using DBCSR, all $O(N^3)$ dense linear algebra operations are replaced with sparse $O(N)$ counterparts, thus avoiding expensive matrix diagonalisation, the bottleneck of traditional DFT calculations. These developments will allow the simulation of very large systems of the order of 1,000,000 atoms to be simulated efficiently, given enough CPU resources.

Cresco4 results the best choice due to possibility to use medium size cluster. In fact, the scalability of cp2k software gives the best performance until 256 core for system considered, as shown in Fig. 2.

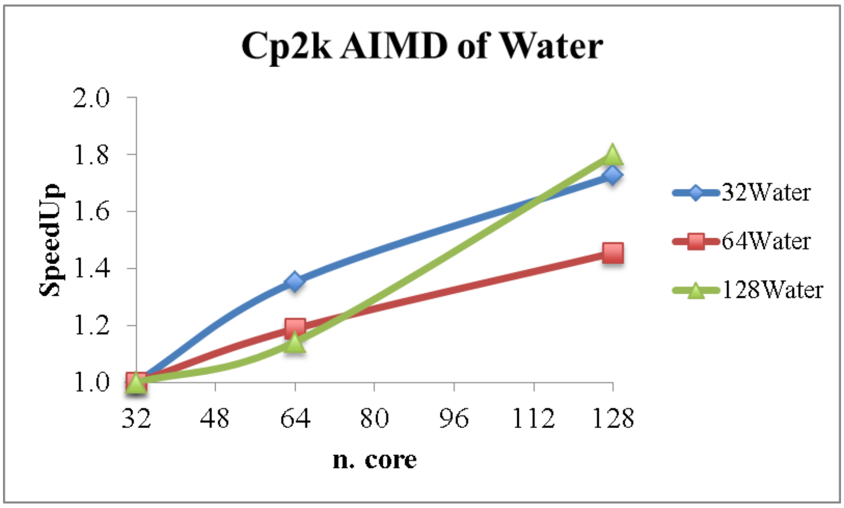

Figure 2: Speedup for CP2K AIMD simulation of three different size box of water molecules.

2 Computational methods

All the molecular dynamics DFT calculations (referred are DFT-MD in the following) were performed using the BornOppenheimer scheme as implemented in the CP2K Quickstep code. The electronic structure calculations were carried out using the PerdewBurkeErnzerhof exchange and correlation functional [5] with the addition of the D3 empirical dispersion term [6]. The CP2K program employs a mixed basis set approach with Gaussian-type orbitals (GTO) and plane waves (PWs). GTO functions are used to expand the molecular orbitals and the charge density in real space, whereas PWs are used for the representation of the charge density in reciprocal space. An energy cutoff of 300 Ry is used for the plane-waves basis set. The GTH-DZVP double-ζ basis set with a polarization function, in conjunction with the Goedecker TeterHutter pseudopotentials, was used for all the atoms [7]. The systems were first equilibrated at 300 K for 1 ps in the NVT ensemble, by fixing the heavy atoms of the cluster, followed by another 1 ps equilibration by relaxing also the position of the heavy atoms of the cluster. A production run was then carried out for 10 ps in the NVT ensemble. The equations of motion were integrated using a time step of 0.5 fs. Temperature was controlled using a canonical-sampling- through-velocity-rescaling thermostat.

3 Conclusions

In conclusion, thanks to HPC resource available on ENEAGRID platform, we are able to perform analysis of the core Mg^{2+}/halide/phosphate/water cluster of the fluoride riboswitch from T. petrophila allowed to clearly explain the following:

i) The core cluster is a stable entity on its own, under both static and dynamic conditions. Once assembled, this structure does not need any additional stabilizing factor from the overall RNA molecule.

ii) Replacing the Mg-bridging water molecule with a hydroxyl group results in a structure perfectly consistent with the experimental data, although it should be considered that this requires having an overall negatively charged cluster, in the negatively charged environment provided by the RNA skeleton.

iii) The Mg-bridging water molecule is quite acidic, with a predicted pKa around 8.4.

iv) Replacing the fluoride with a chloride in the DFT geometry optimization leads to minor structural changes, which indicates that binding of heavier halides could be structurally feasible. However, the DFT-MD simulations indicated that the Cl-cluster is unstable under dynamic conditions, with the substantial rupture of MgCl and Mg-water bonds.

v) Binding of a fluoride in the core cluster of the riboswitch is clearly stronger than binding of a chloride, and this difference can be mainly ascribed to the difference in the MgF and MgCl bonds strength.

vi) Calculations on the F- centered cluster of fluoride-inhibited pyrophosphatase show that also in this case fluoride has a much better ability than chloride to hold together the cluster, both from a structural and energetic point of view.

References

[1] M. Chawla, R. Credendino, A. Poater, R. Oliva, and L. Cavallo. *J. Am. Chem. Soc.*, 137:299–306, 2015.

[2] S. Li, K. D. Smithh, J. H. Davis, P. B. Gordon, R. R. Breaker, and S. A. Strobel. *Proc. Natl. Acad. Sci. U.S.A.*, 110:19018, 2013.

[3] A. Ren, K. R. Rajashankar, and D. J. Patel. *Nature*, 486:85, 2012.

[4] J. K. M. VandeVondele, F. Mohamed, M. Parrinello, T. Chassaing, and J. Hutter. *J. Comp. Phys. Comm.*, 167:103, 2005.

[5] J. P. Perdew, K. Burke, and M. Ernzerhof. *Phys. Rev. Lett.*, 77:3865, 1996.

[6] S. Grimme, J. Antony, S. Ehrlich, and H. Krieg. *J. Chem. Phys.*, 132:154104, 2010.

[7] S. Goedecker, M. Teter, and J. Hutter. *Phys. Rev. B*, 54:1703, 1996.

Nanocrystallization of amorphous $Cu_{64}Zr_{36}$ into the Cu_2Zr Laves phase studied by Molecular Dynamics simulations

J. Zemp[1][*], *M. Celino*[2], *J. F. Löffler*[1] *and B. Schönfeld*[1]

[1]*Laboratory of Metal Physics and Technology, Department of Materials*
ETH Zurich, 8093 Zrich, Switzerland

[2]*ENEA, C. R. Casaccia, Via Anguillarese 301, 00123, Rome, Italy*

Abstract. Amorphous $Cu_{64}Zr_{36}$ was studied using Molecular Dynamics simulations. An annealing treatment for 1000ns at 800K, i.e. slightly above the glass transition temperature of 745K, was applied and the formation of small Cu_2Zr nanocrystallites was observed. The structure of the nanocrystallites is similar to the $MgZn_2$ Laves phase, which consists of icosahedra and CN16 Frank-Kasper polyhedra. Thus, the increasing fraction of icosahedra during annealing is not indicative of relaxation of the glass, but due to early stages of crystallization.

1 Introduction

Icosahedral order is, due to the incompatibility with long-range translational order, commonly attributed to the structure of liquids and glasses. In fact, many metallic glasses (MGs) contain a high fraction of icosahedra, especially in the Cu-Zr series [1]. As a result, the number of icosahedra that are present in a given atomic configuration is taken as a measure for the degree of relaxation [2]. Such a view, however, is problematic as the incompatibility of icosahedra with long-range order does no longer hold for systems with more than one atomic species. For example, the structure of the $MgZn_2$-type Laves phase is entirely made up of Zn-centered icosahedra and Mg-centered CN16 Frank-Kasper polyhedra. Metallic glasses often crystallize into Laves phases, e.g., Cu-Zr-Ti MGs [3] or the bulk glass-former Vit1 [4]. Although the Cu_2Zr ($MgZn_2$-type) Laves phase has not yet been observed experimentally, the MD-interaction potential by Mendelev et al. [5] gives a low potential energy for this phase [6]. Furthermore, the experimental phase diagram is not well understood at high temperatures close to the liquidus temperature. Actually, Kneller et al. [7] suggested the presence of a high-temperature Cu_2Zr phase based on thermal differential analysis data. With this in mind, the concurrent increase in the fraction of Cu-centered icosahedra and Zr-centered CN16 Frank-Kasper polyhedra as observed by Ding et al. [2] might not indicate structural relaxation of the glass, but rather the formation of a Cu_2Zr Laves phase.

---

[*] Corresponding author. E-mail: `jerome.zemp@mat.ethz.ch`.

This report covers the continuation of the work described in Refs. [8, 9, 10]. A long-time annealing for 1000ns at 800K was applied to $Cu_{64}Zr_{36}$ to track the evolution of the icosahedral short-range order and its role in the possible formation of the Cu_2Zr Laves phase.

2 Method

Molecular Dynamics (MD) simulations of $Cu_{64}Zr_{36}$ were carried out using the LAMMPS simulation package [11] and the interaction potential by Mendelev et al. [5]. Samples were initially produced as described in Refs. [8, 9]. In addition, the annealing treatment at 800K was extended to 1000ns. After annealing, the sample was cooled to 50K at a rate of 0.01K/ps. The atomic configurations were characterized using the Voronoi tessellation method: a Voronoi index (VI) is assigned to every atom given by $\langle n_3\, n_4\, n_5\, n_6 \rangle$, where n_i is the number of i-edged faces of the corresponding Voronoi polyhedron (VP). In the case where two center atoms of Cu-centered icosahedra (having a VI of $\langle 0\,0\,12\,0 \rangle$) are nearest neighbors, a cap-sharing bond is formed leading to the formation of icosahedral superclusters (SCs) as described in Ref. [12]. The orientation of cap-sharing bonds is investigated by the (cumulative) bond-angle distribution, where the bond-angle is given by

$$\theta_{ijk} = \cos^{-1}\left(\frac{r_{ij}^2 + r_{ik}^2 - r_{jk}^2}{2\, r_{ij} r_{ik}} \right) , \tag{1}$$

with r_{ij} being the distance between atoms i and j. For a regular icosahedron in a monoatomic system three bond angles, namely 60°, 120° and 180°, are observed with a probability of 0.45 for the 60° and 120° bond angles and 0.1 for the 180° bond angle.

To achieve reasonable simulation times, 64 processors were generally sufficient for the present system size. The simulations were carried out in parallel using open MPI as implemented in LAMMPS [11] on the CRESCO infrastructure. All atomic visualization in this work was done using the software OVITO [8].

3 Results and discussion

After cooling the sample from 2000K to 800K the fraction of Cu atoms with icosahedral symmetry is about 19%. Fig. 1 shows the evolution during annealing at 800K of the VP fraction of Cu-centered icosahedra in comparison with Cu atoms having a VI of $\langle 0\,2\,8\,2 \rangle$ and $\langle 0\,3\,6\,4 \angle$, as well as Zr-centered CN16 Frank-Kasper polyhedra. The fractions of icosahedra and CN16 Frank-Kasper polyhedra increase approximately linearly with time up to nearly 50% and 25%, respectively. In contrast, the VP fractions of Cu-centered $\langle 0\,2\,8\,2 \rangle$ and $\langle 0\,3\,6\,4 \rangle$ VP slightly decrease. This result agrees nicely with the simulations by Ding et al. [2], who, however, annealed for 300ns and used a different interaction potential (see Ref. [13]).

We have previously reported that the increase in the icosahedra and CN16 Frank-Kasper polyhedra is spatially correlated [10, 12]. Fig. 2 shows the Cu-center atoms of icosahedra

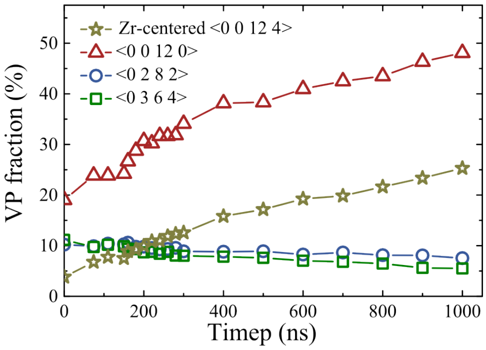

Figure 1: Development of the VP fractions of various Cu-centered VP and Zr-centered CN16 Frank-Kasper polyhedra upon annealing at 800K.

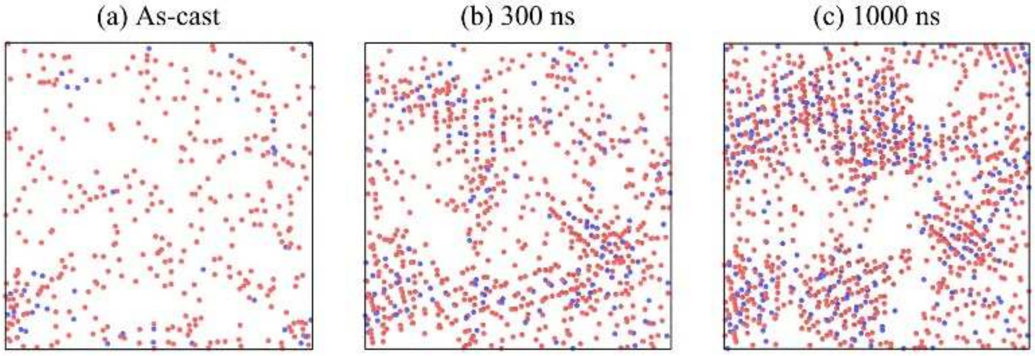

Figure 2: Cu-center atoms of icosahedra (red) and Zr-center atoms of CN16 Frank-Kasper polyhedra (blue) in a slice of 2nm thickness for $Cu_{64}Zr_{36}$ in the (a) as-cast state and after annealing for 300ns (b) and 1000ns (c) at 800K. The side length of the box is 4.7nm.

and Zr-center atoms of CN16 Frank-Kasper polyhedra in a slice, 2nm in thickness, of the atomic configurations in the as-cast state (i.e. without annealing at 800K) and after annealing for 300 and 1000ns at 800K. While in the as-cast state the Cu-centered icosahedra are non-uniformly distributed resulting in a network-like (but still non-periodic) structure, one can clearly identify a spatial correlation of the Cu- and Zr-center atoms and the formation of periodic arrangements, which indicate the presence of nanocrystallites in Figs. 2 (b,c). Because the nanocrystallites present in Fig. 2 are formed from Cu-centered icosahedra and Zr-centered Frank-Kasper polyhedra it seems reasonable to assume that crystallization occurs into the Cu_2Zr Laves phase. To underline this assumption the (cumulative) bond-angle distribution among cap-sharing icosahedra was calculated as shown in Fig. 3. From Fig. 3(a) one notes that the bond angles are getting better defined during cooling and annealing. A splitting of the peak at 120° becomes visible, which is due to an asymmetry in the bond angles as can be seen in Fig. 4, which shows the Cu_2Zr unit cell and the two types of 120°-type bond angles. From the cumulative bond-angle distribution in Fig. 3 (b) the similarity of the simulated structures after annealing and the bond-angle distribution of the ideal Cu_2Zr structure become apparent, while in the as-cast state the fraction of 60°, 120°, and 180°-type bond angles is close to statistical expectation.

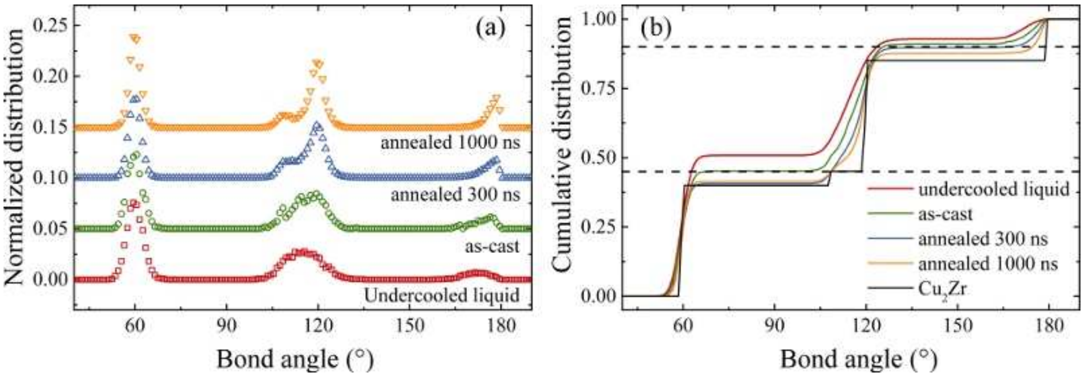

Figure 3: (a) Bond-angle distribution and (b) cumulative bond-angle distribution among icosahedra in the undercooled liquid, as-cast state and after annealing for 300ns and 1000ns at 800K. The dashed black lines in (b) show the statistical expectation value as described in the method section. The solid black line in (b) represents the distribution in the ideal Cu_2Zr Laves phase.

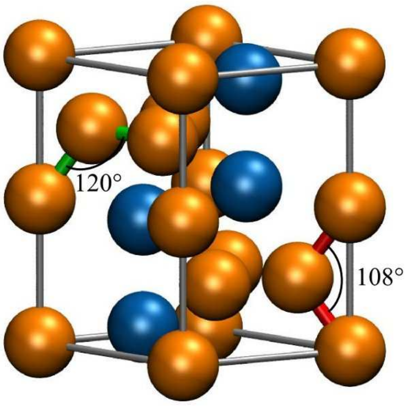

Figure 4: Unit cell of the Cu_2Zr Laves phase (Orange: Cu; Blue: Zr) and an example of the two types of 120°-type bond angles.

4 Conclusion and outlook

Long-time annealing above the glass-transition temperature of Cu64Zr36 leads to the formation of a Cu_2Zr ($MgZn_2$-type) Laves phase. The nanocrystallites can be observed by directly looking at the atomic configurations or - more quantitatively - by the bond-angle distribution among icosahedra, which for the Laves phase shows two types of 120°-type bond angles. Our results demonstrate that it is insufficient to characterize an amorphous structure simply by the fraction of icosahedra. Whether the observed Cu_2Zr Laves phase also forms in nature is undecided and experiments should be done next to clarify this question. Otherwise the interaction potential for Cu-Zr might need to be improved

References

[1] Y. Q. Cheng, H. W. Sheng, and E. Ma. Relationship between structure, dynamics, and mechanical properties in metallic glass-forming alloys. *Phys. Rev. B*, 78:014207, 2008.

[2] J. Ding, Y.-Q. Cheng, and Ma E. Full icosahedra dominate local order in $\mathrm{Cu_{64}Zr_{34}}$ metallic glass and supercooled liquid. *Acta Mater.*, 69:343–354, 2014.

[3] H. Men, S. J. Pang, and T. Zhang. Glass-forming ability and mechanical properties of $\mathrm{Cu_{50}Zr_{50-\mathit{x}}Ti_{\mathit{x}}}$ alloys. *Mater. Sci. Eng. A*, 408:326–329, 2005.

[4] C. C. Hays, C. P. Kim, and W. L. Johnson. Large supercooled liquid region and phase separation in the Zr-Ti-Ni-Cu-Be bulk metallic glasses. *Appl. Phys. Lett.*, 75:1089–1091, 1999.

[5] M. I. Mendelev, M. J. Kramer, R. T. Ott, D. J. Sordelet, D. Yagodin, and P. Popel. Development of suitable interatomic potentials for simulation of liquid and amorphous Cu-Zr alloys. *Philos. Mag.*, 89:967–987, 2009.

[6] C. Tang and P. Harrowell. Predicting the solid state phase diagram for glass-forming alloys of copper and zirconium. *J. Phys. Condens. Mat.*, 24:245102, 2012.

[7] E. Kneller, Y. Khan, and U. Gorres. The alloy system copper-zirconium. I. Phase diagram and structural relations. *Z. Metallkd.*, 77:43–48, 1986.

[8] J. Zemp, M. Celino, B. Schönfeld, and J. F. Löffler. Molecular Dynamics simulations of $\mathrm{Cu_{64}Zr_{36}}$ metallic glasses. *CRESCO Progress Report*, 2011.

[9] J. Zemp, M. Celino, J. F. Löffler, and B. Schönfeld. Shear-band formation in $\mathrm{Cu_{64}Zr_{36}}$ metallic glass under uniaxial compression. *CRESCO Progress Report*, 2012.

[10] J. Zemp, M. Celino, J. F. Löffler, and B. Schönfled. Icosahedral structure and mean-square displacement in $\mathrm{Cu_{64}Zr_{36}}$ metallic glass. *CRESCO Progress Report*, 2013.

[11] S. PLIMPTON. Fast Parallel Algorithms for Short-Range Molecular Dynamics. *J. Comput. Phys.*, 117:1–19, 1995.

[12] J. Zemp, M. Celino, B. Schönfeld, and J. F. Löffler. Icosahedral superclusters in $\mathrm{Cu_{64}Zr_{36}}$ metallic glass. *Phys. Rev. B*, 90:144108, 2014.

[13] Y. Q. Cheng, E. Ma, and H. W. Sheng. Atomic Level Structure in Multicomponent Bulk Metallic Glass. *Phys. Rev. Lett.*, 102:245501, 2009.

Further Investigation on the Structural Properties of a Cadmium Sulfide Nanocluster with Prismatic Shape

Emiliano Burresi[1]* *and Massimo Celino*[2]

[1]*ENEA, SPT-PROMAS-MATAS, S.S. 7 Appia - km 706 - 72100 Brindisi, Italy*

[2]*ENEA, C. R. Casaccia, via Anguillarese 301, 00123 Rome, Italy*

Abstract. In this work we completed the investigation on the structural properties of a CdS nanocluster with prismatic shape, which simulation by means of ab initio molecular dynamics, was reported on CRESCO 2014 activities [1]. Now we added new results about core and surface. This cluster was built with 324 atoms with prismatic shape. After relax, this structure was heated under temperature program ranging between 100 K to 400 K. Formation energy (FE) of the cluster corroborated the presence of a new structure starting at 340 K. Around 340 K, the mean square displacement (MDS) analysis reveals a large displacement of the atoms with respect to the initial positions; this behavior can be due mainly to the significant movement of the surface atoms. Analysis of the MSD curve separately for core atoms and surface atoms revealed a phase transformed of the surface, while on the core the atoms oscillate on their equilibrium position.

1 Introduction

Nanostructured cadmium sulfide quantum dots (CdS QDs) have attracted much attention for their novel optical and electronic properties employed in different technological fields. Structural and electronic properties are not yet completely explained and different phases with different stability could be obtained during the synthesis process. A computational quantum approach can be useful to characterize the different phases from both atomic and crystallographic point of view [2, 3]. Regarding this problems, in this work we report computational study on CdS wurtzite phase nanostructured with prismatic shape.

In CRESCO 2014 [1] we reported the analysis of a cluster built with 162 atoms of Cd and 162 atoms of S heated up to 340 K. Subsequently, we heated up to 400 K and investigated the structural properties of core and surface parts separately. Finally, we reported also an early analysis of the density of states (DOS).

---

*Corresponding author. E-mail: `emiliano.burresi@enea.it`.

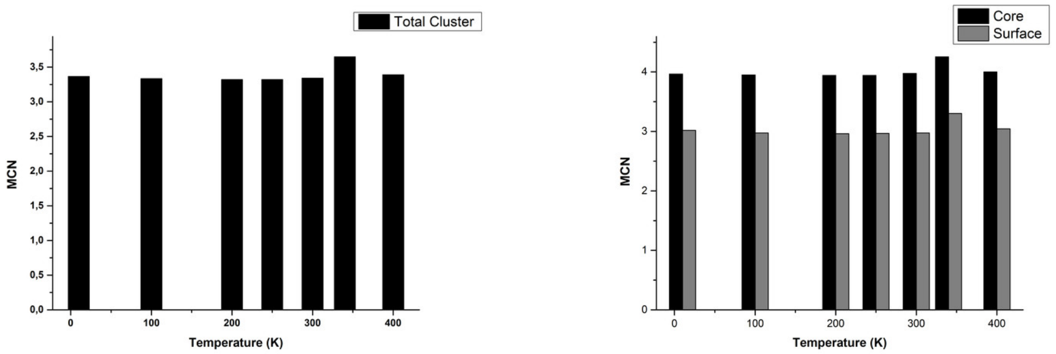

Figure 1: Mean Coordination number (MCN) for total Cluster (left) and core and surface separately (right)

2 Computational details

Car-Parrinello Molecular Dynamics (CPMD) code which employs the density functional theory was used to heat the CdS cluster from 100 K to 400 K [4]. Computational details are reported in the previous report [1]. In order to analyze the computational data obtained with CPMD, a code in FORTRAN language was written to follow the dynamics for the total system (core and surface) and also individually for core and surface. From this code, we can obtain information as MSD, radial distribution function (RDF) and mean coordination numbers (MCN) both for core and surface separately. To calculate DOS we used the GGA approximation in DFT framework and pseudopotential approach as implemented in the Quantum Espresso suite [5]. The cluster has been simulated using a box of 40 Bohr and 30 Ry for cutoff of the kinetic energy. We used CRESCO2 and CRESCO3 clusters to perform each simulation and characterization.

3 Results and discussion

The CdS cluster was built and heated up to 400 K as reported in [1]. Fig. 1 shows the Mean Coordination Number (MCN) for total cluster (left) and for core and surface separately for each temperature (right).

At the temperature of 340 K, the MCN of the total cluster increases, with a major contribution from core atoms. As we already seen for our previous cluster built with 96 atoms [2], also in this case it has been found a new structure more stable [1], with lower surface fraction, in correspondence of 340 K. In Fig. 2 we reported the radial distribution function $g(r)$ for core and surface, comparing the results at 10 K and 400 K. In Fig. 2a RDF shows that first coordination shell did not suffer any change due to the heating program. By analyzing the RDF for surface, we achieve a different result; in this case, the peak for first shell at 400 K is no longer well distinct. In addition in Fig. 2b the cutoff for the first shell seems to be recognizable at 10 K, while it becomes more confuse at 400 K.

The behavior of the atoms in surface with respect the core-shell atoms is well emphasized

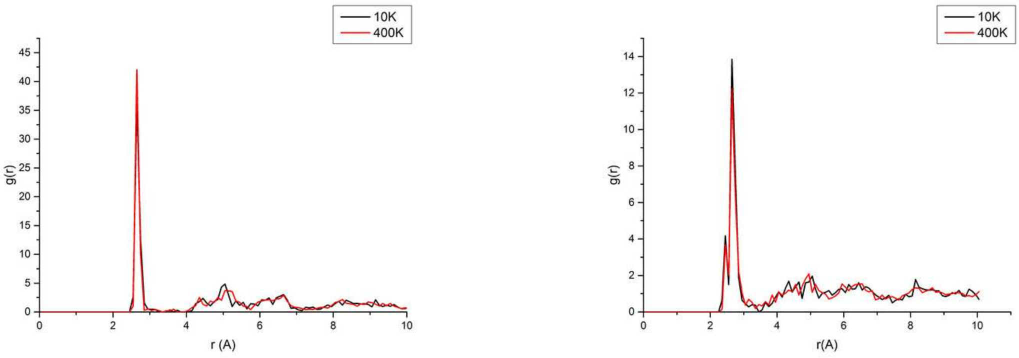

Figure 2: RDF for core (left) and surface (right) comparing the results at 10 K and 400 K

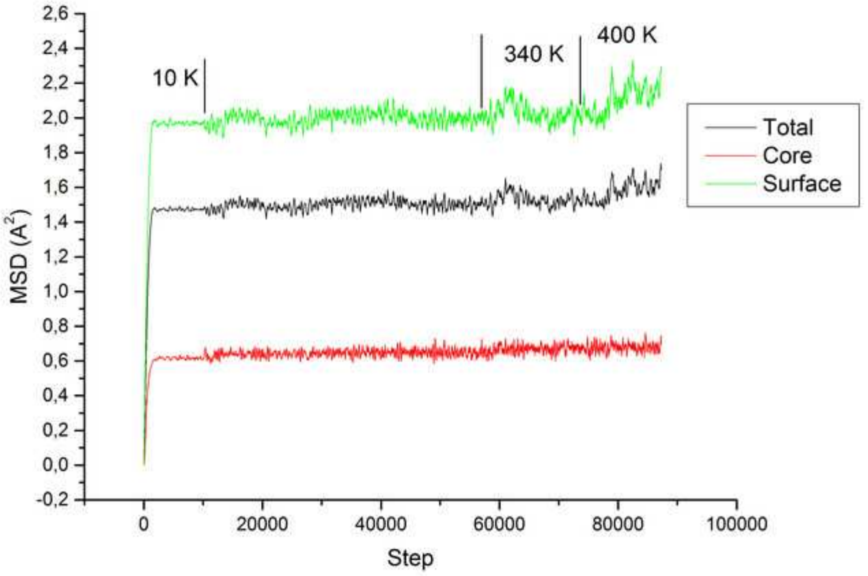

Figure 3: MSD for total cluster (black line),core (red line) and surface (green line)

in the MSD curves reported in Fig. 3. After initial equilibration and relaxation of the structure (at 10 K) the greater displacements encountered up to 400 K are due to the superficial atoms (green curve) compared to the atoms inside the cluster (red curves). The latter curve confirms that the core atoms are not involved in any type of displacements. On the contrary the atoms on the surface can move, as shown by the green line. This surface displacement is the starting point for a superficial phase transition toward a disordered phase. The intrinsic disorder of the high temperature surface is confirmed by the new electronic states that can be seen at the Fermi energy in the electronic Density of States (DOS) reported in Fig. 4.

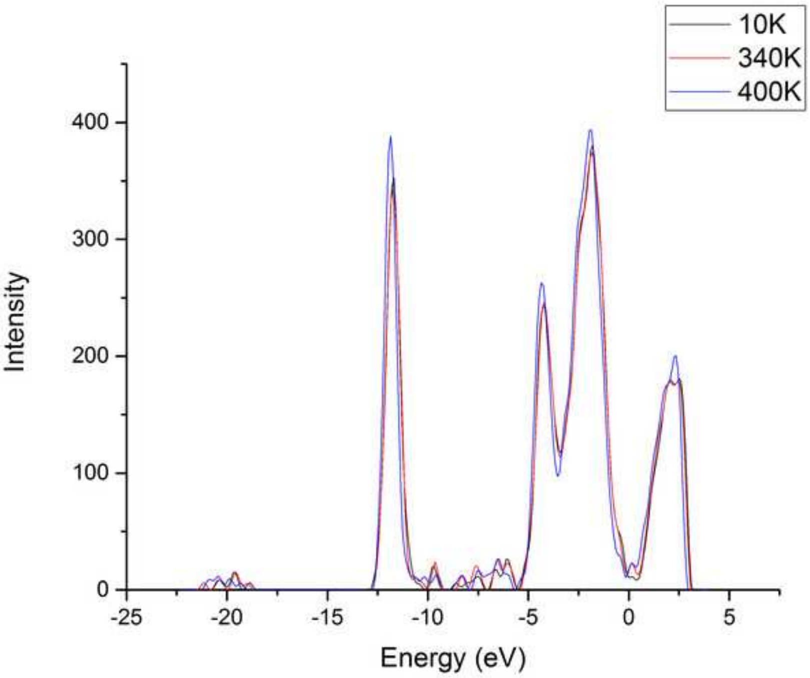

Figure 4: Density of States (DOS) for cluster heated at 10 K, 340 K, 400 K

4 Conclusion

A Fortran code has been written to investigate the structural properties of a CdS nanocluster which has been simulated previously; the results from ab initio simulation were reported in CRESCO 2014 activity. This code was employed to characterize the behavior of the core and surface separately. Different results were obtained for core and surface by means of mathematical tools as RDF, MCN and MSD.

Next step should be the functionalization of the surface, for example studying the interaction between nanocluster and graphene sheets.

References

[1] CRESCO 2014 activities. High Performance Computing on CRESCO infrastructure: research activities and results 2013. *ENEA*, ISBN 978-88-8286-312-8, 2014.

[2] E. Burresi and M. Celino. Methodological approach to study energetic and structural properties of nanostructured cadmium sulfide by using ab-initio molecular dynamics simulations. *Solid State Science*, 14:567–573, 2012.

[3] E. Burresi and M. Celino. Surface states and electronic properties for small cadmium sulfide nanocluster. *Nanoscience and Nanotechnology Letters*, 5:1182–1187, 2013.

[4] CPMD. http://www.cpmd.org/. *Copyright IBM Corp 1990-2008. Copyright MPI für Festkörperforschung Stuttgart*, 1997-2001.

[5] P. Giannozzi et al. Quantum ESPRESSO: a modular and open-source software project for quantum simulations of materials. *J. Phys.: Cond. Mat.*, 21:395502, 2009.

Cooling of turbine blades: a computational analysis

D. Borello[1]*, *F. Rispoli*[1], *P. Venturini*[1] *and A. Salvagni*[1]

[1]*Dipartimento di Ingegneria Meccanica e Aerospaziale*
Sapienza Università di Roma, Via Eudossiana, 18, 00184 Roma, Italy

Abstract. The present contribution aims to illustrate the research activities carried out in 2014 by the group working at Dipartimento di Ingegneria Meccanica e Aerospaziale, Sapienza Università di Roma, using the CRESCO computational resources. The research group has a long record of publication in the field of Computational Fluid Dynamics and it is cooperating with ENEA groups since 2001. During 2014, the numerical investigations were focused on the investigations of the flow and heat transfer in turbine cooling. This work started in previous years and it was continued during the whole year. Two main research lines were pursued in this field: *a*) analysis of particle laden flows in turbines with film cooling [1]; *b*) analysis of the flow in a rotating rib–roughened duct reproducing the internal cooling mechanism in a turbine blade [2]. These activities led to a production of some papers presented to peer–reviewed International Conferences and now submitted for publication in journals or selection of papers. Furthermore, in 2014 some results were presented at a CRESCO initiative in Portici. In the following a brief description of the two simulation is carried out.

1 Particle laden flows in a gas turbine vane with film cooling

First stage of a turbine vane is generally subjected to the hot gas reached from the combustor. Thus, an adequate cooling system is required to prevent blade failure. However, the flow coming from the burner is fed with particles produced during combustions, ashes, soot. Such particles can interact with the solid surface changing the heat transfer coefficient and interacting with the cooling jet, eventually leading to malfunctioning of the turbomachine. We considered flow around a General Electric Energy Efficient Engine (E3) High Pressure Turbine (HPT) vane with film cooling where bronze solid particles were dispersed. Details of the geometry and discretisation were reported in the previous CRESCO Report and in the paper [1]. In Fig. 1, the flow and the temperature field close to the leading edge are shown (a case without film cooling was considered for comparisons). The influence of flow velocity and cooling over the temperature distribution is clearly shown. In the cooled configuration, the presence of film cooling is put in evidence by the presence of temperature iso–surfaces. The influence of film cooling is made evident by lack of temperature uniformity along the span. It is arguable that this must have an influence on the deposit as it will be shown later. In the non–cooled case, the blade temperature

---

*Corresponding author. E-mail: `domenico.borello@uniroma1.it`.

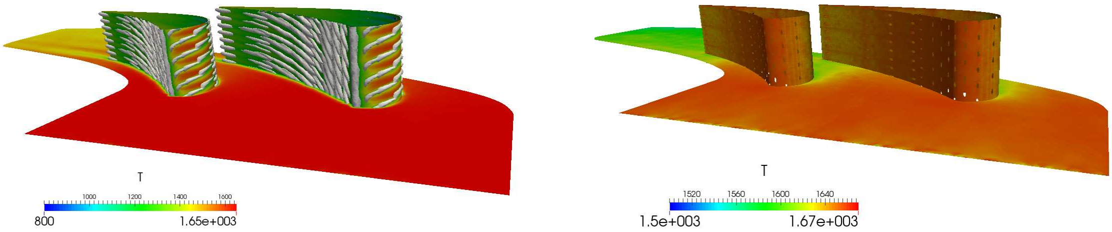

Figure 1: Temperature distribution along the pressure side: left – cooled configuration, the temperature isosurfaces at 1200 K are indicated in grey; right – uncooled configuration.

is more uniform (we changed the temperature range in the plots) and the small reduction of blade temperature is only related to the influence of flow temperature variation. The particles released at the inlet surfaces in 8 planes at different z values. For any plane, 1760 particles were released in a region extending of the pitch across the stagnation line. The particles motion is tracked by using a Lagrangian model where influence of drag force was considered. The impact on the solid surface was modelled by using a statistical model determining the deposit probability on the basis of the particle temperature [1]. In Fig. 2, the particles trajectories are shown. The cooling jets strongly deviate the particle trajectories, while in the non–cooled configuration the particles trajectories do not show relevant deviations from the 2D planes from where they were released. In Fig. 3, the deposit on the solid surfaces is shown. The deposit level was made non–dimensional by dividing for the maximum deposit height measured in the two cases. No deposit was noticed on the suction side. In the cooled configuration, deposit is concentrated on the leading edge (out from the cooling holes) and close to the trailing edge. (see Fig. 3, right). The deposit distribution is influenced by the direction of the cooling jets as the particles entrapped in the vortical region generated by the jets strongly collides with the blade surface and possibly deposit. This is particularly evident close to the leading edge, where the deposit is aligned with inclined jet direction. In the non-cooled configuration, the deposit is more uniformly distributed along the pressure side. No clean region exists and deposit is also present inside the cooling holes. This suggests that, in case of temporary interruption of the cooling injection, together with the temperature shock on the blade surface, we must also consider the possibility of a (partial) blockage of the cooling holes. For this application we used OpenFOAM 2.1.0 code that is available on the CRESCO machines.

2 URANS of blade internal cooling in rotating conditions

For this application we used T–FlowS, a FV unstructured parallel research code developed by some of the authors. We implemented, checked and validated T–FlowS on the CRESCO machines since 2007. The test case is particularly relevant for the analysis of flow in the internal cooling channels, Fig. 4. An accurate analysis is required in this case due to the presence of very small structures generated by the interaction of the several walls and the influence of rotation. Here we present the results of the case with and without rotation. The rotational number is equal to 0.3. This is a very important

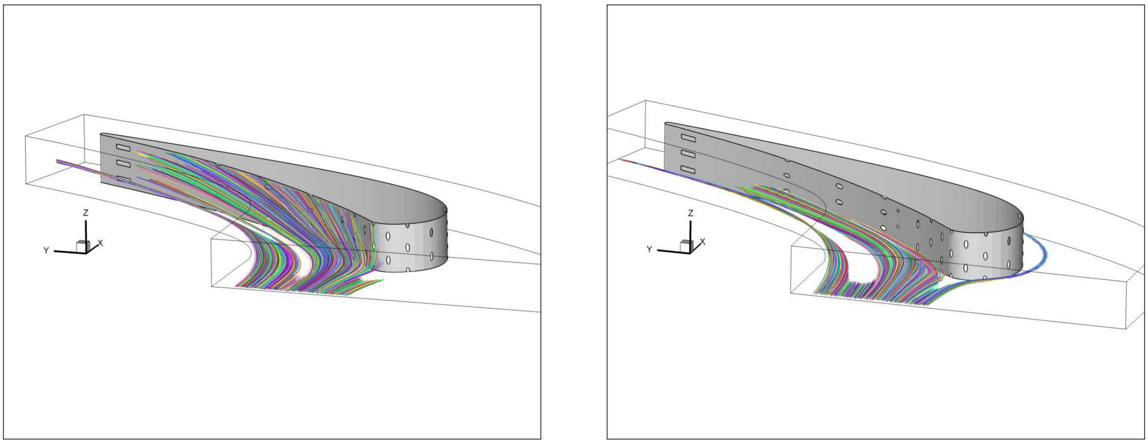

Figure 2: Selection of particle trajectories in the cooled configuration: left – cooled configuration; right – uncooled configuration.

parameter as it can affect the flow unsteadiness. The channel has a wedge shape and it contains seven pedestals in the edge region. The Navier–Stokes equations system is solved in dimensionless variables. As reference variables we used inlet duct hydraulic diameter, bulk flow velocity and air properties at 20 C. The ensuing Reynolds number is equal to 20,000. A Crank–Nicolson/CDS scheme was adopted to obtain a second–order accurate solution. Fully coupled solution of the Navier–Stokes system was obtained using the SIMPLE scheme, while the Preconditioned BiCG solver is adopted for the solution of the algebraic linearized equation system. In inlet we imposed mass flow, while in outlet we imposed convective conditions. On the solid walls no–slip conditions were set. The non-dimensional time step was selected equal to 10–4. The maximum CFL number is smaller than 0.3. The computations were performed on the CRESCO 3 cluster at Portici (ENEA) using up to 32 processors. To obtain an overall evaluation of the rotation influence on the velocity field, in Fig. 5 the velocity magnitude and streamlines on plane 1 are reported. On this plane, the solid body rotation causes an anticipated, stronger streamlines deviation. This leads to the destruction of the recirculation zone present at the tip region. Furthermore, the recirculation bubbles placed downstream of the 90 corner and over the pedestals reduced their extension and the blockage of fluid passage sections between two successive pedestals. Finally, the velocity distribution in the exit region is less uniformly distributed showing a strong mass flow rate downstream the pedestals 3–5. The occurrence of unsteadiness in the flow is now investigated. In Fig. 6, the FFT of the velocity fluctuations computed in a number of monitoring point in the non–rotating and rotating case are shown. The black line identify the main frequency that correspond to the presence of a strong unsteadiness affecting the entire domain. The value of this period is slightly different in the two cases. In particular, in the rotating case the fluctuation period has a smaller value. Assuming as reference the average pedestal height and the inlet bulk velocity, we obtained a Strouhal number of 0.22 for the non–rotating case and of 0.3 for the rotating one. On the other hand, the unsteadiness induced by the rotation is vigorous and with huge amplitude. In particular, in the wedge region upstream of the pedestals, the flow is subjected to a charge–discharge motion, much more pronounced than in the non–rotating case.

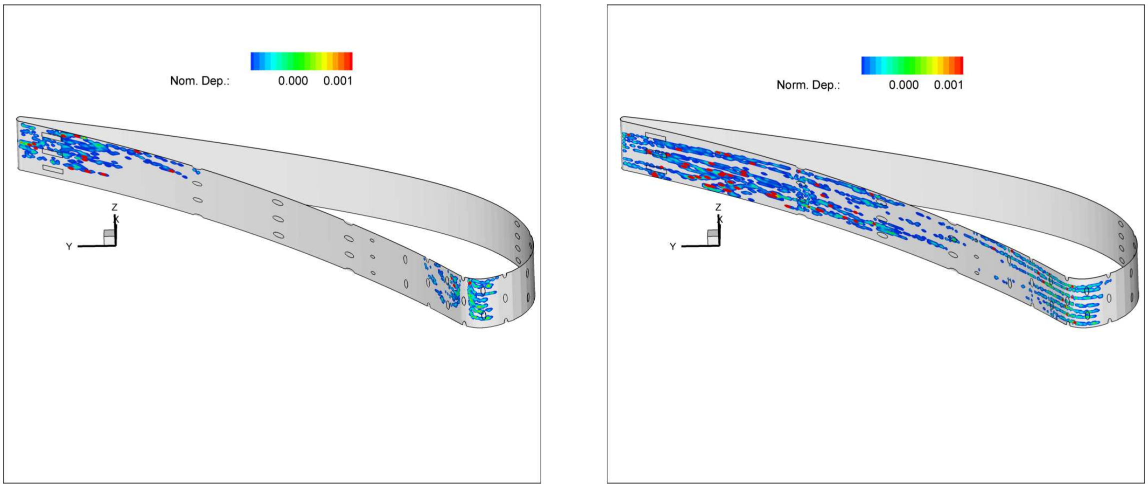

Figure 3: Deposit along the pressure side: left – cooled configuration; right – uncooled configuration.

3 Summary & Conclusions

The authors used the CRESCO computational resources in 2014 for studying turbine cooling applications. The analysis allowed to obtain relevant details about the turbulence structures and unsteadiness also using U–RANS. The results of the simulations allowed to produce two papers presented in peer-reviewed International Conferences and that will be delivered to indexed publications (journals or edited books).

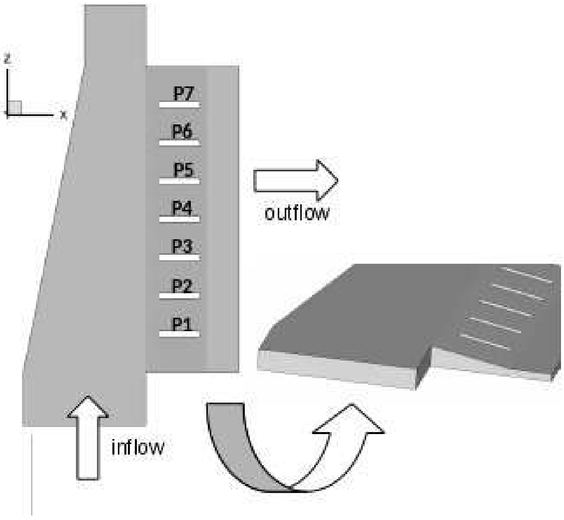

Figure 4: Geometry of the cooling channel.

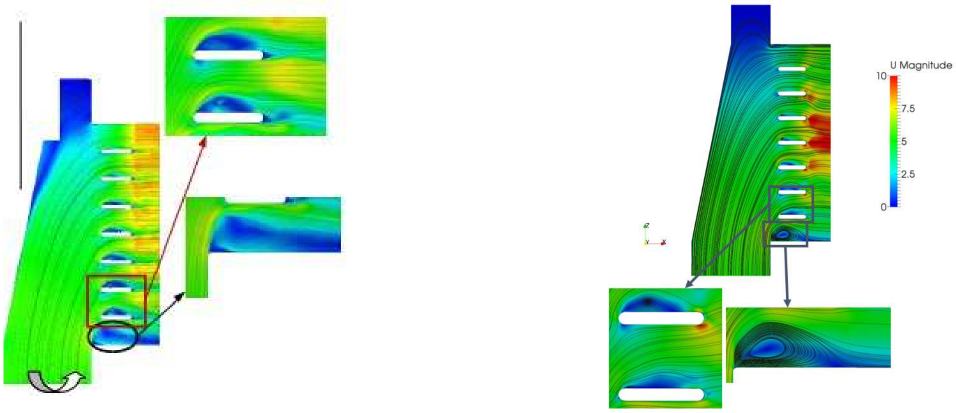

Figure 5: Velocity magnitude plot and streamlines for the non-rotating (left) and rotating (right) configuration.

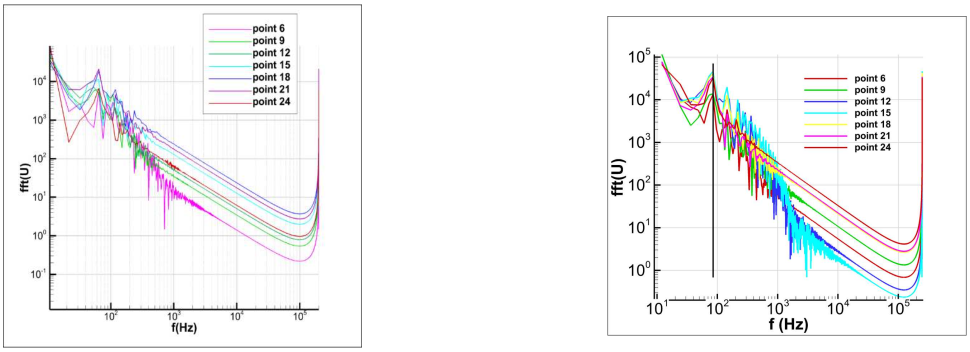

Figure 6: Comparisons of unsteadiness spectra for non rotating (left) and rotating (right) configurations.

References

[1] D. Borello, L. D'Angeli, A. Salvagni, P. Venturini, and F. Rispoli. Study of particles deposition in gas turbine blades in presence of film cooling. *ASME TurboExpo 2014, 16-20 June 2014.*

[2] D. Borello, D. Anielli, F. Rispoli, A. Salvagni, and P. Venturini. Unsteady CFD analysis of erosion mechanism in the coolant channels of a rotating gas turbine blade. *ASME TurboExpo 2015, 15-19 June 2015, Montreal, Canada.*

Theoretical investigation of Mg-MgH_2 interface doped with Ti and TiO_2

R. Vujasin[1]*, *S. Giusepponi*[2], *J. Grbović Novaković*[1],
Nikola Novaković[1] *and M. Celino*[2]

[1] *Vinča Institute of Nuclear Sciences, University of Belgrade*
P.O. Box 522, 11001 Belgrade, Serbia

[2] *ENEA, C.R. Casaccia, via Anguillarese 301,00123 Rome, Italy*

Abstract. Mg-MgH_2 interface and effect of Ti and TiO_2 doping on the structure of the system were investigated. Study of the systems with Ti and TiO_2 in three different positions in interface and near-interface region were based on density functional theory, as implemented in CPMD code. To research Ti and TiO_2 influence on the system, work of adhesion and formation energy of defects were calculated, and structural analysis was performed. Results show that there was a destabilisation of the system after adding titanium and titanium oxide into the magnesium hydride comparing to pure Mg-MgH_2 interface.

1 Introduction

Use of fuel cells and hydrogen energy becomes promising alternative for fossil fuels. It is necessary to provide good hydrogen storage materials in terms of high gravimetric and volumetric capacity, availability, low cost, safety, and non-toxicity. One of the most investigated materials for hydrogen storage is magnesium hydride (MgH_2). The main advantages of this material are high gravimetric capacity (7.6 wt. %), non-toxicity and low cost. However, several drawbacks, namely slow kinetics and relatively high dehydrogenation temperature (more than 300°C for pure MgH_2) prevent its practical application [1]. In order to overcome these drawbacks, hydrogen desorption/adsorption properties of MgH_2 can be improved by adding transition metal and their oxides, such as Ti and TiO_2, which has beneficial effect on destabilization of MgH_2 matrix and cause improvement of kinetic properties of this material [2, 3]. Mechanism of the effect of TiO_2 on improving the kinetics properties of MgH_2 is still unknown. Numerical studies of Mg-MgH_2 interface with Ti atom and TiO_2 molecule in the interface and in the near-interface region were performed with the intention to examine the effects of Ti and TiO_2 on the structural destabilisation and improvement of the hydrogen desorption properties of MgH_2.

---

[*] Corresponding author. E-mail: `radojka.vujasin@gmail.com`.

2 Details of calculations and results

Ionic relaxations calculations were performed by CPMD (Car-Parrinello Molecular Dynamics) code [4, 5] which uses a plane wave/pseudopotential implementation of Density Functional Theory (DFT) [6, 7]. We use the CPMD compiled with Intel Fortran Compiler, MKL (Math Kernel Library), ACML (AMD Core Math Library) and MPI (Message Passing Interface) parallelization on the high performance ENEA CRESCO computing facilities [8]. Our system is MgH_2-Mg interface constituted by 132 atoms of Mg, and 120 atoms of H. Short testing of scalability was done for CRESCO3 and CRESCO4 clusters. Time obtained for wavefunction optimisation using 72, 96, 144 and 288 cores are in good agreement with results reported in previous CRESCO Report [9]. Troullier-Martins norm-conserving pseudopotentials with Perdew-Burke-Ernzerhof approximant GGA exchange-correlation potential were used for all atoms [10, 11]. The electronic wave functions are expended in plane-wave basis set with a kinetic energy cut-off equal to 80Ry.

Interfaces were build using fully relaxed Mg (010) and MgH_2 (110) surfaces. Supercell was extended in y-direction containing, 12 atomic layers. A void region was on each side of the surface preventing the interaction between the external free surfaces. Distance between internal surfaces was varied till the reaching the minimum of total energy of whole system. The final supercell parameters were Lx= $6.21\AA$, Ly= $50.30\AA$, and Lz= $15.09\AA$. Two outer layers in Mg and MgH_2 slab were fixed playing the role of bulk.

The influence of the catalysts on properties of Mg-MgH_2 interface was examined by substitution of an atom of Mg, or one Mg and two H atoms, from MgH_2 part with an atom of Ti, or one Ti and two O atoms at different distances from the interface. Three different interfaces are marked with POS1, POS2 and POS3, which means that substituted atoms are in the first, the second and the third Mg layer of MgH_2 side, respectively.

For these interfaces we performed total energy calculations followed by geometry optimisation. Work of adhesion W and formation energy ΔE_f of the substitutional defect were used to verify the reliability of our model and to predict the mechanical properties and stability of the interfaces. The work of adhesion is defined by the difference in total energy between the interface and its isolated slabs. Formation energies were calculated from total energies according to the following equations:

$$\Delta E_f(\mathrm{Ti}) = \left[E_{\mathrm{inter}}^{\mathrm{Ti}} + E'(\mathrm{Mg})\right] - \left[E_{\mathrm{inter}} + E'(\mathrm{Ti})\right] \tag{1}$$

$$\Delta E_f(\mathrm{TiO_2}) = \left[E_{\mathrm{inter}}^{\mathrm{TiO_2}} + E'(\mathrm{Mg}) + E'(\mathrm{H})\right] - \left[E_{\mathrm{inter}} + E'(\mathrm{Ti}) + 2E'(\mathrm{H})\right] \tag{2}$$

where E_{inter} is total energy of pure Mg-MgH_2 interface, $E_{\mathrm{inter}}^{\mathrm{M}}$ is the total energy of the Mg-MgH_2 interface doped with M=Ti or TiO_2, and E' is total energy of one isolated atom in simulation box. Work of adhesion and formation energies are summarised in Table 1.

Work of adhesion for interfaces with Ti is higher than corresponding values for interface with TiO_2, which means that interaction between Mg and MgH_2 surface is stronger when only Ti atom is present in the system. Values of W decrease with increase of dopants distance from the interface for all systems. Negative value of formation energies for both dopants indicates that substitutional doping is fostered process. Results show that system

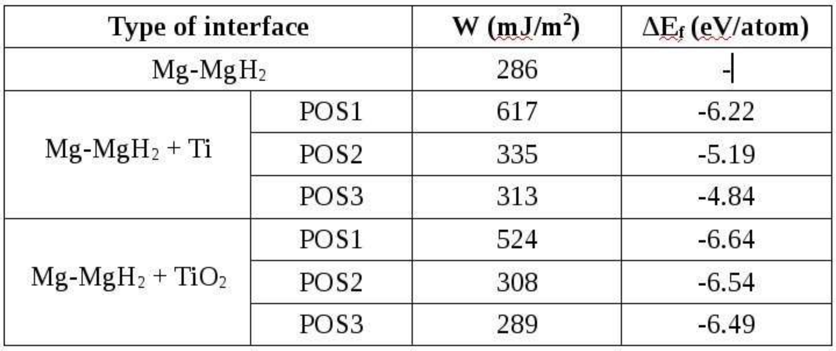

Type of interface		W (mJ/m^2)	ΔE_f (eV/atom)
Mg-MgH$_2$		286	-
Mg-MgH$_2$ + Ti	POS1	617	-6.22
	POS2	335	-5.19
	POS3	313	-4.84
Mg-MgH$_2$ + TiO$_2$	POS1	524	-6.64
	POS2	308	-6.54
	POS3	289	-6.49

Table 1: Work of adhesion (W) and formation energy (ΔE_f) per substituted atom after ionic relaxation of the systems.

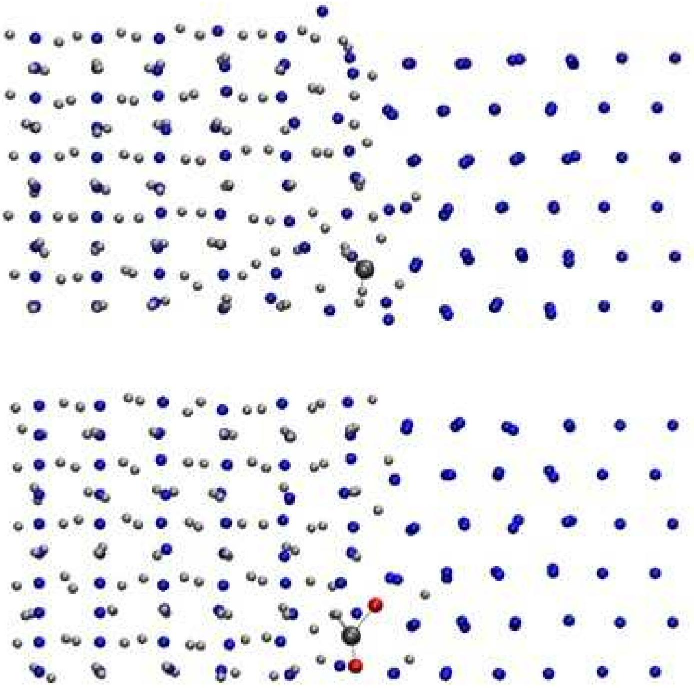

Figure 1: Slab supercell of Mg-MgH$_2$ interface with Ti atom (top) and TiO$_2$ molecule (bottom) in the first layer after geometry optimization of the system (Mg atoms - blue, H atoms - light grey, Ti atoms - dark grey, O atoms - red spheres).

is more stable with TiO$_2$. Values of ΔE_f increase with increase of dopants distance from the interface for systems with Ti and TiO$_2$.

Structural analysis after geometry optimisation was analysed. At the Fig. 1. are shown supercell of Mg-MgH$_2$ interface with Ti atom and TiO$_2$ molecule in the first layer after geometry optimization.

Coordination of the titanium atom before and after geometry optimization, and average distances inside each shell were calculated. Shells are determined on the basis of distances in the MgH_2 bulk. Comparing to bulk MgH_2 there are small differences for H coordination for all systems with additive in the 1st and the 2nd shell. Namely, in all systems H-Ti distances are reduced and atoms from the 2nd shell are moved to the 1st one. Ionic relaxations show that there are no significant difference in Mg coordination for interfaces with Ti and TiO_2 dopant in all positions comparing to bulk MgH_2.

In conclusion, we performed structural analysis of Mg-MgH_2 interface with Ti and TiO_2 in three different positions in interface and near-interface region. Results show that there was a destabilisation of the system after adding titanium and titanium oxide into the magnesium hydride comparing to pure Mg-MgH_2 interface.

Acknowledgments

We acknowledge ENEA-HPC team for supporting our computational activities on the ENEAGRID infrastructure. Part of this work was supported by the Ministry of Education, Science and Technological Development of the Republic of Serbia under the Grant III 45012. Part of this work was supported by the COST Action MP1103 “Nanostructured materials for solid state hydrogen storage”.

References

[1] Schlapbach L. and A. Züttel. *Nature*, 414:353–358, 2001.

[2] G. Liang, J. Huot, S. Boily, A. Van Neste, and R. Schulz. *J. Alloys Compd*, 292:247–252, 1999.

[3] M. Polanski and J. Bystrzycki. *J. Alloys Compd*, 486:697–701, 2009.

[4] R. Car and M. Parrinello. *Phys. Rev. Lett.*, 55:2471–2474, 1985.

[5] CPMD V3.15.1. *Copyright IBM Corp 1990-2011*, Copyright MPI fuer Festkoerperforschung Stuttgart 1997-2001.

[6] P. Hohenberg and W. Kohn. *Phys. Rev.*, 136:B864–B871, 1964.

[7] W. Kohn and L. Sham. *J. Phys. Rev.*, 140:A1133–A1138, 1965.

[8] www.cresco.enea.it.

[9] R. Vujasin, J. Grbovic Novakovic, N. Novakovic, S. Giusepponi, M. Celino, and A. Montone. High performance computing on CRESCO infrastructure: research activities and results 2013 . pages 49–55, 2014.

[10] J. P. Perdew, K. Burke, and M. Erzerhof. *Phys. Rev. Lett.*, 77:3865–3868, 1996.

[11] N. Troullier and J. L. Martins. *Phys. Rev. B*, 43:1993–2006, 1991.

First principles calculations of the electronic properties of bismuth-based nanostructures

Giovanni Cantele[1,*], *Domenico Ninno*[1,2]

[1] *CNR-SPIN, c/o Università degli Studi di Napoli "Federico II",*
Compl. Univ. M.S. Angelo, I-80126, Napoli, Italy

[2] *Università degli Studi di Napoli "Federico II", Dipartimento di Fisica,*
Compl. Univ. M.S. Angelo, I-80126, Napoli, Italy

Abstract. In this report, ab initio calculation of the electronic properties of bismuth–based surfaces and nanostructures are introduced. Special focus is given to applications (e.g. in thermoelectric devices) and to quantum confinement effects. Due to the complex crystal structure and semi-metallic band structure of bulk bismuth, the occurrence of quantum confinement as dimension are reduced down to few nm is quite debated in the literature, with particular reference on a semiconductor-to-semimetal transition upon increasing the material dimensions.

1 Introduction

The bismuth (Bi) crystal has a rhombohedral structure, typical of group V semimetals. Each bismuth atoms has three nearest neighbours at a distance of ~ 3 Å and three next nearest neighbours at a distance of ~ 3.5 Å, resulting in the stacking of Bi bilayers along the rhombohedral [111] direction, as shown in Fig. 1 (left panel).

This material, that in its bulk form is semimetallic [1], has been proposed as a promising candidate for energy applications, due to its good thermoelectric performance at both room and low temperature [2]. Moreover, the unique electronic properties get even more appealing when thin films or nanostructures are considered. For example, it has not yet fully understood how quantum confinement effects, arising when one or more dimensions are reduced down to the nanoscale, show up in bismuth nanostructures [1]. Spin orbit coupling, that is a relativistic effect important for the electronic structure of heavy atoms and their solids, does play a fundamental role, as well. This is especially true in nanostructures where the breaking of the periodicity causes the lifting of electronic level degeneracies due to the loss of inversion symmetry even in materials that have such a symmetry in the bulk.

---

[*] Corresponding author. E-mail: `giovanni.cantele@spin.cnr.it`.

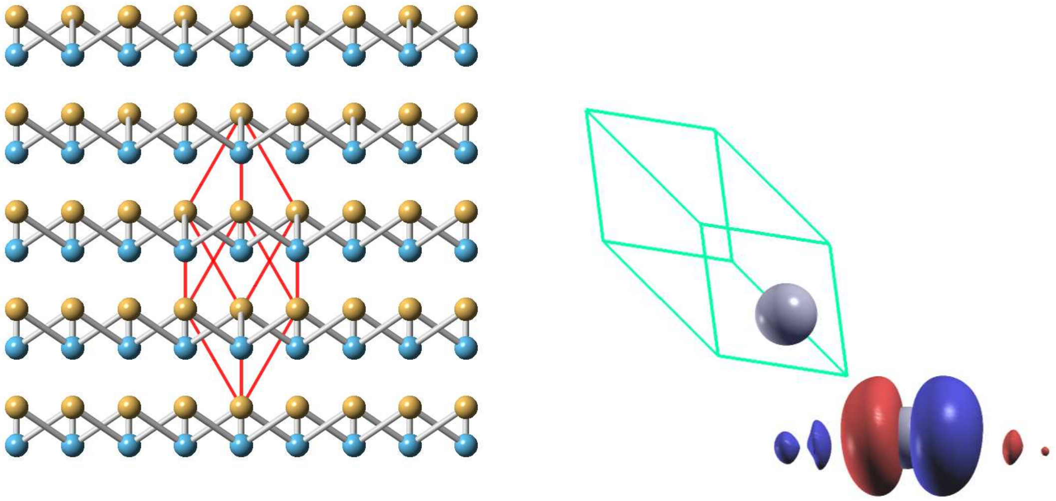

Figure 1: (left) The structure of bulk Bi, showing the stacking of Bi bilayers along the [111] rombohedral direction. The rhombohedral unit cell is highlighted in red. (right) One of the six MLWF, that provide a minimal basis set to describe the six bands around the Fermi level of bilk Bi (see Fig. 2).

2 Software and computational resources

The first principle calculations are based on Density functional Theory. Two main computational packages have been used on the CRESCO infrastructure, both based on plane waves to represent the electronic wave functions and charge density and pseudopotential to represent the ion cores: the open source QUANTUM ESPRESSO package [3] and the copyright-protected software VASP (*Vienna ab-initio simulation program*) [4]. Because the adopted frameworks intrinsically deal with periodic systems, low dimensional systems (surfaces and thin films, nanowires, nanocrystals) are studied within the supercell approach, in which periodic replicas along the non periodic direction(s) are separated by vacuum space, large enough to prevent from spurious interactions. The results shown in the present report have been obtained with the use of high performance computing facilities, in particular the CRESCO3 cluster located at the Portici ENEA center. Typical jobs require 64 to 256 computing units and several tens Gb of disk storage (for electronic wave functions and charge density, needed both during the optimization tasks and for post processing purposes). Parallelization is implemented through the MPI environment. For most calculations projector augmented wave (PAW) pseudopotentials [5] are employed.

Fermi surface and thermoelectric properties, that usually require summation over dense grids in the first Billouin zone, are performed using the Maximally-Localized Wannier Functions (MLWFs) approach, as implemented into the *Wannier90* package [6].

3 Results

The electronic structure of bulk Bi can be described in terms of two filled s bands and three filled p bands, separated by a gap of several eV, as shown in Fig. 2.

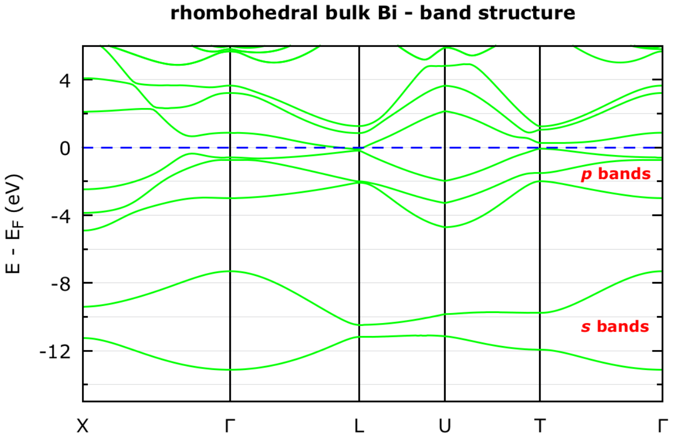

Figure 2: Band structure of bulk Bi, calculated using the QUANTUM ESPRESSO package [8]. The $E = 0$ energy corresponds to the Fermi level E_F, highlighted with the dashed horizontal line.

The nature of the energy bands, crossing around the Fermi level, is easily understood in terms of MLWFs. It turns out that a minimal basis set comprises 3 p-type orbitals per Bi atom in the unit cell, thus providing a tight binding description of the six bands of interest, for example, for thermoelectric applications. As an example, one of the six p orbitals is shown in the right panel of Fig. 1.

Starting from the MLWFs basis set, properties relevant for thermoelectric applications, such as the electrical conductivity, the Seebeck coefficient and the thermal conductivity can be calculated within the Boltzmann transport equations framework [7]. As an example, we shown in Fig.3 the Seebeck coefficient, computed for bulk Bi, using a $150 \times 150 \times 150$ k-point grid.

We are currently using large computational infrastructures, such as CRESCO, to perform this kind of investigations on very large systems, such as Bi nanomentric films, as a function of both the film thickness and orientation. Moreover, work is in progress concerning the study of quantum confinement on systems with lower dimensionality, such as nanowires and nanocrystals.

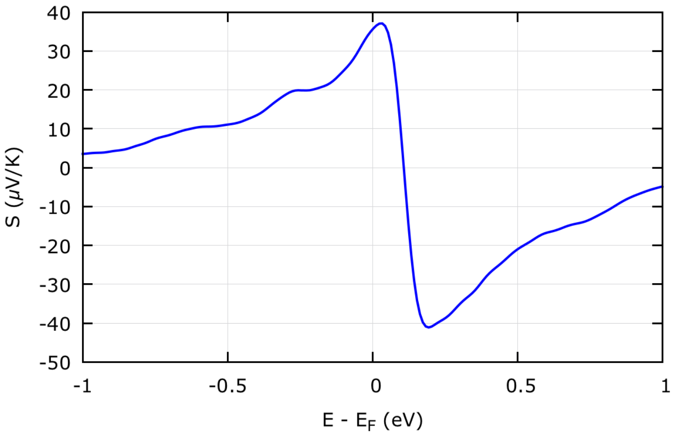

Figure 3: The Seebeck coefficient, computed at 300 K, within the Boltzmann transport equation framework for bulk Bi. The MLWF approach makes computationally feasible to interpolate the bulk band structure along a dense $150 \times 150 \times 150$ k-point grid, needed to accurately compute the integrals over the Brillouin zone.

References

[1] Ph Hofmann. The surfaces of bismuth: Structural and electronic properties. *Prog Surf Sci*, 81(5):191–245, January 2006.

[2] Long Cheng, Huijun Liu, Xiaojian Tan, Jie Zhang, Jie Wei, Hongyan Lv, Jing Shi, and Xinfeng Tang. Thermoelectric Properties of a Monolayer Bismuth. *J Phys Chem C*, 118(2):904–910, January 2014.

[3] P. Giannozzi *et al.* Quantum espresso: a modular and open-source software project for quantum simulations of materials. *J. Phys.: Condens. Matter*, 21:395502, 2009.

[4] G. Kresse and D. Joubert. From ultrasoft pseudopotentials to the projector augmented-wave method. *Phys. Rev. B*, 59:1758, 1999.

[5] P. E. Blöchl. Projector augmented-wave method. *Phys. Rev. B*, 50:17953, 1994.

[6] A. A. Mostofi, J. R. Yates, Y.-S. Lee, I. Souza, D. Vanderbilt, and N. Marzari. Wannier90: A tool for obtaining maximally-localised wannier functions. *Comput. Phys. Commun.*, 178:685, 2008.

[7] Giovanni Pizzi, Dmitri Volja, Boris Kozinsky, Marco Fornari, and Nicola Marzari. BoltzWann: A code for the evaluation of thermoelectric and electronic transport properties with a maximally-localized Wannier functions basis . *Computer Physics Communications*, 185(1):422–429, January 2014.

[8] The pseudopotential Bi.rel-pbe-dn-kjpaw_psl.1.0.0.UPF is chosen from pslibrary 1.0.0, http://www.quantum-espresso.org/pseudopotentials/pslibrary/.

WFR-Chimere Modelling as a Tool of Ozone Risk Assessment to European Forests

Alessandro Anav[1*] *and Alessandra De Marco*[1]

[1]*ENEA, Via Anguillarese 301, 00123 – Rome, Italy*

Abstract. Tropospheric ozone (O_3) produces harmful effects to forests and crops, leading to a reduction of carbon assimilation that, consequently, influences land sink and crop yield production. To assess the potential negative O_3 impacts to vegetation, the European Union uses the Accumulated Ozone over Threshold of 40 ppb (AOT40). This index has been chosen for its simplicity and flexibility in handling different ecosystems as well as for its linear relationships with yield or biomass loss. However, AOT40 does not give any information on the physiological O_3 uptake into the leaves since it does not include any environmental constraints to O_3 uptake through stomata. Therefore, an index based on stomatal O_3 uptake, which describes the amount of O_3 entering into the leaves, would be more appropriate. We compare different potential O_3 risk assessments based on two methodologies (i.e. AOT40 and stomatal O_3 uptake) using a framework of mesoscale models that produces hourly meteorological and O_3 data at high spatial resolution (12 km) over Europe for the time period 2000-2005. Results indicate a remarkable spatial and temporal inconsistency between the two indices, suggesting that a new definition of European legislative standard is needed in the near future..

1 Introduction

Thanks to emissions reduction policies, air pollution showed a flattened trend over Northern America and Europe since 2000. However, since air pollutants and precursors can be transported across hundreds and even thousands of kilometers, air pollution is able to cause damages in areas far away to the source of emissions. Therefore a clear understanding of the pollution impacts on ecosystems is needed to reduce the associated potential risk. Among common air pollutants, ground-level ozone (O_3) is the most damaging to forests and crops and frequently it reaches high concentrations over large regions of the world.

The European standard (Directive 2008/50/EC) used to protect vegetation against negative impacts of O_3 is the Accumulated Ozone over a Threshold of 40 ppb (AOT40), but the European Union (EU) is moving towards an index based on stomatal O_3 flux (or uptake) where the functional dose of O_3 to which plants are exposed is defined as Phytotoxic Ozone Dose with a hourly threshold Y (PODY).

---

[*] Corresponding author. E-mail: `alessandro.anav@enea.it`.

We built-up a multi-model framework able to generate results for use in integrated assessment modeling, and for studies on potential risks caused by O_3 pollution on European forests. This framework relies on a mesoscale model that generates climate forcing used offline to run a Chemistry Transport Model (CTM). The O_3 concentrations computed through the CTM and the climatic variables computed by a regional weather forecast model allowed us identifying the European forest that are mostly subjected to potential O_3 risks [1].

2 Models description

Meteorological data are simulated through the Weather Research and Forecasting (WRF3.6); it is a limited-area, non-hydrostatic, terrain-following eta-coordinate mesoscale model. The model domain covers almost all Europe (except northern Scandinavia and Iceland) and part of North Africa (400 × 300 grid points) with a spatial resolution of 12 km [1].

To simulate gas-phase chemistry, aerosol formation, transport and deposition at regional scale we used the chemistry-transport model CHIMERE (version 2013b). The model was forced by WRF output and anthropogenic emissions, at the same spatial resolution of the atmospheric model. Both models are parallel and have been compiled with the Intel compiler and ran over CRESCO3 with 120 CPUs; the domain decomposition has been achieved with MPI.

The hourly models output, needed to assess the potential ozone impacts on forests, required a large disk space ($\sim$ 15 T to simulate 5 years). Surface air temperature, surface air humidity, solar radiation and soil moisture simulated by WRF, and O_3 concentrations modelled through CHIMERE are used to assess the impacts of ozone. Two different indices are used for ozone risk assessment: 1) the AOT40, defined as the sum of the exceedances above 40 ppb computed over the whole year and when the stomatal conductance is greater than 0 and 2) an index based on stomatal O_3 uptake, where the functional amount of O_3 to which plants are exposed is defined as Phytotoxic Ozone Dose with a hourly threshold of 0 nmol O_3 $m^{-2}s^{-1}$ (POD0).

3 Results and discussion

The AOT40 index (Fig. 1) shows a clear latitudinal gradient with minimum values ranging between 2000-4000 ppb·h over large parts of UK, Southern Scandinavia and North-Western Europe, and maximum values exceeding 50000 ppb*h over Italy, Greece, South-eastern France and Southern Spain.

The higher AOT40, observed in Mediterranean region, depends on the strongest photolysis rates due to the high temperatures typical of this area and on the high O_3 precursor emissions, leading to higher O_3 concentration in the lower troposphere.

Most of the forested areas of UK and Northern Europe, characterized by minimum values of AOT40, are free from exceedances, i.e. they do not exceed the critical limit for forest

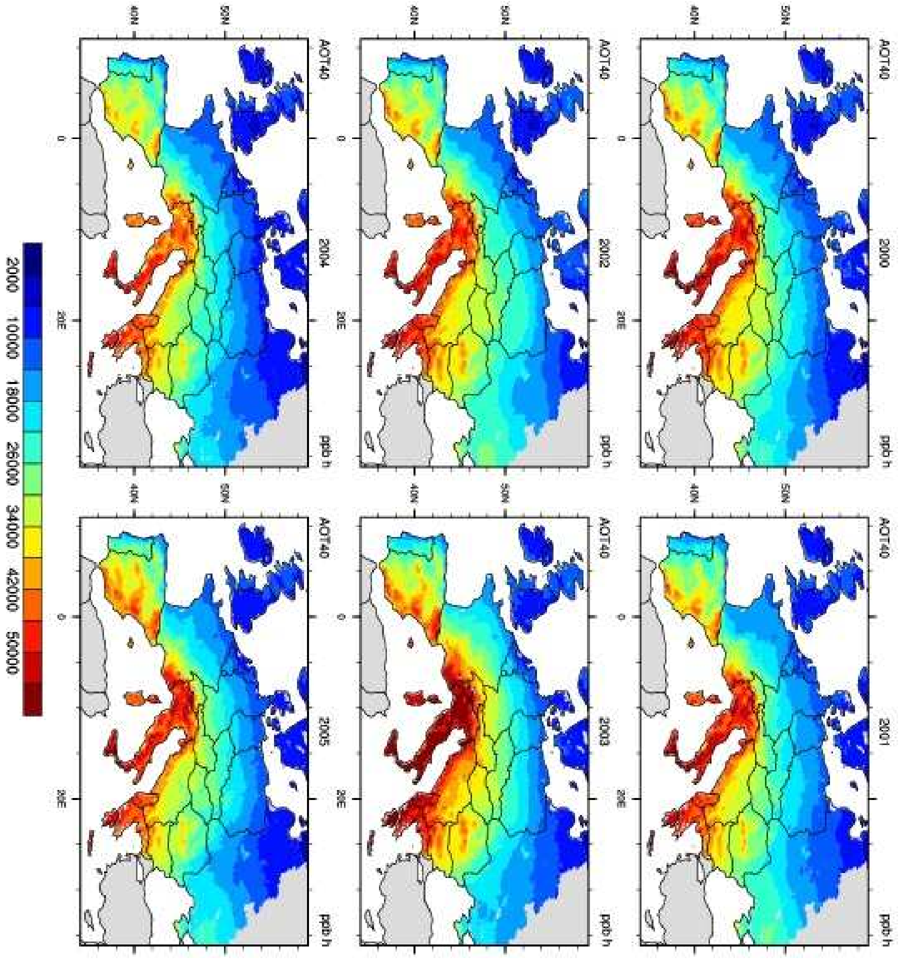

Figure 1: Spatial distribution of AOT40 (in ppb·h) over different years.

protection set to 5000 ppb·h, with a low risk to be subject to O_3 damages. Conversely, below 50°N all the European forests might be potentially damaged by O_3.

Unlike AOT40, POD0 does not show any latitudinal gradient (Fig. 2). The POD0 minimum values (about 12-14 mmol m^{-2}) are located over Eastern Europe, while in the Mediterranean region and along the French Atlantic coasts, the maximum values exceed 40 mmol m^{-2}.

Consistent with AOT40 results, the spatial pattern of POD0 is homogeneous among different years, although its magnitude considerably changes during the years. Notably, because of the heat wave that affected the Mediterranean area, in 2003 there is a relevant decrease in POD0 values: this strong reduction is mainly explained by the dryness of soils that leads to a stomatal closure during the high daily temperature maxima. In fact, the heat wave produced a strong water stress on plants that, in order to minimize the water loss, closed their stomata, leading also to a lower amount of O_3 entering the leaves.

Anyway, comparing the AOT40 and POD0 it is clear that the two indices highlight very different spatial and inter-annual distributions of risks. AOT40 suggests strong exceedances

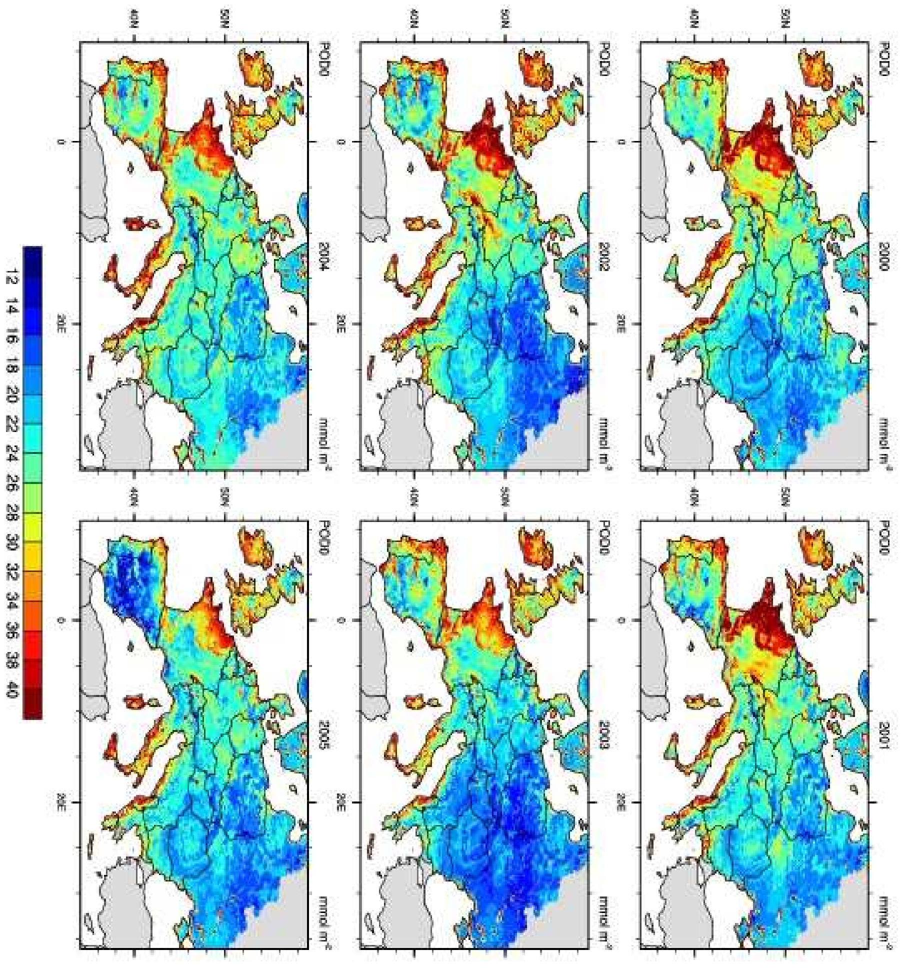

Figure 2: Spatial distribution of POD0 (in mmol m^{-2}) over different years.

in Southern Europe with maximum over Italy and Greece, while POD0 suggests that the potentially mostly damaged forests are located over Atlantic regions of France, Spain and Portugal. This behavior is chiefly evident during the anomalous year 2003: specifically, risk assessment based on AOT40 shows that in 2003 the most sensitive areas to potential O_3 risks are located over the Southern part of the domain and that this index has its maximum value during this particular warm year. Conversely, risk assessment based on POD0 highlights an opposite temporal pattern, namely during 2003 the potential O_3 damages are lower than in other years.

Since both AOT40 and POD0 metrics aim to do the same thing, namely point out the risk of ozone-damage to vegetation, the clear differences between them are not easily reconciled. Thus a clear standard for the near future must be adopted to protect vegetation against O_3.

References

[1] Anav, A. et al. WRF-CHIMERE modelling as a tool of ozone risk assessment to European forests. *Global Change Biology*, under review, 2015.

Activities made by the Soft Matter Molecular Simulation Group

M.S. Byshkin[1,4]*, F. Buonocore*[2]*, A. Di Matteo*[3,4]*, G. Milano*[1,4]*,*
A. De Nicola[1]**, Y. Zhao*[1] *and K. Toshihiro*[5]

[1]*Dipartimento di Chimica e Biologia, University of Salerno, 84084,*
Via Ponte don Melillo, Fisciano, Salerno, Italy

[2]*ENEA Casaccia Research Center, Via Anguillarese 301, 00123 Rome, Italy*

[3]*STMicroelectronics, Via Remo de Feo, 1, 80022 Arzano, Naples, Italy*

[4]*IMAST Scarl, Piazza Bovio 22, 80133 Naples, Italy*

[5]*Department of Physics, Tohoku University,*
Aoba, Aramaki, Aoba-ku, Sendai, Miyagi 980-8578, Japan

Abstract. The increasing interest for the phenomena occurring on different scales (time and dimension) pushed the scientific community to develop different techniques and theoretical approaches to study such phenomena. We report two computational studies in which two different approaches are employed to study multi scale problems. In particular, a gas sensors has been fully characterized by a unified bottom up strategy, and a strategy to obtain large equilibrated system of atomistic polymer melts, by the hybrid MD-SCF technique, are presented.

1 Study 1

In the first study we described a multi scale bottom up procedure, based on an atomistic description, able to model the sensing mechanism of devises based on intrinsic conductive polymers (ICP). It is know that the electrical conductivity of ICP is affected by exposure to various gases and it makes them useful for gas sensing application [1, 2]. ICP materials can be synthesized by copolymerization or structural derivations [1, 3], and micro/nano patterning of these ICP materials jointly with the formation of ultra thin sensing films facilitate enhanced vapor diffusion and response speed when compared with respect to conventional polymeric films. The doping process play a key role in the sensing mechanism of ICP based sensors [4]. ICP can be doped by redox or protonation reactions. The second case of doping due to the protonation reactions is observed for the polyaniline (PANI).

---

*Corresponding author. E-mail: `adenicola@unisa.it`.

It interesting noting that the conductivity can be tuned modifying the dopant type and material preparation method.

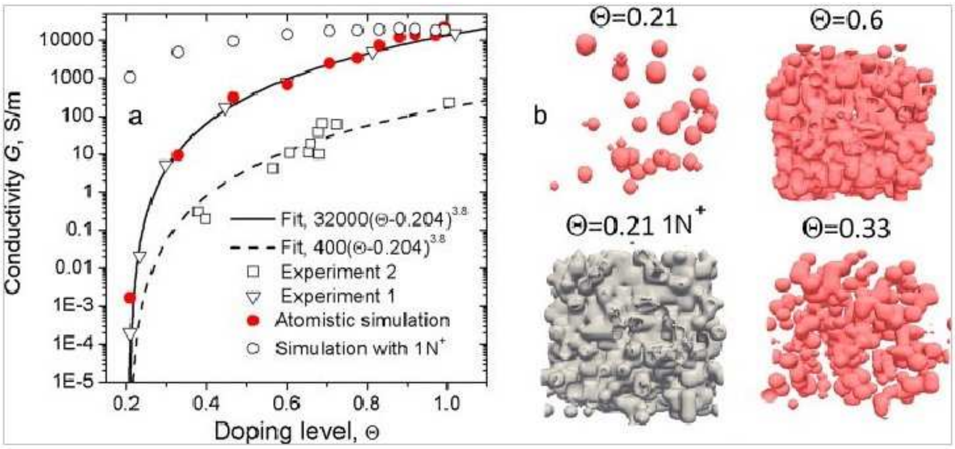

Figure 1: (A) doping level dependence of PANI electrical conductivity G: results of experiments 1 [5] and experiment 2 [6] are compared with the modeling results shown by red filled circles. (B) local conductivity isosurfaces.

Modeling the response of sensor to analyze gases at atomistic love is particular relevant to improve the development of devise. We developed a combination of molecular and finite element simulations to model PANI based gas sensors behavior starting from atomic structure and its modifications during the doping process. In particular, to model the microscopic scale, we propose a scheme based on combination of a recently developed Gran Canonical Monte Carlo (UEMC) [7] and the calculation of electrical conductivity from atomistic PANI structures at different doping levels. The result obtained from the microscopic scale are then casted in a diffusion reaction scheme giving connection between microscopic structures and the response of ICP sensors to analyze gases (Figure 1).

As can be seen from the figure 1, the proposed simulation approach, able to describe at atomistic level the sensing experiments, provides a molecular interpretation of the sensing mechanism in PANI based sensors. These results suggest that the proposed scheme, that can be extended with suitable modifications all to other sensing materials, would allow to understand the basic physic-chemical underlying mechanisms of sensing and to address possible materials modifications and improvements.

2 Study 2

In the second study we present a strategy to generate a well-relaxed systems all-atoms models of large molecular weight polymer melts. Macromolecules, even single chains thereof, exhibit much more complex behavior than simple molecular liquids do, and the main difficulties associated with simulating polymers are related to the intrinsically multi scale nature of macromolecules. In fact, macromolecules structure gives rise to a wide range of coupled length and time scales. Scales of several order of magnitude are strongly connected for a single chain, in which the typical length scales range from the scale of a single chemical bond (1 ang.) to that of the persistent length (1 nm) and finally to that of the radius of gyration of the chain (10 nm). The range becomes even broader if packing of different chains is considered.

High molecular weight polymer chains are very difficult to treat because they are difficult to relax. In fact, for chains longer than the entanglements length, the dynamics is dramatically slowed down [8]. We developed a procedure based on MD-SCF simulations that is able to generate well-relaxed all-atom structures of polymer melts, and capable to overcame all the problems related to the relaxation of different scales [9]. In the paper [9], more details about the description of the theoretical approach are available. In figure 2 we report a scheme of the hybrid SCF description of a polymer chain, jointly with the end-to-end relaxation time of polymer melts, at different molecular weight, for the PMMA.

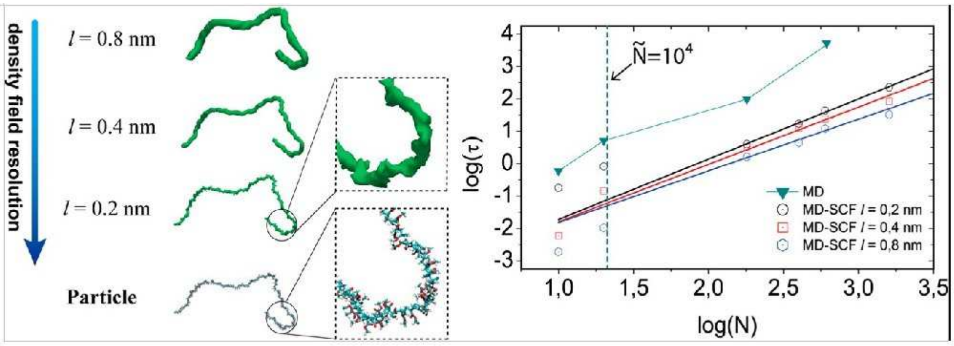

Figure 2: On the right of the figure is reported the SCF representation of the a polymer chain of PMMA. On the left of the figure is reported the log-log plot of the end-to-end relaxation time of systems of PMMA melts at different molecular weight.

The proposed procedure leads to computational costs mainly related on system size rather than to the chain length. Several advantages of the proposed procedure over current coarse-graining/reverse mapping strategies are apparent. No parametrization is needed to generate relaxed structures of different polymers at different scales or resolutions. There is no need for special algorithms or back-mapping schemes to change the resolution of the models. This characteristic makes the procedure general and its extension to other polymer architectures straightforward. A similar procedure can be easily extended to the generation of all-atom structures of block copolymer melts and polymer nanocomposites.

3 Conclusions

We reported two different theoretical approaches to investigate two phenomena occurring on different scales. In particular the proposed studies are mainly dedicated to reproduce the keys properties of the different events occurring on each scale of the total multi scale event. We demonstrated in the second study that the hybrid MD-SCF approach is suitable not only to produce well equilibrated polymer melts, but is also convenient in terms of computational demanding [10].

References

[1] N. E. Agbor, M. C. Petty, and A. P. Monkman. Polyaniline thin films for gas sensing. *Sens. Actuators B: Chem.*, 28:173–179, 1995.

[2] M. M. Ayad, N. A. Salahuddin, M. O. Alghaysh, and R. M. Issa. Phosphoric acid and pH sensors based on polyaniline films. *Curr. Appl. Phys.*, 10:235–240, 2010.

[3] J. Huang, S. Virji, B.H. Weiller, and R.B. Kaner. Nanostructured polyaniline sensors. *Chemi. A Eur. J.*, 10:1314–1319, 2004.

[4] H. Bai and G. Shi. Gas sensors based on conducting polymers. *Sensors*, 7:267–307, 2007.

[5] S. M. Ahmed. Preparation and degradation of highly conducting polyaniline doped with picric acid. *Eur. Polym. J.*, 38:1151–1158, 2002.

[6] A. G. Macdiarmid, J. C. Chiang, A. F. Richter, and A. J. Epstein. Polyaniline: a new concept in conducting polymers. *Synth. Met.*, 18:285–290, 1987.

[7] M. S. Byshkin, A. Correa, F. Buonocore, A. Di Matteo, and G. Milano. A united event grand canonical Monte Carlo study of partially doped polyaniline. *J. Chem. Phys.*, 139:244906, 2013.

[8] K. Kremer and G. S. Grest. Dynamics of Entangled Linear Polymer Melts: A Molecular-Dynamics Simulation. *J. Chem. Phys.*, 92:5057–5086, 1990.

[9] A. De Nicola, T. Kawakatsu, and G. Milano. Generation of Well-relaxed All-Atom Models of Large Molecular Weight Polymer Melts: A Hybrid Particle-Continum Approach Based on Particle-Field Molecular Dynamics Simulations. *J. Chem. Theory and Comp.*, 10:5651–5667, 2014.

[10] Y. Zhao, A. De Nicola, T. Kawakatsu, and G. Milano. Hybrid Particle-Field Molecular Dynamics Simulations: Parallelization and Benchmarks. *J. of Comp. Chemistry*, 33:868, 2012.

Metal Doped Rutile TiO_2 as Electrode in DSSC

Nikola Novaković[1]*, *Radojka Vujasin*[1], *Bojana Paskaš Mamula*[1],
Jasmina Grbović Novaković[1]

[1] *VINCA Institute for Nuclear Sciences,*
Begrade University, P.O. Box 522, 11001, Belgrade, Serbia

Abstract. We have performed density functional theory (DFT) based calculations of the electronic structure and optical properties of metal substitution doped rutile TiO_2 compounds. Dopants influence on electronic structure is constrained on contributing additional states to VB and CB, VB widening and consequently energy gap narrowing, although latter two effects are not particularly pronounced. No dopant states within energy gap were found.

1 Introduction

The solar radiation can be directly transformed into the electric power using photovoltaic solar cells. Dye-sensitized solar cells (DSSCs) based on TiO_2 layers are promising photovoltaic systems for large-scale commercialization. However, the energy conversion efficiency of DSSCs is not sufficient and needs an improvement.

Among metal oxides, TiO_2 is widely used as an electrode in DSSCs, due to its stability, high refractive index and strong UV light absorbing capability. Unfortunately, TiO_2 has a low quantum yield for the photochemical conversion of solar energy. Recently, considerable effort has been devoted to TiO_2 films with nanocrystalline structures as working electrodes in dye-sensitized solar cells (DSSCs) [1, 2, 3, 4, 5]. Even though many metal oxides have been tested for DSSC electrode, efforts on improving DSSCs efficiency were focused mainly on TiO_2 with anatase crystal structure. Rutile crystal structure was and still is out of focus due to even poorer transport properties. Efficiency of DSSC is still lower than that of conventional silicon solar cells, and its improvement is still a major ongoing field of research.

Details of electronic structure (densities of states and band gap structure, position of dopant states and Fermi level) and consequently conduction and optical properties have the crucial role in decision which of the observed real or hypothetical systems could be better materials for DSSC electrodes.

We have performed density functional theory (DFT) based calculations of the electronic structure and optical properties of metal substitution doped rutile TiO_2 compounds. For this we have employed all-electron projected augmented waves method (PAW) and

---

[*] Corresponding author. E-mail: `homovincicus@gmail.com`.

LDA+U Hubbard correction for strongly correlated systems, as implemented in Abinit code. More subtle effects of the electronic structure at the TiO_2-dye-electrolyte interface has not been taken into account.

2 Details of performed calculations

We have performed density functional theory (DFT) -based calculations of the electronic structure and optical properties of both simple (Be, Mg, Ca, Al) and transition metal (Zn, W, Nb) - substitution doped rutile TiO_2 compounds. For this purpose we have employed all-electron projected augmented waves method (PAW) and GGA+U Hubbard correction for strongly correlated systems (such as transition metal oxides). The used state-of-art code was Abinit [6]. We have used GBRV pseudopotentials for all constituting elements. Exchange correlation effects have been employed using generalized gradient parametrization of Perdew, Burke and Ernzerhoff [7]. Hubbard term was chosen to be 2.5 eV for Ti in all cases, while energy cutoff was chosen to be 38 Ha, both after careful convergence studies. To obtain different doping concentrations we have used standard rutile unit cell and supercells with 2x2x2 and 3x3x3 unit cells stacking arrangement. In all cases one Ti atom was replaced with dopant atom. All dopant atoms were embedded in neutral charge state. All ionic positions have been relaxed to reduce lattice stress introduced by doping. To get additional information about strength and nature of bonding in these compounds, we have also performed Bader charge analysis [8]. All calculations have been performed using Cresco3 and Crescof01 ENEAGRID high performance computing facilities.

3 Results and discussion

The results suggest that the doping plays a beneficial role on the electron transport in DSSCs, even without near TiO_2-dye-electrolyte interface effects.

Simple metals change DOS by narrowing the band gap, typically by shifting the valence band (VB) top upwards. Transition metals typically give d-type dopant states within gap but also they can shift conduction band (CB) bottom downwards. The position, width and structure of these states depend strongly on element type, its environment, symmetry and concentration. The narrowing of band gap by VB top and (or) CB bottom shifting could in general improve electron injection from the dye to the CB of TiO_2, while appearance of band gap states can improve transport properties of electrode. The possible downside is, among others, DSSC working voltage decrease and increased optical absorption of electrode.

In Fig. 1. Total and partial DOSes of pure TiO_2 are given. CB cut-off on the higher energy side is due to finite number of states employed in calculation. The same goes for CBs in Fig. 2. The major contributions to the total DOS comes from Ti 3d and O 2p states. In Fig 2. total and dopant atoms DOSes are given. There are no gap states in calculated systems, contrary to findings in [9] for W and Al for anatase structure and for Nb in rutile type structure [10]. Instead, the dopant states are smeared within VB, and to some extent

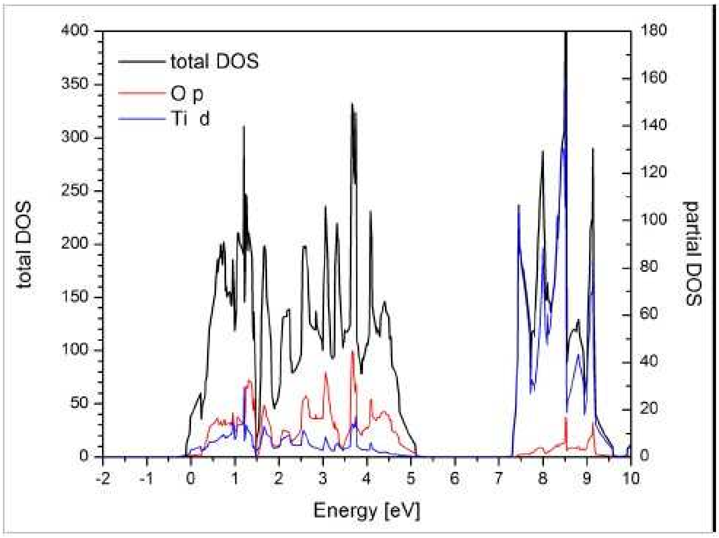

Figure 1: Major contributions to the density of states of pure TiO_2.

within CB. The consequence is widening of VB and consequently smaller width of energy gap. The contribution of dopant atoms to total DOS varies and increases with atomic number Z of dopant (note the change in right scale for dopant DOS contribution). The 3(4,5)d states of transition metals dominates the contribution to VB and are situated near VB bottom. Among earth-alkali metals, minimal contribution to the VB DOS is coming from Mg. The large contribution to the CB is present in case of Nb and W, due to partially filled d orbitals. This is also the reason why CB contribution is almost completely absent in Zn case, since its 3d states are initially completely populated and mostly lies below Fermi level. All dopants acts as electron donors, with the most of the electrons (almost 3) stripped from Al, W and Nb, respectively. Relatively small amount of charge donated by Zn is probably due to its closed shell configuration.

The topology details of charge density and to some extent its laplacian can serve as general criteria for strength and nature of bonding in the system. In particular, bonding critical points (bCPs), as saddle points in charge density located between neighbour atomic sites, could give insight into details and mechanism of bonding. Small values of charge density and large positive values of laplacian in bCP goes in favor of dominant ionic contribution in bonding, as in case of W and Be. In case of Nb there is a large discrepancy in charge density for bCPs in direction of octahedral base plane nearest neighbor O atoms and in direction of remain two O atoms below and above this plane, a sign that O coordination number of Nb is likely to be other then 6. Higher charge density values and therefore stronger localization of charge along bonding path (in case of Zn and Ca) goes in favor of larger covalency share in bonding. Still all dopant-O bonds remain mostly ionic in nature, according to laplacian and its sign.

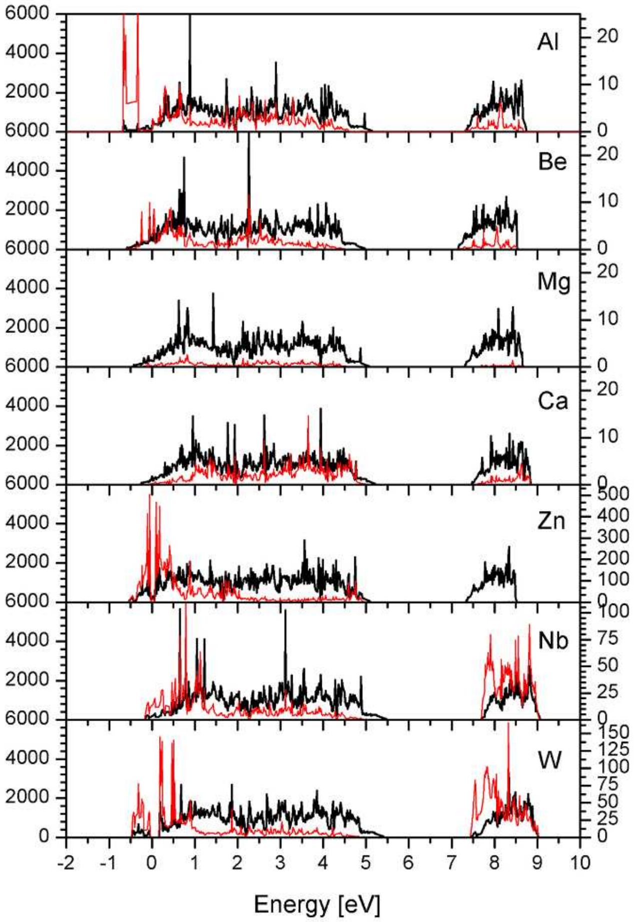

Figure 2: Total DOS (black line) and dopant atomic DOS (red line) of TiO_2 doped with 6.25 at. % of selected metals.

4 Conclusions

We have investigated the influence of simple, earth-alkali and transition metal doping on electronic structure of bulk rutile TiO_2. The trends in electronic structure properties along the different rows of periodic table have proved hard to establish. Dopants influence on electronic structure is constrained on contributing additional states to VB and CB, VB widening and consequently energy gap narrowing, although latter two effects are not particularly pronounced. No dopant states within energy gap were found.Further optical and conduction calculations based on so far performed calculations of investigated systems can give further insight into the way the doping improves (or worsens) properties of TiO_2 essential for its role as a functional electrode in DSSC devices.

References

[1] M. Saito and S. Fujihara. Large photocurrent generation in dye-sensitized ZnO solar cells. *Energy and Environmental Science*, 1:280–283, 2008.

[2] B. Onwona-Agyeman, S. Kaneko, A. Kumara, M. Okuya, K. Murakami, A. Konno, and K. Tennakone. Sensitization of nanocrystalline SnO2 films with indoline dyes. *Japanese Journal of Applied Physics*, 44:L731–3, 2005.

[3] P. Guo and M. A. Aegerter. RU(II) sensitized Nb2O5 solar cell made by the sol-gel process. *Thin Solid Films*, 351:290, 1999.

[4] B. Tan, E. Toman, Y.G. Li, and Y. Y.J. Wu. Zinc stannate (Zn2SnO4) dye-sensitized solar cells. *Journal of the American Chemical Society*, 129:4162–3, 2007.

[5] A. Kay and M. Grätzel. Dye-sensitized core-shell nanocrystals: Improved efficiency of mesoporous tin oxide electrodes coated with a thin layer of an insulating oxide. *Chemistry of Materials*, 14:2930–5, 2002.

[6] X. Gonze et al. ABINIT : first-principles approach to material and nanosystem properties. *Computer Physics Communications*, 180:2582–615, 2009.

[7] J. P. Perdew, K. Burke, and M. Ernzerhof. Generalized gradient approximation for the exchange-correlation hole of a many-electron system. *Physical Review Letters*, 77:3865–8, 1996.

[8] R. F. W. Bader. Atoms in molecules: a quantum theory. *Oxford University Press*, 1994.

[9] T. T. Nguyen et al. Influences of metallic doping on anatase crystalline titanium dioxide: From electronic structure aspects to efficiency of TiO2-based dye sensitized solar cell (DSSC). *Materials Chemistry and Physics*, 144:114–21, 2014.

[10] K. K. Ghuman and C. V. Singh. A DFT+U study of Rh, Nb codoped rutile TiO_2. `http://arxiv.org/abs/1210.7749v1`.

Explosive and adaptive synchronization in complex networks

J.A. Almendral[1,2], *V. Avalos-Gaytán*[3], *S. Boccaletti*[4,5],
I. Leyva[1,2], *A. Navas*[1], *I. Sendiña-Nadal*[1,2]*

[1] *Center for Biomedical Technology,*
Universidad Politécnica de Madrid, 28223 Madrid, Spain

[2] *Complex Systems Group, Universidad Rey Juan Carlos,*
28933 Móstoles, Madrid, Spain

[3] *Postgraduate Division in Systems Engineering,*
Department of Mechanical and Electrical Engineering,
Universidad Autónoma de Nuevo León, San Nicolás de los Garza, Nuevo León, Mexico

[4] *CNR- Institute of Complex Systems,*
Via Madonna del Piano 10, 50019 Sesto Fiorentino, Florence, Italy

[5] *The Italian Embassy in Israel, 25 Hamered st., 68125 Tel Aviv, Israel*

Abstract. This work is the continuation of that produced in the the period 2009-2013 and of use of the ENEA GRID CRESCO system [1, 2, 3]. In this last year, our research has been focused in the relationship between the connectivity structure among dynamical systems into the emergence of a collective synchronous behavior. In particular, we have obtained several important results that provide new insights in the mechanisms underlying the abrupt transitions to synchrony, a process known as explosive synchronization (ES), and the emergence of modularity and degree-degree correlations in the connectivity structure of real networks.

1 The abrupt transition to synchronization

One of the most intriguing processes in complex networks' dynamics is synchronization: the spontaneous organization of the network's units into a collective dynamics. This phenomenon is known to be related to a delicate interplay between the topological attributes of the network and the main features of the dynamics of each graph's unit [6, 4].

---

*Corresponding author. E-mail: `irene.sendina@urjc.es`.

Such a connection between structure and dynamics of a network is of particular importance in the case of the recently reported explosive synchronization (ES), an irreversible and discontinuous transition to the synchronous state. Originally, ES was described in all-to-all coupled ensembles of Kuramoto oscillators [10] for a specific distribution of frequencies [18]. Later on, various kinds of degree-frequency correlations were found to be able to induce ES in networks of periodic and chaotic oscillators [9, 13]. In addition, other microscopic mechanisms were proposed, based on diverse coupling strategies [11, 12], or by introducing adaptive dynamics in a fraction of the network's units [20].

In our studies on this phenomenon we use complex networks of phase oscillators whose instantaneous phases evolve in time according to the simple paradigmatic model of periodic oscillators described by Kuramoto [10]:

$$\dot{\theta}_i = \omega_i + \sigma \sum_{j=1}^{N} A_{ij} \sin(\theta_j - \theta_i) \quad i = 1, ..., N, \tag{1}$$

where θ_i is the phase of the i^{th} oscillator with natural frequency ω_i and σ is the coupling constant. The topology of the network is uniquely defined by the adjacency matrix $\mathbf{A}$, since $A_{ij} = 1$ if node i is connected with node j and $A_{ij} = 0$ otherwise. The frequencies are chosen from a known distribution $g(\omega)$. The level of synchronization can be monitored by looking at the value of $S = \langle \frac{1}{N} | \sum_{j=1}^{N} e^{i\theta_j(t)} | \rangle_T$, with $\langle ... \rangle_T$ denoting a time average over a conveniently large time span T.

By means of extensive calculations performed in CRESCO, in the last year we have obtained several important results that provide new insights in the mechanisms underlying ES. For the numerical integration of our model and the analysis of the results we use homemade *C* and MatLab codes implementing Runge-Kutta integration algorithms. Extensive serial calculations have been performed for large parameters ranges, diverse network topologies and statistical validation of the results.

1.1 Results

1.1.1 Role of the degree correlations

We study the dynamics of Eq. (1) when $\omega_i = k_i$ [9]. While this structure-dynamics correlation is known to induce abrupt transitions to synchronization in growing scale-free networks, the transition has a completely different nature for static random configurations preserving the same structure-dynamics correlation (Fig. 1 (a)). In [19] we show that this difference is due to the further presence of degree-degree correlations. By means of extensive simulations, we show that while high levels of positive and negative mixing consistently induce a second-order phase transition, moderate values of assortative mixing, such as those ubiquitously characterizing social networks in the real world, greatly enhance the irreversible nature of explosive synchronization in scale-free networks. The latter effect corresponds to a maximization of the hysteresis area that differentiates the forward and backward transitions to synchronization, as it is shown in Fig.1(b).

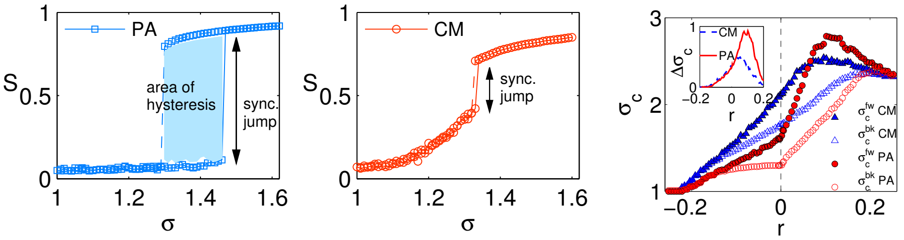

Figure 1: (Color online). (Left and Center) Comparative results on ES between SF networks belonging to two different ensembles: preferential attachment (PA) and configuration (CM) models with exactly the same degree distribution. (Right) Behaviour of critical coupling strengths σ_c at the synchronization transitions during the forward (solid symbols) and backward (hollow symbols) continuations for growing PA ($\circ$) and static CM ($\triangle$) SF networks as a function of the degree mixing r. In all cases, $N = 5 \cdot 10^3$, $\langle k \rangle = 6$, and $\gamma = 2.4$.

1.1.2 Role of the synchronization seeds: the effective centrality measure

The conditions for synchronization in complex networks of identical units can be studied by means of the *Master Stability Function* [6]. However, the general case of non-identical units often needs a numerical approach. In [14] we propose the use of an effective topological network whose structure explicitly reflects the interplay between the topology and dynamics of the original system $C_{ij} \equiv A_{ij}\left(1 - \frac{\Delta\omega_{ij}}{\Delta\omega_{max}}\right)$. In order to quantify the role of each node in the synchronization process, we calculate the eigenvector centrality measure of $\mathbf{C}$, obtaining the *effective centrality* vector $\mathbf{\Lambda^C}$, whose i-th component provides a measure of the importance of the node i in the effective network and quantifies its potential to behave as a seed of synchronization.

In order to have a ground truth of the synchronization process, we calculate the local synchronization matrix $\mathbf{S} = \{S_{ij}\} = A_{ij}|\langle e^{i\Delta\theta_{ij}}\rangle_t|$, whose eigenvector centrality $\mathbf{\Lambda^S}$, provides the actual *synchronization centrality* of each node. In Fig. 2 we report the % of coincidence between the third of the nodes with the highest (lowest) Λ_i^S and Λ_i^C centralities, and the corresponding percentage of coincidence between Λ_i^S and topological Λ_i^A. It can be seen that the ranking based on Λ_i^C is able to predict up to 80% of the nodes with the highest (lowest) dynamical centrality.

2 Synchronization shapes assortativity and modularity

Natural networking systems [6] are vastly characterized by a modular organization of their connectivity structure [7], and by non trivial correlation features in the way units with a given number of connections (degree) tend to link with members of the same degree (assortativity), or with units with seemingly different degrees (disassortativity). Modularity is clearly the result of the need of social, biological, and technological systems to optimize their parallel, yet integrated, functioning by means of an organization into

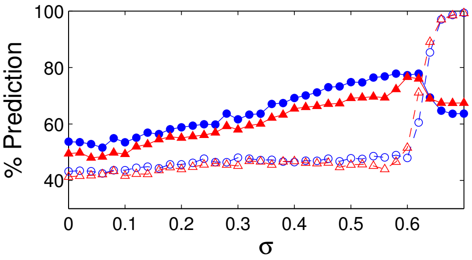

Figure 2: (Color online). Average % of coincidence between the third of the nodes with the highest (red triangles) and lowest (blue circles) Λ_i^S and Λ_i^C and the corresponding % between Λ_i^S and Λ_i^A (empty symbols) on ER networks with $\langle k \rangle = 50$. Each point corresponds to 10 realizations.

meso-scale structures, such as *communities*, i.e. groups of highly interconnected nodes that are sparsely connected to the rest of the graph [8]. On its turn, degree-degree correlation reflects the observed tendency of natural networks to organize the main topology on top of a backbone of nodes that may be star-like (disassortativity) or of highly connected hubs (assortativity).

Thanks to CRESCO, we were able to show that all these features may spontaneously emerge in an adaptive network of interacting oscillators, as the result of a delicate interplay between synchronization processes and co-evolution of the connectivity structure [5]. When the connectivity dynamics is such that links coupling the nodes with synchronous (non synchronous) dynamics are promoted (weakened), we prove that an initially unstructured clique configuration evolves in time toward an emerging structured network displaying both modularity and assortativity.

We start by considering an initial ensemble of N all to all coupled Kuramoto oscillators, Eq. 1, but modified as follows. Each unit of the ensemble $i = 1, \ldots, N$ is characterized by its *phase* θ_i whose dynamics is ruled by

$$\dot{\theta}_i = \omega_i + \frac{\sigma}{N} \sum_{j=1}^{N} w_{ij} \sin(\theta_j - \theta_i), \tag{2}$$

where now $w_{ij} \in [0, 1]$ is the weight of the connection between the units i and j, that co-evolve with the dynamics of the units. Namely, they are taken to be time dependent variables ($w_{ij} = w_{ij}(t)$) that obey the following equation:

$$\dot{w}_{ij} = (p_{ij} - p_c)\; w_{ij}(1 - w_{ij}), \tag{3}$$

where p_{ij} is the *instantaneous phase correlation* between units i and j, resulting from

$$p_{ij}(t) := \left| \cos\left(\frac{\theta_i - \theta_j}{2} \right) \right|, \tag{4}$$

and p_c is the *correlation threshold*), which together with the coupling constant σ are the two parameters of the model.

It is worth noticing that, from Eq. (4), p_{ij} is exactly one for all pairs of units with equal phases, while it vanishes for pairs of oscillators with opposite phases, $\theta_i = \theta_j \pm \pi$. The parameter p_c has the following meaning: a link weight is reinforced at all times at which $p_{ij} > p_c$, whereas it weakens when $p_{ij}(t) < p_c$. Thus, connections improving (reducing) the degree of synchronization between a pair of oscillators are reinforced (weakened). The driving force for the weight dynamics [the RHS of Eq. (3)] has two attractors, leading each weight to asymptotically converge to either one of the values in $\{0, 1\}$.

As a consequence, for any given choice of σ and p_c, a generic random initial condition for all $\theta_i(0)$ and for all $w_{ij}(0)$ results in a progressive pruning of the units' connections, up to when, ultimately, Eqs. (2) and (3) stick into an asymptotic state (defined as $\dot{w}_{ij} = 0$, $\forall i, j$), which corresponds to a specific dynamical organization of the ensemble, and to the spontaneous emergence of a given, un-weighted, network topology.

At this point is where CRESCO was essential to our purposes since the attainment of the asymptotic state is numerically verified by checking either $w_{ij}(t) > 1 - \epsilon$ or $w_{ij}(t) < \epsilon$ from a given time on (in all our trials $\epsilon = 10^{-3}$), ensuring that the original all-to-all weighted connectivity matrix is sufficiently close to a network adjacency matrix. We further require $\dot{w}_{ij} < \epsilon$ to check the stability of the convergence process. Upon reaching a link configuration fulfilling the above conditions, we proceed to rounding each w_{ij} to its nearest integer value. Numerical evidence shows that the model always fulfils the stopping criterion, though the convergence time crucially depends on the specific values of p_c and σ (being, in only a few cases, one or two orders of magnitude longer than a characteristic timescale of the order of 1,000 cycles of the oscillator with lower natural frequency).

2.1 Results

One of the major results of our study is that, as a consequence of the adaptive evolution of the ensemble, specific meso-scales are shaped in the final topology, see Fig. 3 (left). To properly visualize the presence of communities, we measure the *modularity* index $\mathcal{M}$ of the network in its asymptotic state [16].

A second inspected structural feature of the emerging network is represented by assortativity, i.e. the *correlations* features of the degrees of neighboring nodes. For this purpose, we measure the assortativity with two methods. First, we consider the coefficient r [15], which is essentially the Pearson correlation coefficient of the degree between pairs of linked nodes. When the assortativity coefficient, which always lies in $[-1, 1]$, verifies that $r > 0$ it is said that the network is assortative. And second, we compute the average degree of the neighbors of a node with given degree k, $k_{nn}(k) := \sum_{k'} k' P(k'|k)$, where $P(k'|k)$ is the conditional probability for a node with degree k to have a neighbor with degree k' [17]. If $k_{nn}(k)$ is a monotonically increasing function, then the network is assortative.

In Fig. 3 (right) we report the assortativity coefficient r vs. p_c, for different values of σ. Furthermore, the plot in the inset shows the slope of the best linear fit of the function $k_{nn}(k)$ vs. p_c. Remarkably, for $p_c > 0.6$, in perfect correspondence with the transition to increasingly pronounced modular structures already observed in Fig. 3 (left), here both plots also indicate a transition to assortative configurations of the network in its final state.

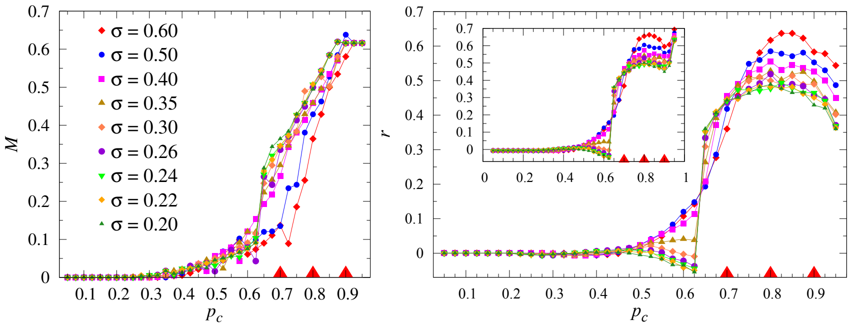

Figure 3: (Left) Modularity index $\mathcal{M}$ vs. p_c. Each curve corresponds to a different value of the coupling strength σ, as it is indicated in the legend. (Right) Assortativity coefficient r vs. p_c, for different values of σ (same stipulations as on the left). The plot in the inset depicts the slope of the best linear fit of the function $k_{nn}(k)$ vs. p_c. Notice that both plots clearly indicate a transition to assortative configurations for $p_c > 0.6$, i.e. in correspondence with the transition to increasingly pronounced modular networks highlighted on the left.

This latter transition (from a non-assortative to an assortative topology) is moreover rather independent of the value of σ, and is always observed in the range $p_c = 0.6 - 0.7$.

References

[1] J.A. Almendral, R. Bajo, S. Boccaletti, J.M. Buldú, R. Gutiérrez, I. Leyva, A. Navas, D. Papo, I. Sendiña-Nadal, and M. Zanin. Synchronization in complex biological networks. In *High Performance Computing on CRESCO infrastructure: research activities and results 2009-2010*, page 33. ENEA, 2011.

[2] J.A. Almendral, R. Bajo, S. Boccaletti, J.M. Buldú, R. Gutiérrez, I. Leyva, A. Navas, D. Papo, I. Sendiña-Nadal, and M. Zanin. Emergent phenomena in biological networks. In *High Performance Computing on CRESCO infrastructure: research activities and results 2010-2011*, page 113. ENEA, 2012.

[3] J.A. Almendral, S. Boccaletti, R. Gutiérrez, I. Leyva, J.M. Buldú, A. Navas, and I. Sendiña-Nadal. Synchronization phenomena in complex networks. In *High Performance Computing on CRESCO infrastructure: research activities and results 2013*, page 174. ENEA, 2014.

[4] A. Arenas, A. Díaz-Guilera, J. Kurths, Y. Moreno, and C. Zhou. Synchronization in complex networks. *Physics Reports*, 469(3):93–153, 2008.

[5] Vanesa Avalos-Gaytán, Juan A. Almendral, David Papo, Satu Elisa Schaeffer, and Stefano Boccaletti. Assortative and modular networks are shaped by adaptive synchronization processes. *Phys. Rev. E*, 86:015101, 2012.

[6] S. Boccaletti, V. Latora, Y. Moreno, M. Chavez, and D.-U. Hwang. Complex networks: Structure and dynamics. *Physics Reports*, 424(4-5):175–308, 2006.

[7] S. Fortunato. Community detection in graphs. *Phys. Rep.*, 486:75, 2010.

[8] M. Girvan and M.E.J. Newman. Community structure in social and biological networks. *PNAS*, 99:7821, 2002.

[9] J. Gómez-Gardeñes, S. Gómez, A. Arenas, and Y. Moreno. Explosive synchronization transitions in scale-free networks. *Phys. Rev. Lett.*, 106(12):128701, 2011.

[10] Y. Kuramoto. *Chemical oscillations, waves and turbulence.* Springer, 1984.

[11] I. Leyva, A. Navas, I. Sendiña-Nadal, J.A. Almendral, J.M. Buldú, M. Zanin, D. Papo, and S. Boccaletti. Explosive transitions to synchronization in networks of phase oscillators. *Sci. Rep.*, 3, 2013.

[12] I. Leyva, I. Sendiña-Nadal, J.A. Almendral, A. Navas, S. Olmi, and S. Boccaletti. Explosive synchronization in weighted complex networks. *Phys. Rev. E*, 88:042808, 2013.

[13] I. Leyva, R. Sevilla-Escoboza, J.M. Buldú, I. Sendiña-Nadal, J. Gómez-Garde nes, A. Arenas, Y. Moreno, S. Gómez, R. Jaimes-Reátegui, and S. Boccaletti. Explosive first-order transition to synchrony in networked chaotic oscillators. *Phys. Rev. Lett.*, 108:168702, 2012.

[14] A. Navas, J.A. Villacorta-Atienza, I. Leyva, J.A. Almendral, I. Sendiña-Nadal, and S. Boccaletti. Synchronization centrality and explosive synchronization in complex networks. *ArXiv e-prints: 1503.00954*, 2015.

[15] M.E.J. Newman. Assortative mixing in networks. *Phys. Rev. Lett.*, 89:208701, 2002.

[16] M.E.J. Newman. Modularity and community structure in networks. *PNAS*, 103:8577, 2006.

[17] R. Pastor-Satorras, A. Vázquez, and A. Vespignani. Dynamical and correlation properties of the internet. *Phys. Rev. Lett.*, 87:258701, 2001.

[18] D. Pazó. Thermodynamic limit of the first-order phase transition in the kuramoto model. *Phys. Rev. E*, 72:046211, 2005.

[19] I. Sendiña-Nadal, I. Leyva, A. Navas, J.A. Villacorta-Atienza, J.A. Almendral, Z. Wang, and S. Boccaletti. Effects of degree correlations on the explosive synchronization of scale-free networks. *Phys. Rev. E*, 91:032811, 2015.

[20] X. Zhang, S. Boccaletti, S. Guan, and Z. Liu. Explosive synchronization in adaptive and multilayer networks. *Phys. Rev. Lett.*, 114:038701, 2015.

A coarse grain model for α-synuclein aggregation

Piero Procacci[1]** *and Gabriella Caminati*[1,2]

[1] *Department of Chemistry, University of Florence, Italy*

[2] *CSGI, Center for Colloid and Surface Science (CSGI)*

Abstract. α-Synuclein (α-syn), a disordered cytoplasmatic protein involved in membrane trafficking in brain cells, plays a fundamental role in the pathogenesis of Parkinson's disease (PD) and is one of the major components of the malignant fibrillar β-aggregates (Lewy bodies) found in the substantia nigra of PD suffering patients. It has been recently shown that the peptidyl prolyl isomerase FKBP12, especially abundant in the central nervous system, enhances aggregation of α-synuclein *in vitro* and *in vivo.* FKBP12 overexpression or unbalancing in brain cells has been hence proposed as a possible cause for neurological disorders. In this study, we devise a rudimental coarse grain model based on the hydrophobic/hydrophilic effect in order to simulate and rationalize the observed morphologies and kinetics in α-synuclein aggregation processes with or without FKBP12.

α-Synuclein (α-syn) is a key player in the pathogenesis of Parkinson's disease (PD)[1, 2, 3]. In pathological conditions, the protein is present in a fibrillar, aggregated form in the brain cells called Lewy bodies. Members of the FK506 binding protein (FKBP) family were shown recently to be involved in neurological disorder and β structure formation[1, 3, 4]. In Figure 1 we show a ribbon representation of α-synuclein (α-syn) with proline binding FKBP12 protein. This specific immunophilin, especially abundant in the central nervous system and brain cells, was recently found to significantly enhance α-syn aggregation kinetics *in vivo* o *in vitro*, suggesting a possible role for FKBP12 in synucleopathies and neurological disorder in general[4]. The α-syn monomer primary structure comprises three distinct segments. The C terminus (92-140) is a polar coil region bearing a strong negative charge of -12 electrons. All five prolines in α-syn are located in the C terminus. The equally polar 1-40 N terminus has a mixture of negatively and positively charged residues with a slight prevalence of the latter (+3 electrons). The so-called NAC domain, the central region of the the α-syn monomer, including aminoacids 40 to 92, is characterized by a sequence of mostly hydrophobic residues and is involved in the β-sheet formation[5, 6]. Several recent studies have shown that α-syn fibrils are characterized by an hydrophobic solvent protected core[7, 8, 9] with external hydrophilic filaments due to the C and N termini. The kinetics of fibril growth is typically sigmoidal, defined by an initial lag phase, a subsequent growth phase in which Thio-T fluorescence increases, and a final equilibrium phase, where Thio-T fluorescence reaches a plateau indicating the end of fibril formation. The curve is consistent with a nucleation-dependent elongation model of fibril formation[10, 11]. The lag phase is assumed to be associated with the formation of *toxic*

---

[*] Corresponding author. E-mail: `piero.procacci@unifi.it`.

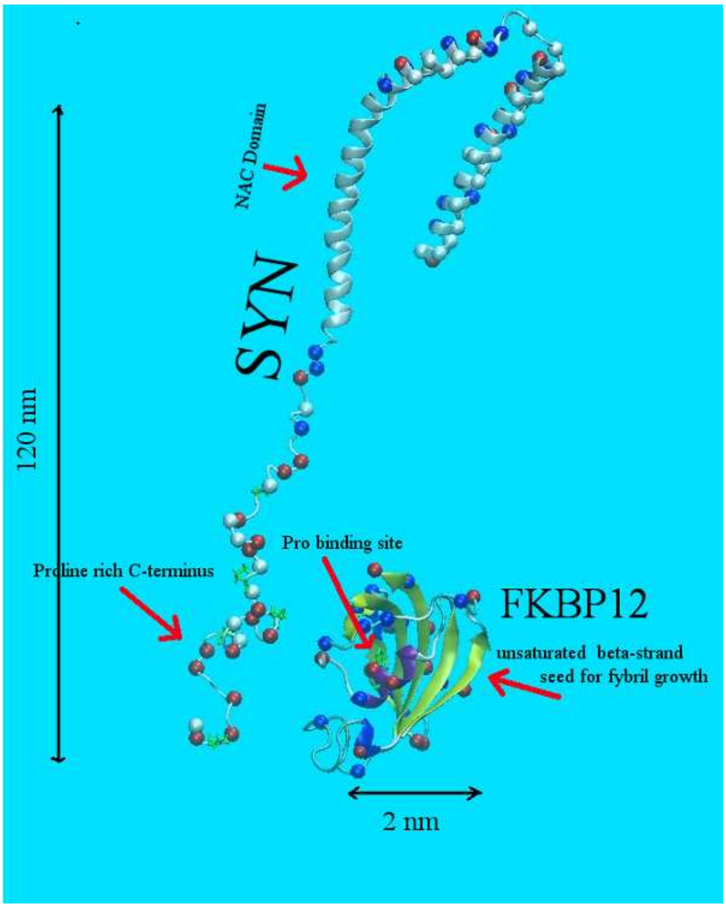

Figure 1: α-synuclein and FKBP12 structures. Red and blue balls indicate negatively and positively charged residues, respectively. Proline are in indicated in green (bond model). β-sheet structure on FKBP12 is in yellow color.

oligomers that then aggregate, in the growth phase, in mature *linear* fibrils. The linear morphology of the fibril in α-syn aggregation is rationalized in terms of an in-register parallel beta-sheet structure with systematic stacking of the hydrophobic NAC domains of the monomers along the fibril axis[6, 12, 9, 13, 14].

When the FK506 binding protein is added to a α-syn solution, the kinetics and morphology of aggregation change dramatically in a dose dependent manner, exhibiting faster growth and branched structures[4]. FKBP12, as a peptidyl prolyl isomerase, binds the proline residues in the disordered C terminal region (see Figure 1). FKBP12 by itself constitutes a seed for toxic β-structure association as it bears a six residues long unsaturated and solvent exposed β-strand in the N terminal region. When an FKBP12 protein is transiently bound to one α-syn molecule (see Figure 1) via a PRO residue at the C terminus, it could then seeds toxic aggregation by forming a single β-sheet involving the NAC domain of the α-syn partner. Given the well established hydrophobic nature of the NAC domain aggregation in α-syn, the *location* of the FKBP12 seeds preferentially at the C hydrophilic termini, rather than the rotamase activity, could be responsible for the observed and dramatic morphology change, with extended ramification instead of linear growth.

In order to show that the balance of hydrophobic/hydrophilic interaction may indeed explain the observed morphologies and kinetics in pure α-syn and α-syn-FKBP12 mixtures (i.e with partially inhibited share of monomeric FKBP12), irrespective of the precise arrangement of the β-sheet structure along the fibrils, we have done extensive molecular dynamics simulations based on an elementary coarse grain model (CG) for α-syn and α-syn-bound FKBP12. Briefly, we assume a 15 beads CG representation of the monomeric synuclein chain, made up of three distinct part of five beads length each, i.e. a central hydrophobic part (corresponding to the NAC domain) and two terminal hydrophilic parts. The five beads approach is based on a recent model for the α-syn mature fibrils based on a five strands monomer[6, 15, 5, 14]. According to the proposed CG model, each hydrophobic bead may represent an unsaturated β-strand. Consecutive beads are bound via a stretching harmonic potential with $r_0 = 1.5$ nm equilibrium distance and with a stiff force constant of 230 in units of $RT\text{Å}^{-2}$. A harmonic bending potential with equilibrium angle α =120° and force constant $k = 230$ in units of $RT\text{Å}^{-2}$ is enforced between three consecutive beads, irrespective of their character. The equilibrium bead-bead distance and bending angle are chosen so that α-syn, when in the fully extended state, has a length of the order of 20 nm (see Figure 1). 512 α-syn monomeric chains are inserted randomly in a cubic box of 200 nm side length corresponding to an initial volume of 0.8×10^7 nm^3, yielding a volume per molecule 1.6×10^4 nm^3 corresponding to an initial concentration of $\simeq 100\mu$M. We make a solvent free model with renormalized bead-bead non-bonded interactions so as to mimic, in a water environment, the aggregation of hydrophobic moieties and solubilization of the hydrophilic groups. To this end, a strongly repulsive atom-atom potential is assigned to the hydrophilic beads (1-5 and 11-15) while an attractive atom-atom potential is used to model the interactions of the hydrophobic NAC domain central beads. The potential functional form for the bead-bead non bonded interaction is of the Lennard-Jones type and mixing rules applies for the hydrophilic-hydrophobic interactions. The Lennard-Jones ϵ well depth and σ parameters for hydrophobic-hydrophobic interactions are tuned so as to obtain, at a distance of $\simeq$ 1.5 nm, approximately a gain of 10 RT units per bead (representing approximately 10 residues), corresponding to a reasonable mean value of 1 RT units gain for the aggregation of two hydrophobic residues in water[16]. Potential data are reported in the Figure 2 that exemplifies the CG model used for α-syn and α-syn/FKBP12 mixtures.

At ordinary temperature, the *in vacuo* diffusivity of a molecule is about four to five order of magnitude faster with respect to that typical of the liquid water solution. The aggregation rate of the α-syn monomers depends on the diffusivity and on the α-syn initial concentration. Given the initial concentration of monomers of $\simeq 100\mu$M , by setting the temperature to T=300 K and by rescaling the mass of the bead to 4 Da (yielding a monomer mass of 60 Da instead of the actual 14.46 kDa), we expect, in our simple CG model, aggregation phenomena to occur in the nanoseconds time scale of the simulation. As shown in Figure 1, when proline bound, the globular protein FKBP12 exposes at the C terminus of α-syn an unsaturated β-strand acting as a seed for the binding of the β-sheet forming NAC domain (either intramolecular or intermolecular). So, the α-syn-FKBP12 equimolar mixture can be modeled in a mean filed spirit, by simply replacing

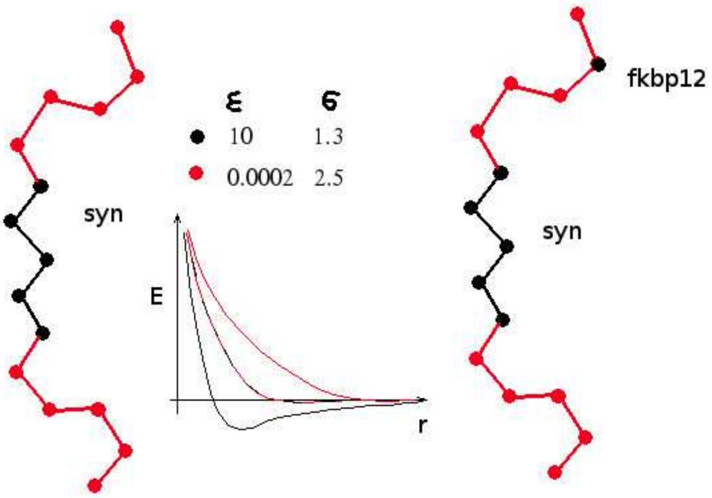

Figure 2: Coarse Grain model for α-syn and α-syn-FKBP12 complex. The ϵ and σ Lennard-Jones parameter are in RT units and nm respectively.

one of the terminal hydrophilic beads with an hydrophobic one in a fraction of α-syn molecules computed according to the equilibrium dissociation constant for the FKBP12-α-syn complex. The effect of the tight-binding inhibitor, as FK506, in the α-syn-FKBP12 equimolar solution is simply that of reducing the FKBP12 effective concentration in a strictly dose dependent manner[3, 17].

Starting from the 512 CG system with 15 beads per monomer (7680 "atoms" system), we therefore performed a 8 ns long molecular dynamics simulation for α-syn alone (Figure 2 left) and four equivalent runs where a fraction of 0.11, 0.33, 0.5 and 1 of the 512 monomers were modified by replacement of a hydrophilic bead with a hydrophobic one the termini ((Figure 2 right). The starting configurations referring to the fraction α-syn-FKBP12(0.11,0.33,0.5) were obtained by modifying, according to the scheme of Figure 2, 56, 128, 256 random molecules of the 512 α-syn units. The equations of motion were integrated using a multiple time step algorithm with longest step of 12 fs. The cutoff for the non bonded interactions was set to 50 nm. All simulations were done using the program ORAC[18, 19]. Each of the 5 simulations at various FKBP12/α-syn ratios was performed in parallel using 16 cores and in triplicates (or equivalent replica) for error assessment for a total 48 cores per simulation. The MPI parallelization strategy was based on a splitting of the total allocated 48 cores per simulation into three MPI communication groups, producing three independent non communicating trajectories and assigning 16 cores for the strong scaling computation of the forces in each of the independent trajectory/MPI communication group. Parallelization of the forces was done using a force decomposition scheme with a parallel efficiency close to 50% on 16 cores. The 48 cores simulations for each system were done on the CRESCO2 656 node system (Nehalem E5530 e Westmere E5620 processors), and ran at a speed of 6.2 ns/day (compared to the serial speed of 0.8 ns/day) lasting about 40 wall clock hours. All simulations ($\simeq 0.12$ μs in total) were carried on at

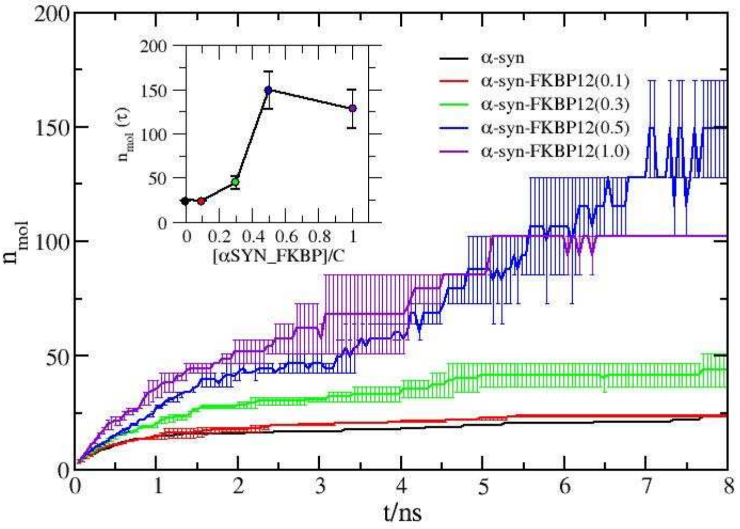

Figure 3: Aggregation kinetics for various fraction of the species FKBP12-α-syn as measured by the average number of monomers composing the aggregate as a function of time. For each fraction, the errors have been evaluated by averaging the data over three independent simulations. In the inset we report the average number of monomers composing the aggregates in the final configuration along with the largest error detected during the whole simulation time span.

constant volume in the NVT ensemble using a Nosé thermostat and were completed in less than two weeks. In Figure 3 we show the kinetics (as measured by the average number of monomers, $n_{\rm mol}$, in the growing aggregated species as a function of time) observed for the pure α-syn and for samples with different fractions of α-syn-FKBP12 complexes. In the final stages of the simulation, the oscillations in $n_{\rm mol}$ increase, widening the error bar in the order parameter. For the highly aggregated 0.5 and 1.0 α-syn-FKBP12 fractions, the final value of $n_{\rm mol}$ in the triplicates ranges from a minimum of 102.4 to maximum of 170.6 corresponding to only five and three supramolecular aggregates, respectively.

Inspection of Figure 3 shows that the kinetics is accelerated with increasing fraction of FKBP12-modified α-syn molecules ($[\mathrm{FS}]/C$). Correspondingly, the final stationary value of the average number of monomers in the aggregates grows with the fraction of FKBP12-bound α-syn up to $[\mathrm{FS}]/C = 0.5$ reaching a plateau. In the inset, we report the final value of $n_{\rm mol}$ as a function of $[\mathrm{FS}]/C$ evidencing the non trivial effect, reminiscent of a transition, of FKBP12 addition. Up to a fraction of $[\mathrm{FS}]/C = 0.33$, the aggregation kinetics resembles in fact that observed in the sample of pure α-syn. Above the threshold fraction of $[\mathrm{FS}]/C > 0.33$, the aggregation kinetics undergoes an abrupt regime change, exhibiting a much faster growth. Correspondingly, as shown in Figure 4, a dramatic change is observed in the morphology of the supramolecular aggregates, that for $[\mathrm{FS}]/C > 0.5$

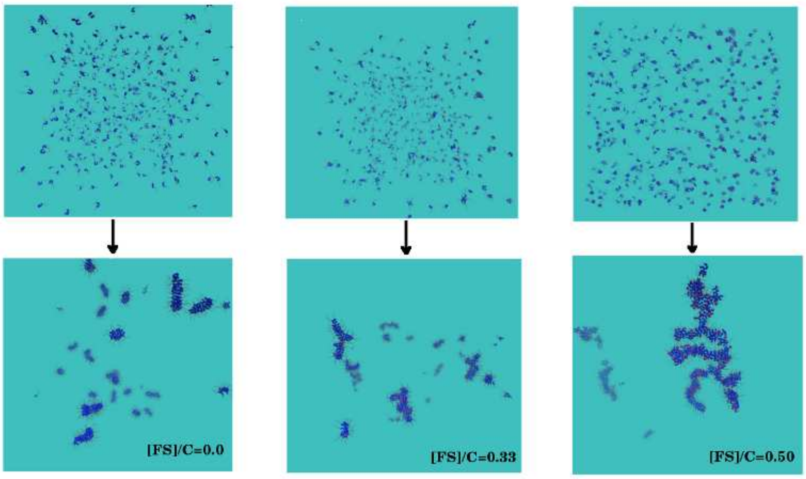

Figure 4: Initial and final configurations of the CG simulations for various fraction of FKBP12-doped α-syn (see text and Figure 2)). Hydrophobic beads are in blue. FKBP12 beads are in red. The lines representation refers to the hydrophilic moieties.

invariably exhibits highly branched structures. In Figure 4 we show the the final states in the simulations of pure α-syn and in the simulations carried on with a fraction of 0.33 and 0.5 of FKBP12-modified α-syn. In striking correspondence with the experimental observations[9], the sample containing only α-syn ($[\mathrm{FS}]/C = 0.0$) spontaneously aggregates in linear fibrils exposing the hydrophilic filaments pointing towards the solvent roughly perpendicularly to the fibril axis. When the concentration of the species, regulated by the FKBP12-α-syn association equilibrium, are such that 1/3 of the monomers are, on the average, FKBP12-bound ($[\mathrm{FS}]/C \simeq 0.33$), the kinetics undergoes only a mild acceleration (see Figure 3). In these conditions, the final supramolecular aggregates are mostly linear or poorly branched, a situation that is observed experimentally upon addition of a tight binding FKBP12 inhibitor to α-syn/FKBP12 mixture.[4] As above outlined, starting from a fraction equal to $[\mathrm{FS}]/C > 0.33$, the kinetics undergoes a drastic change, with the sample ending up in forming few highly branched macro-aggregates.

We finally examine the distribution of the FKBP12 seeds in the supramolecular structures at the end of the aggregation process. There is experimental evidence for a co-localization in brain cells of FKBP12 with the markers of pathology[1, 3]. However FKBP12 has not been yet reported as a major component of Lewy bodies in Parkinson's disease[2]. According to our aggregation model, the FKBP12 globular protein induces ramification of the supramolecular structure and is hence expected to be localized on a hydrophilic segment at the junction of the branches. The localization of FKBP12 in the aggregates is assessed from our configurational data using the Voronoi tessellation algorithm[20]. The final configurations are examined by computing in all samples the Voronoi volumes on the sub-ensemble of beads made by all the hydrophobic units and by all beads (mutated or not) in position 2 of an hydrophilic segment (see Figure 2). Voronoi volumes are evaluated in periodic boundary conditions using the minimum image convention and by closing the polyhedra, when needed, by introducing 8 distant octahedral additional vertices placed

$[\mathrm{FS}]/C$	$c_{\text{buried}}(\text{FKBP12})$	$c_{\text{buried}}(\mathrm{M2-syn})$
0.0	-	0.19 ±0.19
0.11	16.96 ±4.46	0.21 ±0.21
0.33	13.67 ±6.64	0 ±0.13
0.5	8.59 ±1.95	0.39 ±0.39
1.0	1.56 ±0.39	-

Table 1: Percentage of buried FKBP12 $c_{\text{buried}}^{\text{FKBP12}} = N_{\text{buried}}^{\text{FKBP12}}/N_{\text{total}}^{\text{FKBP12}}$ beads with respect to the total number of FKBP12 beads ($N_{\text{total}}^{\text{FKBP12}} \equiv 512 \times [\mathrm{FS}]/C$) and percentage of buried hydrophilic beads at position 2 in normal synuclein $c_{\text{buried}}^{\mathrm{M2-syn}} = N_{\text{buried}}^{\mathrm{M2-syn}}/N_{\text{total}}^{\mathrm{M2-syn}}$ with respect to the total number of normal synuclein ($N_{\text{total}}^{\mathrm{M2-syn}} = 512 - N_{\text{total}}^{\text{FKBP12}}$) as computed from the Voronoi volumes evaluations on the last configurations.

at a distance of 10^4 nm from the central bead. In this manner, exposed beads have faces determined by the distant octahedral vertices, yielding extremely high Voronoi volumes. As discussed above, in the FKBP12-α-syn mixture, a fraction of these hydrophilic beads is replaced by hydrophobic ones. As shown in Figure 5, the Voronoi volume distribution in the final state of pure α-syn peaks at about 20 nm^3 indicating a tight packing of the hydrophobic core of mature fibrils. Based on the distribution of Figure 5, we define a bead to be *buried* (i.e. within the interior of the hydrophobic core of the supramolecular aggregates) when its Voronoi volume is less than 50 nm^3. In Table 1 we show, for various values of the ratio $[\mathrm{FS}]/C]$, the results for the fraction of buried FKB12 beads with respect to the total number of FKBP12 beads compared to the fraction of buried (non mutated) hydrophilic beads in position 2. The FKBP12 beads are clearly much more buried, on the average, with respect to the "normal" hydrophilic beads in position 2, that are basically solvent exposed in the vast majority with $c_{\text{buried}}^{\mathrm{M2-syn}} \simeq 0$. Most of the non buried FKBP12 beads exhibit extremely large Voronoi volume indicating that these units are in general solvent exposed. We also note that, with increasing FKBP12 concentration, the fraction of buried FKBP12 beads decreases down to only 1.56% for $[\mathrm{FS}]/C] = 1$, i.e. in presence of an excess of available (not inhibited) FKBP12.

On the overall, our simulation data appears to confirm that the aggregation in linear fibrils of α-syn is elicited by the hydrophobic aggregation of the central non polar residues of the monomeric unit. Remarkably, our rudimental CG model for the α-syn monomer was able to reproduce the essential morphological features of the supramolecular aggregates in the final stages with no necessity of introducing any detail on the secondary structure. Based on this fact, we may hence infer that the arrangement of the NAC residues in ordered β-structure is probably an event that follows the primary hydrophobic aggregation with β-structure based re-organization of the aggregate being a continuous (and very likely variegate) process in the growth phase. The C and N terminus, as observed in Ref. [9], remain disordered and solvent exposed during the aggregation process. According to our simulation, FKBP12, by binding PRO on these solvent exposed terminal filaments, provides a new seed for branching on the main growing fibril axis.

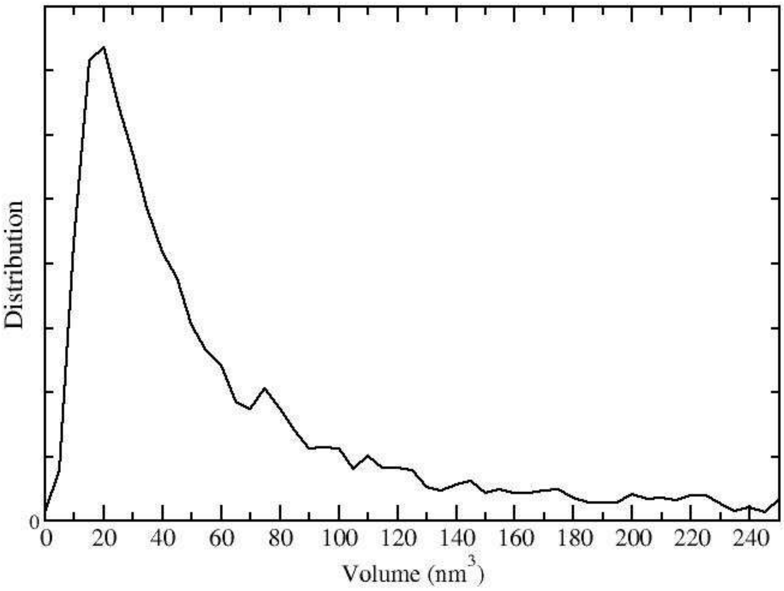

Figure 5: Voronoi volume distribution of the hydrophobic beads in pure α-syn. Volumes for exposed residues are in the range $V = 10^4 \div 10^{12}$ nm.

References

[1] M. Avramut and C.L. Achim. Immunophilins and their ligands: insights into survival and growth of human neurons. *Physiology & Behavior*, 77:463–468, 2002.

[2] Clifford W. Shults. Lewy bodies. *Proceedings of the National Academy of Sciences of the United States of America*, 103(6):1661–1668, 2006.

[3] Melanie Gerard, Angelique Deleersnijder, Veronique Daniels, Sarah Schreurs, Sebastian Munck, Veerle Reumers, Hans Pottel, Yves Engelborghs, Chris Van den Haute, Jean-Marc Taymans, Zeger Debyser, and Veerle Baekelandt. Inhibition of fk506 binding proteins reduces -synuclein aggregation and parkinson's disease-like pathology. *The Journal of Neuroscience*, 30(7):2454–2463, 2010.

[4] Gerard. M., Z. Debyser, L. Desender, J. Baert, V. Baekelandt, and Y. Engelborghs. Fk506 binding protein 12 differentially accelerates fibril formation of wild type alpha-synuclein and its clinical mutants a30p or a53t. *J. Neurochem.*, 106:121–133, 2008.

[5] S. Pornsuwan, K. Giller, D. Riedel, S. Becker, C. Griesinger, and M. Bennati. Long-range distances in amyloid fibrils of -synuclein from peldor spectroscopy. *Angewandte Chemie International Edition*, 52(39):10290–10294, 2013.

[6] Marcal Vilar, Hui-Ting Chou, Thorsten Lührs, Samir K. Maji, Dominique Riek-Loher, Rene Verel, Gerard Manning, Henning Stahlberg, and Roland Riek. The fold of -synuclein fibrils. *Proceedings of the National Academy of Sciences*, 105(25):8637–8642, 2008.

[7] Min Chen, Martin Margittai, Jeannie Chen, and Ralf Langen. Investigation of -synuclein fibril structure by site-directed spin labeling. *Journal of Biological Chemistry*, 282(34):24970–24979, 2007.

[8] Min-Kyu Cho, Hai-Young Kim, Claudio O. Fernandez, Stefan Becker, and Markus Zweckstetter. Conserved core of amyloid fibrils of wild type and a30p mutant -synuclein. *Protein Science*, 20(2):387–395, 2011.

[9] Kim K. M. Sweers, Kees O. van der Werf, Martin L. Bennink, and Vinod Subramaniam. Atomic force microscopy under controlled conditions reveals structure of c-terminal region of -synuclein in amyloid fibrils. *ACS Nano*, 6(7):5952–5960, 2012.

[10] Stephen J. Wood, Jette Wypych, Shirley Steavenson, Jean-Claude Louis, Martin Citron, and Anja Leona Biere. -synuclein fibrillogenesis is nucleation-dependent: Implications for the pathogenesis of parkinsons disease. *Journal of Biological Chemistry*, 274(28):19509–19512, 1999.

[11] P. Bharathi, P. Nagabhushan, and K. S. J. Rao. Mathematical approach to understand the kinetics of α-synuclein aggregation: Relevance to parkinson's disease. *Comput. Biol. Med.*, 38(10):1084–1093, October 2008.

[12] Maria Soledad Celej, Rabia Sarroukh, Erik Goormaghtigh, Gerardo D. Fidelio, and JeanMarie Ruysschaertand Vincent Raussens. Toxic prefibrillar α-synuclein amyloid

oligomers adopt a distinctive antiparallel β-sheet structure. *Biochem. J.*, 443:719–726, 2012.

[13] Kim K. M. Sweers, Ine M. J. Segers-Nolten, Martin L. Bennink, and Vinod Subramaniam. Structural model for [small alpha]-synuclein fibrils derived from high resolution imaging and nanomechanical studies using atomic force microscopy. *Soft Matter*, 8:7215–7222, 2012.

[14] Maryam Hashemi Shabestari, Pravin Kumar, IneM.J. Segers-Nolten, MireilleM.A.E. Claessens, BartD. van Rooijen, Vinod Subramaniam, and Martina Huber. Three long-range distance constraints and an approach towards a model for the -synuclein-fibril fold. *Applied Magnetic Resonance*, pages 1–20, 2015.

[15] S. Esteban-Martín, J. Silvestre-Ryan, C. W. Bertoncini, and X. Salvatella. Identification of Fibril-Like Tertiary Contacts in Soluble Monomeric α-Synuclein. *Biophysical Journal*, 105:1192–1198, September 2013.

[16] Riccardo Chelli, Francesco Luigi Gervasio, Piero Procacci, and Vincenzo Schettino. Inter-residue and solvent-residue interactions in proteins: A statistical study on experimental structures. *Proteins: Structure, Function, and Bioinformatics*, 55(1):139–151, 2004.

[17] Angelique Deleersnijder, Anne-Sophie Van Rompuy, Linda Desender, Hans Pottel, Luc Bue, Zeger Debyser, Veerle Baekelandt, and Melanie Gerard. Comparative analysis of different peptidyl-prolyl isomerases reveals fk506-binding protein 12 as the most potent enhancer of -synuclein aggregation. *J. Biol. Chem.istry*, 286(30):26687–26701, 2011.

[18] P. Procacci, E. Paci, T. Darden, and M. Marchi. Orac: A molecular dynamics program to simulate complex molecular systems with realistic electrostatic interactions. *J. Comp. Chemistry*, 18:1848–1862, 1997.

[19] S. Marsili, G.F. Signorini, R. Chelli, M. Marchi, and P. Procacci. Orac: a molecular dynamics simulation program to explore free energy surfaces in biomolecular systems at the atomistic level. *J. Comp. Chem.*, 31:1106–1116, 2010.

[20] Piero Procacci and Riccardo Scateni. A general algorithm for computing voronoi volumes: Application to the hydrated crystal of myoglobin. *International Journal of Quantum Chemistry*, 42(5):1515–1528, 1992.

Magnetism OF semi-hydrogenated Graphene and effects of the substrate by ab-initio calculations using Quantum-Espresso on CRESCO HPC

Francesco Buonocore[1*]

[1]*ENEA, SSPT-PROMAS-MATPRO,*
Laboratorio Materiali e processi Chimico-Fisici, Casaccia R.C. – Rome, Italy

Abstract. The partial hydrogenation of graphene can induce magnetic properties to this recently discovered 2D-material. This feature make it very interesting as light magnetic material to be considered for substitution of metals and rare earths. We investigated the effects of the adhesion to copper surface on the magnetic properties of semi-hydrogenated graphene (graphone) by first-principles calculations. Our calculations requested the use of the high performance computer facility CRESCO.

1 Introduction

In the last years graphene, a monolayer and planar honeycomb structure of carbon atoms, has attracted great attention for its unique properties deriving from a very simple atomic structure [1]. It combines atomic thinness, high-carrier mobility, linear optical absorption, field-effect sensitivity, and high mechanical strength. Recently, derivatives of graphene have being of large interest because of the possibility to add new functionalities to graphene and tune its electronic properties [2]. Among these graphene-related materials, we can mention, for example, graphane, a two-dimensional hydrocarbon constituted by graphene fully-hydrogenated on both sides of the plane [3]. Modification of graphane by removing hydrogenation from one side results in a new structure termed graphone, another derivative of graphene. Density functional theory (DFT) calculations have estimated that graphone has a narrow band-gap of 0.5 eV and it is predicted to exhibit magnetic properties [4]. This features make graphone very interesting as light magnetic material to be considered for substitution of metals and rare earths. For example, if we suppose that graphone could be packed in a graphite-like structure, the T= 0 K saturation magnetization of graphone can be estimated to be 450 gauss, comparable to the saturation magnetization of nickel, equals to 510 gauss [5], but with one fourth of the weight. Recently, it has been found experimental evidence that highly hydrogenated graphene exhibits a weak ferromagnetism [6]. Graphone could be used as biocompatible magnetic material in biosensors or in carbon-based spintronics applications.

---

[*] Corresponding author. E-mail: `francesco.buonocore@enea.it`.

In the present report we investigate, with the support of density functional theory (DFT) calculations, the adhesion of graphone to copper, using an exchange-correlation functional corrected for long range interactions. We calculated the effects of the adsorption on magnetism in the resulting system.

2 Computational tools and procedure

2.1 Computational package

The computational approach was based on a pseudo-potential plane-wave method using PWSCF code as implemented in the QUANTUM-ESPRESSO package [7]. QUANTUM-ESPRESSO is an integrated suite of computer codes for electronic-structure calculations and materials modeling. It implements a variety of methods and algorithms aimed at a chemically realistic modeling of materials from the nanoscale upwards, based on the solution of the density-functional theory (DFT) [8] problem, using a plane waves (PWs) basis set and pseudopotentials (PPs) [9] to represent electron-ion interactions. The codes are constructed around the use of periodic boundary conditions, which allows for a straightforward treatment of infinite crystalline systems, and an efficient convergence to the thermodynamic limit for aperiodic but extended systems, such as liquids or amorphous materials. Quantum-ESPRESSO code runs on many different computer architectures and allows good scalability till a large number of processors depending on the system size. We use a Quantum-ESPRESSO code compiled with Intel Fortran compiler, Math Kernel Library (MKL) and Message Passing Interface (MPI) parallelization on the Cresco3 cluster of the high performance computer facility CRESCO [10], with a good scalability up to hundreds of cores.

2.2 Computational details

We used the generalized gradient approximation (GGA) with the Perdew, Burke and Ernzerhof (PBE) exchange-correlation functional [11] including the empirical correction of the long range forces (DFT-D) [12]. The pseudo-potential plane-wave calculations were performed using Vanderbilt ultra-soft pseudo-potentials [13]. The convergence of the total energy has been checked by varying cut-offs and grid of kpoints to reach a good compromise between accuracy and computational times. All geometry optimizations were performed with cut-off for the wave functions of 30 Ry, cut-off for the charge density of 300 Ry and 661 Monkhorst-Pack grid, allowing a convergence of the total energy below 0.01 Ry. The final self-consistent calculations of the optimized structure properties used a cut-off for the wave functions of 40 Ry, a cut-off for the charge density of 400 Ry and 10101 Monkhorst-Pack grid granting a convergence below 0.003 Ry. The Cu(111) surface was modelled by the repeated slab geometry which contains six Cu atomic layers with the in-plane 22 unit cell. The 22 cell of graphone can be matched properly to copper surface. The vacuum gap between graphone and slab periodic image was set to 20 Å.

3 Results and discussion

3.1 Isolated graphone

The lattice cell of isolated graphone has been fully optimized resulting in a lattice parameter a= $5.030\mathring{A}$. This parameter preserves a low stress on the cell also when the interface with Cu(111) slab is considered. Upon geometry optimization, carbon atoms are disposed into two distinct layers, where in one layer each carbon atom C_1 has three single bonds with carbon atoms and one single bond with hydrogen atom out of plane, while in the other layer each carbon atom C_2 has three single bonds with carbon atoms and one p-electron unpaired. The magnetic properties are due to the localized and unpaired electrons in the three-coordinated C_2 atoms. This is different from graphene, where π-electrons are delocalized, and from graphane, where the electrons are forming strong σ-bonds. We have found that the ferromagnetic (FM) state is the ground state with total magnetization of 4.00 μ_B. This FM state is 0.16 eV lower in energy than anti-ferromagnetic (AF) and 1.07 eV lower in energy than the non magnetic (NM) state. The FM and AF magnetic configurations of graphone are shown in Fig. 1. The magnetic properties of the investigated systems are resumed in Table 1.

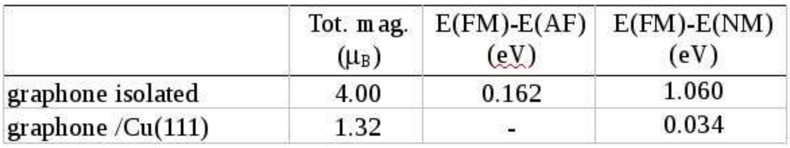

	Tot. mag. (μ_B)	E(FM)-E(AF) (eV)	E(FM)-E(NM) (eV)
graphone isolated	4.00	0.162	1.060
graphone /Cu(111)	1.32	-	0.034

Table 1: Total magnetization of FM state, E(FM)-E(AF) and E(FM)-E(NM) for isolated graphone and graphone adsorbed to Cu(111) surface.

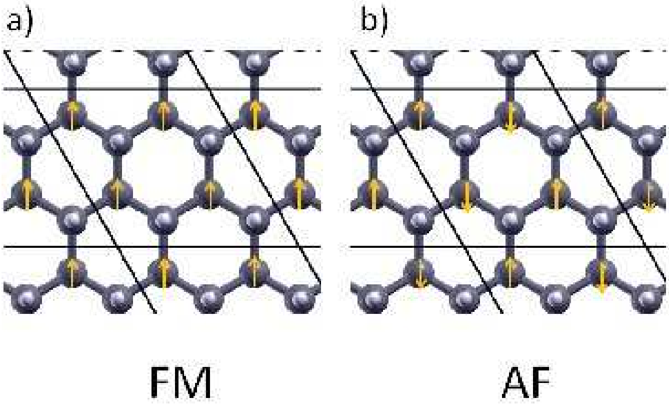

Figure 1: Magnetic configurations of graphone for a) ferromagnetic and b) antiferromagnetic states.

3.2 Graphone adsorbed to copper surface

Next we relaxed the geometric structures of graphone adsorbed to Cu(111) surface. In the most stable configuration, among the examined adsorption geometries, a C_2 atom is on the top of every first layer Cu, as shown in Fig 2, where the C_2-Cu distance of $2.05\mathring{A}$ is consistent with the formation of covalent bonds. This distance is far shorter than the calculated distance of graphene from the same surface, evaluated to be 2.95 . The total magnetization in the FM state is $1.32\mu_{\mathrm{B}}$, corresponding to a magnetism reduced by four times with respect to the isolated graphone, while the AF state of the isolated graphone is found to be not stable. Differently from the isolated graphone case, the geometrical structures of FM and NM states are similar. The FM state is still the ground state, but it lies just 34 meV lower in energy than the NM state. Therefore graphone magnetism is largely reduced by the interaction with copper substrate.

The charge density difference shows that electronic charge is depleted from the substrate and accumulated towards C_2 atoms: C_2 and Cu atoms can pair p- and d-electron, respectively, so that magnetism is partially quenched. However a residual magnetism is still localized, so we can infer that p-electrons are just partially paired.

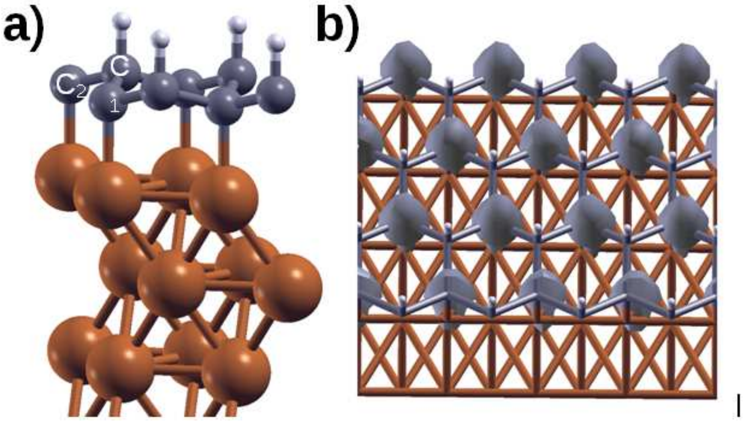

Figure 2: a) Atomistic model of graphone adsorbed to Cu(111) surface; b) spin density isosurface.

Our results demonstrate that there is electronic charge transfer from surface towards C_2 atoms for copper, but the main role in the partial magnetism quenching is played by bond formation and the consequent electron pairing of unpaired p-electrons of three-fold coordinated C atoms with electrons from surface. The AF state of graphone adsorbed to copper is no more stable and a quantitative estimation of T_c is not possible. The very low stability of the FM state let us suppose that graphones magnetism is suppressed at ordinary temperature when graphone is adsorbed to copper surface. However, graphone shows a very good adhesion to substrates with adhesion energy higher than graphene. The coating of selected materials by graphone could enable easy functionalization of surfaces by hydrogen substitution paving the way to several applications.

References

[1] K. S. Novoselov, A. K. Geim, S. V. Morozov, D. Jiang, Y. Zhang, S. V. Dubonos, I. V. Grigorieva, and A. A. Filrsov. Electric Field Effect in Atomically Thin Carbon Films. *Science*, 304:666, 2004.

[2] P. Qing, K. D. Albert, C. Jared, H. Liang, L. Sheng, W. Xiaodong, and D. Suvranu. New Materials Graphyne, Graphdiyne, Graphone, and Graphane: Review of Properties, Synthesis, and Application in Nanotechnology. *Nanotechnol. Sci. Appl.*, 7:1, 2014.

[3] J. O. Sofo, A. S. Chaudhari, and G. D. Barber. Graphane: a Two-Dimensional Hydrocarbon. *Phys. Rev. B*, 75:153401, 2007.

[4] J. Zhou, Q. Wang, Q. Sun, X. S. Chen, Y. Kawazoe, and P. Jena. Ferromagnetism in Semihydrogenated Graphene Sheet. *Nano Lett.*, 9:3867, 2009.

[5] G. Grosso and G. P. Parravicini. Solid State Physics Second Edition. *Academic Press*, 2014.

[6] A. Y. S. Eng, H. L. Poh, F. anek, M. Maryko, S. Matejková, and Z. Sofer. Searching for Magnetism in Hydrogenated Graphene: Using Highly Hydrogenated Graphene Prepared via Birch Reduction of Graphite Oxides. *ACS Nano*, 7:5930, 2013.

[7] Quantum-ESPRESSO. *http://www.quantum-espresso.org.*

[8] R. G. Parr and W. Yang. Density Functional Theory of Atoms and Molecules. *Oxford University Press*, 1989.

[9] W. E. Pickett. . *Computer Physics Reports*, 9:15, 1989.

[10] see http://www.cresco.enea.it for more information. .

[11] J. P. Perdew, K. Burke, and M. Ernzerhof. Generalized Gradient Approximation Made Simple. *Phys. Rev. Lett.*, 77:3685, 1996.

[12] S. Grimme. Soft Self-Consistent Pseudopotentials in a Generalized Eigenvalue Formalism. *Phys. Rev. B*, 41:7892, 1990.

[13] D. Vanderbilt. Soft Self-Consistent Pseudopotentials in a Generalized Eigenvalue Formalism. *Phys. Rev. B*, 41:7892, 1990.

First-principle calculations of structural, electronic and optical properties of surfaces, monolayers and thin films

O. Pulci[1]*, *M. Marsili*[2], *P. Gori*[3], *C. Violante*[1], *A. Mosca Conte*[1] and *I. Kupchak*[1,4]

[1]*ETSF, Dept. of Physics University of Rome Tor Vergata, Roma, Italy*

[2]*Centro S3, Istituto Nanoscience (NANO) -*
CNR, via Campi 213/a, I-41125, Modena, Italy

[3]*Universitá Roma Tre, Dipartimento di Ingegneria*
Via della Vasca Navale 79, 00146 Roma, Italy

[4]*V. Lashkarev Institute of Semiconductor Physics of*
National Academy of Sciences of Ukraine, Kiev, Ukraine

Abstract. We briefly review the part of the research work carried out in 2014 by the members of our groups that made use of the ENEA-CRESCO facility. Most of the studies concern the calculation of structural, electronic and optical properties of materials, focusing especially on 2D materials such as surfaces, monolayers and thin films.

1 Methods and Codes

All the studies presented below are based on the determination of the ground state (geometry, total energy, single-particle Kohn-Sham orbitals, etc...) of the material through density-functional theory (DFT) [4, 5]. We employed the electronic structure code *pw.x* of the Quantum Espresso suite [2] which makes use of plane-wave basis set and pseudopotentials [15]. The excited state properties are determined employing either time-dependent DFT (TD-DFT) [13, 3] and many-body perturbation theory (MBPT) [8].
The codes that were used for the determination of excited state properties, are: the *DP* code (http://dp-code.org/), the *CHISIG* plane-wave GW code, and the *Yambo* suite [7]. Some of the authors developed parts of these codes. Besides *CHISIG*, all the codes that we used are open source codes released under the GPL licence. All the employed codes make use of *LAPACK* and *BLAS* libraries, and present a hybrid MPI and OpenMP parallelism. The Yambo code makes also use of the *NETCDF* libraries which were installed locally by

---

[*] Corresponding author. E-mail: `olivia.pulci@roma2.infn.it`.

some of us. Jobs were run mainly on the Cresco-4 and Cresco-3 clusters using between 64 and 256 cores.

2 Results

2.1 Formation of massive 1D nanostructure at the Ag(110) surface induced by silicon

The Si/Ag(110) interface attracted interest in recent years as a consequence of the claim that the one-dimensional (1D) nanostructures formed at this surface would be silicene nanoribbons [10]. We performed DFT study of the 1D nanostructures forming on Ag(110) upon Si deposition at temperatures above 460 K to complement scanning tunneling microscopy and low-energy electron diffraction measurements. Two different kinds of nanostructures are detected: nanodikes and nanotrenches, massive 1D nanostructures respectively protruding from and engraved on the Ag(110) substrate. The first kind of structure was reported to be constituted by multistacks of silicene nanoribbons [9]. We showed that nanodikes and nanotrenches are the result of silver faceting stabilized by silicon atoms. Indeed, such nanostructures share the very same facet crystallographic features, namely inclination and reconstruction: the top and base parts are Ag(110) planes, while their sides are Ag(221) and Ag(22$\bar{1}$) facets stabilized by Si atoms. Density functional theory calculations suggest that Si atoms may reduce the system energy by partially substituting Ag atoms in such facets (see Fig. 1). The combination of theoretical and experimental results demonstrates that the description of nanodikes as multistacks of silicene has to be reconsidered and that the Ag(110) surface is not inert toward silicon when the sample temperature is higher than 460 K, resulting in surface faceting.

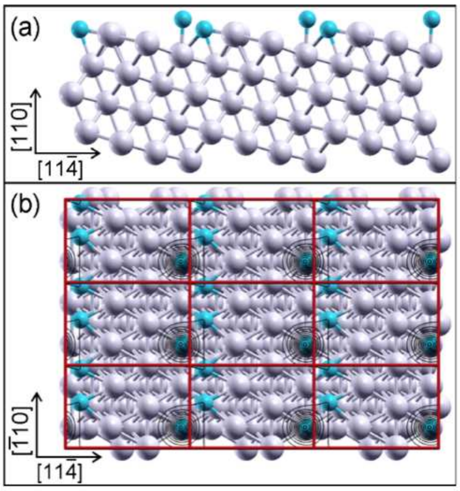

Figure 1: Geometry of the minimum-energy structure of Si/Ag(221) with 3 Si atoms per 12 surface cell; (a) side view and (b) top view. A constant-density simulated STM image (V=-1.0 V) is superimposed as contour plot on the top-view model in (b).

2.2 Chiral properties of a nonchirally oriented phase of tartaric acid on Cu(110)

The chiral properties of a nonchirally oriented phase of tartaric acid deposited on a Cu(110) surface have been studied by means of circularly polarized radiation and ab-initio calculations. The two optical enantiomers R,R and S,S of tartaric acid, separately deposited, produce (40,23) overlayers which show a large dichroic effect and enantiomeric behavior all over the valence energies. The dichroic effects are displayed by native chiral molecular states and molecule-copper interface states. Density-functional theory calculations have been employed to create a model of the adsorption geometry in the (40,23) phase and for determining the site-resolved density of states. This shows the formation of hybrid states at the tartaric acid-copper interface. In particular, the interface state at -1.7 eV (corresponding to -1.25 eV in the theoretical scale, see Fig. 2) in the valence band photoemission spectrum can be attributed to the local chiral electronic interaction between tartaric acid and the bonded Cu atom underneath the molecule, providing a spectroscopic indication of chirality transfer. The circular dichroism effect in the angular distribution of photoelectrons helps to interpret the electronic structure, to disentangle chiral states, and can find application in the analysis of organic molecules on metal surfaces and surface chirality in general.

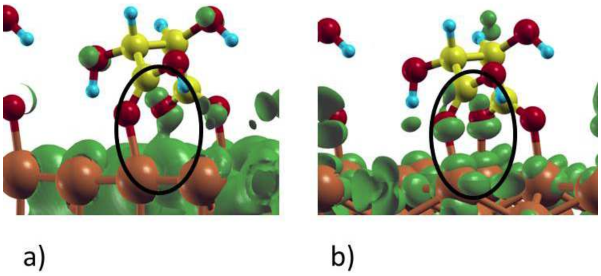

Figure 2: Squared wave functions for the TA/Cu(110) system calculated at the Γ point for the eigenvalues (a) 2.90 eV and (b) 1.25 eV. In orange the Cu atoms, in yellow the C atoms, in red the O atoms and in cyan the H atoms. Isodensity levels: (a) 5.4 · 105 e/Å^3; (b) 8.1 · 104 e/Å^3

2.3 Optical properties of 2D honeycomb crystals

We computed the optical conductivity of 2D honeycomb crystals beyond the usual Dirac-cone approximation. The calculations were mainly based on the independent-quasiparticle approximation of the complex dielectric function for optical interband transitions, and the full band structures were taken into account. In the case of silicene, we studied the influence of excitonic effects using time-dependent DFT (TDDFT) including a non-local, energy-independent XC kernel $\frac{-\alpha}{q^2}$ with $\alpha = 0.2$ (red line) [11]. As shown in Fig. 3 excitonic effects are almost neglegible whereas the inclusion of local fields effects changes significantly the absorbance. Special care was taken to derive converged spectra with respect to the number of k points in the Brillouin zone and the number of bands. In this way both the real and imaginary parts of the optical conductivity were correctly described for small and large frequencies. The results are applied to predict the optical properties reflection, transmission and absorption in a wide range of photon energies. They are discussed in the light of the available experimental data.

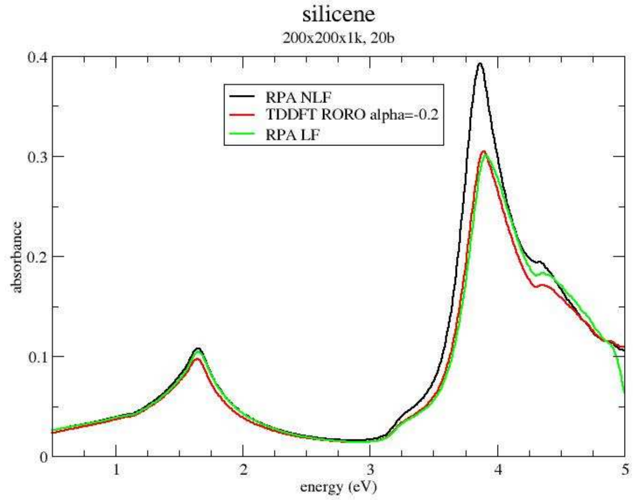

Figure 3: Optical absorption of silicene with (red solid line) and without (black solid line) excitonic effects. Results of an independent-particle approximation using DFT-LDA (black line) are compared with those of the TDDFT. The influence of optical local-field effects is illustrated by the green line.

2.4 Effect of crystal packing on the electronic properties of H_2OEP

Porphyrins are an extremely important class of molecules as they are involved in a variety of fundamental biological processes and they can be easily functionalized by changing their central metal atoms and functional groups. Porphyrin thin films are moreover important as fundamental constituents of biosensors and optoelectronic devices. We studied the effect of crystal packing on the electronic properties of the free-base H_2OEP molecule. H_2OEP crystallizes in a triclinic lattice with one molecule per unit cell. We used the experimental lattice structure [6] as our calculations do not include van der Waals corrections. As shown in Fig. 4 we found that at the DFT and Hartree-Fock level crystal packing doesn't affect significantly the magnitude of the HOMO-LUMO gap of this system. On the contrary, by including quasi-particle corrections (at the G_0W_0 level), the electronic gap of the crystal system is 45% smaller than the HOMO-LUMO gap of the isolated molecule. The results were compared with experimental direct and inverse photoemission data showing a good agreement.

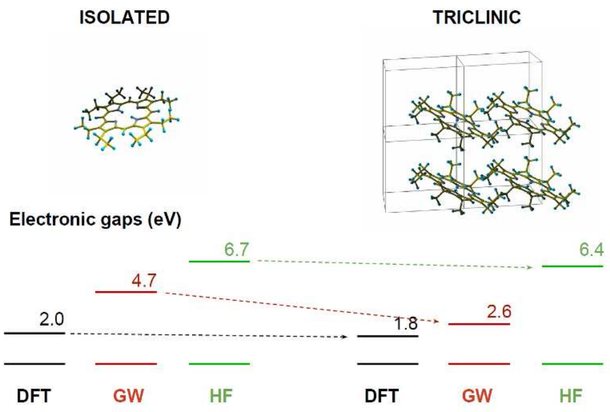

Figure 4: Top: structure of the isolated H_2OEP molecule (left) and triclinic crystal (right). Bottom: electronic gap of the isolated H_2OEP molecule (left) and triclinic crystal (right) at the DFT (black), GW (red) and Hartree-Fock (green) level).

2.5 Optical properties of MoS_2: optimal convergence parameters in view of real-time calculations

Transition-metal dichalcogenide monolayers are a subject of intensive study as semiconducting analogues of graphene. Among them, MoS_2 is probably the best characterized material both experimentally and theoretically. The theoretical, first principle, determination of the excited state properties of this material is challenging due to the interplay of strong many-body effects, spin-orbit coupling, and the need of including Mo semicore states explicitly in the calculation. Of great interest, in view of its application in optoelectronic devices, is the study of the relaxation of excited carriers. This can be achieved in a full ab-initio framework within a recently developed time-domain approach that combines density-functional and non-equilibrium Green's function theories [14] and that was implemented in the Yambo suite [7]. The starting point of the real-time domain calculations is the determination of the equilibrium excited state properties within the standard GW-BSE approach [8]. Being the real-time domain calculations extremely demanding, the standard convergence parameters (plane-wave expansion cutoff, number of unoccupied states, k-point sampling, vacuum depth etc...) need to be optimized in order to reconcile computational accuracy and feasibility. In Fig. 5 we show part of our convergency studies. One of the computational bottleneck of the quasi-particle correction calculations is the number of unoccupied states that are included in the G term of the self-energy $\Sigma = iGW$ [8]. In the left panel of Fig. 5 the quasi-particle correction to the electronic gap is reported as a function of the inverse of the number of bands included in the calculation of the G term. The empty-bands-summation termination scheme proposed in Ref. [1], was also employed and the dependence of the results on the additional pole position [1] was studied. We see that the fastest convergence is obtained employing the termination scheme with a pole located at 80 Ry. In the central panel of 5 the expectation value of the correlation part of the electronic self-energy is shown as a function of the number of k-points sampling the Brillouin zone (BZ): we achieve a reasonable convergence with a 24×24×1 sampling of the irreducible BZ. The left panel shows the dependence of the absorption spectrum on the distance (d_{vacuum}) between two periodic replicas of the system. We see that, since the Coulomb interaction is truncated in the direction perpendicular to the atomic plane [12], the spectra obtained employing 13 Åand 22 Åshow negligible differences.

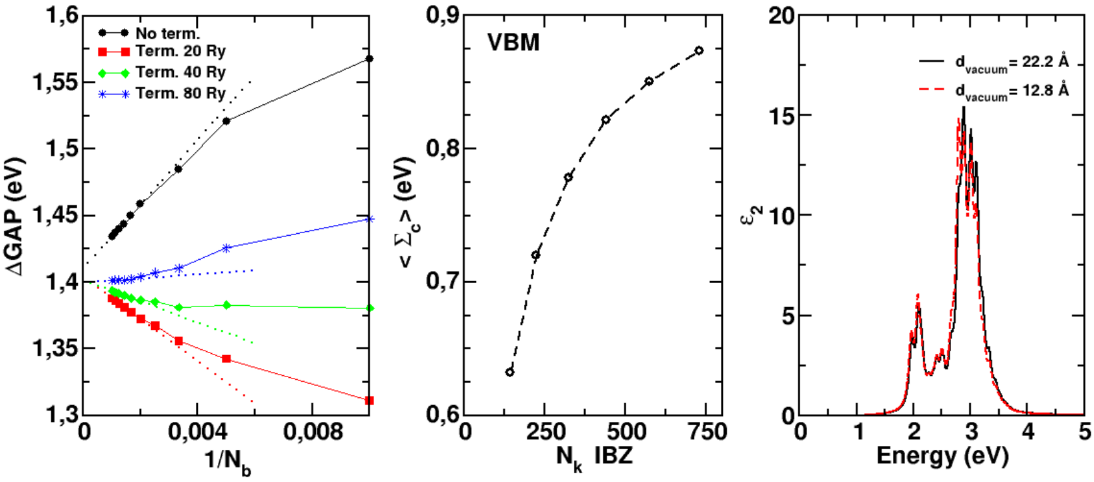

Figure 5: Left panel: quasi-particle correction to the electronic gap vs inverse of the number of empty bands employed in the calculation of G. Black: no termination scheme; red: termination scheme with pole at 20 Ry; green: termination scheme with pole at 40 Ry; blue: termination scheme with pole at 80 Ry. Center panel: expectation value of the correlation part of the electronic self-energy as a function of the number of k-points sampling the Brillouin zone. Right panel: absorption spectrum. Black: 22.2 Ådistance between two periodic replicas; dashed-red: 12.8 Ådistance between two periodic replicas.

References

[1] F. Bruneval and X. Gonze. *Phys. Rev. B*, 78:085125, 2008.

[2] P. Giannozzi et al. *J. Phys.: Condens. Matter.*, 21:395502, 2009.

[3] E. K. U. Gross and W. Kohn. *Phys. Rev. Lett*, 55:2850, 1985.

[4] P. Hohenberg and W. Kohn. *Phys. Rev.*, 136:B864, 1964.

[5] W. Kohn and L.J. Sham. *Phys. Rev.*, 140:A1133, 1965.

[6] J. W. Lauher and J. A. Ibers. *J. Am. Chem. Soc.*, 95:5148, 1973.

[7] A. Marini, C. Hogan, M. Grüning, and D. Varsano. *Comput. Phys. Commun.*, 180:1392, 2009.

[8] G. Onida, L. Reining, and A. Rubio. *Rev. Mod. Phys.*, 74:601, 2002.

[9] P. De Padova, O.Kubo, B. Olivieri, C. Quaresima, T. Nakayama, M. Aono, and G. Le Lay. *Nano Lett.*, 12:5500, 2012.

[10] P. De Padova, C. Quaresima, C. Ottaviani, P. M. Sheverdyaeva, P. Moras, C. Carbone, D. Topwal, B. Olivieri, A. Kara, H. Oughaddou, B. Aufray, and G. Le Lay. *Appl. Phys. Lett.*, 96:261905, 2010.

[11] L. Reining, V. Olevano, A. Rubio, and G. Onida. *Phys. Rev. Lett.*, 88:066404, 2002.

[12] C.A. Rozzi, D. Varsano, A. Marini, E.K.U Gross, and A. Rubio. *Phys. Rev. B*, 73:205119, 2006.

[13] E. Runge and E. K. U. Gross. *Phys. Rev. Lett*, 52:997, 1984.

[14] D. Sangalli and A. Marini. *Europhys. Lett.*, 110:47004, 2015.

[15] N. Troullier and J.L. Martins. *Phys. Rev. B*, 43:1993, 1991.

Development of Monte Carlo Radiation Transport Modelling, Application to PWR Severe Accident Scenario, Implementation of MCNP with MPI on Various CRESCO Sections

K.W. Burn[1]* *and P. Console Camprini*[2]

[1]*ENEA-FSN-SICNUC-PSSN, Via M.M. Sole, 4, 40129 Bologna, Italy*

[2]*ENEA-FSN-ING-PAN, Via M.M. Sole, 4, 40129 Bologna, Italy*

Abstract. A short account is given of the running of state-of-the-art Monte Carlo codes for modelling radiation transport (including substantial in-house modifications) on the various CRESCO Sections. The activity is carried out in collaboration with the *Institut de Radioprotection et de Sûreté Nucléaire*, France in the context of the safety of current and GEN-III+ PWR's.

1 Introduction

Following on from the publication of a full length paper describing a new approach to calculating responses in eigenvalue calculations that employ the source-iteration approach [1], a summary paper was presented to PHYSOR-2014 [2]. This work is directed at the calculation of:

a) spatially limited radiation responses inside the core of nuclear reactors;

b) any radiation response outside the core of nuclear reactors;

c) spatially limited radiation responses in or around storage facilities for spent nuclear fuel.

The test cases described in [1, 2] included problems in categories a) and b), especially linked to large, GEN-III+ thermal power reactors. Problems of type a) represent calculations that with analog Monte Carlo are difficult or impossible to treat. The approach suggested in [1, 2] extends the range of problems that are treatable. Problems of type b) are currently treated by decoupling the calculation (usually using the fission sites at the point of decoupling). The approach in [1, 2] avoids the necessity of decoupling. Problems of type c) which typically might be required in spent fuel repositories, have not yet been treated with the new approach.

---

*Corresponding author. E-mail: `kburn@enea.it`.

2 Support to IRSN on DISCOMS Project: Monitoring Position of Corium following Perforation of Pressure Vessel

The objective of this work has already been described in previous CRESCO reports [3, 4] and will not be repeated here. The *classic* decoupled approach was adopted and it was convenient to generate separate variance reduction ("VR") parameters for the neutron calculation and for the coupled neutron-γ calculation. For this, the in-house VR algorithm for fixed source problems was employed [5]. This problem represents a moderate penetration from the VR point of view and the responses at the point of highest attenuation (under the ZrO_2 insulator layer that lies below the sacrificial concrete at the bottom of the pressure vessel well) could be calculated with an acceptable statistical uncertainty. An axial plot of a sample of the particle collisions for the second, fixed source, part of the decoupled calculation employing VR is shown in Fig. 1. Currently underway is a comparison of this classic approach with the approach with the new algorithm that does not require decoupling the calculation. As discussed in the references, an important aspect of the new algorithm is the necessity to maintain the fundamental mode between (batches of) fission generations whilst at the same time forcing the tracks to one of more, in- or ex-core local detectors. Fig. 2 shows two plots of fission sites in a PWR core with, on the left, analogue sampling and on the right, VR directed at an ex-core local detector in the East direction. This work will be more fully reported in the future.

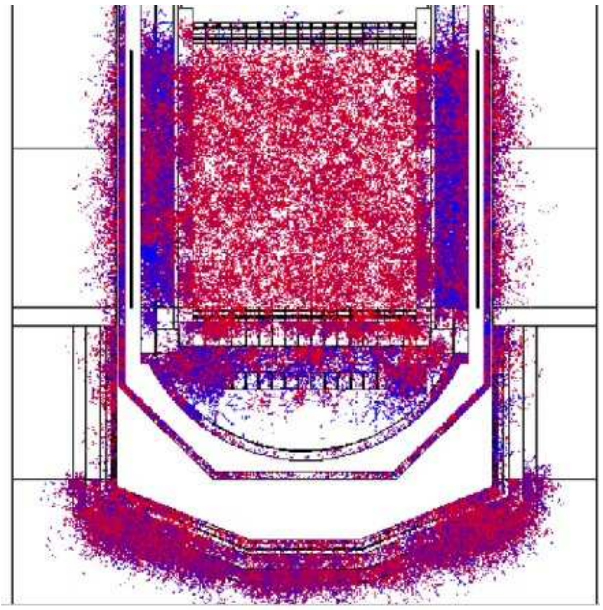

Figure 1: Sample of particle collisions in vertical section of PWR with fission source and variance reduction

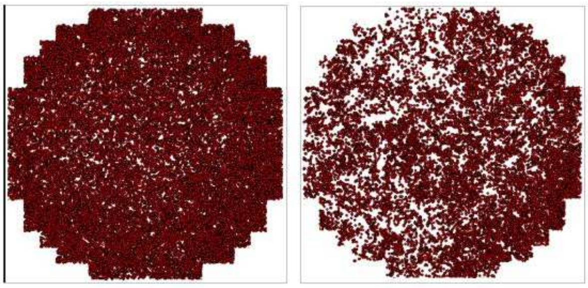

Figure 2: Fission sites in PWR core with (left) analogue sampling and (right) variance reduction directed at an ex-core local detector in the East direction

3 Hardware and Software employed in these activities

As far as software is concerned, as noted in previous CRESCO reports, a patched version of MCNP5 (ver. 1.4) was employed, together with a separate stand-alone code built around the IMSL version 1.0 library. Patches (i.e. local code modifications) were required both for the classic decoupled approach as well as for the new approach.

The patched MCNP versions were run in parallel mode on the Portici CRESCO Section 2 machines. Typically 16 nodes were employed (1 master and 15 slaves). Here it should be mentioned that more than 16 nodes resulted in a degradation in the performance (due possibly to the large amount of data involved in the message passing). Furthermore presumably due to the large memory requested for some calculations, machines of the type cresco-fpga had to be excluded from the candidate machines for the job.

The stand-alone code built around IMSL was run in scalar mode on individual machines of the Frascati CRESCO Cluster.

4 Building MCNP Versions with MPI on various CRESCO Sections

The MCNP source code is employed, rather than the executable program which is part of the distribution package (with various versions to run on different platforms), for the following reasons:

- for nearly all applications, the code must be patched (source description; innovative in-house variance reduction; extra diagnostics; . . .);
- to correct bugs that are reported on the MCNP forum;
- when the manual is not clear, to understand from the FORTRAN source code what the code is actually doing (sometimes with the aid of write statements).

Therefore all the MCNP versions employed in innovative reactor developments need to be compiled from the source code and linked with the MPI modules employed by the particular cluster.

4.1 MCNP version 5

Some time ago MCNP version 5-1.3 was built with MPI on CRESCO Sections 1 and 2. Subsequently MCNP version 5-1.4, which is the current work horse, was built on CRESCO Section 2 employing the same logic. Recently the same logic was again employed to build MCNP version 5-1.4 with MPI on CRESCO section 4. The script to run the job under LSF was based on that in the CRESCO Section 4 documentation: http://www.afs.enea.it/project/eneagrid/Resources/CRESCO_documents/index.html

The standard MCNP test problem suite was not run because the version employed a source patch. However for two long runs, identical results were obtained on CRESCO Section 4 compared with those with the version running on CRESCO Section 2.

4.2 MCNP version 6

Late in 2014 first steps were taken to build MCNP version 6.1 with MPI on CRESCO Sections 3 and 4. The standard unpatched code was built so that the test problem suite could be run and verified, providing some quality control on the built code. On both Sections 3 and 4 a completely different approach was made compared with that employed to build MCNP on CRESCO Section 2. Indications that helped to define the new approach were obtained from postings to the MCNP forum and on the MCNP web site.

On CRESCO Section 4, the default Intel Fortran 90 compiler is: Intel ifort 14.0.1. Employing this compiler produced numerous warnings in the compilation phase. (On the MCNP web site https://laws.lanl.gov/vhosts/mcnp.lanl.gov/mcnp_faq.shtml, although this particular version is not mentioned, other 14 series compilers fail.) The basic tests in the REGRESSION sub-directory were run on typically 12 nodes (1 master and 11 slaves) of CRESCO Section 4 in background but without employing LSF (which did not prove possible in the time available). For many of the sample problems, differences with the distributed output files were obtained. In particular a number of the difm files (differences in the mctal outputs between the local implementation and the standard files distributed with MCNP) were not empty. Although the differences remain to be properly examined, the current situation is that the implementation of MCNP 6.1 on CRESCO Section 4 has failed the quality control.

On CRESCO Section 3, the default Intel Fortran 90 compiler is: Intel ifort 12.1.3. On the MCNP web site, although this particular version is not mentioned, other 12 series compilers successfully compile MCNP. Employing this compiler produced no warnings in the compilation phase. As on CRESCO Section 4, the basic tests in the REGRESSION sub-directory were run on typically 12 nodes (1 master and 11 slaves) of CRESCO Section 3 in background without LSF. Most difx files resulted empty. In particular all difm, dife and difg files were empty. Some difo (comparing the standard output file outp) files were not empty and should be properly examined. Although this work is not finished, there are indications that some level of quality control should be able to be assigned to the implementation of MCNP 6.1 on CRESCO Section 3.

Acknowledgement

S. Podda built MCNP version 5-1.3 with MPI on CRESCO Sections 1 and 2.

References

[1] K. W. Burn. Optimizing Variance Reduction in Monte Carlo Eigenvalue Calculations that Employ the Source Iteration Approach. *Ann. Nucl. Energy*, 73:218–240, 2014.

[2] K. W. Burn. Estimating Local In- and Ex-Core Responses within Monte Carlo Source Iteration Eigenvalue Calculations. *Proc. of PHYSOR-2014, Kyoto, Japan*, JAEA-Conf 2014-003, Sept. 2014.

[3] K. W. Burn. Use of Monte Carlo to Evaluate Signal and Radiation Damage to Corium Detector in PWR Severe Accident Scenario. *CRESCO Annual Report*, pages 179–182, 2013.

[4] K. W. Burn. Use of Monte Carlo in State-of-the-Art PWR Design: Continuing Analysis of the Impact of the Heavy Reflector of a Typical Large Size GEN III+ Reactor Designon some Safety Featurse: Completion of the Ex-Core Detector Calculations and Examination of the Impact on Flux Tilt. Development and Testing of New Algorithms within Monte Carlo Eigenvalue Calculations employing the Source-Iteration Method. *CRESCO Annual Report*, pages 173–178, 2012.

[5] K. W. Burn. Optimizing Monte Carlo to Multiple Responses: the Direct Statistical Approach, 10 Years On. *Nucl. Technol.*, 175:138–145, 2011.

H-Abstraction from Methane in H-ZSM5 Zeolite with extra-framework O atom: DFT and D-DFT in comparison

Amedeo Palma[1]* *and Silvano Tosti*[2]

[1]*CNR-ISMN, Istituto per lo Studio dei Materiali Nanostrutturati,*
Via Salaria km 29.3, UOS Montelibretti, Monterotondo S. (RM), Italy

[2]*ENEA Unità Tecnica Fusione, C.R. ENEA Frascati,*
Via E. Fermi 45, Frascati (RM) I-00044, Italy

Abstract. The interaction of methane with an extra-framework oxygen atom in acidic Zeolite (H-ZSM5) porous substrate has been investigated by means of Density Functional Theory plus Dispersion energy calculations and reaction path has been obtained exploiting Climbing Image Nudged Elastic Band method (c-NEB). Zeolite was modelled by its crystallographic structure subject to periodic boundary condition. The reaction path for the H - abstraction reaction of methane, in presence of an open shell oxygen atom within zeolite along the (010) straight channel, leads to the formation of a slightly distorted H_2O water molecule and CH_3 radical and proceeds with a small barrier. When dispersion energy is applied the barrier disappears revealing known flaws of the approach adopted. These in bulk calculations support anyway the interesting idea that open shell systems, involving an extra cage Oxygen atom, favour the H-abstraction from small hydrocarbons within acidic zeolite channels.

1 Introduction

In the last twenty years zeolites have attracted increasing interest for their potential application in the industrial field because they act as chemical catalysts [1]. For the fact that channels and cages have dimensions similar to those of small molecules, zeolite are shape selective and many reaction occurs in a specific Brnsted acidic site. Methane represents the major constituent of natural gas and its large reserve could serve as a feedstock for the production of chemicals and a source of energy for the next future [2].

Activation of a C-H bond represents the first step for methane conversion, but methane is a very stable molecule, being the C-H strength of nearly 101.6 kcal/mol. Methane activation on metallic surface ranges from tens to hundreds of kcal/mol [3], therefore a possible alternative could be represented by zeolites for their high selectivity. In Ref. [4] using mostly small models for H-ZSM5 zeolite and an embedded approach, authors found

---

[*] Corresponding author. E-mail: `amedeo.palma@ismn.cnr.it`.

that the triplet oxygen species can lead easily to the abstraction of H atom from CH_4 with an estimated activation barrier of 7.12 kcal/mol: small in comparison with that found for the same type of reaction in other types of zeolite, such as for example Fe/ZSM5, where the activation barrier is in the tens of kcal/mol.

In a recent review [5] about H atom transfer from methane, the crucial role of unpaired spin density at the abstracting atom in many metal oxide clusters in gas phase was clarified by computational and experimental studies. Standard Density Functional Theory (DFT) has been often used to describe behaviour of molecules on surfaces or metals within organic materials [6]. We showed that Density Functional Theory plus Dispersion (D-DFT) calculations are necessary to properly describe the energetics of the interaction between a molecule (such as methane) and the zeolite [7].

In this paper, we present first principles calculations for the interaction of methane molecule with an extra-framework O atom bound to the acidic site of a zeolite H-ZSM5 by considering triplet spin state for the composite system with the aim to assess the dispersion energy effects on the activation barrier.

2 Computational Details and Results

H-ZSM5 zeolite is modelled by ZSM5 crystallographic structure [8], in which the silicon atom in the T6 site has been replaced by aluminium obtaining a T_6OT_9 Brønsted acidic site that will be the active site considered in the study of reaction mechanism. All the calculations were performed with Quantum Espresso [9] and open shell systems are treated within the unrestricted formalism. Further details can be found in reference [7].

Dispersion forces are evaluated according to one of the most successful scheme proposed in materials science [10]. This computational approach was able to reproduce [7] silicalite crystallographic structure with a RMSD of 0.21Å and has shown that the inclusion of dispersion energy contribution results essential for a correct description of the energetic balance.

The zeolite crystal model considered in the calculations is the crystallographic unit cell containing 289 atoms (Al, H, $Si_{95}O_{192}$). Therefore the sample has a total of 1550 valence electrons and it is subject to Periodic Boundary Conditions (PBC). In this structure we have inserted an extra-framework oxygen atom and we consider the complete system in the triplet and in the singlet excited state. We have then optimized the corresponding local structures in which oxygen atom is bound to the acidic site of the zeolites in the (010) direction of the 10 Membered Ring (10MR) straight channel. Figure 1 presents the triplet system [O-H-ZSM5]T, optimized without any constraint, and a methane molecule: this represents asymptotic reactants. Considering that carbon atom is methane center of mass, we performed several series of calculations at different fixed C-O distances following a straight line, inside the 10MR channel. The reaction path was subsequently determined more accurately by c-NEB method. Relaxation of all the atoms produces an energy stabilization, almost a homogeneous rigid shift, in H-Zeo and $[O\text{-}H\text{-}Zeo]^T$ systems of 17.47 kcal/mol, 16.69 kcal/mol, respectively. The adsorption energy, in the case in which all atoms of the cell are relaxed, is of 17.54 kcal/mol. In triplet spin electronic state of [O-

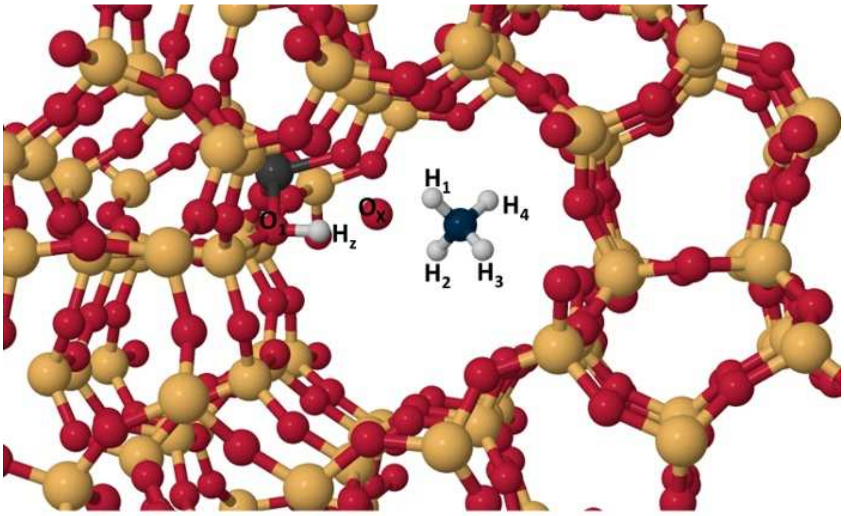

Figure 1: Fully relaxed [O-H-ZSM5]^{T} system subject to periodic boundary conditions, view along the (010) direction of the straight channel with O atom bound to acidic Hydrogen where a Methane molecule has been inserted to model reactants. (O atoms: red balls, Al atom: dark grey, Si atoms: dark yellow, H atom: light grey, C atom: dark blue).

-H–Zeo]^{T} system the extra-cage O_x atom is strongly involved in the interaction and its spin polarization equal to 1.68, an evidence of the fact that the two unpaired electrons are prevalently located on this atom. We optimized also methane molecule, with the same computational procedure, obtaining a structure in good agreement with experimental data (error less than 1%) and a total energy of 16.14 Ry. This structure represents the reactants structure in the initial position since the carbon atom is about 5.6Å far away from OX atom for the triplet system. The energy profile, shown in Figure 2, is relative to methane molecule migration along the 10MR channel. At a C-O_X distance of about 3.0Å, hydrogen atom H_z breaks its bond with oxygen atom O_1 and in a concerted manner binds to O_X atom forming the hydroxyl which reacts with H_1 hydrogen atom of methane giving as products a water-like molecule and CH_3 radical.

Indeed in this water-like structure we observe that the bonds are elongated (O_X-H_z=1.05Å, O_X-H_1=1.03Å) and the bonding angle H_z-O_X-H_1 is equal to 106.44° respect to 104.5° of H_2O.

3 Conclusions

We have used DFT approach to study the interaction between methane and acidic zeolite (H-ZMS5) in its unitary cell subject to PBCs. The reaction between methane and spin unpaired [O-H-Zeo]^{T} yields a CH_3 radical, which has a planar structure typical of Carbon sp^2 hybridization, and a slightly asymmetric water molecule. Both products remain, after complete relaxation, within the (010) straight channel. The oxygen atom (O_a) of the pristine zeolite framework, where some of the spin density is still located, interacts with Hz

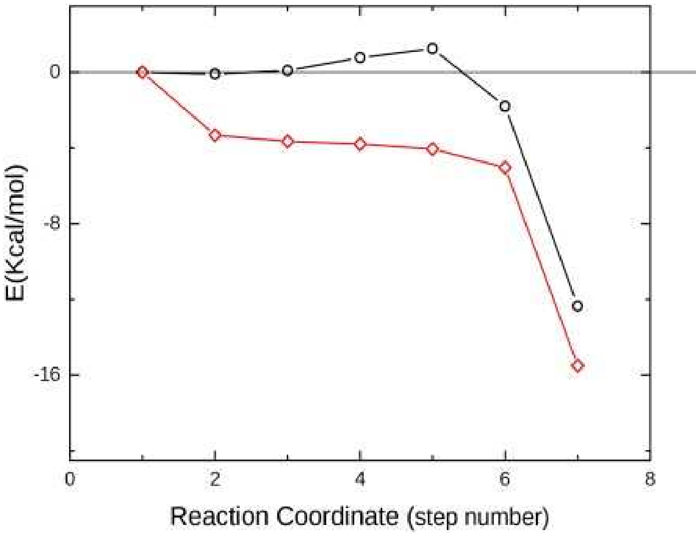

Figure 2: NEB energy profile with (red diamonds) and without (black circles) dispersion energy correction. Values reported in reaction coordinate of the two paths do not represent exactly the same C- O distances, in fact ordering numbers of NEB Images are reported. Path length is about 5.6Å.

atom stretching one of the two O-H bonds of the distorted, newly formed water molecule. The minimum energy reaction path has been determined by c-NEB method obtaining path as a function of C-O_X distance with a small barrier reaction (1.5 kcal/mol). This barrier disappears when semiempirical dispersion energy correction, based on GGA, is added, confirming that D-DFT approach underestimates the activation barrier. The oxidant role of the extra-framework open shell oxygen atom in H-abstraction reaction from methane is anyway evident since reaction occurs with a small barrier inside the 10MR channel along the (010) direction of zeolite.

References

[1] B. Smit and T. L. M. Maesen. Towards a molecular understanding of shape selectivity. *Nature*, 451:671–678, 2008.

[2] J. H. Lunsford. Catalytic conversion of methane to more useful chemicals and fuels: a challenge for the 21st century. *Catalysis Today*, 63:165–174, 2000.

[3] I. M. Ciobîcă, F. Frechard, R. A. van Santen, A. W. Kleyn, and J. Hafner. A DFT study of transition states for C-H activation on the Ru(0001) surface. *J. Phys. Chem. B*, 104:3364–3369, 2000.

[4] G. Yang, J. Guan, L. Zhou, X. Liu, X. Han, and X. Bao. First-principle studies on the exceptionally active triplet oxygen species in microporous zeolite materials: Reservation and catalysis. . *Photoch. Photobio A*, 202:122–127, 2009.

[5] N. Dietl, M. Schlangen, and H. Schwarz. Thermal hydrogen-atom transfer from methane: the role of radicals and spin states in oxo-cluster chemistry. *Angew. Chem. Int. Ed.*, 51:5544–5555, 2012.

[6] C. Zazza, N. Sanna, and A. Palma. In Silico Characterization of a Fourfold Magnesium Organometallic Compound in PTCDA Thin Films. *J. Phys. Chem A*, 113:14813–14817, 2008.

[7] C. Zazza, N. Sanna, M. Rutigliano, M. Cacciatore, and A. Palma. Dispersion energy effects on methane interaction within zeolite straight micropores: A computational investigation. *Comput. and Theor. Chem.*, 967:191–198, 2011.

[8] MFI Topology file, taken from the International Zeolite Association (IZA) structure database . *(http://www.iza-online.org/)*.

[9] P Giannozzi et al. QUANTUM ESPRESSO: a modular and open-source software project for quantum simulations of materials. *J. Phys.: Condens.Matter*, 21:395502, 2009.

[10] S. Grimme. Semiempirical GGA-Type Density Functional Constructed with a Long-Range Dispersion Correction. *J. Comp. Chem.*, 27:1787–1799 and reference cited therein, 2006.

On the applicability of the Ritz–Galerkin method to the Fokker–Planck equation of voter models over community–based networks

Filippo Palombi[1]* *and Simona Toti*[2]

[1]*ENEA Frascati Research Center, UTICT–HPC*
Via E. Fermi 45, 00044 – Frascati, Italy

[2]*Italian National Institute of Statistics*
Via C. Balbo 16, 00184 – Rome, Italy

Abstract. We discuss the applicability of the Ritz–Galerkin method to the stationary Fokker–Planck equation governing the multi–state voter model over community–based networks in presence of zealot candidates and show how the symmetries of the system allow to reduce the multi–clique structure of the Fokker–Planck operator in a weak sense.

1 Multi–state voter model, candidates and cliques

In our recent work we examined the stochastic dynamics of the multi–state voter model over a network based on interacting cliques and zealot candidates [1]. The aim of our research was to investigate the distribution of the excess of votes assigned to candidates in proportional elections with open lists with respect to the average of all competitors from the same party list, in the framework of voter models over heterogeneous networks. Phenomenological motivations stemmed from universality properties observed in the empirical distributions of the excess of votes, see refs. [2, 3] for a complete account.

Let us shortly review the set–up. Consider a clique–based network, represented by a graph $G = (V, E)$ such as depicted in Fig. 1. Each node of the graph belongs to one of Q non–overlapping cliques (all having equal size $\omega_1 = |V|/Q$); it is connected with certainty to any other node in its own clique and with finite probability p to nodes belonging to other cliques, apart from Q special nodes $\{Z_k\}_{k=1}^{Q}$ representing candidates. The latter distribute one–per–clique; they are connected with certainty to the nodes of their own clique, but never to the other nodes.

The stochastic dynamics of the system is defined by the rules of the Q–state voter model [4], with the provision that candidates vote for themselves without ever changing opinion

---

*Corresponding author. E-mail: `filippo.palombi@enea.it`.

(they are *zealots* in the sense of ref. [5]). If $v_k^{(m)}$ denotes the number of votes assigned to Z_k from the *dynamical* voters belonging to the m–th clique, then $\phi_k^{(m)} = Qv_k^{(m)}/|V| = \omega_1^{-1}v_k^{(m)}$ represents the corresponding scaling variable in the language of ref. [2]. The equilibrium probability density of the system is shown in [1] to obey with good approximation a multi–clique Fokker–Planck equation (FPE), namely

$$\begin{aligned} 0 = &-\sum_{i=1}^{Q}\sum_{\ell\neq i}^{1\ldots Q}\partial_\ell^{(i)}\left[A_\ell^{(i)}(\bar\phi)\mathcal{P}(\bar\phi)\right] \\ &+\frac{1}{2}\sum_{i=1}^{Q}\sum_{\ell,m\neq i}^{1\ldots Q}\partial_\ell^{(i)}\partial_m^{(i)}\left[B_{\ell m}^{(i)}(\bar\phi)\mathcal{P}(\bar\phi)\right] = \mathcal{L}_{\text{FP}}\cdot\mathcal{P}(\bar\phi)\,, \end{aligned} \tag{1}$$

where $\partial_\ell^{(i)} \equiv \partial/\partial\phi_\ell^{(i)}$ and $\mathcal{L}_{\text{FP}}$ denotes the stationary Fokker–Planck operator. Drift and diffusion coefficients are given respectively by

$$\begin{aligned} A_\ell^{(i)} = &-\left[1+\omega_1\omega_2(1-\omega_1^{-1})\right]\phi_\ell^{(i)} \\ &+\frac{\omega_1\omega_2(1-\omega_1^{-1})}{Q-1}\left\{\sum_{k\neq i,\ell}^{1\ldots Q}\phi_\ell^{(k)}-\sum_{k\neq\ell}^{1\ldots Q}\phi_k^{(\ell)}\right\}+\frac{\omega_1\omega_2(1-\omega_1^{-1})^2}{Q-1}\,, \end{aligned} \tag{2}$$

$$\begin{aligned} B_{\ell m}^{(i)} = &-2(1-\delta_{\ell m})\phi_\ell^{(i)}\phi_m^{(i)} \\ &-(1-\delta_{\ell m})\frac{\omega_2}{(Q-1)}\left[\phi_\ell^{(i)}\left(1-\omega_1^{-1}+\sum_{k\neq i,m}^{1\ldots Q}\phi_m^{(k)}-\sum_{k\neq m}^{1\ldots Q}\phi_k^{(m)}\right)\right. \\ &\qquad\left.+\phi_m^{(i)}\left(1-\omega_1^{-1}+\sum_{k\neq i,\ell}^{1\ldots Q}\phi_\ell^{(k)}-\sum_{k\neq\ell}^{1\ldots Q}\phi_k^{(\ell)}\right)\right] \\ &+2\delta_{\ell m}\phi_\ell^{(i)}\left[1+\frac{\omega_2(1-\omega_1^{-1})-\omega_1^{-1}}{2}-\phi_\ell^{(i)}\right] \\ &+\delta_{\ell m}\frac{\omega_2}{(Q-1)}\left(1-\omega_1^{-1}-2\phi_\ell^{(i)}\right)\left[1-\omega_1^{-1}+\sum_{k\neq i,\ell}^{1\ldots Q}\phi_\ell^{(k)}-\sum_{k\neq\ell}\phi_k^{(\ell)}\right]\,, \end{aligned} \tag{3}$$

where $\bar\phi = \{\bar\phi^{(k)}\}_{k=1}^{Q}$ denotes the global state vector of the system, $\bar\phi^{(m)} = \{\phi_k^{(m)}\}_{k\neq m}^{1\ldots Q}$ represents the local state vector of the m–th clique[1] and $\omega_2 = p(Q-1)$ is an inter–clique coupling constant. The FPE is left invariant by two symmetry operations:

$$\text{intra–clique symmetry}: \qquad \phi_\ell^{(i)} \longleftrightarrow \phi_m^{(i)}\,, \qquad i=1,\ldots,Q, \quad \ell,m\neq i\,, \tag{4}$$

$$\text{inter–clique symmetry}: \quad \{\phi_k^{(i)}\}_{k\neq i}^{1\ldots Q} \longleftrightarrow \{\phi_k^{(j)}\}_{k\neq j}^{1\ldots Q}\,, \quad i,j=1,\ldots,Q\,. \tag{5}$$

---

[1] the reader should notice that in ref. [1] the vote of Z_m is included in $v_m^{(m)}$, whereas the latter counts here dynamical votes only, *i.e.* we have $\phi_m^{(m)} \equiv 1-\omega_1^{-1}-\sum_{k\neq m}^{1\ldots Q}\phi_k^{(m)}$. It can be shown by an explicit calculation that eq. (1) is left invariant by such counting shift.

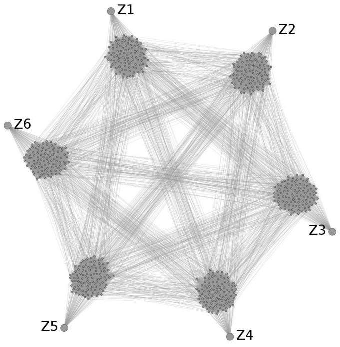

Figure 1: An example of the network topology considered in ref. [1] with $Q = 6$.

Although a community–based network such as by us considered is not realistic, the model is shown to reproduce some qualitative features of the distribution of the excess of votes observed in real Brazilian elections. From a theoretical standpoint, it provides a well–defined framework to investigate universality breaking patterns and analytic features of the FPE of multi–state voter models over heterogeneous networks.

2 Dirichlet distributions

In ref. [1, sect. 5], we simulated the equilibrium probability density $\mathcal{P}(\bar{\phi})$ in terms of the stochastic process associated to eq. (1) and found that it agrees with the Monte–Carlo simulations of the voter model. In the absence of analytic solutions of the FPE, our concern here is to establish whether we can provide some semi–analytic representation of $\mathcal{P}(\bar{\phi})$. This would help shed light on specific aspects of the distribution of the excess of votes, which in the clique language reads

$$\mathcal{F}(x) = \int \delta(\phi_k - x)\mathcal{P}(\bar{\phi})\mathrm{d}\bar{\phi}\,, \tag{6}$$

with

$$\phi_k = \omega_1^{-1} + \sum_{i=1}^{Q} \phi_k^{(i)} = 1 + \sum_{i\neq k}^{1\ldots Q} \phi_k^{(i)} - \sum_{k\neq i}^{1\ldots Q} \phi_k^{(i)} \tag{7}$$

representing the excess of votes assigned to Z_k. Notice that the Fokker–Planck operator of eq. (1) decomposes according to

$$\mathcal{L}_{\mathrm{FP}} = \mathcal{L}_{\mathrm{FP}}^{(\mathrm{intra})}(\omega_1) + \omega_2\mathcal{L}_{\mathrm{FP}}^{(\mathrm{inter})}(\omega_1)\,, \tag{8}$$

where the operator $\mathcal{L}_{\mathrm{FP}}^{(\mathrm{intra})}$ governs the intra–clique dynamics and the operator $\mathcal{L}_{\mathrm{FP}}^{(\mathrm{inter})}$ describes inter–clique interactions. Eq. (8) could suggest to look for perturbative solutions of the FPE. Unfortunately, this is not possible. Indeed, $\mathcal{P}(\bar{\phi})$ becomes singular as $\omega_2 \to 0$, owing to the intra–clique consensus that necessarily occurs when the inter–clique links are switched off. This makes it impossible to perform perturbative expansions of eq. (1) around the point $\omega_2 = 0$.

An alternative approach consists in observing that $\bar\phi^{(m)}$ lives on a cut–off simplex, namely

$$\bar\phi^{(m)} \in \bar T_Q(s)\,, \qquad \bar T_Q(s) \equiv \left\{x \in \mathbb{R}_+^{Q-1} : |x| \le s\right\}, \tag{9}$$

with $s = 1 - \omega_1^{-1}$ (candidates are solely responsible for the cut–off) and $|x| = \sum_k x_k$. If $\omega_2 > 0$, the equilibrium probability density is a regular multivariate function of $\bar\phi$. In this case, it makes sense to represent $\mathcal{P}(\bar\phi)$ in terms of multivariate polynomials. A polynomial basis on the m–th replica of $\bar T_Q(s)$ is provided by the Dirichlet probability density functions

$$\mathcal{D}^{(m)}_{\gamma^{(m)}}(\bar\phi^{(m)}) \equiv \frac{\Gamma(|\gamma^{(m)}|)}{\prod_{k=1}^{Q}\Gamma(\gamma_k^{(m)})}\, s^{1-|\gamma^{(m)}|}\left(\prod_{k=1}^{Q-1}\left[\phi_k^{(m)}\right]^{\not\gamma_k^{(m)}}\right)(s-|\bar\phi^{(m)}|)^{\not\gamma_m^{(m)}}\,, \tag{10}$$

with $\not\gamma_k^{(m)} \equiv \gamma_k^{(m)} - 1$, provided $\gamma^{(m)} \in \mathbb{N}^Q$ (notice that the superscript (m) on the l.h.s. of eq. (10) identifies the diagonal index $\not\gamma_m^{(m)}$ as the exponent of $[s - |\bar\phi^{(m)}|]$, which represents in turn the fraction of votes assigned to Z_m by the *dynamical* agents in the m–th clique). More precisely, it can be proved that

$$\begin{aligned}\bar{\mathcal{H}}_n &\equiv \operatorname{span}\left\{\bar\phi^{\alpha}:\ \alpha \in \mathbb{N}_0^{Q-1} \text{ and } |\alpha| \le n\right\}\\ &= \operatorname{span}\left\{\mathcal{D}^{(m)}_{\gamma^{(m)}}:\ \gamma^{(m)} \in \mathbb{N}^Q \text{ and } |\not\gamma^{(m)}| = n\right\}, \qquad m = 1,\dots,Q\,,\end{aligned} \tag{11}$$

where we make use of the multi–index notation $\bar\phi^{\alpha} \equiv \prod_k \phi_k^{\alpha_k}$. Therefore, if we denote by $\Omega_n = \{\gamma \in \mathbb{N}^Q:\ |\not\gamma| = n\}$ the *bucket space*, we conclude that the set $\{\mathcal{D}^{(m)}_{\gamma}\}_{\gamma\in\Omega_n}$ provides a basis of polynomials on the m–th replica of $\bar T_Q(s)$ with degree $\le n$. Accordingly, it is legitimate to look for an approximate solution of eq. (1) of the form

$$\mathcal{P}_n(\bar\phi) = \sum_{\gamma^{(1)}\in\Omega_n}\cdots\sum_{\gamma^{(Q)}\in\Omega_n} c_{\gamma^{(1)}\dots\gamma^{(Q)}}\,\mathcal{D}^{(1)}_{\gamma^{(1)}}(\bar\phi^{(1)})\dots\mathcal{D}^{(Q)}_{\gamma^{(Q)}}(\bar\phi^{(Q)})\,. \tag{12}$$

The expansion coefficients $c_{\gamma^{(1)}\dots\gamma^{(Q)}}$ should be optimally chosen, so as to let $\mathcal{P}_n(\bar\phi)$ fulfill the stationary FPE in some weak sense. From eq. (12) and some algebra, it follows

$$\begin{aligned}\mathcal{F}(x) &= \int \delta(\phi_k - x)\mathcal{P}_n(\bar\phi)\mathrm{d}\bar\phi\\ &= \sum_{\gamma^{(1)}\in\Omega_n}\cdots\sum_{\gamma^{(Q)}\in\Omega_n} c_{\gamma^{(1)}\dots\gamma^{(Q)}}\mathcal{F}_{\gamma^{(1)}\dots\gamma^{(Q)}}(x)\,,\end{aligned} \tag{13}$$

with

$$\mathcal{F}_{\gamma^{(1)}\dots\gamma^{(Q)}}(x) = \frac{1}{2\pi}\int_{-\infty}^{+\infty}\mathrm{d}q\mathrm{e}^{-\mathrm{i}qx}\prod_{m=1}^{Q} M(\gamma_k^{(m)}, |\gamma^{(m)}|, \mathrm{i}q) \tag{14}$$

and $M(a,b,z) = {}_1F_1(a;b;z)$. We thus see that the expansion coefficients $c_{\gamma^{(1)}\dots\gamma^{(Q)}}$ allow to establish a link between the probability density of the system and the shape of the vote distribution.

3 The Ritz–Galerkin method

An example of this kind of analysis is discussed in ref. [6], where it is shown that the FPE for the binary and multi–state voter models with zealots on a *complete graph* can be approximately solved by means of the Ritz–Galerkin (RG) method, a mathematical technique which is widely renowned among engineers and has been successfully applied to a plethora of physical problems. Let us briefly review the method and — to keep things simple — let us forget for a while the multi–clique structure of the network. We first introduce a scalar product on $\bar{T}_Q(s)$, namely

$$\langle f, g\rangle_\kappa = \int_{\bar{T}_Q(s)} \mathrm{d}\bar{\phi}\, f(\bar{\phi})g(\bar{\phi})\mathcal{D}_\kappa(\bar{\phi})\,, \qquad \kappa \in \mathbb{N}^Q\,, \tag{15}$$

for $\mathcal{H} \ni f, g$ a sufficiently regular function space on $\bar{T}_Q(s)$. If $\mathcal{P}$ is a stationary solution of some FPE, then it also fulfills

$$\langle V, \mathcal{L}_{\text{FP}} \cdot \mathcal{P}\rangle_\kappa = 0 \quad \forall\, V \in \mathcal{H}\,. \tag{16}$$

Conversely, a function $\mathcal{P} \in \mathcal{H}$ fulfilling eq. (16) is called *a weak solution* of the FPE. The idea underlying the RG method is that instead of enforcing eq. (16) across the whole space $\mathcal{H}$, we make do with some subspace $\bar{\mathcal{H}} \subset \mathcal{H}$ with finite dimension, such as $\bar{\mathcal{H}}_n$, thus obtaining an approximate weak solution (or equivalently an RG solution).

The theoretical framework described in sect. 1 is somewhat more complex, since $\mathcal{P}(\bar{\phi})$ is defined on a Cartesian product of cut–off simplices. The idea is therefore to look for a RG weak solution of eq. (1) by restricting the search of weak solutions to the subspace

$$\bar{\mathcal{H}} = \underbrace{\bar{\mathcal{H}}_n \times \ldots \times \bar{\mathcal{H}}_n}_{Q \text{ times}}\,. \tag{17}$$

To this aim, we preliminary need a basis of $\bar{\mathcal{H}}_n$ and we conventionally look for an orthogonal one. Orthogonal polynomials on the simplex are described for instance in ref. [7]. Two possible bases are

(i) the monomial basis

$$V_\alpha(\bar{\phi}) = \sum_{\beta\le\alpha} (-1)^{|\alpha|+|\beta|} s^{-|\beta|} \prod_{i=1}^{Q-1} \binom{\alpha_i}{\beta_i} \frac{(\kappa_i)_{\alpha_i}}{(\kappa_i)_{\beta_i}} \frac{(|\kappa|-1)_{|\alpha|+|\beta|}}{(|\kappa|-1)_{2|\alpha|}}\, \bar{\phi}^\beta\,; \tag{18}$$

(ii) the Appel basis

$$U_\alpha(\bar{\phi}) = \mathcal{D}_\kappa(\bar{\phi})^{-1} \partial_\alpha^{|\alpha|} \left[\phi_1^{\alpha_1+\kappa_1-1} \ldots \phi_{Q-1}^{\alpha_{Q-1}+\kappa_{Q-1}-1} (s - |\bar{\phi}|)^{|\alpha|+\kappa_Q-1}\right]. \tag{19}$$

These can be proved to be orthogonal with respect to eq. (15), *i.e.* for any polynomial P on $\bar{T}_Q(s)$ with $\deg\{P\} < |\alpha|$, they fulfill $\langle V_\alpha, P\rangle_\kappa = \langle U_\alpha, P\rangle_\kappa = 0$. Moreover, they are biorthogonal with respect to each other, *i.e.* $\langle V_\alpha, U_\beta\rangle_\kappa = f_\alpha \delta_{\alpha\beta}$ with f_α a known coefficient. Reasons why we consider both bases are explained in ref. [6, sect. 2]. Since $\{V_\alpha\}_{|\alpha|\le n}$ is a basis of $\bar{\mathcal{H}}_n$, a RG weak solution $\mathcal{P}_n$ of eq. (1) has to fulfill

$$\begin{aligned} &\langle V_{\alpha^{(1)}}\dots V_{\alpha^{(Q)}}, \mathcal{L}_{\rm FP}\cdot\mathcal{P}_n\rangle_\kappa = 0\,, \\ &\qquad\qquad \forall\,\alpha^{(1)},\dots,\alpha^{(Q)}\in\mathbb{N}_0^{Q-1}:\ \ |\alpha^{(k)}|\le n\,,\quad k=1,\dots,Q\,, \end{aligned} \tag{20}$$

where the scalar product is understood to extend eq. (15) to the Cartesian product of Q simplices with a measure amounting to the measure product. Inserting eq. (12) into eq. (20) yields

$$\begin{aligned} 0 &= \sum_{\gamma^{(1)}\in\Omega_n}\cdots\sum_{\gamma^{(Q)}\in\Omega_n}\langle V_{\alpha^{(1)}}\dots V_{\alpha^{(Q)}}, \mathcal{L}_{\rm FP}\cdot\left[\mathcal{D}^{(1)}_{\gamma^{(1)}}\dots\mathcal{D}^{(Q)}_{\gamma^{(Q)}}\right]\rangle_\kappa\, c_{\gamma^{(1)}\dots\gamma^{(Q)}} \\ &= \sum_{\gamma^{(1)}\in\Omega_n}\cdots\sum_{\gamma^{(Q)}\in\Omega_n}\psi_{\{\alpha^{(1)}\dots\alpha^{(Q)}\}\{\gamma^{(1)}\dots\gamma^{(Q)}\}}\, c_{\gamma^{(1)}\dots\gamma^{(Q)}}\,, \end{aligned} \tag{21}$$

with

$$\psi_{\{\alpha^{(1)}\dots\alpha^{(Q)}\}\{\gamma^{(1)}\dots\gamma^{(Q)}\}} \equiv \langle V_{\alpha^{(1)}}\dots V_{\alpha^{(Q)}}, \mathcal{L}_{\rm FP}\cdot\left[\mathcal{D}^{(1)}_{\gamma^{(1)}}\dots\mathcal{D}^{(Q)}_{\gamma^{(Q)}}\right]\rangle_\kappa\,. \tag{22}$$

In this way the stationary FPE turns into a square homogeneous linear system with coefficient matrix $\psi_{\{\alpha^{(1)}\dots\alpha^{(Q)}\}\{\gamma^{(1)}\dots\gamma^{(Q)}\}}$. This system has to be properly complemented with boundary conditions in order to uniquely determine a set of optimal coefficients $c_{\gamma^{(1)}\dots\gamma^{(Q)}}$. Unfortunately, it turns out that the size of ψ is exceedingly large, even for small values of Q and n. Indeed, it holds

$$|\Omega_n| = \binom{n+Q-1}{n} \approx \frac{\exp\{(Q-1)(H_n-\gamma_{\rm E})\}}{\Gamma(Q)}\,, \qquad H_n=\sum_{k=1}^{n}\frac{1}{k}\,. \tag{23}$$

with $\gamma_E = 0.57721\dots$ the Euler–Mascheroni constant. As an example, if $n = 10$ and $Q = 6$, then $|\Omega_n| \simeq 3\times10^3$ and $|\Omega_n|^Q \sim 10^{21}$, which is evidently out of reach from any practical point of view. We thus see that the RG method is not naïvely applicable to solve the FPE of voter models defined over community–based networks.

4 Two–clique weak reduction of the FPE

A viable approach to simplifying the problem consists in using the symmetries of the FPE. Another possibility would be to group clique variables [8], in a way similar to the spin blocking technique developed by Kadanoff in the context of the Ising model [9]. Here, we focus on the use of symmetries. Thanks to eqs. (4)–(5), the multi–clique structure of the FPE can be substantially reduced *in a weak sense*: it turns out that an effective two–clique Fokker–Planck operator governs the dynamics of the system, provided we restrict the search of solutions to a symmetric polynomial subspace. This should not be entirely surprising if we consider that the model has a well defined thermodynamic limit, given by

$$Q\to\infty\,,\qquad (\omega_1,\omega_2) = \text{ const.} \tag{24}$$

In this limit the distribution of the excess of votes converges, as proved in ref. [1], whereas the FPE becomes a partial differential equation in a formally infinite number of variables. In other words, as $Q \to \infty$ physics becomes insensitive to the actual number of cliques, while it keeps hanging on the essential features of the dynamics. These are that a microscopic interaction always involves only two agents, who either belong to the same clique or to a pair of them, regardless of which one (cliques are indeed all equivalent). The mathematical description of the model should reflect this property.

To show how the two–clique weak reduction works, we first notice that eqs. (4)–(5) entail the coefficient symmetries

$$\begin{array}{l}\text{intra–clique :}\\ c-\text{symmetry}\end{array} \quad c_{\gamma^{(1)}\ldots\{\sigma^{(\text{intra})}\cdot\gamma^{(k)}\}\ldots\gamma^{(Q)}} = c_{\gamma^{(1)}\ldots\gamma^{(k)}\ldots\gamma^{(Q)}}\,, \quad k = 1,\ldots,Q\,, \tag{25}$$

$$\begin{array}{l}\text{inter–clique :}\\ c-\text{symmetry}\end{array} \quad c_{\sigma^{(\text{inter})}\cdot\{\gamma^{(1)}\ldots\gamma^{(Q)}\}} = c_{\gamma^{(1)}\ldots\gamma^{(Q)}}\,, \tag{26}$$

where $\sigma^{(\text{intra})} \in S_{Q-1}$ is any permutation of a set of intra–clique indices and $\sigma^{(\text{inter})} \in S_Q$ is any permutation of the clique indices. Then, we observe that the Fokker–Planck operator additively splits into Q contributions, namely

$$\mathcal{L}_{\text{FP}} = \sum_{i=1}^{Q} \mathcal{L}_{\text{FP}}^{(i)}\,, \qquad \mathcal{L}_{\text{FP}}^{(i)}\cdot\mathcal{P} = \sum_{\ell\neq i}^{1\ldots Q} \partial_\ell^{(i)}[A_\ell^{(i)}\mathcal{P}] + \frac{1}{2}\sum_{\ell,m\neq i}^{1\ldots Q} \partial_\ell^{(i)}\partial_m^{(i)}[B_{\ell m}^{(i)}\mathcal{P}]\,. \tag{27}$$

By using eqs. (25)–(26) and the Dirichlet differentiation rules listed in [6], it is not difficult to show that $\langle\tilde{V}_{\alpha^{(1)}\ldots\alpha^{(Q)}}, \mathcal{L}_{\text{FP}}^{(i)}\cdot\mathcal{P}_n(\bar{\phi})\rangle = \langle\tilde{V}_{\alpha^{(1)}\ldots\alpha^{(Q)}}, \mathcal{L}_{\text{FP}}^{(k)}\cdot\mathcal{P}_n(\bar{\phi})\rangle$ for $i \neq k$ (provided the weight function of the scalar product has both intra– and inter–clique symmetries), with

$$\tilde{V}_{\alpha^{(1)}\ldots\alpha^{(Q)}}(\bar{\phi}) = \sum_{(\beta^{(1)},\ldots,\beta^{(Q)})\in\{\sigma^{(\text{inter})}\cdot(\alpha^{(1)},\,\ldots,\alpha^{(Q)})\}} V_{\beta^{(1)}}(\bar{\phi}^{(1)})\ldots V_{\beta^{(Q)}}(\bar{\phi}^{(Q)}) \tag{28}$$

denoting the symmetrization of the polynomial $V_{\alpha^{(1)}}\ldots V_{\alpha^{(Q)}}$. Accordingly, it follows

$$\langle\tilde{V}_{\alpha^{(1)}\ldots\alpha^{(Q)}}, \mathcal{L}_{\text{FP}}\cdot\mathcal{P}_n(\bar{\phi})\rangle = Q\,\langle\tilde{V}_{\alpha^{(1)}\ldots\alpha^{(Q)}}, \mathcal{L}_{\text{FP}}^{(1)}\cdot\mathcal{P}_n(\bar{\phi})\rangle\,, \tag{29}$$

Notice that eq. (29) cannot be promoted to an operatorial identity, *i.e.* we are not entitled to write $\mathcal{L}_{\text{FP}} = Q\mathcal{L}_{\text{FP}}^{(1)}$. This identity holds only *in a weak sense*, *i.e.* within a totally symmetric scalar product. The operator $\mathcal{L}_{\text{FP}}^{(1)}$ still depends on the global state vector $\bar{\phi}$, yet the coefficient symmetries allow (in a weak sense) to turn all its contributions into terms involving only $\bar{\phi}^{(1)}$ and $\bar{\phi}^{(2)}$. We prove this explicitly for the drift terms, *i.e.*

$$\begin{aligned}\mathcal{L}_{\text{FP}}^{(\text{drift})}\cdot\mathcal{P}(\bar{\phi}) = &-Q(Q-1)[1+\omega_1\omega_2(1-\omega_1^{-1})]\mathcal{P}(\bar{\phi}) + [1+\omega_1\omega_2(1-\omega_1^{-1})]\sum_{i=1}^{Q}\sum_{\ell\neq i}^{1\ldots Q}\phi_\ell^{(i)}\partial_\ell^{(i)}\mathcal{P}(\bar{\phi})\\ &-\frac{\omega_1\omega_2(1-\omega_1^{-1})}{Q-1}\sum_{i=1}^{Q}\sum_{\ell\neq i}^{1\ldots Q}\sum_{k\neq i,\ell}^{1\ldots Q}\phi_\ell^{(k)}\partial_\ell^{(i)}\mathcal{P}(\bar{\phi}) + \frac{\omega_1\omega_2(1-\omega_1^{-1})}{Q-1}\sum_{i=1}^{Q}\sum_{\ell\neq i}^{1\ldots Q}\sum_{k\neq\ell}^{1\ldots Q}\phi_k^{(\ell)}\partial_\ell^{(i)}\mathcal{P}(\bar{\phi})\\ &-Q\frac{\omega_1\omega_2(1-\omega_1^{-1})^2}{Q-1}\mathcal{P}(\bar{\phi})\,.\end{aligned} \tag{30}$$

If we insert eq. (12) into eq. (30) and let derivatives and monomials act on the respective Dirichlet density functions, we obtain linear combinations of new Dirichlet density functions. For instance, we have

$$\phi_\ell^{(k)}\mathcal{D}^{(k)}_{\gamma^{(k)}}(\bar\phi) = s\frac{\gamma_\ell^{(k)}}{|\gamma^{(k)}|}\mathcal{D}^{(k)}_{\gamma^{(k)}_{\ell+}}(\bar\phi)\,, \tag{31}$$

$$\partial_\ell^{(k)}\mathcal{D}^{(k)}_{\gamma}(\bar\phi) = s^{-1}(|\gamma^{(k)}|-1)[\theta_{\gamma_\ell^{(k)},2}\mathcal{D}^{(k)}_{\gamma^{(k)}_{\ell-}}(\bar\phi) - \theta_{\gamma_k^{(k)},2}\mathcal{D}^{(k)}_{\gamma^{(k)}_{k-}}(\bar\phi)]\,, \tag{32}$$

$$\phi_\ell^{(k)}\partial_\ell^{(k)}\mathcal{D}^{(k)}_{\gamma^{(k)}}(\bar\phi) = \theta_{\gamma_\ell^{(k)},2}(\gamma_\ell^{(k)}-1)\mathcal{D}_{\gamma^{(k)}}(\bar\phi) - \theta_{\gamma_i^{(k)},2}\gamma_\ell\mathcal{D}_{\gamma^{(k)}_{\ell+k-}}(\bar\phi)\,, \tag{33}$$

where $\gamma^{(k)}_{\ell\pm} \equiv \{\gamma_1^{(k)},\dots,\gamma_{\ell-1}^{(k)},\gamma_\ell^{(k)}\pm 1,\gamma_{\ell+1}^{(k)},\dots,\gamma_Q^{(k)}\}$ denotes a shifted index array. Index shifts operate sequentially and make a commutative group. Having inserted eqs. (31)–(33) into eq. (30) and projected the latter onto $\tilde V_{\alpha^{(1)}\dots\alpha^{(Q)}}$, we can relabel the indices of the Dirichlet sums and use the c–symmetries to let the various terms of $\mathcal{L}_{\rm FP}^{(\rm drift)}$ act in a weak sense on the first two–cliques only. We can finally apply the same reduction mechanism to the diffusion terms. The aftermath is that $\mathcal{L}_{\rm FP}$ collapses in a weak sense into an effective two–clique operator $\mathfrak{L}_{\rm FP}$ depending only upon $\bar\phi^{(1)}$, $\partial^{(1)}$, $\bar\phi^{(2)}$, $\partial^{(2)}$ and fulfilling

$$0 = \langle\tilde V_{\alpha^{(1)}\dots\alpha^{(Q)}},\mathfrak{L}_{\rm FP}\cdot\mathcal{P}_n(\bar\phi)\rangle\,. \tag{34}$$

By inserting eq. (12) into eq. (34), we obtain

$$0 = \sum_{\gamma^{(1)}\in\Omega_n}\dots\sum_{\gamma^{(Q)}\in\Omega_n}c_{\gamma^{(1)}\dots\gamma^{(Q)}}$$

$$\left\langle\tilde V_{\alpha^{(1)}\dots\alpha^{(Q)}},\left\{\mathfrak{L}_{\rm FP}\cdot\left[\mathcal{D}^{(1)}_{\gamma^{(1)}}(\bar\phi^{(1)})\mathcal{D}^{(2)}_{\gamma^{(2)}}(\bar\phi^{(2)})\right]\right\}\mathcal{D}^{(3)}_{\gamma^{(3)}}(\bar\phi^{(3)})\dots\mathcal{D}^{(Q)}_{\gamma^{(Q)}}(\bar\phi^{(Q)})\right\rangle\,. \tag{35}$$

Eq. (35) is manifestly invariant under inter–clique permutations. The size of the RG linear system is much lower than $|\Omega_n|^Q$. We are currently developing a feasible adaptation of the RG method based on eq. (35).

5 Orthogonal vs. non–orthogonal projections

The computational building block of the RG method is represented by the single–clique scalar product $\chi_{\alpha\gamma} = \langle V_\alpha,\mathcal{D}_\gamma\rangle_\kappa$. This amounts to

$$\chi_{\alpha\gamma} = s^{1-Q}\frac{\Gamma(|\gamma|)\Gamma(|\kappa|)}{\Gamma(|\kappa|+2|\alpha|-1)}\left[\prod_{m=1}^{Q-1}\frac{\Gamma(\kappa_m+\alpha_m)}{\Gamma(\kappa_m)}\right]\frac{\Gamma(\kappa_Q+\gamma_Q-1)}{\Gamma(\kappa_Q)\Gamma(\gamma_Q)}$$

$$\cdot\sum_{\beta\le\alpha}\frac{\Gamma(|\kappa|+|\alpha|+|\beta|-1)}{\Gamma(|\kappa|+|\gamma|+|\beta|-Q)}\prod_{m=1}^{Q-1}(-1)^{\beta_m}\binom{\alpha_m}{\beta_m}\binom{\kappa_m+\gamma_m+\beta_m-2}{\gamma_m-1}\,, \tag{36}$$

for $|\alpha| \le |\not{\gamma}|$. Since a Γ–function with integer argument is a factorial (it can be computed with multiple–precision arithmetic via standard numerical software libraries), the above

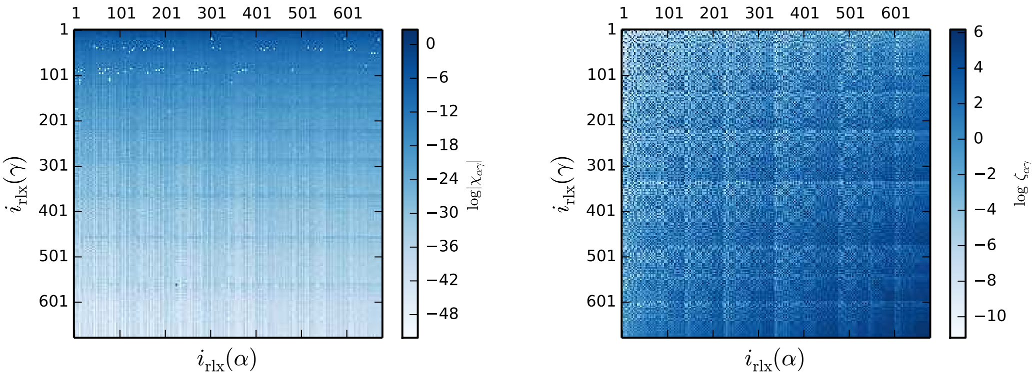

Figure 2: (left) matrix plot of $\chi_{\alpha\gamma}$ for $Q = 4$, $n = 14$ and $\kappa = \{2, 2, 2, 2\}$; (right) matrix plot of $\zeta_{\alpha\gamma}$ for the same choice of parameters. In both plots, $i_{\mathrm{rlx}}(\alpha)$ denotes *reverse lexicographic ordering* of the index array α.

representation is a closed–form expression, *i.e.* it can be exactly evaluated in a finite number of algebraic operations. Nonetheless, it is computationally expensive, due to the non–factorizable multi–sum

$$\sum_{\beta\leq\alpha} \equiv \sum_{\beta_1=0}^{\alpha_1} \cdots \sum_{\beta_{Q-1}=0}^{\alpha_{Q-1}} , \tag{37}$$

which blows up exponentially as Q increases. In addition, $\chi_{\alpha\gamma}$ spans a huge range of numerical values: an example is given in Fig. 2 (left), where the complete matrix χ corresponding to $Q = 4$, $n = 14$ and $\kappa = \{2, 2, 2, 2\}$ is shown (for this choice of parameters it holds $|\Omega_n| = 680$). We see that $\chi_{\alpha\gamma}$ ranges over 48 orders of magnitude, meaning that a numerical precision of *at least* 48 digits is required in order to correctly represent the matrix ψ (for that specific choice of parameters), without taking into account the additional numerical cancellations related to the algebraic structure of $\mathcal{L}_{\mathrm{FP}}$.

Is there any alternative? The answer is affirmative: the choice of the projection basis is totally arbitrary. Moreover, different polynomial bases on $\bar{T}_Q(s)$ overlap differently with the Dirichlet probability density functions. It is common lore that orthogonal bases are the cheapest choice in terms of required numerical precision (see for instance ref. [10] for a recent one–dimensional theoretical argument), which is why we also considered monomial and Appel bases in ref. [6] and the previous sections. Nevertheless, we should observe that the use of Dirichlet distributions to represent $\mathcal{P}(\bar{\phi})$, which has been fully motivated in ref. [6], automatically spoils the worthiness of projecting the FPE onto orthogonal bases, since ψ is anyway a dense matrix, irrespective of the chosen projection basis.

Accordingly, it makes sense to consider also non–orthogonal bases, the easiest of which is in fact the Dirichlet one. It turns out that the scalar product $\zeta_{\alpha\gamma} = \langle\mathcal{D}_\alpha, \mathcal{D}_\gamma\rangle_\kappa$, given by

$$\zeta_{\alpha\gamma} = s^{2(1-Q)} \frac{\Gamma(|\alpha|)\Gamma(|\gamma|)\Gamma(|\kappa|)}{\Gamma(|\alpha+\gamma+\kappa|-2Q)} \prod_{m=1}^{Q} \frac{\Gamma(\alpha_m+\gamma_m+\kappa_m-2)}{\Gamma(\alpha_m)\Gamma(\gamma_m)\Gamma(\kappa_m)} , \tag{38}$$

is also represented as a closed–form expression, but fortunately its evaluation does not require the computation of any internal multi–sum (as such, it is much faster!). Moreover, the complete matrix ζ corresponding to $Q = 4$, $n = 14$ and $\kappa = \{2, 2, 2, 2\}$ is shown in Fig. 2 (right) to allow for a comparison with χ. We observe that $\zeta_{\alpha\gamma}$ spans 16 orders of magnitude, which is a much more compact range than seen in Fig. 2 (left). This is clearly due to the fact that $\{V_\alpha\}_{|\alpha|\leq n}$ is made of non–positive polynomials, all with extended support on $\bar{T}_Q(s)$, whereas $\{\mathcal{D}_\alpha\}_{\alpha\in\Omega_n}$ is a basis of positive polynomials having localized support in some sub–domain of $\bar{T}_Q(s)$. The choice of the Dirichlet density functions as a polynomial projection basis could be computationally advantageous despite their non–orthogonality.

6 Summary & conclusions

This contribution is part of a project addressing the problem of understanding whether and to what extent voter models defined over heterogeneous networks are suitable to describe results of real political elections.

We know that the empirical distribution of the intra–party excess of votes in proportional elections with open lists is universal and correctly reproduced by a word–of–mouth model (WoMM) [2]. However, if the election rules are (even slightly) modified, universality gets broken [3]. An interesting case is represented by Brazil, whose election rules differ from a standard proportional system with open lists by just one feature, namely the compulsoriness of voting. This seems to be responsible for a distortion of the left tail of the distribution of the excess of votes with respect to the universal curve. Unfortunately, Brazilian elections cannot be described by the WoMM.

By contrast, compulsory voting is well represented by voter models, since here agents express political preferences at each time of the stochastic dynamics. What we tried to do in ref. [1] was to look at the excess of votes in the context of the multi–state voter model, over a network which mostly resembles that of ref. [2] (stochastic trees of the WoMM are replaced by cliques). Numerical simulations allowed us to confirm that the left tail of the distribution of the excess of votes reproduces at least qualitatively that observed in Brazilian elections. In search for an analytic description of this result, we studied the model in terms of an *ad hoc* mean field theory, specifically tuned to take into account the network topology. In this framework, we derived eq. (1) (see [1, sect. 4]).

We then observed that the distribution of the excess of votes can be analytically represented as a linear superposition of Fourier transforms of products of Kummer functions, provided the probability density of the system is represented as a linear superposition of products of Dirichlet distributions (see [1, app. A]). This brought us to the RG method as a mean to determine the weights of such a linear superposition directly from the FPE. In ref. [6], we explained how to apply the method to birth–death systems and we concretely tested the procedure on the binary and multi–state voter models over a *complete graph.*

We are presently at the stage of applying the RG method to eq. (1). Owing to the multi–clique topology of the network, the kinematic domain of the model is a Cartesian product of simplices. As a consequence, the number of Dirichlet contributions is exceedingly large, even for modest choices of the number of cliques and polynomial degrees. Nevertheless, the multi–clique structure of the Fokker–Planck operator can be substantially reduced in a weak sense by using the symmetries of the system. We are currently developing a feasible adaptation of the Ritz–Galerkin method to eq. (1), based on such a reduction [8]. In fact, a two–clique weak reduction of the Fokker–Planck operator is ultimately made possible by the interaction rule of the voter model, which always involves only two agents, either belonging to the same clique or to a pair of them, in a community–based network such as by us considered. Models involving more than two agents, such as the q–voter model [11], would not allow for such a feature.

References

[1] F. Palombi and S. Toti. Stochastic Dynamics of the Multi-State Voter Model over a Network based on Interacting Cliques and Zealot Candidates. *J. Stat. Phys.*, 156:336–367, 2014.

[2] S. Fortunato and C. Castellano. Scaling and Universality in Proportional Elections. *Phys. Rev. Lett.*, 99(13):138701, September 2007.

[3] A. Chatterjee, M. Mitrović, and S. Fortunato. Universality in voting behavior: an empirical analysis. *Sci. Rep.*, 3, January 2013.

[4] M. Starnini, A. Baronchelli, and R. Pastor-Satorras. Ordering dynamics of the multi-state voter model. *J. Stat. Mech.*, P10027, 2012.

[5] M. Mobilia, A. Petersen, and S. Redner. On the role of zealotry in the voter model. *J. Stat. Mech. Theor. Exp.*, 2007(08):P08029+, 2007.

[6] F. Palombi and S. Toti. Use of Dirichlet distributions and orthogonal projection techniques for the fluctuation analysis of steady-state multivariate birthd eath systems. *Int. J. Mod. Phys. C*, 26:1550139, 2015.

[7] C. F. Dunkl and Y. Xu. *Orthogonal Polynomials of Several Variables.* Encyclopedia of Mathematics and its Applications. Cambridge University Press, 2001.

[8] F. Palombi and S. Toti. in preparation.

[9] L. P. Kadanoff. Scaling laws for ising models near T_c. *Physics*, 2:263, 1966.

[10] C. Schwartz. Nonorthogonal bases in variational calculations and the loss of numerical accuracy. *arXiv:1411.2965.*

[11] C. Castellano, M. A. Muñoz, and R. Pastor-Satorras. The non-linear q–voter model. *Phys. Rev. E*, 80:041129, 2009.

Feasibility Study for the Characterization of New Fuels Containing Minor Actinides for Fast Sodium Reactors

Giorgio Baiocco[1]*, *Romolo Remetti*[1], *Luigi Lepore*[1],
Giuseppe A. Marzo[2], *Nadia Cherubini*[2] *and Giulia Abbate*[2]

[1]*Sapienza, Università di Roma – Rome, Italy*

[2]*ENEA, C. R. Casaccia – Rome, Italy*

Abstract. An adequate management of radioactive waste produced by a nuclear reactor at the end of the fuel cycle is a critical issue. Into advanced fuel cycles Minor Actinides (MA) contained in high level waste are the most responsible for the radiotoxicity and the heat generated by radioactive waste in the long term. This is why one of the goals of generation IV fast reactors is the transmutation of minor actinides through an adiabatic cycle fuel. In this paper the Monte Carlo transport code MCNP is used for a 3D neutron kinetic calculation coupled with the deterministic burn-up code ORIGEN, in order to study the impact of different MA burning strategies into CP-ESFR (Collaborative Project on a European Sodium Fast Reactor). The purpose of the study is a comparative evaluation of the efficiency of homogeneous and heterogeneous core configurations for MAs transmutation suggesting the best strategy to achieve their minimization into the fuel cycle.

1 Introduction

A typical 1000 MWe LWR (Light Water Reactor) produces every year about 30 t of spent fuel containing uranium, plutonium, fission products (FP) and minor actinides (MA) [1]. Into advanced fuel cycles uranium and plutonium are recovered and used to fabricate mixed-oxide fuels (MOX) while MA and FP are planned to be stored in geological repositories. In this case MA are the major contributors to radiotoxicity and heat generation especially after 100 years [2]. As of the year 2006, it is estimated that about 110 tonnes of minor actinides are being contained in spent fuel storage worldwide, and an additional 40 tonnes are contained in high level waste products from reprocessing. Without options, such an amount will double by the year 2020 [1].

A possible solution to the problem of MA is represented by transmutation. This strategy would allow the minimization of already accumulated nuclear wastes coming from LWR open fuel cycles and may have a positive impact on final repository requirements [3, 4].

---

*Corresponding author. E-mail: `gio.baiocco@gmail.com`.

This work has been performed in the frame of the European PELGRIMM (PELlets versus GRanulates: Irradiation, Manufacturing & Modelling) project. The objective of the project is to develop new MA bearing fuels for IV generation sodium cooled fast reactors [5]. In this paper different transmutation strategies are explored by studying the fuel burn-up into CP-ESFR core [6]. The core design and the MA loading patterns are analyzed in Section 2.

From the computational point of view the simulation was performed using three different computer codes:

- MCNP5 was used for core simulation and transport calculations [7, 8, 9]
- ORIGEN2.2 was used for burn-up calculations [10]
- MONTEBURNS2.0: was used to link the previous two [11]

In Section 3 the core modeling and calculation strategy are described and the results discussed in Section 4. Finally, Section 5 summarizes the main conclusions.

2 CP-ESFR Core Description

2.1 Reference core configuration

The reference configuration for the analysis is the so called CONF2 core [6]. CP-ESFR is a 3600 MWth Sodium Cooled Fast Reactor: the core consists of hexagonal fuel assemblies contained in wrapper tubes made of ferritic martensitic steel (EM10). The assemblies contain a triangular arrangement of 271 fuel pins with helical wire wrap spacers. The fuel pin consists of MOX pellets in ODS steel cladding. There are 225 inner fuel assemblies and 228 outer fuel assemblies. The inner and outer fuel regions have different Pu mass content (respectively 14.43% and 16.78%) in order to flatten the core power shape at end of cycle. There are two types of control and safety devices: 24 CSD (Control and Shutdown Device) for reactivity control and shutdown and 9 DSD (Diverse Shutdown Device) for shutdown only. CSD are made of rods containing natural B4C, while in DSD there is B4C with 90% enriched 10B.

Outside the core, the reflectors consist in three rings of assemblies. The axial layout of the CONF2 configuration presents, just above the active core, a large sodium plenum. Further above in the axial direction there is a layer of neutron absorbent material (boron carbide) and another layer of steel reflector. In the lower part, just below the active core, there is a fertile region in order to provide neutron absorptions. Cross section and vertical views of the reactor core are shown in Fig. 1 and 2 respectively. More detailed specifications can be found in [12, 13, 14, 15].

2.2 Minor Actinides loading patterns

Two recycling models are explored in this paper:

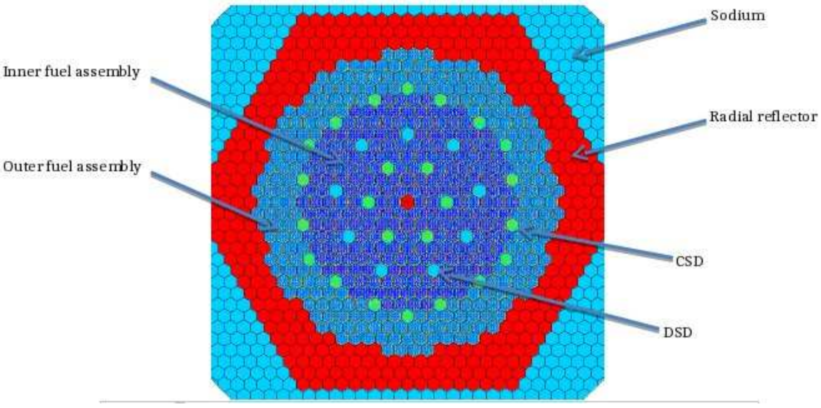

Figure 1: Cross section view of the CP-ESFR core, MCNP Visual Editor view

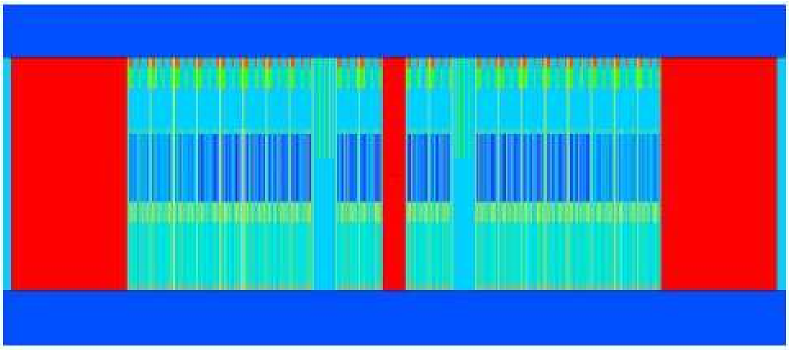

Figure 2: Vertical view of the CP-ESFR core, MCNP Visual Editor view

- The heterogeneous configuration HET2 consists of the same layout of CONF2, with the same isotopic composition in inner fuel, outer fuel and lower fertile blanket, but with an additional ring of 84 radial blanket assemblies, containing 20% by weight of MA [15];
- The homogeneous configuration HOM4 is based on the CONF2 core with 4% by weight of MA homogeneously included within the core [15].

3 Modelling and Calculation

Three dimensional MCNP models were developed for CONF2, HET2 and HOM4 configurations. The core was divided in four radial rings. Four assemblies, highlighted in Fig. 3, one for each zone, were chosen, considering that the neutron flux depends essentially only on the distance from the center of the core. The middle pin of each element is representative of the entire ring. These pins have been divided into ten cells each, in order to take into account the axial variation of the neutron flux. The neutron spectrum was calculated for each of these 40 cells and then burn-up calculations were performed coupling MCNP with ORIGEN through Monteburns.

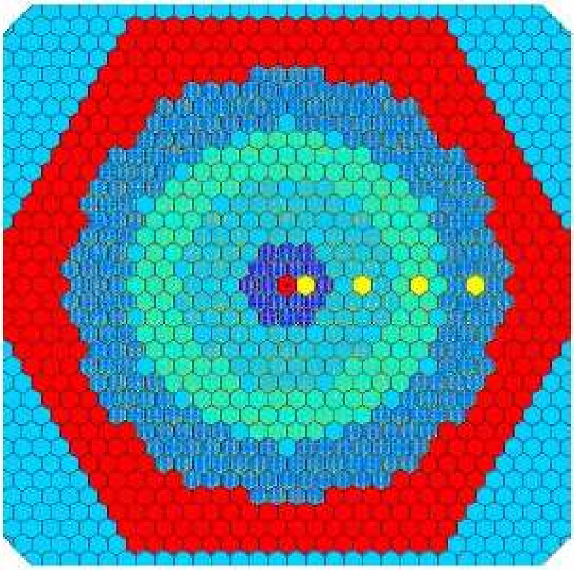

Figure 3: Core subdivision

Into this approach a cycle length of 2050 days was considered. This cycle was divided into four periods of 512.5 days. No reloading scheme was applied: the core evolves from the fresh fuel situation to fully depleted situation;

100 active cycles and 3 million histories/cycle were used in order to obtain accurate results. Parallel computations have been performed using CRESCO 4 infrastructure.

4 Results

4.1 Pu mass balance

Fig. 4 (left) shows the mass balance of ^{239}Pu from Beginning of Life (BOL) to End of Life (EOL). It can be observed that all cases under study are breeders, leading to a net accumulation of ^{239}Pu.

The total ^{239}Pu breeding is more important in HET2 due to the 84 extra radial ring loaded in the core periphery.

4.2 MA mass balance

The MA behaviour is depicted in Fig. 4 (right). In the CONF2 there is a global accumulation of MA. In HET2, after a small increase, there is a substantial balance between MA produced and destroyed. Finally, in HOM4, a net consumption of MA is observed.

It is important to emphasize that, both in HET2 that HOM4, there is a net consumption of ^{237}Np and ^{241}Am.

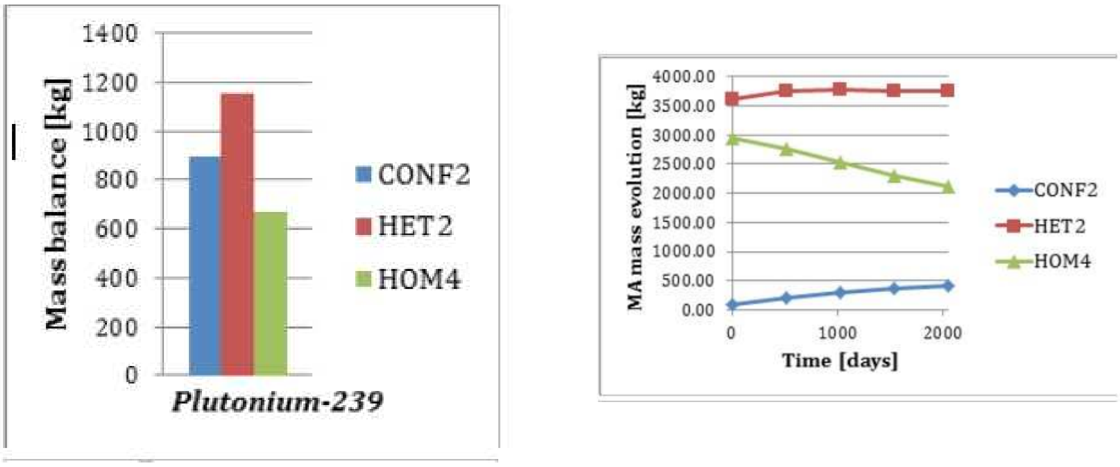

Figure 4: (left) Plutonium mass balance; (right) Minor Actinides mass balance

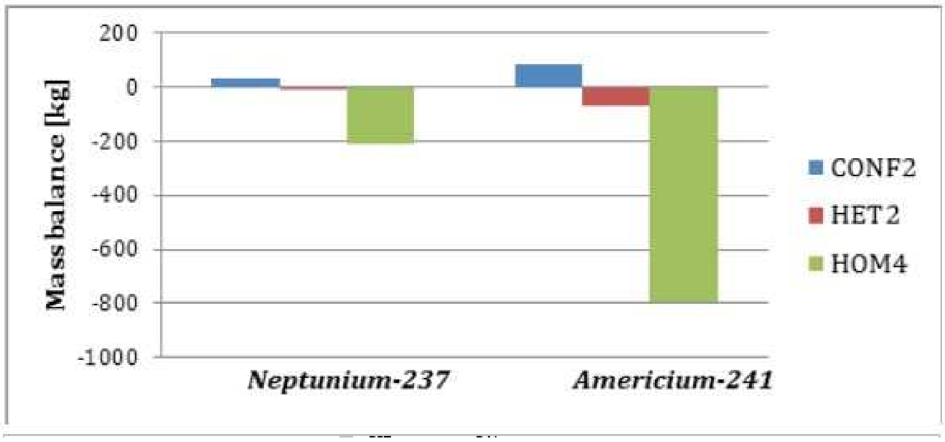

Figure 5: ^{237}Np and ^{241}Am mass balance

This is very promising, both for the reduction of radiotoxic inventory in the long term (due to the long half-life of 237Np), and the less decay heat generated from wastes (due to the strong alpha emission of 241Am, mainly). It is observed that the major transmutation of MA in HOM4 is due to the neutron flux. The MA assemblies in HET2 are arranged far from the center of the core and therefore they are subjected to a lower neutron flux.

5 Conclusions

This work, based on parallel calculations performed using CRESCO 4 infrastructure, shows that both the homogeneous and heterogeneous transmutation strategies are possible. These configurations lead to two significantly different results:

- In the heterogeneous load of MA, despite a slight accumulation of MA, a net consumption of 237Np and 241Am can be obtained; In the homogeneous load of MA, the CP-ESFR behaves as a burner reactor. This would allow a significant reduction of the MA already present in the world.

- It must be emphasized, however, that having MA within the reactor core leads to a reduction of reactivity and delayed neutron fraction. Additional studies are essential to assess the actual feasibility of these strategies, in terms of reactor control and safety issues.

References

[1] INTERNATIONAL ATOMIC ENERGY AGENCY. Status of Minor Actinide Fuel Development. *IAEA - Nuclear Energy Series*, NF-T-4.6, 2009.

[2] M. Cumo. Impianti Nucleari. *Università La Sapienza*, 2009.

[3] J. H. Bultman. Actinide Transmutation in Nuclear Reactors. *Ph.D. Thesis*, Delft University of Technology, 1995.

[4] C. Sudati. Bruciamento di Attinidi Minori e Plutonio in reattori PWR. *Tesi di dottorato di ricerca*, Politecnico di Milano, 2000.

[5] D. Schmitt et al. PELGRIMM Characteristics of the selected core design for a pellet shaped fuel. *European commission - 7th framework programme*, 2013.

[6] L. Buiron et al. CP ESFR Working Horses Core concept definition. *European commission - 7th framework programme*, 2009.

[7] X-5 MONTE CARLO TEAM. MCNP - A General Monte Carlo N-Particle Transport Code, Version 5. *Volume I: Overview and Theory*, Los Alamos National Laboratory, 2008.

[8] X-5 MONTE CARLO TEAM. MCNP A General Monte Carlo N-Particle Transport Code, Version 5. *Volume II: Users Guide*, Los Alamos National Laboratory, 2008.

[9] Brewer R. Criticality Calculations with MCNP5: A Primer. Los Alamos National Laboratory, 2009.

[10] OAK RIDGE NATIONAL LABORATORY. ORIGEN 2.2: Isotope Generation and Depletion Code, Matrix Exponential MethodORIGEN 2.2: Isotope Generation and Depletion Code, Matrix Exponential Method. 2002.

[11] OAK RIDGE NATIONAL LABORATORY. MONTEBURNS 2.0: An Automated, Multi-Step Monte Carlo Burnup Code System. 2003.

[12] RINEISKI A et al. CP ESFR Synthesis of options to optimize feedback coefficients. *European commission - 7th framework programme*, 2012.

[13] MARTIN-FUERTES F. et al. CP ESFR Transumation options assessments. *European commission - 7th framework programme*, 2011.

[14] MARTIN-FUERTES F. et al. CP ESFR Choice of options, final report. *European commission - 7th framework programme*, 2011.

[15] R. Sunderland et al. ESFR Cores with Optimized Characteristics: Final Report. *European commission - 7th framework programme*, 2012.

Monte Carlo simulation of radiation response of a novel diamond detector for radiotherapy dosimetry

Maria Pimpinella[1]* *and Antonella Stravato*[2]

[1]*ENEA-FSN-INMRI, Istituto Nazionale di Metrologia delle Radiazioni Ionizzanti*
C.R. Casaccia, Via Anguillarese 301, 00123 Roma, Italy

[2]*Medical Physics Service, Department of Radiation Oncology,*
Humanitas Clinical and Research Hospital, Rozzano, 20098 Milan, Italy

Abstract. The EGSnrc Monte Carlo code has been used for calculating the response in terms of absorbed dose to water for a novel diamond detector for radiotherapy dosimetry developed at Rome Tor Vergata University and commercialized by PTW-Freiburg. The detector was modelled using the egs++ geometry package and its irradiation in water with electron and photon beams was simulated. The detector response, calculated as ratio of absorbed dose in the detector sensitive volume to absorbed dose to water, has been calculated for clinical electron and photon beams in the energy range from 6 MeV to 18 MeV and from 6 MV to 15 MV, respectively. Simulations were also performed for a Co-60 gamma ray beam. Results show that changes in microDiamond response are within 2% in the whole energy range here considered.

1 Introduction

Recently a new diamond detector for radiotherapy dosimetry, the PTW-60019 microDiamond, has been commercialized by PTW-Freiburg, Germany (http://www.ptw.de/2732.html). Such detector is based on the synthetic single crystal diamond detector (SCDD) developed at the Industrial Engineering Department of Rome Tor Vergata University [1] and characterized in cooperation with the Italian National Institute for Ionizing Radiation Metrology (ENEA-FSN-INMRI) in order to assess its dosimetric performance [2, 3, 4, 5]. The major feature of microDiamond is the very small sensitive volume (0.004mm^3) that makes this dosimeter especially suitable for dosimetry in advanced radiotherapy. Since the quantity of interest in radiotherapy is the absorbed dose to water (D_w), properties of detector material should be similar to that of water in terms of radiation interaction. According to the atomic number (Z=6) diamond can be considered a water-equivalent material, however its high density (about 3.5g/cm^3) as well as the properties of other materials utilized for

---

*Corresponding author. E-mail: `maria.pimpinella@enea.it`.

the SCDD encapsulation could affect the dosimeter response. Therefore, in order to fulfil the accuracy requirement of dosimetry in radiotherapy [6], the microDiamond response in terms of D_w should be determined and its energy dependence evaluated.

In the present work Monte Carlo (MC) simulation of electron and photon transport in matter has been applied for the above purpose. MicroDiamond was modelled according to the manufacturers design and its response under irradiation was calculated as a function of electron and photon beam energy in the megavoltage range.

2 Calculation details

Simulations have been run on ENEA CRESCO HPC facility using the EGSnrc MC code system [7] freely available for research and other no-commercial purposes at http://www.nrc-cnrc.gc.ca/eng/solutions/advisory/egsnrc/download_egsnrc.html . This software works on different platforms including Linux, Unix and Windows. It requires Fortran, C and C++ compilers and GNU make utility. The source code version V4 2.4.0 has been compiled and installed on CRESCO4 and embarrassing parallelism has been implemented.

EGSnrc allows to simulate electron and photon transport through matter in the energy range from 1keV to 10GeV. The software package includes a C++ geometry library for modelling experimental set-ups and radiation sources. Fig. 1 shows the computational geometry used in this work. It mimics a typical measurement set-up for external beam radiotherapy dosimetry [6]. The detector is placed in a water tank with its sensitive region at the depth of measurement and the radiation beam impinges on the water surface. The detector position is varied along the x, y and z direction to obtain transverse relative dose profiles and depth dose curves. Fig. 1 also shows details of the detector model. All the materials surrounding the sensitive volume (within 3cm distance) have been included into the model. This implies simulation of the radiation transport through layers of materials having thickness of the order of 10^{-7}m. The quantity scored in the MC simulations is the energy released by radiation in a region coincident with the detector sensitive volume. It is worth noting that while the scoring region has a volume of about 0.004 mm^3 the radiation has to be transported through a cube of water with side 30cm thus leading to time-consuming calculations. Moreover, to correctly simulate the electron transport in regions with sizes of order of 10^{-6} 10^{-7}m, the energy cut-offs were set to 1keV further increasing the calculation time. Nevertheless, application of variance reduction techniques, as photon cross-section enhancement and correlated sampling [8, 9], together with use of parallel jobs allowed to reach the required statistical uncertainty (less than 0.3%) in reasonable time (less than 10h for each simulation).

3 Method

The SCDD has a multi-layered structure consisting in highly-conductive *p*-type diamond and intrinsic diamond layers (20μm and 1μm thick) grown on a commercial HPHT Ib single crystal diamond substrate 300μm thick [1]. Thin metallic contacts are thermally

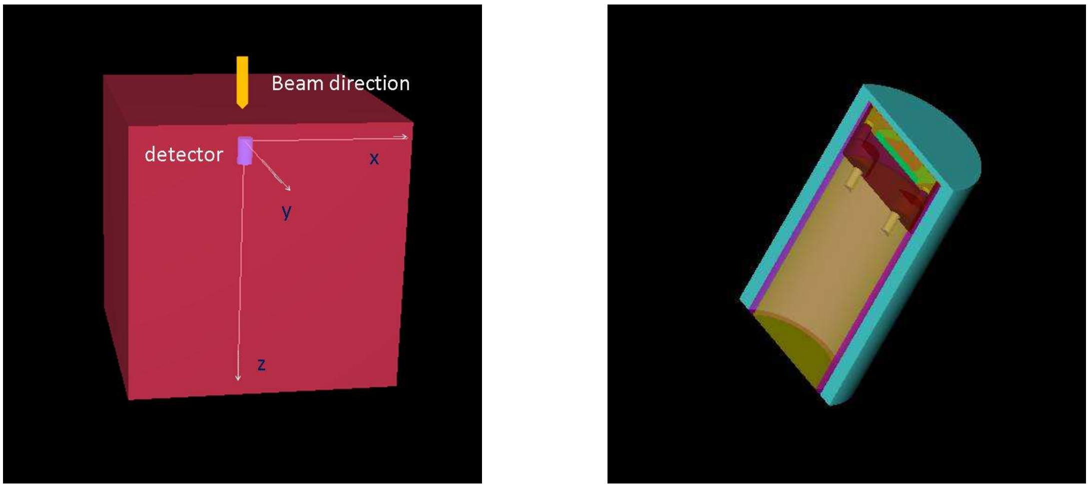

Figure 1: (left) Model bathymetry and computation domain. (right) Map showing location of data sources used for validating the model : CTD data (red dots), Acqua Alta CNR Platform (yellow dot), Vida buoy (green dot). Purple dots show the location of river inputs.

evaporated on the intrinsic diamond surface and on the p-type diamond. Due to the built-in potential at the metal/intrinsic-diamond interface an electric field is formed in the region under the metallic contact between the intrinsic and the p-type diamond layers. Thus positive and negative charge carriers generated by incident radiation in that region can be collected producing a current signal. Assuming absence of charge recombination, the collected charge is proportional to the energy deposited by the incident radiation and therefore to the absorbed dose to diamond (D_d). Starting from the cavity theory and following the formalism introduced for ionization chamber dosimetry [10] the relation between D_w in absence of the dosimeter and D_d is given by

$$D_w = D_d (s/\rho)^w_d p \,, \tag{1}$$

where $(s/\rho)^w_d$ is the water to diamond stopping-power ratio averaged over the radiation spectral distribution at the measurement point and p is a correction factor accounting for the dosimeter non-water equivalence. Thus the dosimeter response, R, can be expressed as

$$R = \frac{D_d}{D_w} = (s/\rho)^w_d p^{-1} \,, \tag{2}$$

with $p = 1$ for an ideal detector. D_d, D_w and $(s/\rho)^d_w$ have been determined for the microDiamond by MC simulations for 6 MeV to 18 MeV electron beams, 6 MV to 15 MV photon beams and Co-60 gamma ray beam using the set-up relevant to reference dosimetry [6].

4 Results and discussion

MC results have been found quite sensitive to the detector constructional details and to the choice of MC calculation parameters. Results obtained after optimizing the calculation parameters and using a detailed detector model are shown in Fig. 2.

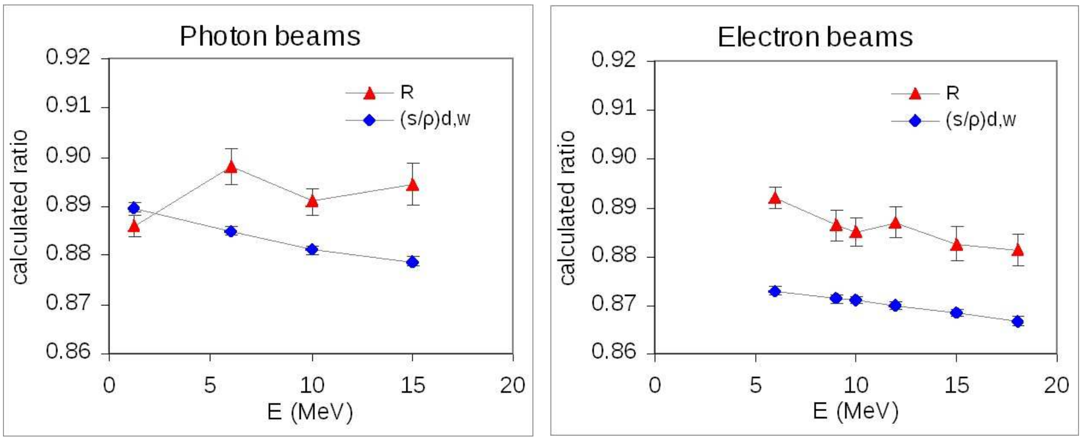

Figure 2: Calculated microdiamond response, R, in photon beams, including Co-60 gamma ray beam, and electron beams. The ratio of diamond to water stopping-power ratios are also shown. Uncertainty bars represent the type A uncertainty.

The differences between R and values shown in Fig. 2 indicate that corrections accounting for the dosimeter non-water equivalence are up to about 2%. In comparison with previous results obtained for an SCDD prototype [2, 3] perturbation effects have been found slightly different with a tendency of microDiamond to over respond in high energy photon beams compared to Co-60 beam. Differences are ascribed to the different non-water equivalent materials used for the marketed dosimeter. A variation of about 2% in the detector response does not significantly affect depth dose and transverse dose profile measurements, therefore no correction factors are required for relative dosimetry by microDiamond. On the contrary, beam quality correction factors have to be applied for reference D_w measurements based on a Co-60 calibration to fulfil the requirement of 2.5% uncertainty on the delivered dose in radiotherapy treatments.

5 Conclusions

MC simulations with EGSnrc have been performed in order to calculate the microDiamond response in terms of D_w in megavoltage electron and photon beams, including Co-60 gamma ray beam. Results show differences in the detector response from Co-60 to high energy beams within 2% and indicate that perturbation effects for microDiamond are small but not negligible. Simulations are on-going with aim to analyse the perturbation effects in terms of dosimeter components as well as to evaluate the field size dependence of the microDiamond response in photon beams.

Acknowledgments

The authors would like to thank PTW-Freiburg, Germany, for providing a detailed drawing of the commercial version of the detector and M Marinelli, G Verona-Rinati and the whole group of the Industrial Engineering Department of Rome Tor Vergata University, for developing the SCDD detector. We are grateful to Luca Silvi and the ENEA-HPC team for their support in compiling and installing EGSnrc code on CRESCO4. This work is supported by the EMRP joint research project MetrExtRT which has received funding from the European Union on the basis of Decision No 912/2009/EC. The EMRP is jointly funded by the EMRP participating countries within EURAMET and the European Union.

References

[1] S. Almaviva, M. Marinelli, E. Milani, G. Prestopino, A. Tucciarone, C. Verona, G. Verona-Rinati, M. Angelone, M. Pillon, I. Dolbnya, K. Sawhney, and N. Tartoni. Chemical vapor deposition diamond based multilayered radiation detector: Physical analysis of detection properties. *J. Appl. Phys.*, 107:014511–7, 2010.

[2] M. Pimpinella, R. Consorti, A. S. Guerra, M. Marinelli, E. Milano, A. Petrucci, A. Stravato, and G. Verona-Rinati. A synthetic diamond detector as transfer dosimeter for Dw measurements in photon beams with small field sizes. *Metrologia*, 49:S207–10, 2012.

[3] M. Pimpinella, M. Anton, M. Rouijaa, and A. Stravato. Comparison of Dw measurements by alanine and synthetic diamond dosimeters in photon beams with 1cm x 1cm field size. *Metrologia*, 49:S211–4, 2012.

[4] C. Di Venanzio, M. Marinelli, E. Milani, G. Prestopino, C. Verona, G. Verona-Rinati, M.D. Falco, P. Bagalá, R. Santoni, and M. Pimpinella. Characterization of a synthetic single crystal diamond Schottky diode for radiotherapy electron beam dosimetry. *Med. Phys.*, 40:021712–9, 2013.

[5] C. Di Venanzio, M. Marinelli, A. Tonnetti, G. Verona-Rinati, P. Bagalá, M. D. Falco, A. S. Guerra, and M. Pimpinella. Comparison between small radiation therapy electron beams collimated by Cerrobend and tubular applicators. *Journal of Applied Clinical Medical Physics*, 16:329–335, 2015.

[6] P. Andreo, D.T. Burns, K. Hohlfeld, M. Huq, T. Kanai, R. F. Laitano, V. Smyth, and S. Vynckier. Absorbed dose determination in external beam cancer therapy; An International Code of Practice for Dosimetry Based on Standards of Absorbed Dose to Water. *IAEA-TRS*, 398:Vienna IAEA, 2000.

[7] I. Kawrakow, E. Mainegra-Hing, D.W.O. Rogers, F. Tessier, and B.R.B. Walters. The EGSnrc Code System: Monte Carlo simulation of electron and photon transport. *NRCC Report*, PIRS–701, 2013.

[8] J. Wulff, K. Zink, and I. Kawrakow. Efficiency improvements for ion chamber calculations in high energy photon beams. *Med. Phys.*, 35:1328–36, 2008.

[9] M. Pimpinella, C. Caporali, A. Stravato, A.S. Guerra, and M. D'Arienzo. Monte Carlo calculation of correction factors for dosimetry in radiotherapy using the correlated sampling method. *Romanian Reports in Physics*, 66:109–119, 2014.

[10] R.F. Laitano. Fondamenti di dosimetria delle radiazioni ionizzanti. *ENEA (2013)*, ISBN 978-88-8286-295-4.

Experimental realization of maximally synchronizable networks and the effect of topological noise

R. Sevilla-Escoboza[1], *J. M. Buldú*[2,3], *S. Boccaletti*[4,5] *and R. Gutiérrez*[6*]

[1]*Centro Universitario de los Lagos, Universidad de Guadalajara,*
Enrique Díaz de Leon, Paseos de la Montaña, Lagos de Moreno,
Jalisco 47460, Mexico

[2]*Laboratory of Biological Networks, Center for Biomedical Technology,*
Technical University of Madrid, Pozuelo de Alarcón, 28223 Madrid, Spain

[3]*Complex Systems Group & GISC, Universidad Rey Juan Carlos,*
28933 Móstoles, Spain

[4]*CNR-Istituto dei Sistemi Complessi, 50019 Sesto Fiorentino, Italy*

[5]*The Italian Embassy in Israel, Tel Aviv 68125, Israel*

[6]*Department of Chemical Physics, Weizmann Institute of Science,*
Rehovot 76100, Israel

Abstract. Maximally synchronizable networks, i.e. networks of dynamical systems whose synchronized dynamics have the highest possible stability throughout a range of coupling strengths, present an interesting limiting case for the understanding of synchronization in ensembles of oscillators and extended systems. We propose an experimental implementation of maximally synchronizable networks, and consider theoretically and numerically the influence of "topological noise" (i.e. uncertainties in the connection weights) on the stability of synchronization. The experimental implementation is based on nonlinear oscillating circuits, while the numerical work greatly benefited from the use of the Cresco facility in Portici. This report summarizes recent work that has been submitted for publication [1].

1 Introduction

Synchronization is a paradigmatic example of collective behavior in the physical and biological sciences [2, 3]. Among the recent developments in the study of synchronous

---

[*] Corresponding author. E-mail: `rcd.gutierrez@gmail.com`.

dynamics, the *master stability function* (MSF) approach [4, 5] is a cornerstone of network synchronization research, as it provides a framework for the study of the stability of synchronization in which topology and dynamics are in a sense uncoupled. In this framework, the stability of the synchronized dynamics or *synchronizability* is established by computing the maximum Lyapunov exponent of a modified kernel that depends on a parameter ν, which is proportional to the coupling strength in the network σ, $\nu = \lambda \sigma$. This Lyapunov exponent can be seen as giving the exponential divergence/convergence of perturbations orthogonal to the synchronization manifold, and when parameterized in terms of ν gives the MSF curve, which we denote as $\Lambda(\nu)$. The proportionality constant λ represents one of the nonzero eigenvalues of the graph Laplacian matrix. The graph Laplacian matrices of the networks considered in this work have a real and non-negative spectrum, with eigenvalues $0 = \lambda_1 < \lambda_2 \leq \lambda_3 \leq \cdots \leq \lambda_N$, where N is the number of nodes (dynamical units). Moreover, as the networks are connected, only one eigenvalue is zero, and thus the ν corresponding to the different oscillation eigenmodes will be positive, $\sigma\lambda_i > 0$ for $i \geq 2$. At those values of ν for which the MSF is negative, perturbations transversal to the synchronization manifold damp out exponentially fast, and therefore it is of special interest to study the boundaries of the region/s for which $\Lambda(\nu)$ is negative. If, for a given σ and topology, $\Lambda(\nu)$ is negative for all $\sigma\lambda_i$ ($i = 2, \ldots, N$), the synchronization manifold is stable and the network is said to be synchronizable.

A topology with a smaller eigenratio $R \equiv \lambda_N/\lambda_2$ is easier to synchronize as the different eigenmodes that have to be accommodated within the synchronization region are packed together more closely. Accordingly, the optimal case is that for which $\lambda_2 = \lambda_3 = \cdots = \lambda_N$, in which all the $\sigma\lambda_i$ for $i = 2, 3, \ldots, N$ become equal, and the eigenratio R reaches its minimum, $R = 1$, thus maximizing synchronizability. Networks with this particular structure are known as *maximally synchronizable networks* (MSN) [6].

In the following sections we summarize our experimental study of MSNs, as well as a theoretical proposal for the study of topological noise, which is then validated experimentally. The numerical solution of ordinary differential equations by means of Runge-Kutta numerical integrators and the computation of Lyapunov exponents in connection to MSFs were performed using codes written by the authors. The compilers and computational resources at the ENEA Cresco facility in Portici made this computationally demanding analysis possible.

2 Maximally synchronizable networks: experimental implementation

Any undirected (connected) network can be converted into a MSN by the procedure illustrated in Fig. 1 [6]. The resulting topology is that of a directed network with a weighted adjacency matrix such that $W_{ij} = 1/k_i^{in}$ if there is a link $(j \to i)$ or zero otherwise. The elements of the Laplacian matrix are

$$\mathcal{L}_{ij} = \begin{cases} 1 & \text{if } i = j > 1 \\ -1/k_i^{in} & \text{if } j < i \text{ and } i \text{ and } j \text{ are connected} \\ 0 & \text{otherwise} \end{cases} \tag{1}$$

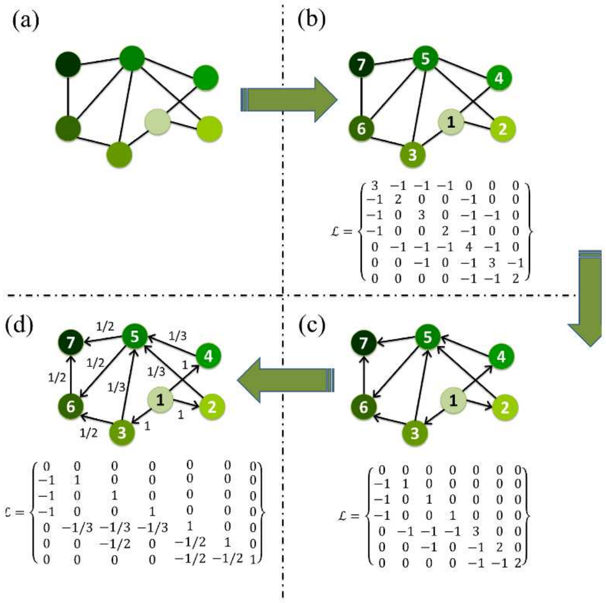

Figure 1: **Construction of MSN.** (a) Starting from a weighted undirected network, (b) the first step is the numbering process, which consists in selecting an initial node and sequentially numbering its first neighbours. The process is repeated for successive layers of neighbors until the whole network has been numbered. (c) Next, directions are given to the links with arrows pointing from the node with the lower number to the node with the higher number. (d) Finally, the weights of the links pointing to node i are set to $1/k_i^{in}$.

This procedure can be applied to arbitrary large networks of electronic circuits by adapting the methodology first developed in Ref. [7]. In simple terms, a large unidirectional network of nonlinear circuits is obtained by the sequential recording of the time series of successive layers of neighbors and the weighted reinjection of the data from previous layers using just one electronic circuit.

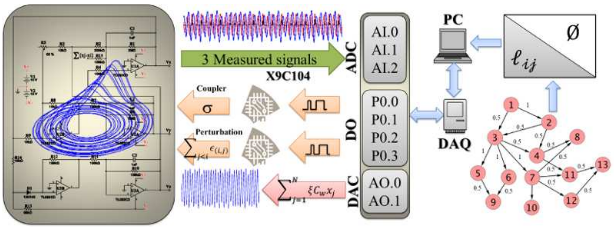

Figure 2: **Electronic implementation of a network of Rössler oscillators.** The state variables are recoded by means of an analog-to-digital card (ADC) and stored in a computer. The same circuit is used to simulate all nodes of the network, whose coupling matrix is sent from the computer to the circuit through a digital-to-analog card (DAC). A digital line (DO), controls the coupling strength and the gain product of perturbations by means of digital potentiometers.

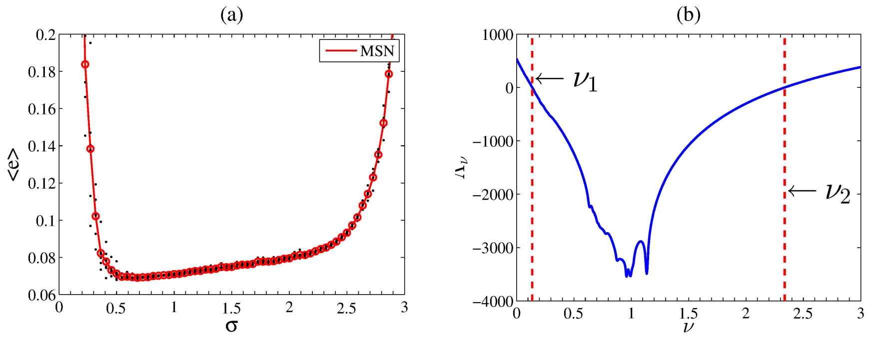

Figure 3: **Synchronization error and MSF of the system.** (a) Synchronization error $\langle e \rangle$ of experimental MSN for 6 different realizations (black dots) and the average across realizations (red continuous line). (b) Numerically obtained MSF. Dashed lines indicate the values of $\nu_1 = 0.137$ and $\nu_2 = 2.337$.

Our experimental system is a network of piecewise linear Rössler-like electronic circuits [8, 9, 10]. The full set-up is illustrated in Fig. 2. Regarding the network topology, we have considered both scale-free and random networks of different sizes. We report the results obtained with scale-free networks of $N = 200$ (the largest size considered), as this is the most relevant case from an experimental viewpoint.

We capture the dynamics of the $x(t)$ variable of each circuit and compute the overall synchronization error in the network as $\langle e \rangle = \sum_{i,j} D_{x_i x_j}/N^2$, where $D_{x_i x_j} = \langle |x_i(t) - x_j(t)| \rangle$ and the angular brackets stand for time averaging. The synchronization error $\langle e \rangle$ as a function of the coupling strength σ is shown in Fig. 3 (a), where points corresponding to six different dynamical realizations of the same MSN are shown, and the continuous line is the average. We can see that the system is synchronized from, roughly, $\sigma = 0.40$ to $\sigma = 2.40$. The fact that the system becomes unsynchronizable for low and high values of σ indicates that the Rössler system coupled through the x variable is a class III system (i.e. a system with a bounded synchronizability region). This fact is confirmed when the MSF is calculated numerically, as shown in Fig. 3 (b). Since the MSN has $\lambda_2 = \cdots = \lambda_N = 1$, one can identify ν with σ here. We see that while the second zero $\nu_2 = 2.337$ is close to the upper boundary of the synchronization region in the experimental results of Fig. 3 (a), the first zero $\nu_1 = 0.137$ is significantly smaller than the lower boundary in relative terms, a fact that is related to the accumulation of experimental error across network layers (see Ref. [1] for a detailed explanation).

3 Topologically perturbed maximally synchronizable networks

In experiments and applications, not only is the intrinsic *dynamical* noise of the system present, but also deviations from the optimal topology can be expected (i.e., link weights could be affected by perturbations). In this section we propose some theoretical estimates about effect of *topological noise* on synchronizability, and validate these predictions numerically and experimentally. Moreover, as frequently a very detailed knowledge of the topology may not be readily available, we favor an approach to the study of this issue based on a very limited knowledge of the system topology.

Let us assume the link weights in the MSN are uniformly perturbed with additive noise. The perturbation that affects the link between the (connected) nodes i and j is denoted $\epsilon_{(i,j)}$. The Laplacian matrix of a generic perturbed MSN has one zero and $1+\epsilon_i$ for $i=2,3,\ldots,N$ along its main diagonal, where $\epsilon_i \equiv \sum_{j<i} \epsilon_{(i,j)}$ considering $\epsilon_{(i,j)}=0$ for unconnected i and j, and $\epsilon_2 = \epsilon_{2,1}$. Thus, the Laplacian spectrum is given by $\mathrm{diag}(\mathcal{L}') = \{0, 1+\epsilon_2, 1+\epsilon_3, \ldots, 1+\epsilon_N\}$. For a given perturbed topology (i.e., for a given realization of $\epsilon_{(i,j)}$ for all i and j), we define $\epsilon_{\max} = \max\{\epsilon_2, \epsilon_3, \cdots, \epsilon_N\}$, and $\epsilon_{\min}$ analogously. The perturbed graph eigenvalues that affect the synchronizability properties of the system are therefore $\lambda_2^{\text{pert}} = 1+\epsilon_{\min}$ and $\lambda_N^{\text{pert}} = 1+\epsilon_{\max}$.

In order to make some concrete predictions, one has to assume a particular distribution for the noise terms. Let us make the reasonable assumption that $\epsilon_{(i,j)}$ for all i and j are independent Gaussian random variables of zero mean and standard deviation Σ, which we denote $\mathcal{G}(0,\Sigma)$. Here, Σ plays the role of the topological noise strength. From the well-known properties of the sums of Gaussian random variables, ϵ_i are therefore random variables distributed according to $\mathcal{G}(0,\sqrt{k_i}\Sigma)$. We assume the only knowledge on the topology we have access to is a suitably defined *typical degree* k_{typ} of the network. In regular random graphs such as Erdös-Rényi graphs, it makes sense to consider the mean degree, $k_{\text{typ}} \sim \langle k \rangle$; however, in scale-free networks where $\langle k \rangle$ may be so much affected by the very large connectivity of some of the hubs, the median of the degree distribution may be a better choice $k_{\text{typ}} \sim \tilde{k}$. This very rudimentary knowledge is useful in giving estimates to the effect of noise, if one has also some information about the noise strength. A typical node is perturbed by a noise $\bar{\epsilon}$ distributed according to $\mathcal{G}(0,\sqrt{k_{\text{typ}}}\Sigma)$, and we define the probability to obtain a value of $\bar{\epsilon}$ that is larger than $\Delta > 0$ as $p_\Delta \equiv (1/\sqrt{2\pi k_{\text{typ}}}\Sigma) \int_\Delta^\infty dx\, \exp\left(-x^2/2k_{\text{typ}}\Sigma^2\right)$. Obviously, the probability that $\bar{\epsilon}$ is smaller than $-\Delta$ is also p_Δ. As the noise affecting different nodes is stochastically independent, if $p_\Delta \geq 1/(N-1)$ holds, we may expect to have on average at least one node with noise intensity equal or greater than Δ in absolute value.

The procedure we propose consists in inverting the previous chain of reasoning. For a network of size N and typical degree k_{typ}, one first obtains the value $\Delta > 0$ such that the inequality above is exactly satisfied as an equality, $p_\delta = 1/(N-1)$. We denote this value as δ, while p_δ denotes the probability that a random variable distributed according to $\mathcal{G}(0,\sqrt{k_{\text{typ}}}\epsilon)$ takes on values larger than δ. We expect that there will be on average one node in the network that is affected by a noise term greater than δ and also another one that is affected by a noise term smaller than $-\delta$. Thus, we expect $\epsilon_{\max} \simeq \delta$ and $\epsilon_{\min} \simeq -\delta$, and therefore $\lambda_2^{\text{pert}} \simeq 1-\delta$ and $\lambda_N^{\text{pert}} \simeq 1+\delta$. Given the simplicity of the approximation, which is based only on knowledge of N, k_{typ} and ϵ, one cannot expect the estimates that result from it to be very precise. Nevertheless, we will see that it usefully predicts the effect of topological noise on the network synchronizability quite satisfactorily.

As we can observe in Fig. 4, the onset of synchronization is seen to occur for larger σ as the noise strength is increased, as one would expect by the fact that the smallest

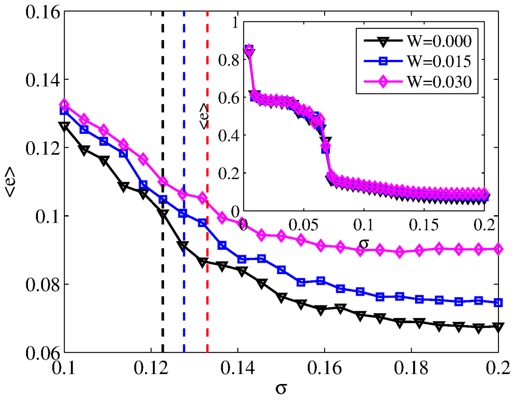

Figure 4: **Synchronization error around the first MSF zero for different topological noise strengths.** Experimental results (averages of 20 independent realizations) for $\Sigma = 0.000, 0.015, 0.030$ with $N = 50$.

eigenvalue is expected to decrease with respect to the MSN case (see the explanation above). Moreover estimates of the effect of noise on the onset of synchronization based on the previous reasoning were also obtained (using the median of the degree distribution $\tilde{k}$ as the only topological information, which plays the role of k_{typ}), showing that indeed the method outlined above is useful in predicting the effects of topological perturbations on the network synchronizability. In the experiment, it is difficult to establish a well-defined onset of synchronization, as complete synchronization is never perfectly reached, and the level of synchronization achieved for any σ is dependent on Σ. We consider the synchronization threshold to be $\langle e \rangle = 0.1$, which indicated with a black vertical dashed line for $\Sigma = 0$. The associated increases in the coupling strength σ that are needed to reach the first zero of the MSF (considering $\sigma = \nu_1/(1-\delta)$) are 4% (for $\Sigma = 0.015$) and 8.4% (for $\Sigma = 0.030$). The vertical lines in Fig. 4 mark the position of these estimates, which show a correspondence with the synchronization error curves that is seemingly in agreement with the argument above, despite its being based on rather drastic approximations. The inset shows the error across a much larger interval of σ.

4 Conclusions

We have proved the feasibility, effectiveness and robustness of the maximally synchronizable network method by means of an experiment with chaotic electronic oscillators. By doing so, we have validated the technique also in the case of non perfectly identical systems. Furthermore, our experiment allowed to monitor the propagation of the synchronization error throughout the network as the system approaches the synchronization region (not shown here), as well as to analyze the effects of deviations from the optimal topology (the maximally synchronizable configuration), in such a way elucidating the crucial role played by different types of noise in experimental realizations.

References

[1] R. Sevilla-Escoboza, J. M. Buld, S. Boccaletti, D. Papo, D. U. Hwang, G. Huerta-Cuella, and R. Gutiérrez, *arXiv preprint* arXiv:1507.02551 (2015).

[2] A. Pikovsky, M. Rosenblum, and J. Kurths, *Synchronization: A Universal Concept in Nonlinear Science* (Cambridge Univ. Press, New York, 2001).

[3] S. Boccaletti, J. Kurths, G. Osipov, D. L. Valladares, and C. S. Zhou, *Phys. Rep.* **366**, 1 (2002).

[4] L. M. Pecora and T. L. Carroll, *Phys. Rev. Lett.* **80**, 2109 (1998).

[5] M. Barahona and L. M. Pecora, *Phys. Rev. Lett.* **89**, 4 (2002).

[6] T. Nishikawa T. and A.E. Motter, *Phys. Rev. E* **73**, 065106 (2006).

[7] A. N. Pisarchik, R. Jaimes-Reátegui, R. Sevilla-Escoboza and S. Boccaletti, *Phys. Rev. E* **79**, 055202 (2009).

[8] T. Carroll T. and L. Pecora , *Nonlinear Dynamics in Circuits* (World Scientific Publishing, Singapore, 1995).

[9] A. N. Pisarchik, R. Jaimes-Reátegui and J. H. García-Lopez, *Phil. Trans. R. Soc. A* **366**, 459 (2008).

[10] A. N. Pisarchik, R. Jaimes-Reátegui, J. R. Villalobos-Salazar, J. H. García-López and S. Boccaletti, *Phys. Rev. Lett.* **96**, 244102 (2006).

Computational activities carried out at the ENEA Neutron Metrology Laboratory

Lina Quintieri[1]*, *Guido Guarnieri*[2]

[1]*ENEA Centro Ricerche della Casaccia,*
via Anguillarese, 301, 00123-Rome, Italy

[2]*ENEA Centro Ricerche di Portici,*
Piazzale Enrico Fermi, 1 - Località Granatello 80055 Portici-Napoli, Italy

Abstract. Beside its institutional role (development and establishment of primary standards of physics units for neutron measurements and their related dissemination) and the duty for neutron dosimetry equipments calibration (both assigned by the national law N. 273/1991), the Neutron Metrology Department of ENEA-INMRI (Istituto Nazionale di Metrologia delle Radiazioni Ionizzanti) is involved in multiple and various research activities, that, very often, come in the frame of scientific collaborations with other major national and foreign Nuclear Institutes, as well as in the frame of membership of European research programs. The computational activities in 2014 have concerned and supported the following research topics: study and development of innovative neutron detectors, design and characterisation of neutron sources (mainly accelerator driven), neutron dosimetry computation, design of shielding and particle dumps. All these tasks foresee to use extensively suitable codes (typically nuclear Monte Carlo codes) to predict the interaction and transport of particles through matter and, quite often, to use finite element codes to predict the thermo-mechanical response of the instrumentations and equipments concerned with the particle interaction. This report wants to present the main computational activities that have been carried out during 2014 by exploiting, in profitable way, the resources and potentialities of the CRESCO cluster. Since the detailed description of the scientific works shown in this report, can be mostly found in the dedicated and specialised published reviews (as indicated in bibliography), we focus mainly in describing the framework in which each calculation activity has been carried out, highlighting the eventual scientific contribution and, when relevant or "didactically" valid, providing with technical computational details for the way the simulations have been made running on the CRESCO cluster.

1 Monte Carlo simulations with Fluka, Geant4 and MCNPX

An intensive simulation activity is routinely carried out in the Neutron Department of INMRI ENEA. This foresees to use several major Monte Carlo (MC) codes to simulate

---

[*] Corresponding author. E-mail: `lina.quintieri@enea.it`.

radiation interaction and transport in matter. We are usually concerned with general-purpose codes that can reproduce geometric 3D configurations of materials and simulate generation and transport of many different particles over a wide energy range that goes rom few meV up to TeV: Fluka[1] [2] (60 different particles), MCNP/X[3][4](34 nuclear particles and light ions) and Geant4[5],[6](100 different particles definition).

Among the main computational activities developed during 2014, three of these are presented here:

1. MC simulations for the design and development of a new neutron detector based on GEM technology [7](in collaboration with INFN Frascati);
2. Design of a photoneutron source by high energy electrons on target (inside the "IRIDE" project [8])[9]);
3. Energy deposition profile characterisation in a high energy electron beam dump (in the frame of "ELI" project[10]);

1.1 Design of a new GEM based neutron detector: efficiency optimisation

- **Work context and scientific collaboration**: With the end of the Cold War, ^3He production from Tritium decay has been reduced significantly, while since September 2001 the demand of ^3He has increased drastically due to security program launched in US and other countries. The consequent severe depletion of the existing He stockpile and shortage reflects also on the need of a new conception of high efficiency neutron detectors in alternative to the ^3He based ones. In collaboration with INFN-LNF we contributed to the study and design of a new thermal neutron detector based on the Gas Electron Multiplie (GEM) technology: the "Side-On" neutron detector [11], whose conceptual schematic is shown in figure 1. It consists of a sequence of glass plates with their wider coated surface perpendicular to the neutron incident beam. The electric field is perpendicular to the main neutron beam direction and to the GEM foils.

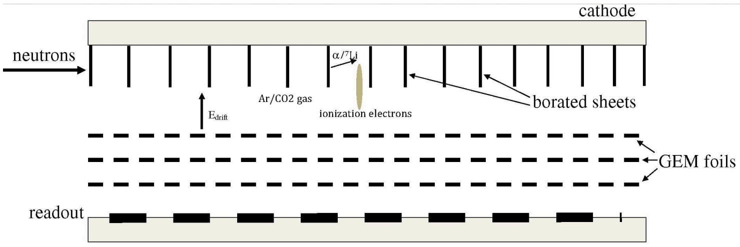

Figure 1: Schematic of the SideOn detector

Monte Carlo simulations have been performed using both Fluka and Geant4 code, aimed at seeking the optimal geometrical set-up and material thickness to achieve the best possible detector efficiency: that is performing the optimal choice of the employed materials, of the thickness of the converter coating and substrate and, finally, of the gas gap volume and pressure.

- **Main results**: The designed detector relies on the conversion, by suitable nuclear reactions, of the impacting neutrons into charged particles that can ionise the surrounding gas (Ar/CO_2). The secondary electrons produced by ionisation in gas are then accelerated toward the collecting cathode by GEM foils. Each GEM foil is made of a thin Kapton substrate (60μm thick), coated with 5 μm Copper. The GEM foils are perforated with conic holes (50 μm average diameter) distributed uniformly on the surface according an horizontal and vertical pitch of 140 μm. The electric filed lines concentrate in the holes, causing in such a way a more effective multiple ionisation process and so allowing to reach much higher gain for electric signals with lower voltage. Simulations have been performed with Fluka and Geant4 in order to individuate the configuration that maximises the conversion efficiency, defined as the number of charged particles that enter into the gas and ionise it, per incident neutron. Two different coating materials have been considered: ^{10}B and LiF. The related nuclear reactions that allow to convert neutron in charged particle are $^{10}B(n,\alpha\gamma)^7Li$ in the Boron coating and $^6Li(n,\alpha)^3H$ in the LiF coating, respectively. MC results of our simulations show that, increasing the converter thickness, the number of charged particles produced differs significantly from the number of charged particles that reach the gas region and this effect becomes appreciable for coating thickness much lower than the respective α and ion ranges in the converter materials. This is explained considering that the reaction products are emitted quite isotropically, so that the charged particles that are traveling with a large solid angle have a higher probability to be absorbed inside the coating. Accordingly to this, figure 2.a shows how the angular distribution of the α entering into the gas changes as a function of the coating thickness. The spatial distribution is quite uniform over all the solid angle only for very thin coating thickness ($< 400nm$, whose distribution is shown in figure 2.b), while for higher values, two regions can be distinguished: a central zone, where the particle density is quite uniform and an external one, where the particle density decreases almost linearly with the θ angle (defined as the solid angle between the emitted particle and the perpendicular to the plate coating surface). In figure 3 the energy deposition profile in case of a single plate with 300nm ^{10}B thickness is shown together with the energy spectra of α and ^7Li ions. Finally, in order to increase the detection efficiency, several parametric calculations have been performed to individuate the optimal configuration of a multiple plates stacked in a fixed volume: the results of these calculations provided with the optimal distance between plates according to the nergy deposition profile in the gas and the optimum converter material thickness for a fixed number of plates. We found that, for example, in case of 5 plates detector with 0.6 cm gas gap in between, there is an optimum thickness that maximises the charged particle conversion efficiency (per incident neutron): for ^{10}B coating, it is about 2μm for the 5 plates arrangement (the analysis of LiF coating case is still in progress).

- **Computational details**: In Fluka, light fragments (α,triton) from neutron capture in ^{10}B and ^6Li are transported if the option *"point-wise transport"* is activated by the

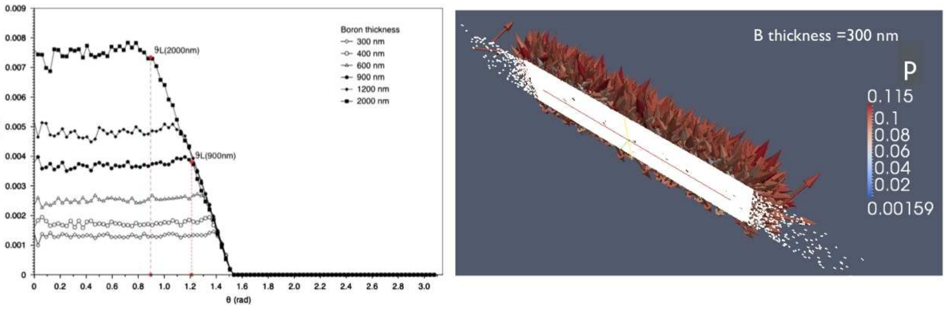

Figure 2: Left side (a): Forward angular distribution, with respect to the neutron primary beam direction, of the α leaving the plate and entering into the gas as a function of the ^{10}B thickness. Right side (b): vectorial plot of momentum of α entering into the gas for the case of 300 nm ^{10}B thickness.

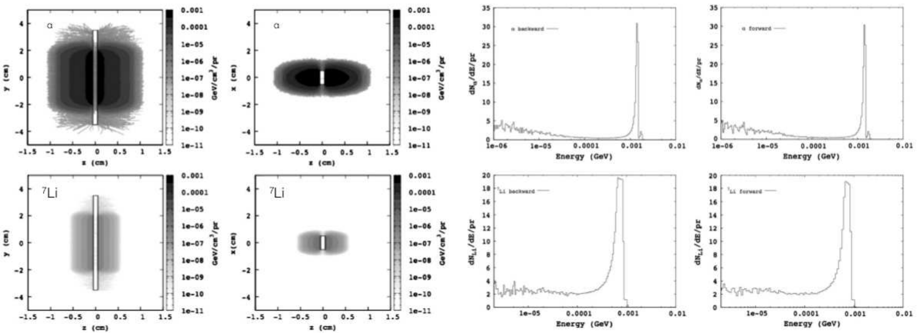

Figure 3: Left side (a): spatial distribution of the energy deposited by α (top) and ^{7}Li ions (bottom) in case of 300 nm ^{10}B thickness. Right side (b): energy spectra of α (top) and ^{7}Li ions (bottom) escaping from boron layers and entering into the gas region, in case of 300 nm ^{10}B.

user. All other charged secondaries, including fission fragments, are not transported but their energy is deposited at the point of interaction (kerma approximation). Moreover when using the evaluated data libraries, there is non-correlation between energy and angle for secondary particles produced by neutrons in inelastic processes (with gamma emission), so that, when possible, it would be preferable to use theoretical models do describe the physical processes. In order to explicitly produce, in Fluka, α and ^{7}Li ion pairs from the neutron interaction on ^{10}B, it is needed to:

- Define a monoisotope material named BORON-10 and associated to it the ^{10}B low energy cross section (< 20 MeV)
- Activate the ion transport (i.e. α and ^{7}Li) with IONTRANS card and set an appropriate ion transport threshold with PART-THR applied to 4-HELIUM (Li7 will get the same energy per nucleon threshold)
- Choose the option *point-wise* -XS (cross Sections) in LOW-NEUT transport card: this is available and possible only for few isotopes: ^{10}B and ^{6}Li

The same procedure has to be applied for ^{6}Li in case of LiF coating.

In Geant4, the inelastic interactions at low energies are handled by one of the intranuclear cascade models or the precompound model. In particular, the nuclear capture of neutrons at rest is described using either the Chiral Invariant Phase Space (CHIPS) model or the Bertini intranuclear cascade. For our simulations, the *QGSP-BIC-HP* referenced physics list has been used. Geant4 and Fluka have been run in serial way and in batch mode on CRESCO3 and CRESCO4 clusters. The resources of CRESCO clusters, as well as all the resources of the Enea computational grid, are managed by LSF (Load Sharing Facility) software. To submit batch jobs on CRESCO clusters the LSF command bsub is available. The commands used to run in batch on CRESCO facility are listed below:

Fluka:
```
bsub -o file.dat -e file.err -q cresco_queue /path/jobScript
```

Geant4:
```
bsub -o file.dat -e file.err -q cresco_queue -R "select[type==huge_mem]"
/path/bin/Linux-g++/executable
```

where

- *jobScript* is an executable file (by command: chmode +x *nomefile*) that contains the following instructions for launching Fluka:

  ```
  export FLUPRO=$path/fluka2011.2b
  #$FLUPRO/flutil/rfluka -e $path1/myfluka -N0 -M10 $path2/input.inp
  $FLUPRO/flutil/rfluka -N0 -M50 /path2/serial_neut.inp
  ```

- "*executable*": is the executable produced by compiling the Geant4 application

The option [`-R "select[type==huge_mem]"`] is used in order to select the computational nodes with large amount of memory, whereas [`-o file.dat -e file.dat`] is used to redirect the standard output and the standard error of the job and, finally, [`-q cresco_queue`] is used to select the appropriate submission queue.

1.2 Design of an accelerator driven photoneutron source: the IRIDE project

- **Work context and scientific collaboration**: IRIDE [8] is a proposal and preliminary conceptual design of an intense particles beam factory. It should produce high fluxes of electrons, photons (from infrared to γ-rays), neutrons, protons and eventually positrons, for multidisciplinary investigations in a wide field of scientific, technological and industrial applications. The IRIDE collaboration involves research Institutions and Universities from many countries all over the world: Italy, France, Germany, Portugal, Spain, Poland, Ukraine, USA, China and Brazil. Neutrons are intended to be produced by sending high energy electrons against a heavy target. Electrons interact in the target producing mainly bremsstrahlung radiation with continuous energy spectrum, whose end point is equal to the maximum electron energy. These secondary photons can excite the nuclei of the target, that decay back into the fundamental state evaporating nucleons (typically one or more neutrons) or expelling hadrons (pion, proton, etc). In this context, our main task was the study, design and optimisation of the target for photo-neutron production. Finally the energy spectra of the secondary hadrons (neutrons, protons and pions) escaping from the target have been estimated in order to properly and completely characterise the hadron source.

- **Main results**: The designed target for neutron production for IRIDE is a bulk cylinder made of natural Tungsten with 7 cm diameter and 6 cm height. The neutron yields and the fluence energy spectra (integrated over all the solid angle) have been estimated as a function of the impinging electron energy, from 50 MeV to 2 GeV. The electron beam has been assumed to have a gaussian energy profile, with an energy spread less than 0.1%. Moreover, the primary electron beam is supposed to impinge at the center of one of the two flat faces, along the cylinder axis, with 0 divergence and with a transversal spot size of 2mm diameter. The isolethargic energy spectra profile parametrised by the primary electron energy are shown in figure 4.a. It can be seen that for $E_{e-} < 100MeV$ the only relevant mechanism of production is the GDR (Giant Dipole Resonance): neutrons are emitted from the nuclei mainly for evaporative process with average energy around 1 MeV. The main contribution in the spectra at higher energies comes from the Quasi Deuteron Effect and from the pion decay intranuclear cascade. The bump around 140 MeV is due to the pion reabsorption. In order to predict, with a certain confidence level, the expected yields and energy spectra of neutrons from the IRIDE target, several Monte Carlo (MC) simulations have been performed using Fluka, MCNPX and Geant4. The comparison of results obtained with different codes, when experimental benchmarking is not easy to accomplish, is of great importance especially for the assessment of the estimation of the high energy component of the generated neutrons. In fact due to the poorness of experimental nuclear data for energy higher than 20 MeV, the MC predictions have to rely mainly on different implemented physical models (intranuclear cascade, etc). In figure 4.b, the energy spectra of the escaping neutrons (integrated over 4 π) as predicted by Fluka, MCNPX and Geant4, respectively, are compared: for $E_n > 5$ MeV, the energy spectrum profile of Geant4 and Fluka match closely each other, while MCNPX shows a pion reabsorption bump smoother than expected. On the

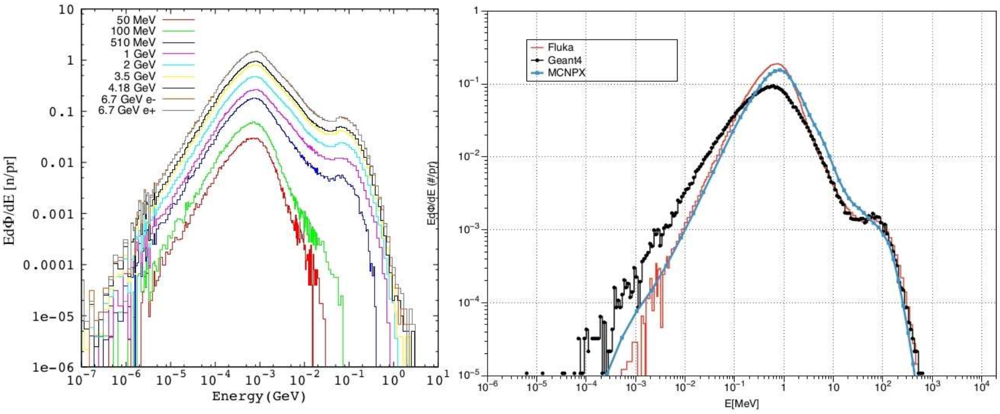

Figure 4: Left side (a): Expected energy spectra of neutron leaving the target parameterized with the primary electron energy; Right side (b): Energy spectrum of neutron escaping from the target: comparison between Fluka, Geant4 and MCNPX at 1 GeV

Table 1: IRIDE neutron yield for 1 GeV electron primary beam

code	‘n/pr’	Evaporation Peak [MeV]
Fluka	0.42	0.72
MCNPX	0.39	0.79
Geant4	0.3	0.65

contrary, For $E_n < 5$ MeV, the giant dipole resonance estimated by Geant4 appears wider and lower with resect to the more consistent Fuka/MCNPX ones. The total neutrons leaving the target are reported in Table 1 together with the evaporation peak energy: the neutron yield predicted by Fluka and MCNPX is quite well in agreement (within 7%), while Geant4 underestimates of more than 20%. Fluences of other hadrons escaping from the target have been also estimated: in case of 1 GeV primary electrons, the total yield of protons is estimated to be more than 2 order of magnitude less intense than the the neutron yield (around 1E-3 p/pr, in the specific case, against 0.4 n/pr). This can be easily explained since the expulsion of protons from nuclei is strongly repressed from the columbian barrier in case of high Z nuclei. Protons leaving the target have an energy spectrum that extends from 1 MeV utp to 1 GeV, mostly peaked around 100 MeV. In figure 5 the spatial distribution of expected neutrons and protons around the target is shown: while neutrons are emitted quite isotropically, protons are mostly directed forward along the primary electron beam impinging direction (z axis form right to left).

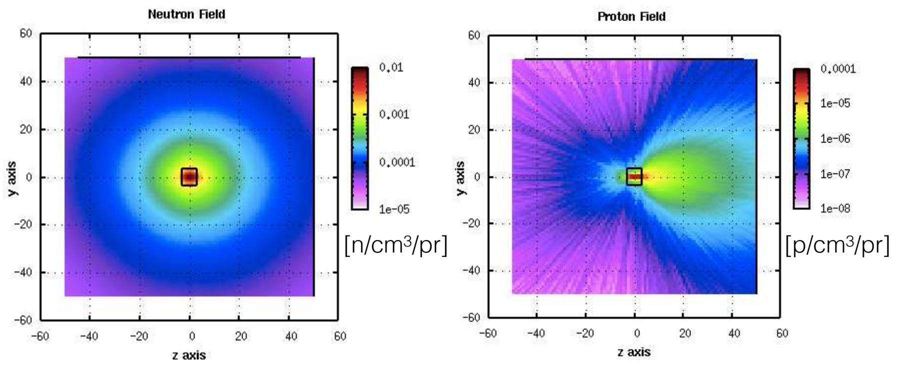

Figure 5: Neutron and proton density around target.

- **Computational details**: Photonuclear calculations are typically complex and heavy from the computational point of view, since they require extensive libraries of isotopic data, high statistics simulations and, very often, adequate biasing techniques (due to the low photo-neutron cross sections). In order to have accurate predictions for the photo-neutron yields, high statistics and variance reduction methods have been applied, so that the possibility to perform parallel calculations on CRESCO cluster was fundamental to achieve statistically significant results with reasonable cpu time.

Intensive parallel computation has been performed with MCNPX. Simulations have been submitted in batch by the following command:

```
/path/bin/mcnpx.run n_core file.inp file.out cresco4_256h24
```

In this case `mcnpx.run` a wrapper for LSF environment that needs as parameters the input file and the submission queue.

On the other side, since Fluka has been run in serial mode, in order to improve the statistics and to save computational cpu time, the LAM-BIAS card has been activated to reduce the inelastic interaction length of photons of two order of magnitude, as specifically shown hereafter:

```
LAM-BIAS          0.0       0.01  TUNGSTEN    PHOTON
```

In this way, the photon inelastic interaction probability is artificially increased by a factor 100 (photon inelastic interaction length set equal to 0.01), but, at the same time, the physics in not affected, since the weight of the produced neutrons is automatically set equal to 0.01, saving the neutron balance (n = probability $\cdot$ weight). The great advantage in using this bias is that the statistic error is reduced because it goes with the inverse of the square root of the generated neutrons ($1/\sqrt{N}$).

2 Finite element simulations: ANSYS calculation for thermal transient analysis

2.1 Thermal transient in the Eli dump

- **Work context and scientific collaboration**: The project Extreme Light Infrastructure (ELI)[10] is part of a European plan to build a new generation of large research facilities selected by the European Strategy Forum for Research Infrastructures (ESFRI).The first facility (ELI Beam lines) will be located in the Czech Republic and will create a new generation of secondary sources for interdisciplinary applications in physics, medicine, biology and material sciences. The second centre (ELI Attosecond) is being arranged in Hungary and is to be focused on physics of ultrashort optical pulses in attosecond order. And finally, the third centre (ELI Nuclear Physics) aimed at photonuclear physics should be located in Romania. In collaboration with the INFN, we did the preliminary design of the main dump for 800 and 320 MeV electron beam lines, respectively. Particle dumps are commonly used in accelerators with the main goal to absorb completely the energy of the primary beam, limiting as much as possible the release of the ensuing secondary radiation produced inside the dump itself. For this reason the high energy particle dumps are made of several materials, to shield and absorb either electromagnetic radiation (electrons, gammas, positrons) either the hadronic one, mainly constituted of photo-produced neutrons. Several configurations have been studied and analysed in order to individuate the best configuration, according the following design criterium: keeping the ambient dose around the dump at the safe required level, minimising the geometrical dimension and reducing, as much as possible, the need of an active cooling system. The information about the axial and radial profile of the energy density has been first estimated by Fluka and afterward properly insert in the input of ANSYS simulation, to perform adequately the transient thermal analysis. In figure 6 the finite element model for one of the studied ELI dump configuration is reported; different colours are associated to different materials: green for concrete, magenta for Lead, red for Tungsten and blu for air. The results recalled and commented in the next paragraph item refer to this configuration: a multi layered cylinder with 150 cm external diameter and 140 cm total length.

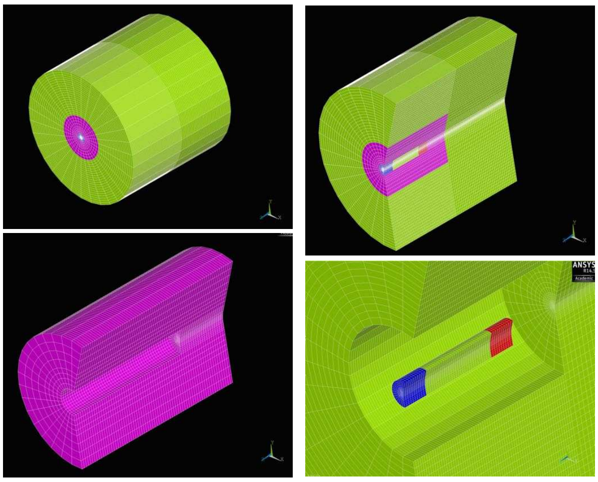

Figure 6: 3D mesh of ANSYS model for the Eli preliminary dump configuration: green is concrete, magenta is Lead, red is Tungsten and finally blue is STP air .

- **Main results**: In figure 7 the axial profile of the energy density deposition as predicted by Fluka is shown for the case of 840 MeV primary electron energy. Both the radial and longitudinal profiles have been implemented in the ANSYS finite element model, in order to apply correctly the thermal load. A first transient analysis has been performed supposing the external dump boundary to be adiabatic. The thermal load is applied according the following duty cycle: 1340 W deposited continuously (with the radial and longitudinal profile estimated by Fluka) for 168h followed by 8 hours of injection stop. This sequence is repeated until the melting temperature in Lead shell is reached ($T_{ML} = 600K$). The results of this simulation allowed to get a first insight about how much severe could be the thermal scenario for the assumed power and duty cycle and, contextually, individuate the more practical technical solutions to avoid the material melting. The envisaged solution, still, under study, foresees to implement a copper clad cooled at 40 C. Figure 8 shows both the maximum temperature in the Lead shell as a function of time and the spatial temperature distribution in Lead volume at the Lead molten point.

- **Computational details**: ANSYS calculations have been run on CRESCO4 in par-

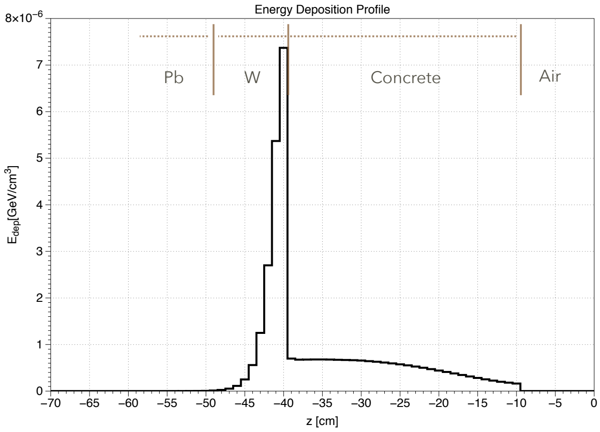

Figure 7: Linear profile of the energy deposition along the cylinder axis for 800 MeV impinging electrons. Electrons enter at z=-10 cm and move in sequence to concrete, Tungsten and final Lead dump

allel on a optimised number of cores: in fact, long transient with small time step have been simulated, requiring a remarkable amount of cpu. Moreover, the model we realised has a structured mesh, extremely fine in zone where we expect large thermal gradients and this has caused to have a huge amount of elements (672000) and nodes (2.688E+6), making the parallel option an important requirement to obtain the simulations results in reasonable time.

The command we used to submit in batch the ANSYS parallel calculations on CRESCO4 is reported in the following:

```
bsub -o file.dat -e file.err -q cresco4_16h24 jobansys
```

where *jobansys* is a wrapper for LSF environment, containing the following instructions:

```
#!/bin/sh
macchine=‘echo $LSB_MCPU_HOSTS | sed -e "s/ /:/g"‘
/path/ansys/bin/ansys145 -dis -machines $macchine -j filename -i filename.inp -b
```

The environment variable on the second row of the wrapper is created by LSF and contains the list of the computational nodes that the scheduler has reserved for the job and the number of reserved cores for each node. This variable is very useful to match the ANSYS batch command syntax on the line below.

3 Conclusion and future planning: synergic collaboration with the ENEA ICT Department

An intensive simulation activity is routinely carried out in the Neutron Metrology Laboratory of INMRI ENEA. Particularly, during the last year, the quality and quantity of

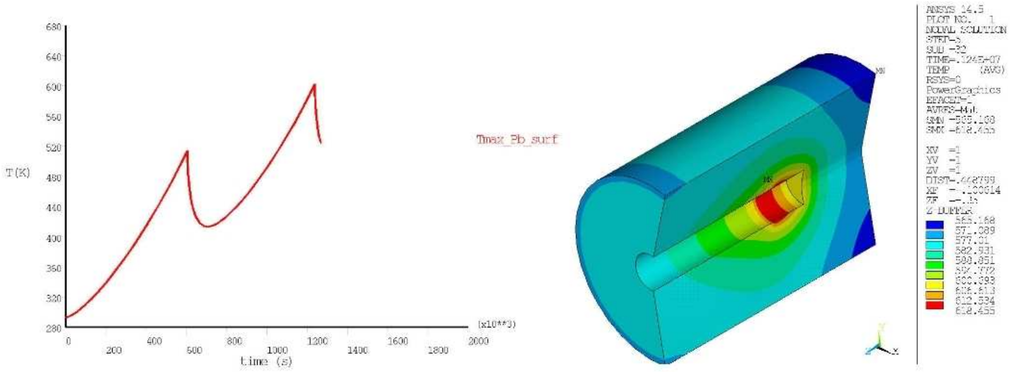

Figure 8: Maximum Lead shell temperature as a function of time and spatial temperature distribution ad melting point.

the scientific work have been increased substantially thanks to the high performance of CRESCO4 clusters. Moreover, a fundamental support and a high qualified assistance have been provided by the UT-ICT ENEA department with fruitful and synergic interactions. For the next future the computational activity is foreseen to become more intensive due to the participation of ENEA-INMRI in an important European EMPIR project: "*Metrology for accuracy of dose to patients in hadron therapy*". In the frame of this project, our task will be focused on performing simulations with the major neutron transport Monte Carlo codes, to accurately predict the unwanted neutron dose delivered to patients in accelerator facilities for cancer treatment.

Moreover, the synergic collaboration with the UT-ICT group is going to be properly addressed to describe and analyse the simulations results also in terms of those parameters that can allow to usefully assess the different CRESCO machine performances: i.e cpu comparison for the same calculations performed in different modalities or on different machines, uniformity of results as obtained by running the same simulation on different computing platforms, and many other options, that can contribute to improve the CRESCO service. One of the main goal of the collaboration is, infact, to provide a direct feedback on the performances of some important Monte Carlo nuclear codes (MCNPX, Fluka,Geant4), widely and extensively used on the CRESCO cluster, in order to individuate the optimal configuration parameters, suitable code compilation and best operative running modalities to obtain the most accurate and stable results with minimum cpu time.

4 Acknowledgment

The authors wish to thank Dr. Adolfo Santagata for the useful suggestion and discussion on MCNPX compilation.

References

[1] Nuclear Data Sheets 120, 211-214 (2014)

[2] CERN-2005-10 (2005), INFN/TC_5/11, SLAC-R-773

[3] X-5 Monte Carlo Team, "MCNP - Version 5, Vol. I: Overview and Theory", LA-UR-03-1987 (2003).

[4] D.B. Pelowitz, Ed., "MCNPX Users Manual Version 2.7.0" LA-CP-11-00438 (2011).

[5] Nuclear Instruments and Methods in Physics Research A 506 (2003) 250-303

[6] IEEE Transactions on Nuclear Science 53 No. 1 (2006) 270-278.

[7] CERN Courier, 27 November 1998. http://cerncourier.com/cws/article/cern/27921

[8] IRIDE White Book, An Interdisciplinary Research Infrastructure based on Dual Electron linacs&lasers, arXiv:1307.7967 [physics.ins-det]

[9] Nuclear Instruments and Methods in Physics Research A740 (2014) 138146

[10] White Book ELI Extreme Light Infrastructure; Science and Technology with Ultra-Intense Lasers, DOI: 10.13140/2.1.1227.0889

[11] Nuclear Instruments and Methods in Physics Research A 729 (2013) 117126

Arg and Lys selective adsorption on (101) TiO_2 anatase surface in water solution.

Lorenzo Agosta[1], *Giuseppe Zollo*[2], *Caterina Arcangeli*[3,4],
Francesco Buonocore[3,4,5], *Fabrizio Gala*[2] *and Massimo Celino*[3,4]

[1]*Department of Material and Environmental Chemistry, Stockholm University,*
2014 Arrhenius Laboratory, Svante Arrhenius väg 16C, Stockholm, Sweden

[2]*Dipartimento di Scienze di Base e Applicate per l'Ingegneria (Sezione di Fisica),*
Università di Roma "La Sapienza", Via A. Scarpa 14–16, 00161 Rome, Italy

[3]*NAST Centre c/o Università degli Studi di Roma Tor Vergata,*
Department of Physics, 00133 Rome, Italy

[4]*ENEA Italian National Agency for New Technologies,*
Energy and Sustainable Economic Development,
C.R. Casaccia, Via Anguillarese, 301, 00123 Rome, Italy

[5]*Center for Nanophase Materials Sciences Oak Ridge National Laboratory*
P.O. Box 2008 Oak Ridge, TN USA

Abstract. The adhesion of Arg, Lys and Asp amino acids on the (101) TiO_2 anatase surface in water solution is studied by total energy "ab-initio" calculations based on the Density Functional Theory to understand their contribution to the RKLPDA peptide adhesion. The amino acids have been considered in their charge states occurring in neutral water solution and bot the surface and the amino acid side chains were hydrated. The obtained results show that the polar screening of the hydration shell reduces the adsorption energy of the protonated amino acids by a small extent, thus evidencing that both Arg and Lys strongly adhere on the (101) anatase TiO_2 surface in neutral water solution playing the major role for the adhesion of the RKLPDA peptide.

1 Introduction

Interfaces between biomolecules and inorganic materials are quite important in nanotechnology, medicine and pharmacology [20] and a full understanding of the specific affinities is needed though atomistic scale modeling studies [18, 11, 25]. In particular, the RKLPDA peptide (Arg–Lys–Leu–Pro–Asp–Ala, minTBP-1) has been demonstrated to display a large and selective affinity to TiO_2 [18] that is important to develop biocompatible devices. Various experiments have indicated that the charged residues of Arg, Lys and

Asp, as well conformational patterns, have a role in the specific binding [18] indicating a competition between the two adjacent positively charged groups (Arg–Lys) [7, 9].

Classical Molecular Dynamics (MD) simulations suggested that the surface recognition is mediated by water layers at the interface and by the ability of the amino acids side chains to sense the molecular solvent structure at the surface-water interface [21, 19, 2]. Recently, ab-initio calculations have been used to model the water adsorption on various TiO_2 surfaces both of the rutile and the anatase phases [10, 22, 12, 24, 3, 14, 15, 26]. Most of the above studies were conducted on neutral amino acids but we know that in neutral water solutions they are charged. Moreover, no explicit role of water to mediate the adsorption was considered in most of the above articles and no data were reported on the amino acids included in the RKLPDA sequence.

Hence, here we report on ab-initio Density Functional Theory (DFT) studies of the adhesion on the (101) anatase surface of Arg ($C_6H_{14}N_4O_2$), Asp ($C_4H_7NO_2$) and Lys ($C_6H_{14}N_2O_2$) that are considered important for the adhesion of the RKLPDA sequence; the study is performed taking explicitly into account the role of water by using an hydrated surface [10], protonated (Lys and Arg) and de-protonation (Asp) charge states of the amino-acids typical in water solution, and solvated side chains. Our DFT scheme adopts a generalized gradient approximation (GGA) of the electron exchange and correlation energy using Perdew-Burke-Ernzerhof formula (PBE) [16], as implemented in the parallel version of QUANTUM-ESPRESSO package [5]. Ultra-soft pseudopotentials (US-PPs) [23] have been used for all the atomic species with wave functions and density energy cut-off values of 60 Ry and 400 Ry.

The (101) anatase TiO_2 surface has been modeled by using a slab geometry laying in the xy plane; the artificial electric field across the slab induced by the periodic boundary conditions and the long range forces have been corrected [4, 8], and a (2x2x1) Monkhorst-Pack k-point grid [13] for the Brillouin zone sampling has been employed. The ground state configurations have been obtained using the BFGS algorithm [6]. To avoid the difficulties due to the local charges, The adsorption energy of charged structures have been calculated on a neutral systems obtained by adding a counter-ion to the ground state configuration.

2 Results and Discussion

The (101) TiO_2 surface energy is measured as E_s= 0.523 J/m^2 with the topmost surface layer made of two-fold O^{2f} and five-fold Ti^{5f} coordinated atoms while the hydration pattern of the surface, shown in Fig. 1, is the ground state one as reported by other authors [10]. The water molecules are stably adsorbed on the anatase surface through one Ti^{5f}–O dative bond and two hydrogen bonds involving two O^{2f} surface oxygens, the adsorption energy per water molecule being E_a= -0.73 eV, in good agreement with the literature [22]. According to the recent literature, the first water layer is expected to play a major role in mediating the adsorption [21, 19, 14].

The ground state adsorption configurations of protonated Lys and Arg and de-protonated Asp on the dry (101) anatase surface are reported in Fig. 2. Both Lys and Arg are adsorbed through two hydrogen bonds (with a large electrostatic component) between

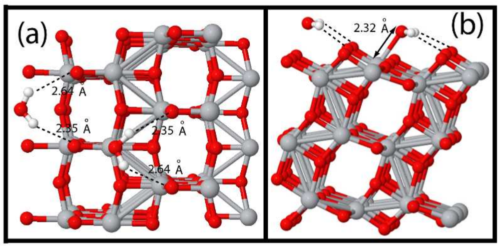

Figure 1: (Color online) Fully relaxed configurations of the hydrated (101) anatase TiO_2 surface: top (a) and side (b) views.

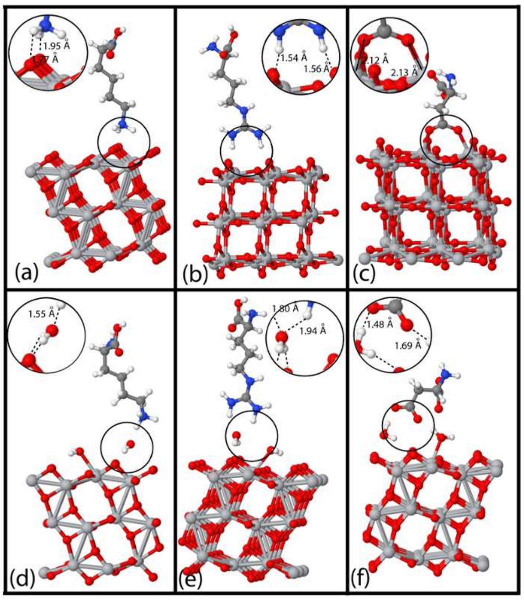

Figure 2: (Color online) Ground state adsorption configurations for Lys (a, d), Arg (b, e) and Asp (c, f) on the (101) anatase TiO_2 surface. Adsorption on the dry and the hydrated surfaces are reported in the upper and lower panels respectively.

two O^{2f} surface oxygens and two hydrogens of the -NH_3^+ terminal group (Lys) or of the protonated -$C(NH_2)_2^+$ terminal group (Arg). The last ones are stronger than the ones for Lys. On the contrary, negative charged de-protonated Asp is adsorbed at two Ti^{5f} atoms via two Ti–O bonds. The adsorption energies have been calculated including a counter-ion (OH^- for the Lys and Arg molecules, and H_3O^+ in the Asp case) in the relaxed adsorption configuration as:

$$E_{ads} = E_T - E_S - E_{amino} - E_{CI} \tag{1}$$

where E_{amino} and E_{CI} are the total energies of the isolate amino acid and its corresponding counter-ion, E_T is the total energy of the system and E_S is the slab energy.

On the hydrated surface, the amino acid adsorption is mediated by the water molecules, as shown in Fig. 2. The protonated side chains of Lys and Arg stick on the hydrated surface through a water molecule that is detached from the original Ti^{5f} adsorption site and stays close to the protonated terminal groups of the side chains, with the two H–O water bonds oriented upwards; in both cases this is due to the oxygen lone pairs that are attracted towards the electron-depleted regions of the protonated side chains.

In neutral water solution, Asp has the carboxyl group of the side chain de-protonated into -COO$^-$. Its ground state adsorption configuration on the hydrated surface, see Fig. 2(f), is such that the water molecules that mediate the adsorption still stick on the surface through one O-Ti^{5f} and one H-O^{2f} bonds while two hydrogen bonds are formed between the the -COO$^-$ group and the hydrogens of two water molecules.

The amino acids adsorption energies on the hydrated surface have been calculated again through the Eq. 1 where E_S must be replaced by $E_{S+(H_2O)_2}$ (i.e. the energy of the hydrated slab) and are reported in the Table 1. While on the dry surface Arg is just nearly 65 meV more stable than Lys, on the hydrated one Arg adsorption results favored by nearly 220 meV with respect to Lys (in Table 1). The reason of this difference is related to the kind and the number of bonds formed on the dry and the hydrated surface. On the dry surface, Lys stays attached with two H–bonds that are relatively weak [see Fig. 2(a)]. On the hydrated surface instead, Lys is adsorbed via only one O–H bond involving the water oxygen that is oriented to form a much stronger bond with a larger electrostatic contribution [see Fig. 2(d)]. Arg adsorption on the hydrated surface is still mediated by two hydrogen bonds that are weaker with respect to the dry surface (but at a smaller extent with respect to Lys). Thus, the Arg adsorption is weaker on the hydrated surface because of a bond softening with respect to the dry surface rather than a change in the number of adsorption bonds as occurs in the Lys case. The de-protonated Asp adsorption is largely weakened on the hydrated surface with respect to the dry one because of the formation of two H-bonds between the -COO$^-$ and the water hydrogens on the hydrated surface. The adsorption on Arg, Lys and Asp amino acids on the hydrated surface is thus largely mediated by the water adsorbed on the (101) anatase surface; the mechanism evidenced indicates that water molecules, linking the charged amino acids to the surface, are partially detached from the surface. Hence a question arises whether or not the amino acid adsorption may favor the desorption of the system composed of the amino acid itself and the water molecules that mediate the adsorption. The calculation of the relevant adsorption energy formula (not described here, see [1] for the details) are reported in Table 1 (see event A) showing that the occurrence of this phenomenon is unlikely. This circumstance still holds if one considers the possible involvement of another water molecule that might replace the site set free by the detachment of a water together with the amino-acid (event B in Table 1) Except for the Asp case, the adsorption energy is still quite large being approximately E_{ads}=-1.3 eV for both Lys and Arg (with a Arg slightly favored over Lys by about 30 meV) indicating that the adsorption is stable for Lys and Arg even if the dynamical equilibrium of water adsorbed on the surface is considered. On the contrary, the Asp adsorption energy drops markedly if such a dynamical equilibrium is considered.

Concerning the amino acid hydration, we have limited our analysis just to Arg and Lys that, up to the previous results, have the largest adsorption energy on the anatase surface. The solvation of the two amino acids in water solution with the RT density has been initially studied by classical MD showing that the hydration shells include 19 and 12 water molecules for Arg and Lys within 5 Å from the terminal group of the side chain.We

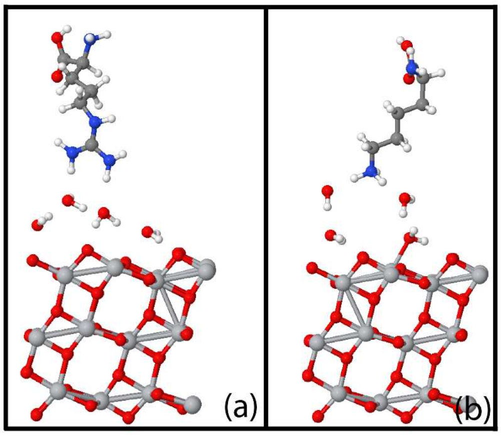

Figure 3: (Color online) Ground state adsorption configurations of protonated and hydrated Arg (a) and Lys (b) on the hydrated (101) anatase TiO_2 surface. The hydration core shell of the amino acids have been reduced to include only two water molecules in order to avoid artificial hydrogen bond chains (see the text).

have also found five regions for both the Arg and the Lys where the water molecules stay most frequently during the MD run.

After structural optimization, removing of long water networks that form at 0 K and are unlikely to survive at RT, an lastly a further structural optimization, we have obtained the ground state adsorption model shown in Fig. 3 with adsorption energy giving nearly equal values for Arg and Lys, respectively E_{ads}= -1.529 eV and E_{ads}= -1.524 eV (see Tab. 1). It is worth noticing that for these configurations, both the (101) anatase surface and the amino acids are basically separated by two water layers. The adsorption energy data of the protonated and hydrated amino acids reveal that a considerable surface adhesion is still present and that the screening of the closest hydration shell reduces the adsorption energy of Arg to the same value as Lys that have the same charge states, thus showing that the presence of water makes the interaction studied basically of electrostatic nature. In summary the adsorption of protonated (Arg and Lys) and de-protonated (Asp) amino acids on both dry and hydrated (101) anatase TiO_2 surface has been studied using ab-initio calculations. On the dry surface the three amino acids have large adsorption energies, the protonated species being preferred over the Asp due to the stronger bonds involving Ti^{5f}. On the hydrated surface the adsorption energy values are slightly reduced but are still large to ensure the stability of the adsorption configuration. In this case the adsorption involves water molecules and the protonated species attach via a water-oxygen mediated adsorption while the Asp undergoes a weaker water-hydrogen mediated adsorption; Arg seems to show a larger affinity with respect to Lys at this stage but the the water screening of the protonated side chains reduces the adsorption energy of both Arg and Lys to the same value, evidencing that both of them may contribute at the same extent to the stable adhesion of the RKLPDA sequence. Given these results further studies should focus on the Arg–Lys complex to clarify how the two protonated amino acids cooperate and why the substitution of one of them reduce the adhesion.

Computational resources for this work have been provided by the CRESCO3 and CRESCO4

Table 1: Adsorption energies E_{ads}(eV) of amino acids on the (101) anatase TiO_2 surface with and without water (first and second rows). Adsorption energies of the processes involving the desorption of surface waters (one for Lys and Arg, two for Asp) that mediate the adsorption on the (101) anatase TiO_2 surface according to events A and B (see text) are in the third and fourth rows respectively. Adsorption energy of partially solvated Lys and Arg in the fifth row (see text).

	LYS	ARG	ASP
dry (101)	-2.297	-2.362	-1.277
hydrated (101)	-1.703	-1.923	-0.427
event A	-2.151	-2.180	-1.690
event B	-1.296	-1.327	-0.233
solvated amino	-1.529	-1.524	

sections of ENEAGRID High Performance Computing infrastructure and its staff[17]. CRESCO/ENEAGRID High Performance Computing infrastructure is funded by ENEA, the Italian National Agency for New Technologies, Energy and Sustainable Economic Development and by Italian and European research programmes, see http://www.cresco.enea.it/english for information.

This work was partly supported by META-Materials Enhancement for Technological Application-Project (FP7-PEOPLE-2010-IRSES-Marie Curie Actions, PIRSES-GA-2010-269182).

References

[1] L. Agosta, G. Zollo, C. Arcangeli, F. Buonocore, F. Gala, and M. Celino. Water driven adsorption of amino acids on the (101) anatase tio_2 surface: and *ab initio* study. *Physical Chemistry Chemical Physics*, 17:1556–1561, 2015.

[2] C. Arcangeli, I. Borriello, G. Gianese, M. Celino, and P. Morales. Organic Functionalization of Metal Oxide Surfaces: An Atomic Scale Modeling Approach. *Nanoscience and Nanotechnology Letters*, 5(11):1147–1154, 2013.

[3] A. V. Bandura and J. D. Kubicki. Derivation of force field parameters for tio2h2o systems from ab initio calculations. *The Journal of Physical Chemistry B*, 107(40):11072–11081, 2003.

[4] L. Bengtsson. *Phys. Rev. B*, 59:12301, 1999.

[5] P. Giannozzi et al. Quantum espresso: a modular and open-source software project for quantum simulations of materials. *J. Phys.: Condens. Matter*, 21(19):395502–1–19, 2009.

[6] R. Fletcher. A new approach to variable metric algorithms. *The Computer Journal*, 13(6):317–22, 1970.

[7] M. Fukuta, N. Zettsu, I. Yamashita, Y. Uraoka, and H. Watanabe. The adsorption mechanism of titanium-binding ferritin to amphoteric oxide. *Colloids and surfaces. B, Biointerfaces*, 102:435–40, February 2013.

[8] S. Grimme. Semiempirical gga-type density functional constructed with a long-range dispersion correction. *J. Comput. Chem.*, 27(15):1787–99, 2006.

[9] T. Hayashi, K. Sano, K. Shiba, K. Iwahori, I. Yamashita, and M. Hara. Critical amino acid residues for the specific binding of the Ti-recognizing recombinant ferritin with oxide surfaces of titanium and silicon. *Langmuir*, 25(18):10901–6, September 2009.

[10] Y. He, A. Tilocca, O. Dulub, A. Selloni, and U. Diebold. Local ordering and electronic signatures of submonolayer water on anatase tio_2 (101). *Nature Materials*, 8:585–589, 2009.

[11] Xiaojuan Khoo, Paul Hamilton, George a O'Toole, Brian D Snyder, Daniel J Kenan, and Mark W Grinstaff. Directed assembly of PEGylated-peptide coatings for infection-resistant titanium metal. *Journal of the American Chemical Society*, 131(31):10992–7, August 2009.

[12] M. Lazzeri, A. Vittadini, and A. Selloni. Structure and Energetics of Stoichiometric TiO_2 Anatase Surfaces. *Phys. Rev. B*, 63:155409, 2001.

[13] H.J. Monkhorst and J.D. Pack. Special points for brillouin-zone integrations. *Phys. Rev. B*, 13(5):5188–92, 1973.

[14] Susanna Monti, Michele Alderighi, Celia Duce, Roberto Solaro, and Maria Rosaria Tiné. Adsorption of ionic peptides on inorganic supports. *The Journal of Physical Chemistry C*, 113(6):2433–2442, 2009.

[15] J.M.R. Muir, D. Costa, and H. Idriss. {DFT} computational study of the {RGD} peptide interaction with the rutile tio2 (110) surface. *Surface Science*, 624(0):8 – 14, 2014.

[16] J.P. Perdew, K. Burke, and M.Ernzerhof. Generalized gradient approximation made simple. *Phys. Rev. Lett.*, 77(4):3865–68, 1996.

[17] G. Ponti, F. Palombi, D. Abate, F. Ambrosino, G. Aprea, T. Bastianelli, F. Beone, R. Bertini, G. Bracco, M. Caporicci, B. Calosso, M. Chinnici, A. Colavincenzo, A. Cucurullo, P. dAngelo, M. De Rosa, P. De Michele, A. Funel, G. Furini, D. Giammattei, S. Giusepponi, R. Guadagni, G. Guarnieri, A. Italiano, S. Magagnino, A. Mariano, G. Mencuccini, C. Mercuri, S. Migliori, P. Ornelli, S. Pecoraro, A. Perozziello, S. Pierattini, S. Podda, F. Poggi, A. Quintiliani, A. Rocchi, C. Scio, F. Simoni, and A. Vita. The role of medium size facilities in the hpc ecosystem: the case of the new cresco4 cluster integrated in the eneagrid infrastructure. *IEEE HPCS*, 6903807:1030–1033, 2014.

[18] Ken-Ichi Sano and Kiyotaka Shiba. A hexapeptide motif that electrostatically binds to the surface of titanium. *Journal of the American Chemical Society*, 125(47):14234–5, November 2003.

[19] Julian Schneider and Lucio Colombi Ciacchi. Specific material recognition by small peptides mediated by the interfacial solvent structure. *Journal of the American Chemical Society*, 134(4):2407–13, February 2012.

[20] Kiyotaka Shiba. Exploitation of peptide motif sequences and their use in nanobiotechnology. *Current opinion in biotechnology*, 21(4):412–25, August 2010.

[21] Adam A Skelton, Taining Liang, and Tiffany R Walsh. Interplay of sequence, conformation, and binding at the Peptide-titania interface as mediated by water. *ACS applied materials & interfaces*, 1(7):1482–91, July 2009.

[22] Chenghua Sun, Li-Min Liu, Annabella Selloni, Gao Qing (Max) Lu, and Sean C. Smith. Titania-water interactions: a review of theoretical studies. *J. Mater. Chem.*, 20:10319–10334, 2010.

[23] David Vanderbilt. Soft self-consistent pseudopotentials in a generalized eigenvalue formalism. *Phys. Rev. B*, 41:7892–7895, Apr 1990.

[24] A. Vittadini, A. Selloni, F. P. Rotzinger, and M. Grätzel. Structure and energetics of water adsorbed at tio2 anatase 101 and 001 surfaces. *Phys. Rev. Lett.*, 81:2954–2957, Oct 1998.

[25] E. Jayne Wallace, Robert S. G. D'Rozario, Beatriz Mendoza Sanchez, and Mark S. P. Sansom. A multiscale simulation study of carbon nanotube interactions with designed amphiphilic peptide helices. *Nanoscale*, 2:967–975, 2010.

[26] Chunya Wu, Mingjun Chen, Chuangqiang Guo, Xin Zhao, and Changsong Yuan. Peptidetio2 interaction in aqueous solution: Conformational dynamics of rgd using different water models. *The Journal of Physical Chemistry B*, 114(13):4692–4701, 2010.

Storage architecture and backup strategy of ENEAGRID/CRESCO systems

F. Ambrosino, G. Bracco, A. Colavincenzo, A. Funel,
G. Guarnieri, S. Migliori, G. Ponti

Energy Technologies Department - ICT Division
ENEA — Italian National Agency for New Technologies,
Energy and Sustainable Economic Development
Lungotevere Thaon di Revel 76 – 00196 Rome, Italy

Abstract. We present the storage architecture and the backup strategy of ENEAGRID, the computing infrastructure of ENEA. Data are organized in two file systems: AFS of ∼40 TB and IBM GPFS of ∼1.3 PB. AFS is geographically distributed and provides a common work environment for accessing services and computing resources independently of the location of users. GPFS is mainly used by parallel applications to better exploit the potenziality of HPC CRESCO clusters, the main computing facilities of ENEAGRID.

1 Introduction

All computing resources of ENEA [1] are integrated into ENEAGRID [2], an infrastructure which provides a common hardware/software work environment to users. The computing resources are hosted in 6 ENEA Research Centers: Portici, Frascati, Casaccia, Brindisi, Bologna and Trisaia. ENEAGRID is based on AFS (Andrew File System) [3] a geographically distributed file system and uses Kerberos [4] for secure authentication. In addition to computing resources, the technology adopted by ENEAGRID allows to access remotely scientific instruments, rendering machines for 3D visualization, and facilitates the collaboration by providing groups of users working in the same sector of activities a common data sharing area (virtual laboratory). The main computing facilities of ENEAGRID are the HPC CRESCO [5] (Linux x86_64) clusters. In the framework of a technological renewal CRESCO1 and part of CRESCO2 have been dismissed. The systems currently in operation are: at Portici CRESCO2 (∼600 cores), CRESCO3 (2016 cores), CRESCO4 (4864 cores) and special machines SP (∼300 cores, large memory, GPU, Xeon Phi); at Frascati CRESCOF (480 cores); at Casaccia CRESCOC (192 cores). Because AFS does not support concurrent I/O and is not suitable to be used for high parallel jobs, which is the case of many scientific codes, CRESCO clusters located at Portici and Frascati are equipped with IBM GPFS (General Parallel File System) [6] a scalable, high performance parallel file system optimized for big data storage management. To guarantee data preservation and reliability , along with availability during a reasonable period of time, it is essenzial to plan an efficient backup strategy. In the next sections we will describe the storage architecture of AFS and GPFS, and their backup.

2 AFS

AFS is a geographically distributed filesystem, originally developed at Carnegie Mellon University and developed as a product by Transarc Corporation (now IBM Pittsburgh Labs). It offers a client-server architecture for federated file sharing and replicated read-only content distribution, providing location independence, scalability, security, and transparent migration capabilities. AFS is available for a broad range of heterogeneous systems including UNIX, Linux, MacOS X, and Microsoft Windows. IBM branched the source of the AFS product and made a copy of the source available for community development and maintenance (OpenAFS).

An AFS infrastructure consists of DBservers (for storing metadata and authorization information), and file servers (for storing actual files). The Dbservers host three different types of servers: vlserver (stores metadata), ptsserver (stores authorization information) and backup server (stores metadata about the native AFS backup). Any machine that needs to access AFS has to install the AFS client, which as written above, is available for many different architectures.

While AFS authentication mechanism was based upon an internal implementation of Kerberos 4 nowdays it is fully integrated with modern Kerberos 5 whose tickets are converted into AFS tokens so that the access to directories in AFS is granted according to the token available to the user. The connected authorization mechanism is based on an ACL mechanism, much more powerful and flexible than the standard POSIX permissions.

The main entity of AFS space is the AFS cell (`/afs/enea.it/` for ENEAGRID) while the physical data space is organized in logical units called Volumes. Each AFS volume can be a read-write volume (fully accessible space), or a read-only (a replica). A feature of AFS is its ability to be able to maintain a snapshot of each volume, stored in a special, optimized backup volume.

In ENEAGRID AFS is used as a unified, scalable and distributed data space mainly for users homes, for shared software applications and libraries and finally for project collaborative data area. In all these contexts the rich AFS ACL mechanism offers a very flexible solution to tailor the access to the users and projects requirements. A dedicated web server, `www.afs.enea.it`, exports to the web the content of selected data area both for users, software and projects. Another web server, `okbox.enea.it`, provides direct web access to user defined data area dedicated to collaborative project activities, offering a user delegated mechanism to grant access to non ENEAGRID users, mainly project partners and collaborators.

At this moment ENEAGRID AFS cell operates with 3 main DBservers located at the Frascati site, and other 5 slave dbservers located in the other Centers (clone DBservers in AFS framework), two of them in the main CRESCO site at Portici. AFS data are stored in 10 files servers (3 of them at Portici site) for a total of about 10 TB out of 30 TB of capacity structured in about 3000 AFS volumes.

3 GPFS

GPFS is a high performance distributed parallel clustered file system developed by IBM. It provides concurrent high speed file access to applications running on multiple nodes of a cluster running any mix of AIX, Linux or MS Windows Server OS. A GPFS file system is a collection of NSD (Network Shared Disk) that can store data and metadata. Usually a GPFS cluster is structured to have dedicated I/O servers and distinct compute clients running applications that access virtual disks via file system. A virtual disk can be accociated to any device (HD, partions, LUN on storage system etc.). The current maximum GPFS cluster size limit is 9620 nodes for Linux. The architectural limit of the number of files in a file system is 2^{64}; the current architectural file system size limit is 2^{99} bytes and the maximum number of file systems that can be mounted in a GPFS cluster is 256. In addition to file system storage capabilities, GPFS provides powerfull tools for management and administration of the GPFS cluster and allows for shared access to file systems from remote GPFS clusters providing a global namespace. GPFS achieves high performance I/O by striping blocks of data across multiple disks, and reading/writing them in parallel. If a high speed interconnect is available for data movements the I/O throughput takes additional advantage. A wide range of file system block size are supported to match I/O requirements. Preservation of data during concurrent access is guaranteed by a sophisticated token management system based on block level locking. GPFS provides access to files through standard POSIX interfaces, but provides also non-POSIX advanced features the most important of which are: DMAPI (Data Management Application Programming Interface) which allows to monitor events associated with a GPFS file system; ILM (Information Lifecycle Management) which allows to define policy-driven automation and tiered storage managements; AFM (Active File Management) which enables data sharing across unreliable or high latency network; Native RAID which is a software implementation of storage RAID whitin GPFS. For each file system disk quota control can be activated at user and group level. A GPFS file system supports ACL for files and directories either on the POSIX or NFS v4 model.

4 Storage

In Fig. 1 is shown the ENEAGRID/CRESCO GPFS storage architecture of the Portici site which is organized in two clusters each of which with its own private IB (InfiniBand) [7] network, the one (GPOR) based on IB 4xDDR (20 Gbps), the other (GPORQ) on IB 4xQDR (40 Gbps). The computing nodes of GPOR are those of CRESCO2 whereas to GPORQ belong the nodes of CRESCO3, CRESCO4 and SP. GPOR and GPORQ can access remotely each other file systems via public GEthernet (1 Gbps) interface. GPOR storage is provided by two systems: an IBM DCS9550 and a Server Storage Supermicro SC846E1. Data stored on IBM DCS9550 are organized in 4 file systems 30 TB each, with 4 NSD servers; data on Supermicro SC846E1 are organized in four file systems each of which of 20 TB and with 1 NSD server, dedicated to MINNI [8] project.

GPORQ storage is distributed over various systems. A DDN S2A9900 provides 600 TB (raw) out of which 270 TB are organized in two file systems of 90 TB each dedicated to

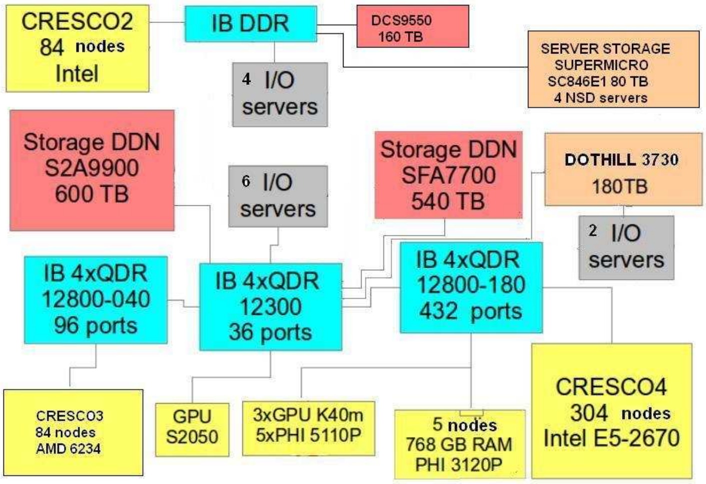

Figure 1: The storage architeture of ENEAGRID/CRESCO. In figure is shown the configuration of the Portici site, which hosts the main part of the storage.

users, and one file system of 90 TB dedicated to climate research. These file systems use 6 I/O NSD servers. To MINNI project is also dedicated a DotHill 3730 storage system of 180 TB (raw) out of which 130 TB are organized in a file system with 2 I/O NSD servers. This storage system is also used by the VMWare Cloud infrastructures hosted in Portici. There are two installations, both based on VMWare vSphere ESXi 5.5, one with the VMWare free solution and the other with the licensed one. There are proper areas on the DotHill 3730 storage system (i.e., LUNs) dedicated to these systems to host the virtual resources, for a total of 15 TB. In detail:

- 2 LUNs of 2 TB for VMWare free;
- 2 LUNs of 2 TB for VMWare licensed;
- 1 LUN of 1 TB shared between the two systems;
- 1 LUN of 6 TB as backup area of the virtual machines.

In 2015, a DDN SFA7700 storage system of 540 TB (raw) has been purchased, which is under test for production at the moment.

To ENEAGRID/CRESCO infrastructure belongs another GPFS cluster (GFRA) hosted in Frascati site whose computing nodes are those of CRESCOF. The network of GFRA is based on IB 4xQDR (40 Gbps). Its storage is provided by an IBM DS4700 system and data are organized in a file system of 8 TB with 2 I/O NSD servers. GPFS clusters of Portici and Frascati have a geographic multicluster configuration which allows the computing nodes of one cluster to access the file systems of the other over WAN.

Figure 2: The IBM Tape Library TS3584.

5 Backup

As illustrated in the previous sections the ENEAGRID/CRESCO data space architecture is based on two main components, the open source OpenAFS for user homes, software and project collaborative area, and the proprietary high performance parallel file systm GPFS, for HPC data I/O, both for scratch area and long term data preservation. Both OpenAFS and GPFS data area are covered by backup systems using different technologies.

OpenAFS data space has a limited size in the order of 10 TB and its backup is managed using the native AFS backup system. OpenAFS backup system operates at AFS volume level. It obviously fully supports the OpenAFS ACL and permits both full and incremental backup operations. AFS backup operation makes use of a dedicated volume snapshot, performed every night on all the AFS file-servers so that the backup procedure can run together with the normal operation of the file system without any problems.

In ENEAGRID/CRESCO the AFS backup server is located in Portici and all AFS backup data are saved on a storage local to the backup server (at the moment 36 TB raw, divided into 2 independent RAID6 arrays). A full backup of the entire `enea.it` AFS cell is run every 6 months, and it takes about two weeks time. On the first day of each month an incremental backup (with respect to the available full) is run, lasting at most a couple of days, while each night an incremental daily backup, (with respect to the monthly backup) is run lasting about one hour. In this way it is always possible to restore an AFS Volume at its status at the night of each day of the previous six months. The AFS backup data are also replicated on the GPFS file system and subjected to the standard GPFS backup procedure, that will be described later.

On CRESCO HPC cluster GPFS is used both as scratch area and as long term storage system. In the backup context GPFS backup is mainly devoted to data recovery in case of severe problems to the storage hardware, as a disaster recovery solution.

The GPFS backup system is based on another IBM product, TSM [9], and the backup media on Portici site is a 5 frames IBM Tape Library TS3584, (see Fig. 2), located in the original CRESCO Computer Room. At present it has 7 LTO4 drives serving 1540 cartridges (a total of 1.2 TB) and 2 LTO6 drives for 420 cartridges (a total of 1050 TB). The library is divided in two virtual library to separate the LTO4 and the LTO6 environments.

The LTO4 backup system is in operation since 2008, is based on TSM 5.5.0 and operates with a double copy of each cartridge and with the policy of a retention period of 1 year. A new TSM service using LTO6 technlogy is currently in deployment, based on TSM 7.1.1. The GPFS backup takes into advantage of the integration between the two IBM software products, as provided by the GPFS command `mmbackup`.

References

[1] http://www.enea.it/.

[2] http://www.eneagrid.enea.it/.

[3] https://www.openafs.org/.

[4] http://www.kerberos.org/.

[5] http://www.cresco.enea.it/.

[6] http://www 03.ibm.com/software/products/en/software/.

[7] http://www.infinibandta.org/.

[8] http://www.minni.org/progetto en.

[9] https://en.wikipedia.org/wiki/IBM_Tivoli_Storage_Manager.

Edito dall'ENEA
Unità Relazioni e Comunicazione

Lungotevere Thaon di Revel, 76 – 00196 Roma

www.enea.it

Stampa: Laboratorio tecnografico – Centro Ricerche ENEA Frascati

Dicembre 2015

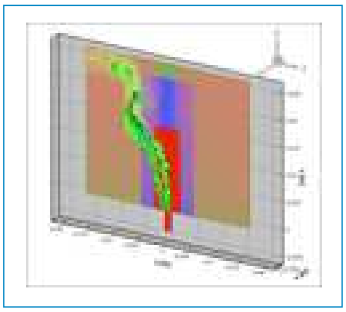
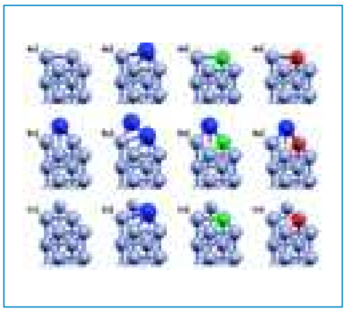
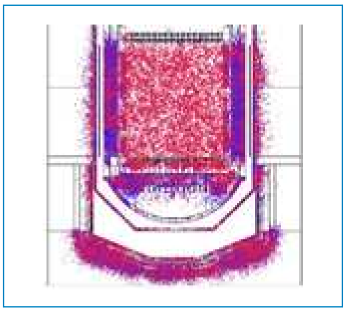
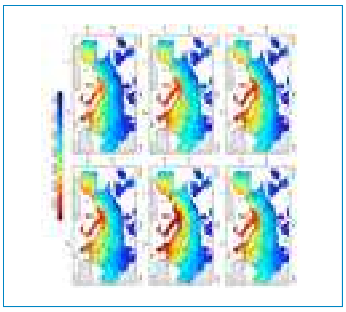
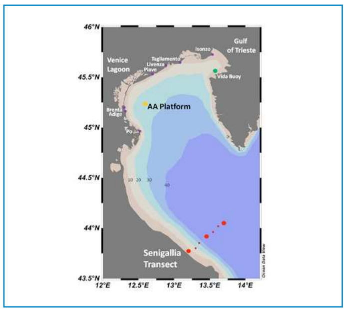
46°N
45.5°N
45°N
44.5°N
44°N
43.5°N
12°E
12.5°E
13°E
13.5°E
14°E
Venice Lagoon
Tagliamento
Livenza
Piave
Isonzo
Gulf of Trieste
Vida Buoy
AA Platform
Brenta
Adige
Po
Senigallia Transect
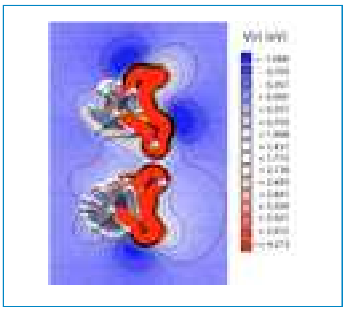
V(r) (eV)
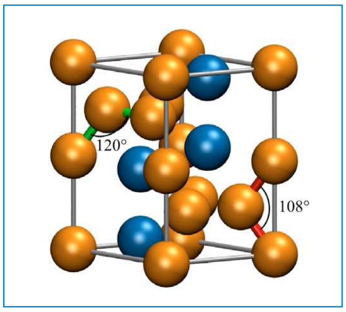
120°
108°


a)
b)